Experimental Characterization of Field-Induced Droplet Dynamics

A thesis submitted

in partial fulfillment of the requirements

for the Degree of

Doctor of Philosophy

by

Bhaskarjyoti Sarma

Department of Mechanical Engineering

Indian Institute of Technology Guwahati

Guwahati - 781 039

February 2021

TH-2590_156103041

TH-2590_156103041

CERTIFICATE

It is certified that the work contained in the thesis entitled **"Experimental Characterization of Field-Induced Droplet Dynamics"**, by **Bhaskarjyoti Sarma** has been carried out under our supervision and that this work has not been submitted elsewhere for a degree.

(Amaresh Dalal)
Professor
Department of Mechanical Engineering
Indian Institute of Technology Guwahati

(Dipankar Narayan Basu)
Associate Professor
Department of Mechanical Engineering
Indian Institute of Technology Guwahati

February 2021

TH-2590_156103041

TH-2590_156103041

Abstract

The manipulation of a discrete liquid droplet or a group of droplets with or without the deformation of the liquid-vapour interface in the presence of an externally stimulating field is an integral part of *Lab-On-Chip* devices, which in turn determines the performance of target applications. A detailed appraisal of the underlying rich physics associated with the deformation and/or disruption of the continuous two-phase interface and the behaviour of the contact line during the actuation of a droplet over an open surface or inside a closed channel, engendered in the presence of an external force, apparently contribute towards enhancing the efficacy of numerous microfluidics applications. In this regard, a plethora of complex hydrodynamic features during actuation, mixing, merging, or splitting of discrete droplets have been unfurled by the scientific community over the past years. However, owing to the growing demand for microfluidics platforms in a host of cutting-edge engineering and biomedical applications, it has become necessary to assess the existing or novel droplet-based physical systems more comprehensively. Thanks to the advancement of high-speed visualization tools and computational techniques, the latter task has become easier nowadays. The present thesis work draws enormous motivation from the aforementioned observations and makes an honest attempt to uncover the rich physics associated with the behaviour of single liquid droplets in the presence of external potentials, such as electric field, magnetic field, imposed inertia, etc., in a few interesting and unexplored physical systems. The problems addressed within the scope of the present thesis include the growth dynamics of a droplet from a yarn, softness mediated magnetowetting of sessile ferrofluid droplets, electric-discharge-mediated atomization of a conducting sessile droplet, and impact dynamics of viscous droplets on a superhydrophobic surface. Overall, the focus has been laid on experimentally characterizing the temporal evolution of the shape and contact line(s) during the growth/deformation phase of a droplet and the subsequent atomization dynamics of the primary droplet. Apart from the externally applied field, the effect of thermophysical properties of the liquid and properties of the substrate in contact have also been characterized during the systematic experimental investigation of the aforementioned systems. High-speed imaging/videography techniques are used primarily to analyze the intricate physical details of the systems under consideration. Also, the experimental results are strengthened by scaling analysis and numerical simulations. The comprehensive experimental analysis of each system unveils several interesting hydrodynamic features, such as liquid jet formation, crown formation, bursting ejecta sheet, lamella ejection, capillary pinch-off, high-speed hair-like jets emanating from a parent droplet exposed to different external stimulations. The aforementioned flow morphologies contribute enormously towards the effective atomization of the parent droplet, desirable for many microfluidics applications. The contributions from this thesis work are expected to pave the way for several new research avenues in microfluidics.

TH-2590_156103041

TH-2590_156103041

कर्मण्येवाधिकारस्ते मा फलेषु कदाचन |
मा कर्मफलहेतुर्भुर्मा ते संगोऽस्त्वकर्मणि | | २-४७

karmaṇyēvādhikārastē mā phalēṣu kadācana |
mā karmaphalahēturbhūrmā tē saṅgo'stvakarmaṇi
| | 2.47

To work alone you have the right,
and not to the fruits. Do not be impelled by the fruits of
work. Nor have attachment to inaction.

- Bhagavad Gita.

Sānkhya Yog : The Yog of Analytical Knowledge.



Dedicated to

Maa and *Deuta*

TH-2590_156103041

TH-2590_156103041

Acknowledgements

"The roots of all goodness lie in the soil of appreciation for goodness."

- Dalai Lama, *XIV*

Research is often all about the journey, not the destination. If one had to work single-handedly on the complete journey of doctoral research, he/she/they would have never been able to reach the goal. The thesis work presented herein is built upon many individuals' contributions, both personally and professionally, in the past five years. It is not easy to name each individual and their contributions in a short note, although I am forever indebted to them. However, I will take this opportunity to name a few of my well-wishers who helped me at the forefront during my doctoral research at the Indian Institute of Technology Guwahati.

I express heartfelt gratitude to my supervisors Dr. *Dipankar Narayan Basu* and Dr. *Amaresh Dalal* for their guidance during this thesis work. Their selfless contributions and omnipresence have significantly lowered the weight of this humongous task and helped complete the dissertation work. They have always been kind enough to accept my inefficiencies, provide a conducive environment for research, and make me see the better side of things. I consider myself to be exceptionally blessed to have worked under their supervision.

I sincerely acknowledge the contributions of Prof. *Dipankar Bandyopadhyay* of the *department of chemical engineering, I.I.T. Guwahati*, that played a significant role in shaping this thesis. Since the beginning of my Ph. D., I was fortunate enough to have his guidance since the beginning of my Ph.D., whose words of wisdom helped me grow both personally and professionally as a research scholar. I am grateful to him for the endless support in using all the lab equipment endlessly and introducing

TH-2590_156103041

me to an outstanding research team and the environment in his *S.M.A.R.R.T.* lab.

Sincere acknowledgments are in order for Dr. *Ganesh Natarajan* of the *department of mechanical engineering, I.I.T. Palakkad*, who has been a constant source of motivation. I am thankful to him for providing me guidance whenever needed in my doctoral days and also prior to it as a junior research fellow in his lab in my B. Tech. days. The research experience obtained during the summer fellowship while working under his guidance shaped my research interest roots. I take this opportunity to thank Dr. *Vinayak Kulkarni* whom I met as the chairman of my doctoral committee during my Ph.D. His constructive ideas regarding the experimentation and the thesis's objectives have immensely helped shape the thesis in its present format. I would also like to sincerely thank my other doctoral committee members Dr. *Partho Sarathi Gooh Pattader*, Dr. *Pranab K. Mondal* and Dr. *Balkrishna Mehta* (currently working in I.I.T. Bhilai), who were equally insightful and constructive in their comments towards my work.

I have been blessed with amazing friends and seniors on and off-campus. Specifically, I would like to thank my seniors **Dr. Sunny Kumar, Dr. Ratan Sharma, Dr. Seim Timung, Dr. Subrat Kotoky, Dr. Amit Kumar Singh** for their constant motivation and technical support whenever needed. I am also thankful to my colleagues and juniors from the **Anupravaha lab** and **S.M.A.R.R.T. lab** for all the support. Outside the workspace, I thoroughly enjoyed the company of **jagadish, dhanesh, bastav, pranab, kankan, apratim**. With you guys being on my side, I have dared to move forward without hesitation and work towards my goal. Words will never be enough to express my gratitude towards **smita**, for the never-ending support, guidance, and motivation. I always had the luxury to take your time and relieve my stress in this long process. I cannot be more thankful for **Mr. Sunil Sarma** who has been like a guardian at I.I.T. Guwahati, helping me with the most helpful advice in different aspects of my personal and professional life

TH-2590_156103041

in the past five years.

My family is the sole reason for my accomplishments; however small it may be. I feel a deep sense of gratitude towards my *maa, deuta, and bhaiti* who have been extremely patient, understanding, and supportive throughout this journey and beyond. I sincerely appreciate the sacrifices you have made during this journey for turning my dream into reality.

Bhaskarjyoti Sarma

TH-2590_156103041

TH-2590_156103041

Contents

Abstract v

Dedication vii

Acknowledgements ix

Contents xiii

List of Figures xix

List of Tables xli

1 Introduction 1

1.1 Wetting states of a sessile droplet on a solid surface 4

1.2 Review of literature 7

1.2.1 Dynamics of liquid droplets in the presence of gravitational field 8

1.2.2 Droplet dynamics in electric field 10

1.2.3 Droplet dynamics in magnetic field 13

1.2.4 Drop shaping and atomization by intense energy deposition . . 15

1.3 Motivation and objectives 19

1.4 Thesis overview 20

2 High-speed visualization and image processing 23

2.1 High-speed imaging system 23

TH-2590_156103041

2.2 Image processing method 30
2.3 Validation of the image processing method 36
2.4 Summary 39

3 Experimental characterization of the growth dynamics during capillarity-driven droplet generation 41
3.1 Introduction 41
3.2 Experimental method and materials 43
3.3 Results and discussion 46
3.3.1 Growth dynamics of water droplets 48
3.3.2 Effect of enhanced viscosity of the penetrating fluid 52
3.3.3 Self-similar contact line and interface profile evolution 54
3.3.4 Estimation of critical volume required for sliding 60
3.3.5 Dynamics of droplet detachment: Static pinch-off 62
3.4 Summary 64

4 Magnetowetting dynamics of sessile ferrofluid drops on soft surface 65
4.1 Introduction 65
4.2 Experimental section 68
4.2.1 Materials 68
4.2.2 Methods 69
4.3 Results and discussion 71
4.3.1 Shape evolution of a FF droplet during magnetowetting: The macroscopic events 73
4.3.2 Dynamics of the three-phase contact line: Stick-slip vs pinned state 78
4.3.3 Effect of substrate elasticity on droplet splitting dynamics. . 88
4.4 Summary 91

TH-2590_156103041

5 Electric-discharge-mediated jetting, crowning, bursting, and atomization of a droplet 93

5.1 Introduction . . . 93

5.2 Experimental method and materials . . . 96

5.2.1 Experimental procedure . . . 96

5.2.2 Dielectric substrate preparation . . . 98

5.2.3 Droplet preparation . . . 98

5.2.4 Imaging and experimental analysis . . . 100

5.3 Results and discussion . . . 100

5.3.1 Initial dynamics of discharge and generation of cavitation bubbles . . . 102

5.3.2 Overview of the fragmentation regimes . . . 107

5.3.3 Jetting regime . . . 111

5.3.4 Crown formation regime . . . 119

5.3.5 Bursting regime . . . 127

5.3.6 Dynamics of microjetting . . . 131

5.3.7 Characterization of hydrodynamics . . . 132

5.3.8 Comparison with existing methods and target applications . . . 135

5.4 Summary . . . 137

6 Interfacial dynamics of viscous droplets impacting a superhydrophobic candle soot surface: Overview and comparison 139

6.1 Introduction . . . 139

6.2 Experimental methods and materials . . . 145

6.2.1 Experimental set-up . . . 145

6.2.2 Superhydrophobic surface preparation . . . 145

6.2.3 Imaging technique . . . 148

6.3 Results and discussion . . . 148

6.3.1 Overall temporal dynamics post impact . . . 148

TH-2590_156103041

6.3.2 Dynamics of droplet spreading . . . 153
6.3.3 Dynamics of droplet retraction . . . 156
6.3.4 Contact time dynamics . . . 159
6.3.5 Droplet rebound dynamics . . . 161
6.3.6 Splashing dynamics . . . 162
6.3.7 Partial rebound dynamics . . . 168
6.4 Summary . . . 171

7 Conclusions and scope of future work 173
7.1 Conclusions . . . 173
7.2 Scope of future work . . . 181

List of Publications 223

Appendix A Cleaning methodology of glass substrates 229
A.1 Cleaning process of ITO-coated glass . . . 229
A.2 Cleaning process of glass micro-slides . . . 229

Appendix B Droplet on a yarn 231
B.1 Estimation of the drop shape . . . 231
B.2 Details of regression analysis . . . 232

Appendix C Soft magnetowetting 235
C.1 Magnetic Bernoulli equation . . . 235
C.2 Evaporation of ferrofluid droplets . . . 237
C.3 Comparison of surface energy . . . 238

Appendix D Discharge-driven droplet atomization 241
D.1 Effect of contact angle . . . 241
D.2 Comparison of different potential energy . . . 242
D.3 Numerical simulation of electric field . . . 244

TH-2590_156103041

D.4 Instability of viscous jets 245

Appendix E Droplet impaction on a superhydrophobic surface 247

E.1 Comparison of the spreading parameter 247

E.2 Total number of secondary droplets from splashing 249

TH-2590_156103041

TH-2590_156103041

List of Figures

1.1 (a) Different wetting conditions encountered by a sessile droplet atop a solid surface, defined in terms of the equilibrium contact angle (θ_{eq}). (b) Components of surface tension namely, γ (liquid-vapour), γ_{sg} (solid-vapour), and γ_{sl} (solid-liquid), for a sessile droplet on a solid surface, following the Young-Lipmann Law. 4

1.2 Wetting states for a hydrophobic rough surface: (a) Cassie-Baxter wetting state, and (b) Wenzel wetting. 6

1.3 (a) The Gibbs energy curve for the liquid droplets resting on a rough surface, with several minima points. (b) Advancing (θ_{adv}) and receding contact angle (θ_{rec}) for a droplet sliding along a tilted surface (α). 7

1.4 Schematic of different regimes originating from a droplet impact on a solid surface. 9

1.5 (a) Formation of *Taylor cone* from a droplet at the end of a capillary tube in an electric field. (b) Taylor cone formed from a sessile droplet [4]. (c) Electrowetting-on-dielectric of a sessile droplet placed atop a conducting substrate-dielectric layer pair in an external electric field. 11

1.6 Formation of (a) Rosensweig instability and (b) Labyrinthine instability on the liquid-vapour interface of a ferrofluid layer in the presence of a magnetic field. Image taken from [103]. 14

1.7 Drop shaping by laser pulse impact as described in Klein *et al.* [5]. . 17

TH-2590_156103041

2.1 (a) Crown-shaped splash captured by Worthington [29] using spark illumination during the impact of a water droplet on a layer of milk mixed with water. (b) High-speed flash photography of a milk drop coronet captured by Edgerton [151], the pioneer of modern stroboscopic imaging. Here the milk drop impacts a thin layer of milk deposited atop a solid surface. The crown shape in both the cases, (a) and (b), is aided by the liquid surface tension. 25

2.2 (a) The high-speed Photron fastcam mini UX camera, and (b) Navitar zoom lens, used in the current set-up. 26

2.3 Schematic representation of the various terminologies associated with high-speed visualization techniques, namely *frame rate, interframe time, exposure time* and *illumination time* in a series of successive frames [image inspired from [54]]. (a) It shows the process of recording experiments aided by continuous illumination and an exposure time shorter than the interframe time, which helps freeze the motion of the object without motion blur. (b) Shows the process of recording high-speed events when several pulsed illuminations decide effective exposure. This video recording method allows flexibility to arbitrarily set the exposure time, up to a maximum limit equal to the interframe time. 27

2.4 (a) Experimental image of a liquid droplet hanging from a surface. (b) The contour of the droplet after applying the *edge detection* tool in ImageJ [164]. 32

2.5 Flow chart depicting the various stages of the image processing method considered in this thesis work. 33

TH-2590_156103041

2.6 (a) Shows the different stages (in sequence) of the image-processing method adopted in this thesis work for the analysis of the high-speed events in in ImageJ [164]. (b) Shows the calculations of different quantitative parameters, namely volume, length, and radius of a deforming droplet. 35

2.7 Droplet growth at the exit of an orifice near pinch-off. The scale bars shown on the right-hand side correspond to 1 mm. 37

2.8 Contour of the droplet interface as extracted by using the current image processing method, corresponding to Figure 2.7. The zoomed view shows the necking phenomenon in detail. 37

2.9 Temporal evolution of the droplet length for the events near pinch-off, corresponding to Figure 2.7. 38

3.1 Schematic diagram of the experimental set-up with all the components. 44

3.2 SEM images of the yarn surface with different magnifications (a) 130x; (b) 275x; and (c) 600x showing the capillary networks. 45

3.3 Schematic diagram of the different stages involved in drop formation from a yarn namely, (a) growth (*radial* and *axial*), (b) *motion*, (c) *necking* and (d) *detachment*. The yellow arrows show the sequence of the occurrence of the events. The two red arrows in (a) show the position of two points of interest, namely, *tip* and *bottom*, referred for describing the growth dynamics of the droplets in yarn. The variables l_d and r_d, shown in (b) with respective positions of measurements, represent the droplet's length and radius, respectively. The red dashed line drawn in the yarn's free end in (b) represents the datum's position, $z = 0$, considered for various measurements during the study. 47

TH-2590_156103041

3.4 Spatiotemporal evolution of the droplet interface during the generation of a water droplet from a yarn. The corresponding experimental conditions are, $We = 1.078 \times 10^{-6}$, $Oh = 0.0043$, $Fr = 3.76 \times 10^{-3}$. The red arrows mark the position of the TPCL of the droplet (z_{tp}) at different instances, whereas the yellow dashed lines in the snapshots refer to the location of the datum. The scale bar shows 1 mm in length. The events have been recorded at 25 frames per second using a SONY camcorder. 49

3.5 (a) The temporal variation of the position of the tip, z_{tp} and bottom, z_{bt} points during the growth of a water drop. (b) The variation of length, l_d, and radius, r_d of a water drop during its growth stage. Position of the tip and bottom below the datum, i.e., $z = 0$ (yellow dashed line in Figure 3.4), is considered negative, while the position above it has been considered as positive. The dashed vertical lines delineate the three stages of drop growth in both (a) and (b). The corresponding experimental conditions are, $We = 1.078 \times 10^{-6}$, $Oh = 0.0043$, $Fr = 3.76 \times 10^{-3}$. The uncertainties in the measurement of the position of the respective identities at each instant are marked by the error bars associated with each data point. 50

3.6 (a) Spatiotemporal evolution of the interface during the growth of (i) tween 20 and (ii) hexadecane droplets from a yarn. The red arrows mark the position of the TPCL at different instants. The scale bar shows 1 mm in length. The corresponding experimental conditions are listed in Table 3.2. The yellow dashed lines in the snapshots of rows (i) and (ii) show the datum. 53

TH-2590_156103041

3.7 The temporal variation of z_{tp} and z_{bt} for two experimental fluids (marked by different colours), namely, Tween20 and Hexadecane, during droplet growth in a yarn [corresponding to Figure 3.6]. The differently colored dotted vertical lines delineate all the three stages seen during the drop growth period. 54

3.8 (a) The variation of the non-dimensional tip position, z^*_{tp} with non-dimensional time t^* is plotted in a log-log scale for all the experimental conditions. The vertical shaded regimes correspond to the transition regimes separating the three stages of drop growth. Plots (b) and (c) compare the experimental data of z^*_{tp} with the derived asymptotic relation (dashed-dotted line), Eq. 3.5, for water (DIW) and 60% glycerol (Gly60) solution, respectively. 55

3.9 (a) Linear plot of variation of non-dimensional radius, r^*_d with non-dimensional time, t^* of a continuously growing droplet at different experimental conditions corresponding to Table 3.2. Logarithmic plots of r^*_d with t^* exhibit the good agreement between the derived scaling law (dashed-dotted line), Eq. 3.6, and the experimental data for (b) water and (c) 60% glycerol solution, respectively. 58

3.10 Force balance in case of a drop continuously growing on a yarn just prior to the initiation of sliding motion. The different geometrical parameters of the drop considered in the force balance are shown with dimensional arrows. F_g is the gravitational pull experienced by the droplet due to its weight, F_c is the capillary force along the contact line, and F_{fc} is the capillary force due to the liquid film acting along the wetting length l_{wt}. 61

3.11 Comparison between the experimentally and theoretically (obtained from the correlation, Eq. 3.10, proposed by Harkins and Browns [227]) measured primary droplet volume. 63

TH-2590_156103041

4.1 (a) Schematic of the experimental set-up for investigating the magnetowetting behaviour of sessile ferrofluid (FF) drops dispensed atop a PDMS coated glass substrate. The magnet and the drop are positioned co-axially to avoid any lateral deformation. (b) shows a zoomed view of the FF droplet along with all the components of the surface tension (γ_{ij}) and equilibrium parameters (radius, r_{eq} and contact angle, θ_{eq}) in the absence of a magnetic field. Here, i, j signify the solid (s)-liquid(l), liquid-vapour(g) and solid-vapour components of the surface tension. (c) Schematic of the surface deformation near the TPCL on a soft surface. The red dashed-dotted line indicates the position of the solid-liquid-air interface prior to the deposition of the liquid drop, whereas the vertical yellow dotted line shows the height of the wetting ridge (h_{wr}) formed above the free surface. 67

4.2 Magnetic flux density (B) as a function of the vertical gap (H, also denoted as z here) between the magnet and the PDMS coated glass substrate. 71

4.3 Shape evolution of ferrofluid droplets during magnetowetting on the three different PDMS coated glass substrates with elastic moduli (E) (i) 1.5, (ii) 0.06, and (iii) 0.02 MPa, respectively. The other experimental parameters are, $\phi_0 = 3$ µL, $B = 450$ mT, and $Bo_m = 131$. The volume concentration of the nanoparticles is 1.2%. A non-dimensional time scale, t^*, has been considered to show the progress of the dynamics, where $t^* = 0$ corresponds to the moment of introduction of the magnetic field. The scale bars are shown in the first image of each row. 72

TH-2590_156103041

4.4 Time-averaged behavior of different parameters related to the deformation of a FF droplet of 3 μL volume when dispensed atop three substrates of different elasticity (E) and subjected to an axial magnetic field B = 450 mT (Bo_m = 131). Plot (a) corresponds to the change in dynamic contact angle, θ_d^*, whereas plot (b) corresponds to the change in the contact diameter, d_c^* of the droplet. The colored regimes around the trajectory in plot (b) corresponds to the error bars derived from repeated events. (c) Variation of the temporal variation of the aspect ratio, A_R, corresponding to the events of Figure 4.3. The non-dimensional scale for time is the splitting time, t_s, whereas the equilibrium value of the contact angle, θ_{eq}, and diameter d_{eq}, before the introduction of the magnetic field have been used as a scale for non-dimensionalizing the concerning quantities. 75

4.5 Schematic representation of the force balance at the interface between the magnetizable liquid medium (1) and non-magnetizable surrounding (2). The same has been written as FHD boundary condition in Eq. 4.2. 78

4.6 (a)-(c) Variation of contact angle (θ_d or θ_d^*) and contact radius (r_c or r_c^*) at a higher temporal resolution shows distinct *stick-slip* pattern during magnetowetting of a sessile FF droplet on an apparently rigid substrate (E =1.5 MPa). The other experimental conditions are, ϕ_0 = 3 μL, Bo_m = 131, B = 450 mT. The non-dimensional time scale is derived using the splitting time, t_s. (d) Shows position of measurement of left (θ_d^L) and right (θ_d^R) contact angles for this study. 79

TH-2590_156103041

4.7 Variation of contact angle (θ_d or θ_d^*) and contact radius (r_c or r_c^*) of a FF droplet as a function of time for soft solids in presence of magnetic field. Plots (a and b) and (c and d) correspond to two soft substrates of elastic moduli, E = 0.06 MPa, and E = 0.02 MPa, respectively. The other experimental conditions are, ϕ_0 = 3 μL, Bo_m = 131, B = 450 mT. 81

4.8 Temporal evolution of the (a) apparent contact angle and contact radius, (b) aspect ratio, during magnetowetting on a rigid glass substrate. 83

4.9 Schematic representations of (a) stick-slip and (b) stick-break mechanisms during elastocapillary mediated magnetowetting events [252]. . 84

4.10 Average values of first potential energy barrier, $\overline{U_1}$, derived using Eq. 4.4 for PDMS coated glass substrates with different elastic moduli, E. 85

4.11 (a) Variation of receding contact angle (circle), dynamic contact angle at the end of primary pinning phase (diamond) as well as just prior to splitting (filled triangle) with the substrate stiffness (E). (b) Droplet splitting time, t_s, corresponding to different elastic moduli (E) of the underlying substrate. 87

4.12 The temporal evolution of the interface of a FF droplet prior to splitting in the presence of a magnetic field. Images (a)-(f) in row (i), (ii) and (iii) show the necking dynamics associated with different substrate having elastic moduli, E = 1.5, 0.06, and 0.02 MPa, respectively. The other experimental conditions are, ϕ_0 = 3 μL, B = 450 mT, and Bo_m = 131. The beginning of time, t = 0, is considered the instant of droplet splitting, whereas the frames before that have been shown as negative in the time scale for convenience. The images are captured at a frame rate of 2000 fps. 88

TH-2590_156103041

4.13 Variation of splitting ratio, $S.R$ [= volume of daughter droplet (ϕ_d)/ volume of residual droplet (ϕ_r)] with the substrate elasticity (E). The plot also shows the variation of the ratio of the daughter droplet volume to the volume of parent droplet (ϕ_r) along the right-hand side axis. 89

5.1 Schematic diagram of the experimental set-up. Image (a) shows an isometric view where a droplet is dispensed upon a thin PDMS film coated on an ITO-glass substrate. A pointed Pt wire connected from the top of the droplet acts as the anode. The different layers of the isolator-cathode-isolator substrate composed of PDMS-ITO-glass are shown as an inset in the image (b). (c) Shows the photographic side view of an experiment from which the position of the droplet and Pt anode can be visualized. The notation h_e indicates the distance between the droplet base and anode. A high-speed camera has followed the spatiotemporal evolution of the concerned hydrodynamic features, and a light source provides the illumination positioned opposite the camera. 96

5.2 (a)-(f) Schematics of the *mode 1* and *mode 2* of bubble formation after discharge in the droplet. (a) also showing the experimental footage of the discharge covering the droplet. (g)-(n) experimental snapshots of bubble formation inside a DI-water droplet (solution 4, Table 5.2) in mode 1. The red arrow on the image (h) marks the onset of bubble formation. (o)-(v) show the bubble formation inside a droplet of glycerol (65%) and water (35%) mixture (solution 7, Table 5.2) in mode 2. 103

TH-2590_156103041

5.3 (a)-(f) Show growth dynamics of a cavitation bubble after discharge inside a highly viscous drop of glycerol (80%)-water (20%) mixture (solution 9, Table 5.2) post-discharge. The droplet volume is 5 μL, whereas the electric potential applied is $\psi = 500$ V ($\Psi = 16.98$ kV/cm). Plot (g) shows the temporal variation of the cavitation bubble radius (r_b) oscillating inside a highly viscous liquid. 105

5.4 Distribution of the electric field vector and equipotential lines when a potential, $\psi = 400$ V is applied to a droplet of radius, $r_d = 1$ mm, for different position of the electrode, h_e^* = (a) 0.05, (b) 0.4, (c) 1.2, and (d) 1.65. The colored plots underneath each column represent the enlarged view of the two boxed areas (in each plot), which show the electric field distribution (surface plot) within the dielectric layer. The non-dimensional electrode distance is, $h_e^* = h_e/r_d$. 108

5.5 (a) Schematic diagram showing the locations (A-I) in the dielectric layer, which is considered for the other plots. (b) The resulting field intensity (Ψ) inside the dielectric layer at the locations indicated in the image (a) when $\psi = 400$ V and the location of the electrode (h_e^*) is varied. (c) The variation of field intensity at location E, Ψ_E, (and C in the inset, Ψ_C) with h_e^* for liquid droplets of different radius (r_d), while the electrode diameter is kept same (0.150 mm). (d) Experimental points showing different regimes, namely, jetting, crowning, and bursting, at the different applied electric fields, Ψ, with the variation in h_e^*. 109

TH-2590_156103041

5.6 Sequence of jet formation due to the electric discharge inside a droplet (solution 5, Table 5.2) and subsequent breakup of the jet ejecting secondary droplets. Images (a)-(j) show the growth of the jet, in which image (j) shows the pinch-off region, the area marked between the arrows indicating neck formation phenomena. Images (k) and (l) show the second pinch-off event along with the separated secondary droplets. The other experimental conditions are, ψ = 1000 V, Ψ = 20.86 kV/cm, ϕ_0 = 5 μL, C_s = 1.0 M, and η = 0.886 mPa s. The broken yellow line shown in image (a) has been considered as datum during the jet height and velocity measurement. 110

5.7 (a)-(l) Sequence of liquid jet formation due to the electric discharge inside a droplet (solution 4, Table 5.2) and subsequent breakup of the jet ejecting secondary droplets after discharge. The first pinch-off event is marked by the arrows in image (e), while the pair(s) of arrows in images (g,i) mark(s) different breakup events of the liquid jet. The other experimental conditions are, ψ = 800 V, Ψ = 13.51 kV/cm, ϕ_0 = 5 μL, C_s = 0.5 M, and η = 0.887 mPa s. The broken yellow line on image (a) represents the datum. 111

5.8 Continued on the following page. 114

TH-2590_156103041

5.8 Images (a)-(f) show the time evolution of a jet originating from a droplet with moderate viscosity subjected to an electric discharge. Experimental conditions are, ψ = 500 V (Ψ = 7.06 kV/cm), ϕ_0 = 5 μL, C_s = 0.1 M, and η = 6.88 mPa s. Images (g)-(l) show the time evolution of the jet formed when a very high viscosity droplet is subjected to an electric discharge. The experimental conditions are, ψ = 500 V (Ψ = 9.19 kV/cm), ϕ_0 = 5 μL, C_s = 0.1 M, and η = 66.96 mPa s. The arrows mark the position of jet breakup at different instants. Image (m) schematically describes the underlying mechanism of the breakup of a viscous jet and subsequent formation of secondary droplets from the jet. Image (n) shows characteristic trajectories of three different positions of a viscous thread, namely, the tip of thread (■), the tail of unbroken thread (●), and neck (▲) for droplets of different viscosity (represented by different colours as well as symbols). The broken lines differentiate the time of occurrence of events. 115

TH-2590_156103041

5.9 The plot (a) shows the variation in the non-dimensional jet height (h_j^*) before the first breakup with time ($\tau = t/t_{vis}$) when electric discharge is instigated inside the droplets of different viscosity (solutions 5, 6, 8, and 9, Table 5.2). Here, $t_{vis} = \eta L/\gamma$ is the viscous time-scale corresponding to the experimental conditions. The plot in the inset shows the merging trend of the experimental data points following a unified scaling law, $h_j^* = a\tau^b Oh^c$, with coefficients: $a = 20.169 \pm 1.582$, $b = 0.436 \pm 0.047$, and $c = 0.781 \pm 0.060$. The plot (b) shows the variation in the normalized spacing of the secondary droplets - experimental (λ/r) and theoretical (λ_{max}/r) with Oh, where λ and r are the average spacing and radius of secondary droplets, obtained from experiments, while λ_{max} is obtained from the theoretical analysis. Here, λ_{max} signifies the wavelength of the fastest-growing disturbance responsible for the breakup of the thread. The Oh number is calculated based on the initial equilibrium radius of the primary droplet (r_d). The experimental conditions are $\psi = 500$ V (all three cases, except for solution 5, where $\psi = 1000$ V), $\phi_0 = 5$ μL, and $C_s =$ 0.1 M. 118

5.10 Images (a)-(i) show the time evolution of the interface of a drop of KCl solution (solution 4, Table 5.2), subjected to an electric field discharge, leading to the formation of a liquid crown. Experimental conditions are, $\psi = 1000$ V, $\Psi = 9$ kV/cm, $\phi_0 = 5$ μL, $C_s = 0.5$ M, and $\eta = 0.887$ mPa s. Images (c),(f) show the positions of measurement of the crown height, h_c, with respect to a datum marked by the broken yellow line, and neck diameter (or radius), d_c (or r_c), respectively. . . 120

TH-2590_156103041

5.11 Images (a)-(l) show the spatiotemporal evolution of a high-viscosity droplet of aqueous KCl solution and glycerol mixer (solution 7, Table 5.2) subjected to an electric discharge. Experimental conditions are, ψ = 800 V, ϕ_0 = 3 μL, C_s = 0.1 M, and η = 18.25 mPa s. Image (a) shows the initial shape of the drop prior to discharge, images (b),(c) show propagation of discharge within the drop and initiation of crown formation, images (d)-(g) show the expansion of the crown, and images (h)-(l) show the sealing and collapse of the crown. Images (f),(l) show the positions of measurement of the crown height, h_c, with respect to a datum marked by the broken yellow line, and neck diameter (or radius), d_c (or r_c), respectively. 122

5.12 Images (a),(c) represent the contour of the liquid-air interface of the crown for a low (Oh = 0.003) and a high (Oh = 0.056) viscosity droplet, respectively. Here, a set of different symbols, namely, circle, square, and triangle filled and bordered with black, blue, and green colour, respectively, are used to depict the previously mentioned three distinct stages of crown evolution, namely, the droplet before electric discharge, the crown formation, and expansion, and finally the sealing and collapse of the crown, with the help of contours. The blue arrow pointing towards the left indicates the direction of expansion of the crown, while the green arrow pointing rightward indicates the direction of crown sealing. Plots (b) and (d) show the rate of change of the neck radius, r_c, corresponding to the crown formation events shown in Figures 5.10 and 5.11, respectively. 124

TH-2590_156103041

5.13 The snapshots show the spatiotemporal evolution of a liquid drop of high electrical conductivity (1 M) and low viscosity ($\eta = 0.886$ mPa s) subjected to an electric field discharge. The other experimental parameters are, $\psi = 1200$ V, $\Psi = 60$ kV/cm, and $\phi_0 = 5$ μL. The yellow broken line on image (a) shows the position of the datum. The frames are captured at a rate of 10000 frames per second. 126

5.14 The snapshots show the spatiotemporal evolution of a liquid drop of moderate viscosity (solution 6, Table 5.2) and low electrical conductivity (0.1 M) subjected to an electric field discharge. The other experimental parameters are, $\psi = 800$ V, $\Psi = 16$ kV/cm, and $\phi_0 = 5$ μL. The yellow broken line on image (a) shows the position of the datum. The frames are captured at a rate of 10000 frames per second. 128

5.15 The snapshots show the spatiotemporal evolution of a liquid drop of high viscosity (solution 9, Table 5.2) and low electrical conductivity (0.1 M) subjected to an electric field discharge. The other experiment parameters are, $\psi = 500$ V, $\Psi = 18.9$ kV/cm, and $\phi_0 = 5$ μL. The yellow broken line on image (a) shows the position of the datum. The frames are captured at a rate of 10000 frames per second. 129

5.16 (a)-(f) Dynamics of microjetting for a DI-water droplet (solution 3, Table 5.2). The yellow broken circle in image (b) indicates the incipience of microjet formation. (g) Dynamics of microjetting for a droplet of glycerol (50%)-water (50%) mixture (solution 6, Table 5.2). 131

TH-2590_156103041

5.17 Different regimes of electric-discharge-induced droplet atomization, namely, jetting (square-red), crown formation (circle-blue+cyan), bursting (triangle-olive), and jetting + bursting (diamond-purple) with the variation in the electric field intensity, expressed in terms of the electric bond number (Bo_E) and the molar concentration of KCl in the droplet (C_s). The rectangular dashed region marked is shown in an enlarged view in the right-hand side plot. The approximate borders are indicated with broken lines and coloured/hatched regions. 133

5.18 Schematics (a)-(c) show the different locations of electric field discharge observed (zone with a red circle with a "+" sign at the centre) with respect to the geometric centre of the droplet (zone with a black circle with a "+" sign at the centre) during the experiments. The dimensionless distances between these two points in the vertical and horizontal planes are denoted as δ_z, and δ_x, respectively. The plot (d) shows the occurrence of liquid jetting (A), crown formation (B), and bursting (C) in the (δ_x, δ_z) plane. The broken line between the regions B and C divides the two regimes. The error bars are due to the uncertainty in determining the centre for both the electric discharge and droplet. The red broken circle marks the area shown in the inset. 134

6.1 Schematic diagram of the experimental set-up. 144

6.2 (a)-(d) Schematics of different steps involved in the surface preparation method by flame deposition of candle soot. 146

6.3 The surface morphology of the superhydrophobic surface prepared from candle soot nanoparticles as viewed in scanning electron microscopy (SEM) at (a) 5000 x and (b) 50000 x. The scale bars in (a) and (b) represent 1 μm and 100 nm, respectively. The morphology of the surface is similar to the Iqbal *et al.* [379], indicating a similar nanometric roughness. 147

TH-2590_156103041

6.4 Spatiotemporal evolution of the interface of droplets of (a) DIW ($Oh = 0.003$) (b) Gly65 ($Oh = 0.062$), and (c) Gly80 ($Oh = 0.23$) solutions after impacting the superhydrophobic surface with different velocities mentioned in the first column. The second column shows the instants just before droplet impact, referred to as $t = 0$ ms, whereas the subsequent columns show the interface's evolution post-impact. The scale bars represent 1 mm in all the images. 149

6.5 (a) Temporal evolution of the spreading ratio, $\beta = r(t)/R_0$, in the case of a water droplet ($Oh = 0.003$) impacting the surface at $We \approx$ 4, 19, 36, 70, 101, and 160. (b) Spreading ratio, β, and (c) non-dimensional droplet height, h_d/R_0, as a function of time for different viscosity droplets ($Oh = 0.003$, 0.023, and 0.062) impacting the surface at $We \approx 36$. The colored rectangular regions in (b) and (c) mark the transition zones between the spreading and retraction regime for different events considered. The dash-dotted lines in (b) mark the contact time for different events. The arrows in (c) mark the point of pinch-off. 150

6.6 $We - Re$ map showing different regimes during the impact of viscous droplets on a superhydrophobic surface. The various experimental liquids are represented with different symbols, whereas the colored zones depict different hydrodynamic features, namely, complete rebound, partial rebound, receding breakup, splashing, and complete pinning. 151

6.7 Temporal evolution of the spreading ratio, β/β_{max} of (a) DIW ($Oh =$ 0.003), (b) Gly50 ($Oh = 0.023$), (c) Gly65 ($Oh = 0.062$), and (d) Gly80 ($Oh = 0.23$) droplets for different impact We. 153

TH-2590_156103041

6.8 Variation of the (a) maximum spreading radius (r_{max}), and (b) maximum spreading ratio (β_{max}) with the impact We for different viscosity liquids. Variation of the maximum spreading ratio, β_{max} (c) with the impact We, when the theoretical scaling law, $\beta_{max} = We^{\frac{1}{2}}$ is applied and (d) with the impact Re, when the theoretical scaling law, $\beta_{max} = Re^{\frac{1}{4}}$ is applied. 154

6.9 Comparison of the experimental data (β_{max}^{exp}) of maximum spreading for different viscosity droplets to the theoretical data (β_{max}^{tho}) obtained from Eq. 6.4. 155

6.10 Temporal evolution of the normalized retraction rate [negative values of $\dot{\beta}R_0/V_0$] of (a) DIW ($Oh = 0.003$), (b) Gly50 ($Oh = 0.023$), (c) Gly65 ($Oh = 0.062$), and (d) Gly80 ($Oh = 0.23$) droplets for different impact We. 157

6.11 (a) Retraction velocity, v_{rec}, of the contact line V/S height of the liquid film, h_f, at maximum spreading. (b) Normalized retraction rate, $(\dot{\beta}/\beta_{max})$ (R_0/V_0), V/S the We, following the Taylor-Culick law (red-solid line) [412, 413]. 158

6.12 Variation of the (a) normalized contact time, τ_c, with the We for different liquids. (b) Normalized contact time, $\tau_c(= t_c/t_h)$, as a function of We and Re. (c) Contact time, t_cV_0/R_0 as a function of We for different superhydrophobic surfaces. (d) Maximum spreading ratio, β_{max} V/S We for different superhydrophobic surfaces. 159

6.13 Variation of the (a) coefficient of restitution, ε with the impact velocity, V_0 for liquids of different viscosity. (b) Comparison of the rebound coefficient, ε, for different superhydrophobic surfaces as a function of impact We. 161

TH-2590_156103041

6.14 Sequential snapshots depicting the dynamics of (a) receding breakup and (b) splashing during the impact of water droplets on the CSNPs coated superhydrophobic surface. The dashed yellow line marks the datum's position, while the broken red circle in (b) shows the generated secondary droplets as the droplet is spreading. The impact velocities in (a) and (b) are 2.2 and 2.8 m/s, respectively. Schematic of (c) prompt splash and (d) lamella ejection event. 163

6.15 (a-d) Size distribution (d/D_0) of secondary droplets during splashing at different impact velocities and liquid viscosity. (e-f) Probability distribution functions, $P(D)$, corresponding to the size distribution in (a-d). The continuous red line indicates the fitting of the experimental data with a log-normal distribution. 165

6.16 Variation of the (a) mean size [i.e., Sauter mean diameter, d_{32}] of the droplet, expressed in a non-dimensionalized form, i.e., d_{32}/D_0, as a function of the We and Re. The red dashed line is derived from Eq. 6.9. (b) No. of droplets, N_d as a function of the impact We. 167

6.17 (a) We-Re regime map showing complete rebound, partial rebound, and splashing regimes during the impact of water droplets on various soot-coated superhydrophobic surfaces. Variation of (b) maximum spreading ratio and (c) retraction rate with the We for the impact of water droplets on different soot-coated superhydrophobic surfaces. (d) Schematic depicting the proposed mechanisms of the complete rebound and partial rebound regime. 168

TH-2590_156103041

B.1 (a) Schematic of an axisymmetric drop attached to a capillary with all the spatial and angular variables defining the shape at each instant. (b) Comparison between the numerically obtained droplet shape (yellow curve) with the droplet shape obtained experimentally by fitting the former upon the latter. The axisymmetric equations can describe the shape well, as the yellow curve fits the experimental shapes completely. The experimental conditions encountered are, $Q^{Twn20} = 8.68 \times 10^{-11}$ m^3/s, $We = 5.03 \times 10^{-8}$, $Oh = 0.0063$, and $Fr = 5.73 \times 10^{-4}$. 231

C.1 Schematic representation of the force balance at the interface between the magnetizable liquid medium (1) and non-magnetizable surrounding (2). The same has been written as FHD boundary condition in Eq. C.2. 235

C.2 Temporal variation of the (a) dynamic contact angle, θ_d, and (b) contact radius, r_c during the evaporation of FF droplets ($\phi_0 = 3$ μL) in absence of magnetic field dispensed atop three substrates with different elastic moduli, $E = 1.5$, 0.06, and 0.02 MPa. The time scale has been non-dimensionalized with the evaporation time scale, (t_e). The magnetowetting behavior of the same FF droplets is shown in the inset for $B = 450$ mT ($Bo_m = 131$). (c) Shows the variation of mass of FF droplets during evaporation on substrates of different stiffness. 238

TH-2590_156103041

D.1 Image (a) shows the equilibrium configuration of a conducting sessile droplet resting on an isolator-substrate pair. The notations r_d and θ_{eq} denote the radius of the droplet and equilibrium contact angle, respectively. Image (b) shows the droplet in equilibrium when a potential difference (ψ) is applied between the flat bottom (blue colour) and pointed top electrodes. The notation θ_{a0} corresponds to the advancing contact angle of the drop due to electric stress accumulated at the contact line. The plot (c) shows the variations in interfacial potential energy (E_s), gravitational potential energy (E_g), the potential energy of the dielectric layer under electric field (E_e), and the total energy (E_t) with the variation in the droplet volume (ϕ_0), obtained from both experimental as well as theoretical analysis, for a droplet configuration as shown in the image (b). 242

D.2 The computational domain for the numerical simulations. 244

D.3 Image (a) schematically shows the different stages of the instability of an infinite cylindrical jet leading to the generation of secondary droplets. The plot (b) shows the dispersion curves (σ vs. x) in which the effect of viscosity on the capillary instability of an infinite cylinder has been shown. The red coloured solid lines for, $J = 2.74$ and $J = 12.22$, are associated with solutions 8 and 9 in Table 5.2. The broken lines show the variation of σ for a range of viscosity values. Plot (c) shows the variation of λ_{max}/r with J derived from Eqs. D.6 and D.7, as shown by the continuous lines. The red symbols correspond to solutions 8 and 9 in Table 5.2. 245

E.1 Maximum spreading ratio, β_{max}, variation with the impact (a) We, when the theoretical scaling law, $\beta_{max} = We^{\frac{1}{2}}$ is applied and (b) Re, when the theoretical scaling law, $\beta_{max} = Re^{\frac{1}{4}}$ is applied. 247

TH-2590_156103041

E.2 (a),(b) Comparison between the two representative methods of secondary droplet counting, namely: number of droplets in the current frame and total number of droplets. 249

TH-2590_156103041

List of Tables

3.1 Properties of experimental fluids. 45

3.2 Experimental conditions during droplet generation from a yarn. . . . 46

4.1 Properties of differently crossed-linked elastomer films: Young's Modulus (E) and thickness (h_f) (row (i) and (ii)]; equilibrium contact angles (θ_{eq}), advancing (θ_A) and receding contact angles (θ_R) of a 3 μL ferrofluid droplet on polymeric films of different elasticity in the absence of magnetic field [row (iii)-(v)]. 70

5.1 Properties of DI water and PDMS [301]. 97

5.2 Composition and properties of the experimental solutions ([a][303], [b][304]). 99

5.3 Comparison between the current study and recent experimental studies for liquid-jet generation. 136

6.1 Comparison of different candle soot-based superhydrophobic surfaces in terms of the fabrication method, fabrication time, static equilibrium contact angle (θ_{eq}), and roll-off angle (θ_{roll}). 142

6.2 Thermophysical properties of the experimental fluids, equilibrium contact angle, and experimental conditions. 147

C.1 Surface energy of different substrates measured by Owens-Wendt method. 239

TH-2590_156103041

C.2 Surface tension of probing liquids with respective polar and dispersive components. 239

D.1 Equilibrium contact angle, θ_{eq} (in degrees), of the experimental solutions. 242

TH-2590_156103041

Chapter 1

Introduction

"There is Plenty of Room at the Bottom"

- Richard P. Feynman, *1959*

"Be less curious about people and more curious about ideas"

- Marie Curie, *1937*

Liquid droplets play a major role in numerous natural as well as industrial processes. While they form the backbone of almost all the life-saving processes of living beings, the mesmerizing beauty of the events of liquid drops interacting with the living or non-living beings has been captured eloquently by poets and artists for ages. Apart from that, many industrial processes, such as those involving drying, printing, melting, and casting, largely depend on the cumulative behaviours of the liquid droplets. Interestingly, with the advent of industrial processes or medical sciences, miniaturized devices such as *Lab-on-a-Chip (LOC)* [1] or *Organ-on-a-Chip (OOC)* [2] platforms (e.g., lung-on-a-chip, heart-on-a-chip etc.) have garnered remarkable appreciation for the last couple of decades. Many of these devices or techniques rely on the behaviour of small and discrete liquid volumes during their operation, which comes under the purview of *microfluidics* [1–3].

One of the primary objectives in microfluidics is to achieve precise manipulation of discrete liquid volumes (10^{-6} to 10^{-18} liters) by either passive (e.g., geometrical modifications of the substrate) or active control techniques (e.g., use of external potential fields such as electric, magnetic, optical) [3]. Also, the liquid droplets can be

TH-2590_156103041

deposited, merged, split, or mixed by using these active or passive actuation techniques, which further act as a backbone of a host of cutting-edge technologies, such as chemical microreactors, bioanalytic microsystem for cells in high throughput experiments, or as an electric or magnetic microlens, etc. Apart from actuation mode (passive or active), the individual droplets' interaction with the surrounding surfaces is another crucial aspect of microfluidics systems. The latter aspect becomes crucial when the contact line's wetting dynamics (CL) serve as a driving mechanism in industrial processes such as self-cleaning, anti-icing, or rapid condensation, etc. In this regard, two major focus areas have been developed in microfluidics: (i) *droplet-based microfluidics* and (ii) *digital microfluidics*, based on the interaction of single liquid droplets with the surface [3]. Briefly, in droplet-based microfluidics, discrete liquid volumes are generated and manipulated inside micro-channels or micro-devices. Here the generated miniature droplets are dispersed in a secondary phase comprised of immiscible fluids. On the other hand, in digital-microfluidics, the liquid drops are maneuvered across surfaces in an unconfined environment, and the immiscible phase is often replaced by air. It is to note that passive and active actuation techniques are used to actuate liquid droplets in both droplet-based and digital microfluidics, as mentioned previously. The broad objective of the present thesis work resonates strongly with the fundamentals of digital microfluidics, which shall be discussed shortly [3].

Although there are several passive techniques for manipulating liquid droplets in digital microfluidics platforms, the active manipulation techniques, specifically the use of external fields such as electrical, magnetic, optical, or acoustics, are more regularly used for the same purpose [3]. On a similar note, we can broadly categorize the dynamics of liquid droplets during external field-induced manipulation in two focus areas: firstly, the interaction of the liquid droplets with the adjacent surface, and secondly, the behaviour of the liquid-vapour interface in the presence of external stimulations. The interaction between the molecules of the contact line and the surface in contact strongly affects the ensuing hydrodynamics during droplet actuation. This desirable/undesirable interaction is manifested in the form of *contact line resistance (friction)* and/or *contact angle hysteresis (CAH)*, thereby felicitating/hindering the movement of the contact line. This aspect is generally considered under the purview of the wettability of the surface in digital microfluidics. On the other hand, the deformation or the spatiotemporal evolution of the liquid-vapour interface of a sessile or suspended droplet in the presence of an external field is the

TH-2590_156103041

backbone of many industrial processes [4–8]. For example, the deformation of a sessile liquid droplet in an externally applied electric field often results in the formation of a *Taylor cone* configuration, which, in turn, can engender numerous secondary droplets via *tip-streaming* [4]. Interestingly, such extreme deformations of the conducting liquid droplets, mediated by the formation of the Taylor cone, can be a host of several cutting-edge applications, including electrospinning, electrospraying, to name a few. Again, during ink-jet printing, the spreading behaviour of each droplet determines the quality of the print, which can further be manipulated by applying external electrical fields. Similarly, the fluid flow resulting from the deformation and fragmentation of tin microdroplets by a laser pulse controls the illuminance of a EUV light source, thereby affecting the high throughput in microchip manufacturing by EUV-nanolithography [5]. Interestingly, in the ongoing *COVID-19* pandemics, scientific communities have proved that the deformation leading to the bifurcation and the transportation of the *Novel Coronavirus* or *SARS-CoV-2* carrying respiratory (nano)droplets is one of the prime sources of the community spreading [7]. These respiratory droplets are generated as we speak or exhale, which become much smaller after evaporation in air and thus, can stay longer in the surrounding medium, thereby acting as an airborne source of virus transmission [7, 8]. These examples establish that elucidating the rich physics associated with the deformation of the liquid-vapour interface of a droplet experiencing external stimulation is of paramount importance for enhancing the efficacy of various digital microfluidics platforms as well as for understanding the criticalities of several life-saving processes. Notably, the advent of high-speed imaging techniques and numerical simulation tools has helped enormously in analyzing the aforementioned intricate details of the micron-scale events, as reflected in several recent studies [9].

Overall, the deformation of liquid volumes engendered by externally applied fields, influenced by substrate wettability and liquid properties, can manifest into a host of intriguing physical phenomena. The latter sentence is the driving mechanism in many existing engineering applications, including some state-of-the-art applications such as laser-induced breakdown spectroscopy (LIBS) [10]; needle-free injection technology [11], gas dynamic virtual nozzle (GDVN) [12, 13], etc. The present dissertation aims to analyze intriguing and complex fluid flow configurations involving droplet-substrate interaction by performing extensive experimentation and subsequent theoretical analysis. The importance of understanding such complex and physically rich systems will be further detailed in Section 1.2 through an extensive

TH-2590_156103041

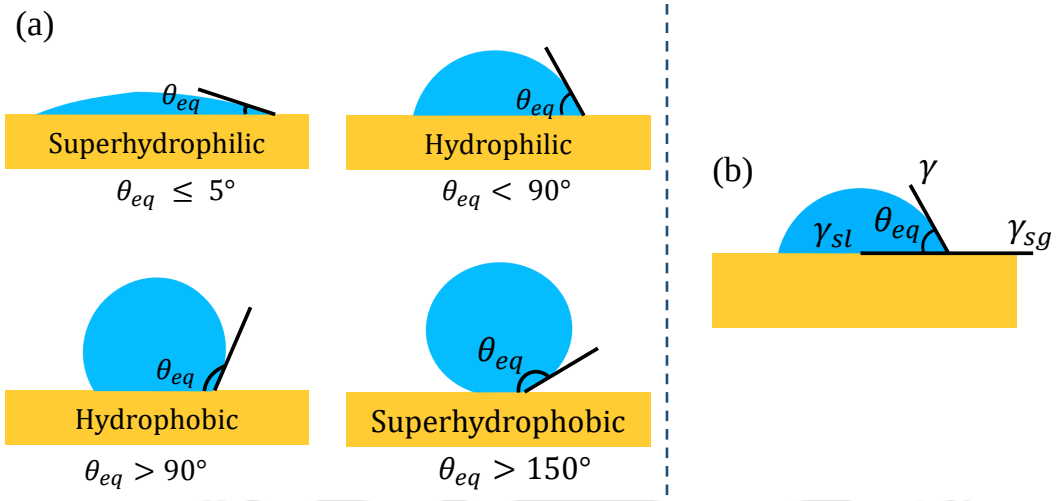


Figure 1.1: (a) Different wetting conditions encountered by a sessile droplet atop a solid surface, defined in terms of the equilibrium contact angle (θ_{eq}). (b) Components of surface tension namely, γ (liquid-vapour), γ_{sg} (solid-vapour), and γ_{sl} (solid-liquid), for a sessile droplet on a solid surface, following the Young-Lipmann Law.

literature survey, based on which the objectives of this thesis work will be discussed in Section 1.3. In the following section, a few necessary concepts of substrate wettability are discussed briefly, which play a significant role in shaping the desired flow morphologies.

1.1 Wetting states of a sessile droplet on a solid surface

The affinity of liquids to stay in contact with a solid surface is known as wettability. Some surfaces exhibit a strong affinity for water, known as hydrophilic surfaces, while there exist surfaces that tend to have lower affinity for the former, exhibiting *hydrophobicity*. In the study of digital microfluidics, understanding the wettability of the surfaces involved is of utmost priority, as it, in turn, affects the dynamics of droplet manipulation. When a droplet is gently deposited on a solid surface, depending upon the wettability of the surface, it can assume any of the configurations shown in Figure 1.1(a). As shown in Figure 1.1(a), the degree of wettability of a surface can be characterized by the macroscopic angle between the solid surface and the liquid-vapour interface at the point of intersection of them, known as the

TH-2590_156103041

equilibrium contact angle (θ_{eq}). In the wetting studies, when $\theta_{eq} \leq 90°$, the surface is known as *hydrophillic surface*, having a strong affinity for water. On the other hand, a sessile water drop on a hydrophobic surface assumes nearly a spherical shape ($\theta_{eq} \geq 90°$) and does not spread, as shown in Figure 1.1(a). The shape of the droplet, in both the hydrophilic and hydrophobic surfaces, can be described by considering force balance among the three phases (solid, liquid, and vapour), popularly known as the Young-Dupré equation, as follows:

$$\gamma_{sg} = \gamma_{sl} + \gamma \cos\theta_{eq}, \tag{1.1}$$

where, γ_{sl}, γ_{sg}, and γ represent the solid-liquid, solid-vapour, and liquid-vapour interfacial energies, respectively [refer to the schematic Figure 1.1(b)]. When $\theta_{eq} \leq 90°$, Eq. 1.1 suggests that, $\gamma_{sg} - \gamma sl \geq 0$, thereby facilitating the spreading of a water drop. Again, when $\theta_{eq} \geq 90°$, we find that, $\gamma_{sg} - \gamma sl \leq 0$, which hinders the droplet spreading. As such, by tuning the surface energies of a solid surface with the help of chemical treatments, the wettability of the surface can be altered very easily.

Interestingly, Eq. 1.1 is only applicable to ideally smooth and chemically homogeneous surfaces. On the other hand, the surface roughness or in-homogeneity can also affect the macroscopic wetting behaviour of a solid surface. Notably, with the help of chemical patterning or lithography techniques, different kinds of microstructures can be built on an initially flat surface, thereby altering the wettability of the surface. On these rough surfaces, depending upon the thermophysical properties of the liquid, two primary wetting states can be observed: (i) *Cassie-Baxter* [Figure 1.2(a)] and (ii) *Wenzel* [Figure 1.2(b)]. In the former one, there exists an air gap between the surface and droplet, and the liquid hardly wets the micro-/nano-structures or roughness, as shown in Figure 1.2(a) [14], while the liquid impregnates the surface topography in the latter case [15]. In the Cassie-Baxter state, the droplet sits on the top of the microstructures, where the *apparent contact angle (APCA)*, θ^*, is related to the equilibrium contact angle, θ_{eq} as follows:

$$\cos\theta^* = f_s(\cos\theta_{eq} + 1) - 1. \tag{1.2}$$

Here, f_s and 1-f_s are the areal fraction of the solid and liquid interfaces underneath the drop, respectively. Interestingly, in digital microfluidic applications, this

TH-2590_156103041

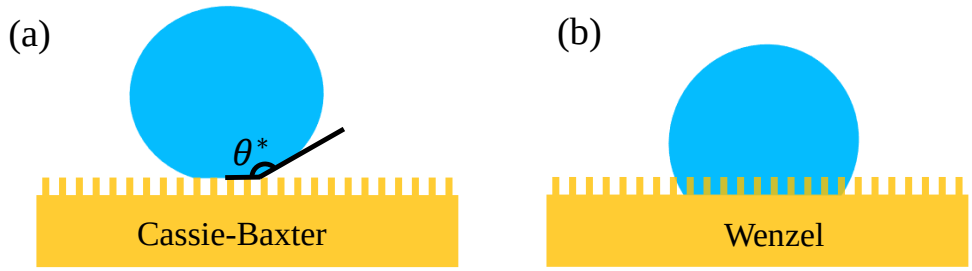


Figure 1.2: Wetting states for a hydrophobic rough surface: (a) Cassie-Baxter wetting state, and (b) Wenzel wetting.

air-entrapped Cassie-Baxter state, or alternatively *fakir state* facilitates easy gliding of the droplets along the surface, due to very high slip length.

Again, the apparent contact angle, θ^*, for a droplet in Wenzel state is given by,

$$\cos\theta^* = r_f \cos\theta_{eq}, \tag{1.3}$$

where r_f is the ratio of the actual wetted area to the projected area (the one circumscribed by the contact line). It is to note that, Eqs. 1.1-1.3 is applicable when the radius of the droplet is substantially larger than the characteristic lengths of surface heterogeneities. Furthermore, several metastable wetting states can be found other than the aforementioned states for a droplet resting on a rough surface as indicated by the multiple minima points on the Gibbs energy curve shown in Figure 1.3(a) [16, 17].

Although the Eqs. 1.1-1.3 provide the sole value of the apparent contact angle for specific combinations of liquid, solid and gaseous phases, multiple different contact angles can be seen during the experiments, even for atomically flat surfaces. This is argued to be an artefact of the long-range interactions between the liquid molecules at the air-water-solid *three-phase contact line (TPCL)* and the molecules comprising the solid surface. The maximum contact angle exhibited by a liquid droplet on a solid surface is generally termed as *advancing contact angle* (θ_{adv}), whereas the smallest one is referred to as *receding contact angle* (θ_{rec}). The presence of the θ_{adv} and θ_{rec} becomes significant during droplet sliding along an inclined plane as shown in Figure 1.3(b). This difference between the θ_{adv} and the θ_{rec} is known as the contact angle hysteresis ($\delta\theta$), which can be attributed to the pinning of the TPCL in the surface roughness or defects. The pinning results in a potential energy

TH-2590_156103041

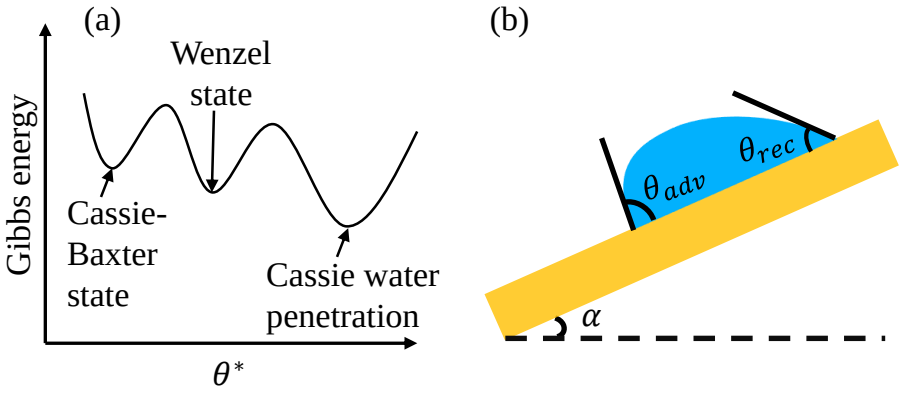


Figure 1.3: (a) The Gibbs energy curve for the liquid droplets resting on a rough surface, with several minima points. (b) Advancing (θ_{adv}) and receding contact angle (θ_{rec}) for a droplet sliding along a tilted surface (α).

barrier ($\overline{U}$), which is to be surpassed by the contact line during motion. The general expression for the contact angle hysteresis is as follows:

$$\delta\theta = \theta_{adv} - \theta_{rec} = \left(\frac{8\overline{U}}{\gamma R_0}\right)^{\frac{1}{2}} f(\theta_{eq}), \tag{1.4}$$

where, R_0 is the initial radius of the droplet prior to deposition on the surface and $f(\theta_{eq})$ happens to be the function of the equilibrium contact angle, as earmarked by Whyman *et al.* [18].

In general, a superhydrophobic surface is expected to exhibit low $\delta\theta$ and high θ_{eq} (or high θ^*) in order to facilitate easy droplet maneuvering in digital microfluidics.

1.2 Review of literature

As mentioned previously, the nature and extent of the deformation of the liquid-vapour interface, engendered by external stimulations, such as electric, magnetic, optical, or gravity, is a key driving mechanism in numerous industrial processes, including ink-jet printing [19], self-cleaning [20], evaporation [21], among many others. Each attribute is discussed in the following sections.

TH-2590_156103041

1.2.1 Dynamics of liquid droplets in the presence of gravitational field

The formation and breakup of liquid drops are seen abundantly in most of the free surface flows. A plethora of engineering and medical applications, starting from inkjet printing to DNA sampling [22, 23] rely on the processes of generation of droplets at a nozzle or an orifice. As such, the formation of drops from vertical capillary tubes has been studied experimentally and computationally by many researchers, where they have identified two modes of drop formation, namely dripping and jetting [24]. Formation of a slender neck prior to the incipience of a drop, the evolution of the most unstable wavelength along the jet, and the transition from the dripping to the jetting regime and vice versa due to change in the viscosity or surface tension of the medium or the fluid are some of the most crucial dynamics obtained from the previous studies [24–27]. The relevant studies have shown that the breakup of the liquid jets, and subsequent production of secondary droplets, due to the most unstable wavelength, is an artifact of the imbalance between the inertial and capillary forces. On the other hand, the same necking dynamics are seen even in the absence of flow in situations like a drop detaching from a ceiling. However, gravity becomes a dominating factor in determining hydrodynamics in the absence of flow [28].

In contrast, high-speed jets, emerging out of a liquid surface, ascending in air and subsequent generation of secondary droplets from the jet is one of the most common and striking phenomenon elucidated at the beginning of the 20^{th} century by Worthington [29], where observations were made by allowing a liquid drop to hit upon a horizontal plate. Worthington and Cole [30, 31] reported another experimental evidence of jet formation made by dropping a solid sphere in a pool of liquid, and they concluded that the jet arises due to the collapse of air-filled cavities. Also, the impact of a drop on a liquid interface [32–39] is commonly accompanied by the ejection of columnar jets whose velocities can be larger than that of the impacting drop at some instant. Jet emerging from the free surface of a sparkling drink, e.g., champagne, is another instance of a *Worthington jet*, which appears due to bubbles bursting at the liquid interface [40–43]. Radially focused capillary waves [44, 45] or Faraday waves [46–48] also give rise to jet in axial direction, where surface tension plays the most crucial role. On the other hand, pressure waves engendered by the sudden deceleration inside the bulk liquid [49–51] also produce liquid jet from the

TH-2590_156103041

free surface, wherein the inertial force initially produced governs the jet dynamics. While many existing studies have not considered gravity's effect in their analyses, the latter can be a defining parameter in a few critical conditions. For example, Borthakur *et al.* had shown that gravity affects the trajectory and breakup characteristic of a jet issued in a direction perpendicular to gravity [52].

During the impact of a drop on a surface, another beautiful hydrodynamic

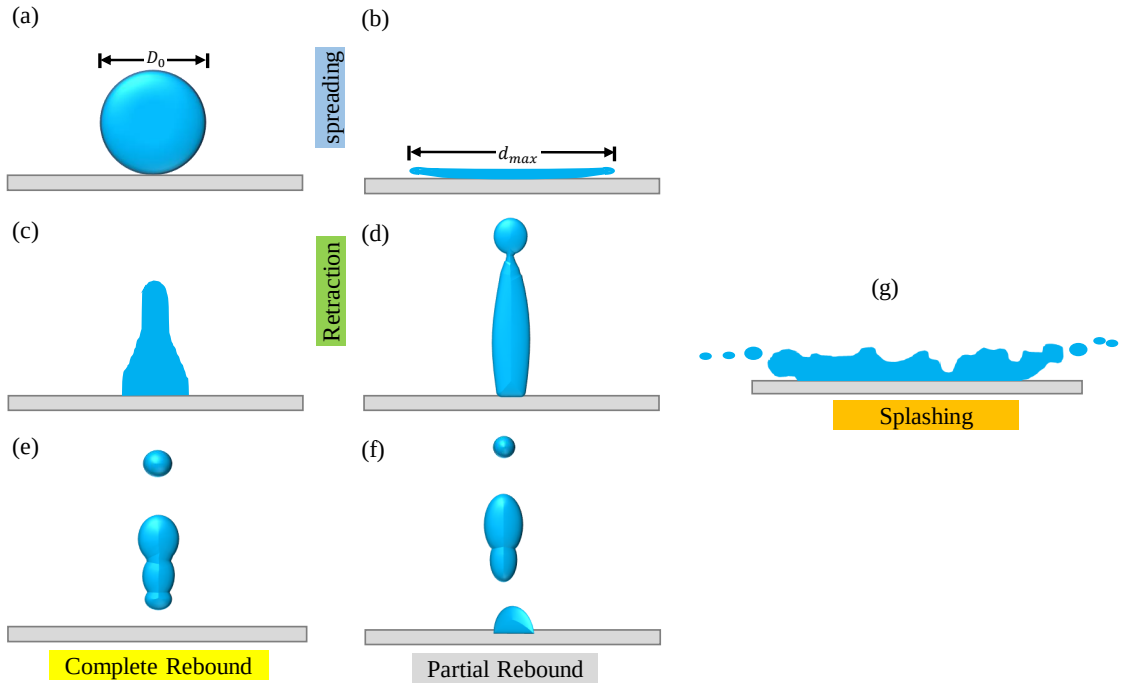


Figure 1.4: Schematic of different regimes originating from a droplet impact on a solid surface.

feature, known as *splashing*, appears, which was first discussed eloquently in the literature entitled *a study of splashes* [53]. The literature clearly states that the resulting sequence of events following an impact is entirely dependent upon the various independent factors such as a combination of the surface and the drop and their properties, the velocity of the impacting object and impact angle, etc. Although people observed splash crown formation centuries back, the critical hydrodynamic features like splash dome formation, early surface sealing, etc., would have remained unnoticed to naked eyes if it would not have been the development of high-speed photography [54, 55]. To analyze the details while an object hits a liquid surface displacing the fluid below, one can approximate the former as a locally flat object. The initial dynamics of splashing can then be solved as *Wagner problem*

TH-2590_156103041

[56, 57]. However, the finer details of the splashing, such as the exact shape of the splash, the reason behind the breakup of the splash to secondary droplets, number of secondary droplets, buckling instability, and surface sealing are some of those parameters challenging to predict, and researchers are still striving to solve them theoretically [38, 58, 59]. Recently, Marston *et al.* [60] captured the buckling instability prior to surface sealing of the crown in a mesmerizing way with the help of high-speed photography. The study revealed the unstable wavelengths responsible for the ribbon-like structures during buckling instability, initially observed by May [61]. Whether be it the formation of jets or splash crown, gravity can affect the preceding events such as the cavity formation and collapse dynamics.

On a similar note, droplet impact on a solid surface also results in a host of flow morphologies as shown in Figure 1.4. The liquid droplet starts spreading once it touches the solid surface and subsequently reaches its maximum extent. The droplet then retracts itself back and can produce liquid jets, splash crown, or ejecta sheet, leading to the atomization of the parent droplet. The occurrence of different regimes depends on several factors, including the property of the liquid droplet and solid surface, impact speed, and direction [38]. Apart from imparting the desired velocity to the impacting object, gravity can be a defining factor in the temporal evolution of the associated flow morphologies.

1.2.2 Droplet dynamics in electric field

Deformation and breaking of drops during thunderstorms, chaotic behaviour of jets, and drops during inkjet printing are examples of deformation of a fluid interface under an external electric field. The fate of discrete droplets placed in an electric field depends on the electrohydrodynamic (EHD) stress generated at the interface of the drop and surrounding medium. This instability of an interface between an electrically conducting liquid droplet confined by another medium is explained in the seminal work from Lord Rayleigh [62], which provides the criteria for maximum charge a liquid mass can hold before its deformation. Experiments of Macky [63] established an instability criterion for conductive droplets in an electric field, which was further supported by Taylor [4] with his theoretical model. The unstable drop after attaining a critical charge generates secondary droplet from its conical tip which is known as *EHD tip streaming* or *cone-jetting phenomenon* as shown in Figure 1.5(b) [4, 64]. Often referred to as electrospraying [refer to Figure 1.5(a)],

TH-2590_156103041

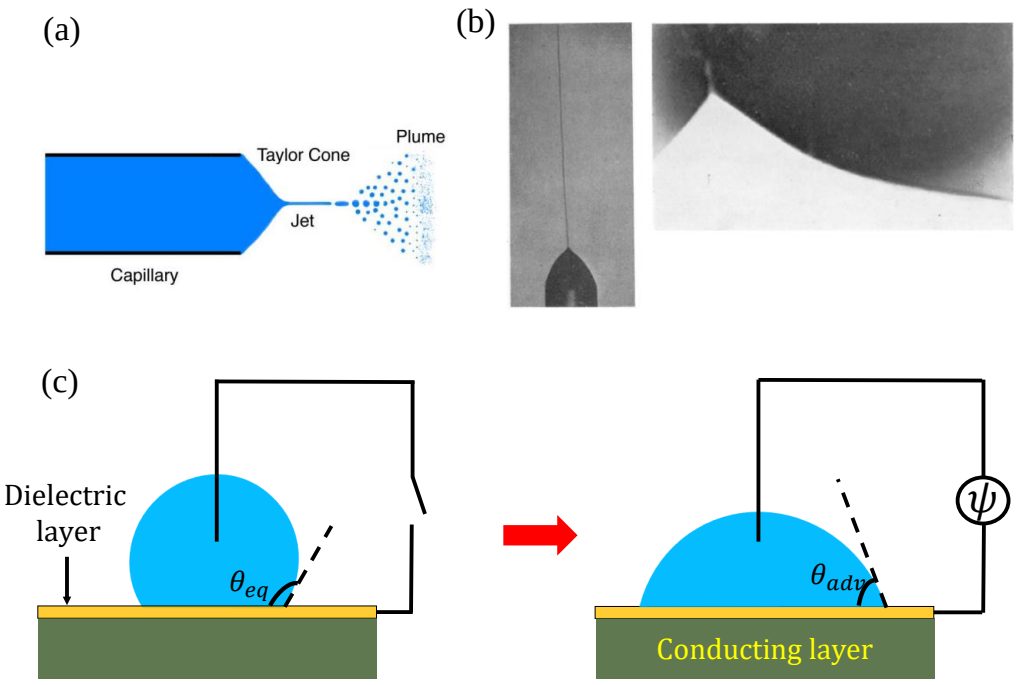


Figure 1.5: (a) Formation of *Taylor cone* from a droplet at the end of a capillary tube in an electric field. (b) Taylor cone formed from a sessile droplet [4]. (c) Electrowetting-on-dielectric of a sessile droplet placed atop a conducting substrate-dielectric layer pair in an external electric field.

this streaming phenomenon can be seen abundantly in various natural as well as industrial processes, starting with the ejection of streams of small charged drops from pointed tips of raindrops in thundercloud [65] to the immensely popular mass spectroscopy [66], used for assaying large biomolecules. With the help of numerical simulations, Collins *et al.* [67] had shown that even a liquid droplet suspended in a lighter medium could exhibit tip streaming in a uniform electric field. Furthermore, Brosseau and Vlahovska [68] reported the events of *equatorial streaming* in the presence of an external electric field. The study showed that the streaming results from an interfacial instability at the stagnation line of the EHD flow, which creates a sharp edge.

Again, the EHD stresses acting at the contact line of a conducting sessile droplet may increase the wettability of the underlying substrate, a phenomenon known as *electrowetting (EW)*. Lippmann [69] was among the pioneers to identify the underlying rich physics of the EW process through his seminal contribution to the theory of electrocapillarity. The formulation uncovered the reasons behind the capillary

TH-2590_156103041

depression of mercury when in contact with electrolyte solutions in the presence of an external electric field [70]. Later, interesting behaviours of the electrically conducting liquid droplets on different types of surfaces under the influence of alternating (AC) or direct (DC) current electric fields were explored [71–73]. Much later, Taylor [4] unveiled the role of EHD stresses originating from the accumulation of the induced charges at the droplet-substrate interface as the significant reason behind the change in the equilibrium contact angle of the liquid droplet during electrowetting. Interestingly, the term electrowetting was coined by Beni, and Hackwood [74] in 1981, much later after its discovery, while they employed the former to design display devices.

In recent times, the EW processes have been employed as a model prototype to study the field-induced deformation or actuation of soft and deformable multicomponent and multiphase microsystems [75, 76]. However, after the invention, for an extended period, the applicability of the EW processes was rather limited because, in most of the situations, the droplets composed of electrolytes were placed on one of the electrodes, which caused electrolysis [76]. The utility of the EW processes escalated only after the introduction of the concept of *electrowetting-on-dielectric (EWOD)* [77]. The EWOD setup proposed the placement of the droplet on a hydrophobic insulating isolator, which in turn was placed on the electrode substrate [78]. In a typical EWOD setup, the electric field is applied through an external circuit in which the bottom substrate acts as one of the electrodes, while an electrically conducting wire, touching the droplet from the top acts as the other electrode as shown schematically in Figure 1.5(c). The placement of the thin hydrophobic isolator between the droplet and the substrate electrodes in the EWOD setup helps in (i) arresting the electrolysis, (ii) making the process reversible, (iii) developing enough EHD stresses for rapid EW [79], and (iv) tuning the electrical, thermal, and surface properties of the isolator to develop a diverse range of applications [80].

In the recent past, the electrowetting processes have been employed for microscale mixing [81, 82], reactors [83], energy harvesting [84, 85], droplet actuation [86], electronic displays [87, 88] and Bio-MEMS devices [89], among others. In particular, the hydrodynamic, elastic, and interfacial properties of the isolator have been found to influence the electrocapillarity of the droplet significantly. For example, while the superhydrophobic isolators composed of nanowires or nanorods showed a reversible EW [90, 91], a reverse EWOD process of a large number of microdroplets could harvest high-density power [92] by converting mechanical energy into the electrical one

TH-2590_156103041

[93, 94]. Interestingly, many recent works have shown that the energy storage and dissipation at the TPCL of the advancing front of a microdroplet, undergoing EW, can provide additional control over the ensuing EW dynamics [94, 95]. In particular, the elasto-capillary effects at the soft and deformable isolators or viscous dissipation on the liquid isolators could develop EW processes having reversible to transient responses important for various optoelectronic applications. In this direction, the EW of a microdroplet on a strongly slipping surface is an interesting system where the contact-line shows interesting motions captured by Kumar *et al.* [6] in their recent study. They coined the name of the process as *electrowetting-on-liquid* or *EWOL* as the slipping surface used in this case was water. In the electric field's presence, the drop showed lateral movement and oscillation, whereas, in the presence of a magnetic field alongside the electric field, *Lorentz force* rotated the drop both in anti-clockwise and clockwise directions. The above discussions further strengthen the previous claim of the utility of electric field-mediated droplet deformations in many industrial processes.

1.2.3 Droplet dynamics in magnetic field

In the presence of a magnetic field, both uniform and non-uniform, the interface of a paramagnetic liquid volume exhibits shape deformation, which may even lead to the disintegration of the liquid interface. Such an instability developed in the air/fluid interface also leads to beautiful patterns, and the artists, with their craftsmanship, have been honouring these instabilities for decorative purposes for decades. These instabilities originating from the imbalance between the magnetic force and liquid surface tension are known as *magnetohydrodynamics (MHD)* or *ferrohydrodynamics (FHD)* [96, 97]. The shape deformation of the liquid interface further depends on the size, confinement configuration, and the relative direction of the applied magnetic field, which has been studied extensively in the past [96–100]. In this regard, Figure 1.6(a) illustrates the so-called normal field instability of a ferrofluid layer with an air interface, known as *Rosensweig instability* [98, 101]. In contrast, a ferrofluid layer confined between two parallel plates, under the effect of a magnetic field in a direction normal to the surface of the ferrofluid, engenders a *Labyrinthine pattern* [99, 102, 103] as shown in Figure 1.6(b). Interestingly, the deformation and associated dynamics of a paramagnetic interface are the backbones of a plethora of engineering applications such as shock absorbers, heat transfer fluids in loudspeakers

TH-2590_156103041

[103], magnetocaloric pumps and heat pipes, bearing lubricants [104], microfluidic pumps and valves [105], microfluidic actuators and devices [106], stepper motors [107], accelerometers, and inclinometers in sensor applications [108], separation processes [109], catalytic reaction supports [110, 111] and leak-proof seals for pneumatic and hydraulic micro-actuators [112] and water purification [113], among many others.

In the study of the magnetic field-induced deformation, ferrofluids play a sub-

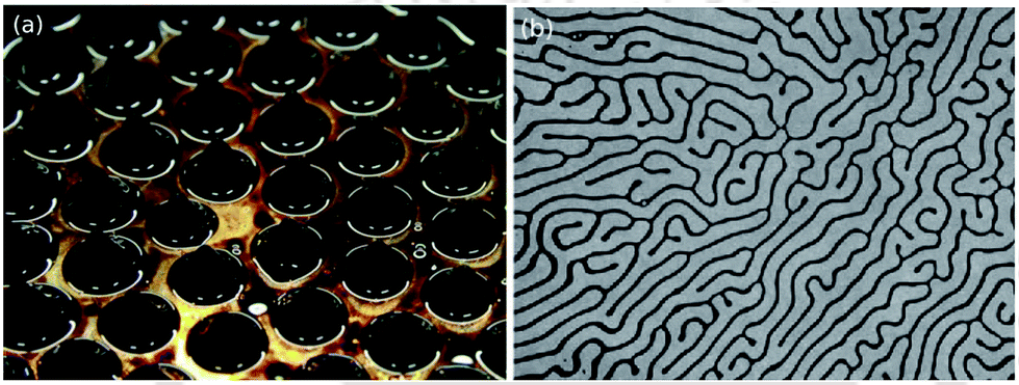


Figure 1.6: Formation of (a) Rosensweig instability and (b) Labyrinthine instability on the liquid-vapour interface of a ferrofluid layer in the presence of a magnetic field. Image taken from [103].

stantial role, which is generally a colloidal suspension of magnetic nanoparticles. To be precise, ferrofluids contain nanoparticles whose size is less than 10 nm, thereby allowing the carrier liquid (oil or water) to retain its fluidic nature and exhibit deformation in a magnetic field. Notably, an isolated ferrofluid droplet in a magnetic field can be actuated precisely and easily over a surface in the non-contact mode, thereby giving rise to several interesting dynamics. Each magnetic nanoparticle constituting the ferrofluid behaves as a magnetic dipole and aligns itself in the magnetic field's direction very quickly. Hence, it becomes easier to position the droplet precisely along any surface. Due to the very fact mentioned above, the ferrofluid droplets can be considered a potential host for many digital microfluidics applications such as mixing, merging, splitting of magnetic droplets, or in targeted drug delivery [114–116]. Numerous studies have explored the actuation of discrete ferrofluid droplets atop substrates of different wettability and topography, depending on the targeted applications [100, 114, 117–120]. For example, Egatz-Gómez *et al.* [100] showed that ferrofluid drops resting on a superhydrophobic surface can also be displaced,

TH-2590_156103041

merged, and split with the application of a magnetic field. Most recently, Kumar *et al.* [6] reported both anti-clockwise and clockwise rotation of non-magnetic oil droplets over a slippery surface upon the application of both electric field as well as the magnetic field in a perpendicular direction to each other.

Another interesting aspect of ferrofluid droplets experiencing magnetic stimulation is the significant shape deformation and subsequent disintegration of the interface. The contact angle of the drop evolves continually (decreases or increases) in the presence of the magnetic field, owing to the excess magnetic stress at the TPCL, popularly known as *magnetowetting*, a term bearing similar significance as that of electrowetting [114, 115, 121]. Nguyen [115] has shown that a sessile droplet in a non-uniform magnetic field can even exhibit Rosensweig instability. Again, a sessile paramagnetic droplet gets bifurcated multiple times beyond a critical magnetic intensity and subsequently shows dynamic and switchable self-assembly [122]. On the other hand, Kumar *et al.* has reported the actuation of magnetic salt-based ferrobots on a liquid surface and subsequent self-assembly induced by splitting of the droplet [123]. Further, Jamin *et al.* [124] studied the quasistatic and dynamical behaviour of capillary origami of a ferrofluidic droplet whose shape is strongly dependent on the applied uniform magnetic field and also the onset of overturning instability beyond a threshold value of the external magnetic field. The relevant phenomena have further been explored in a plethora of engineering applications such as ferrofluidic droplet generation [125, 126], droplet manipulation over functional substrates [114, 117–120], static and dynamic self-assembly [122, 127], cell assembly, and tissue engineering [103, 119], magneto-capillary origami [128], mechanical sealing and acoustics [112], and water purification [113], among many others.

1.2.4 Drop shaping and atomization by intense energy deposition

The shape evolution of the liquid droplets irradiated by a laser pulse during the EUV nanolithography or laser-induced breakdown spectroscopy process affects the desired outcome. The underlying driving mechanism of such processes lies in the shape optimization or atomization of the liquid interface by depositing intense energy inside the droplet or directly at the interface between the drop and the surrounding medium. The energy supplied to the droplet or the interface via optical,

TH-2590_156103041

electrical, or acoustic methods can also engender a plethora of interesting flow morphologies such as jetting, splashing, bursting ejecta sheet, forward and backward plumes, partial or complete atomization, etc. The concerned energy deposition inside the droplet often engenders cavitation bubbles alongside the shock waves and plasma formation. These cavitation bubbles undergo rapid expansion and collapse, thereby releasing the excess energy as shock waves. The interaction of the shock waves and vapour bubbles inside the droplet further determines the course of the hydrodynamic features and the fate of the droplet interface. Similarly, the plasma formed at the interface also interacts with the liquid matter of the droplet and can engender several interesting metastable hydrodynamic features. For example, laser ablation of soft tissues is often replicated by illuminating a liquid drop with intense laser energy. The resulting hydrodynamics are characterized to obtain a quantitative overview of the material expulsion process from the drop [129]. Similarly, the collapse of a cavitation bubble near a drop surface also results in fine jetting from the surface. An earlier study by Blake and Gibson [130] reported the formation of jets or spikes due to the collapse of a single cavitation bubble near a free surface, engendered by a transient laser pulse. Previously, Gibson *et al.* [131] had explained the dynamics of jetting near three different types of surfaces due to the collapse of cavitation bubbles produced by an electrical spark.

Thoroddsen *et al.* [43] reported the evolution of cylindrical liquid sheets and spray, emanating from the free surface of the sessile drop when exposed to a laser pulse target from below. Depending on the focal point of the laser and the thermophysical properties of the experimental fluids, several metastable hydrodynamic features are observed, including larger spray or jetting [43]. The liquid interface also exhibited the high-speed microjetting phenomenon due to the interaction between the shock-wave and the micron-sized bubbles underneath the apex of the sessile droplet [43]. Previously, Fletcher and Palankar [132] had also reported high-speed microjets relevant in needle-free surgical processes or soft tissue incision. The study showed that the collapse of a vapour bubble, engendered by an electrical spark, in a micro-nozzle configuration could produce pulsed liquid microjets of 30 μm diameter, propagating at a velocity as high as 90 m/s. The succeeding studies showed that such high-speed microjets could be used in various medical applications such as intravascular injection [133], drug delivery [134], electrosurgery [135], etc., to name a few.

Interestingly, the collapse of cavitation bubbles generated during electric dis-

TH-2590_156103041

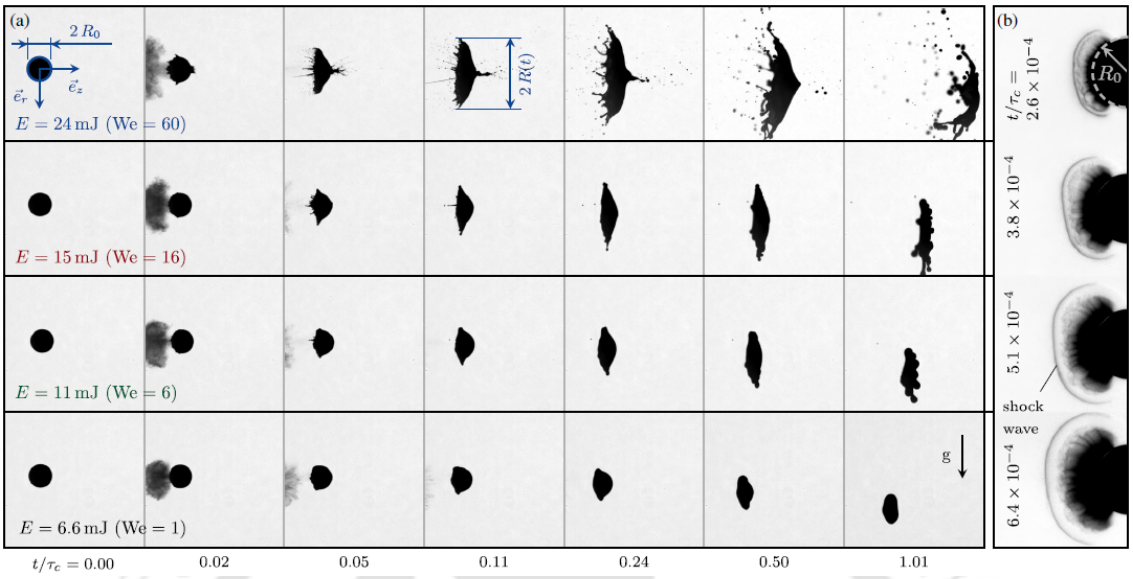


Figure 1.7: Drop shaping by laser pulse impact as described in Klein *et al.* [5].

charge inside a centimeter size drop can induce jetting as well as splashing, even in a microgravity environment, as reported by Obreschkow *et al.* [136]. The study showed the formation of counter-jets and micro-jets at the liquid interface, even in the weightlessness condition. Surprisingly, micro-jets and counter-jets are formed even if the cavitation bubble undergoes expansion and collapse inside a liquid jet, as shown by Robert *et al.* [137]. However, they have used pulsed laser energy to generate the cavitation bubble and experimented in normal gravity conditions, unlike Obreschkow *et al.* [136]. Furthermore, the interaction between the shock wave and the cavitation bubbles inside a droplet may also engender liquid jets within the bubble [138, 139]. However, the jet dynamics depend on the interacting shock wave profile, the initial bubble shape, the initial bubble size, and the bubble arrangement, as earmarked in the study. Although the underlying mechanism of overpressure creation is pretty much different in all of the aforementioned jetting scenarios, the overall dynamics of jet growth and disintegration have striking similarities to that of the Worthington jet discussed in Section 1.2.1.

Apart from jetting, laser ablation of liquid drops produces cylindrical liquid sheets [43, 60], similar to the *splash crown* formed during the impact of a liquid drop as discussed in Section 1.2.1. For example, Thoroddsen *et al.* [43] reported that the liquid sheets originating from a sessile droplet after the deposition of pulsed laser energy exhibited similar sealing mechanism and buckling instability prior to

TH-2590_156103041

the closure of the crown [9]. Marston *et al.* [60] showed that the ejecta sheets dome over the free surface of the sessile droplet during free surface ablation, similar to that of the regular crown, and subsequently undergoes rupturing due to hole nucleation and propagation. Interestingly, the crown sealing and ejecta sheet disintegration dynamics remain unaltered even at reduced ambient pressure [60].

Furthermore, the temporal evolution of the intriguing hydrodynamic features discussed above, primarily liquid jets and crowns or ejecta sheets, also contributes towards the material ejection and effective atomization of the droplet. As we know, the efficiency of liquid droplet atomization and material expulsion are amongst the few critical parameters relevant to a series of industrial processes, specifically those targeting enhanced heat, mass, and momentum transfer via atomization. In this regard, the best example is the shattering of raindrops as they descend towards earth, a phenomenon seen ubiquitously in nature [140, 141].

A few early studies involving drop fragmentation by laser irradiation of monodisperse droplets showed that the partial fragmentation of the large droplets finally resulted in a thin liquid film surrounding the high velocity fragmented droplets, resembling a jellyfish [142–144]. On a similar note, Avila and Ohl [145] studied the dynamics of the cavitation bubble inside a liquid drop and their contribution towards droplet fragmentation. They have demarcated several atomization regimes based on the initial drop size and laser energy input and subsequently calculated the efficiency of atomization for each regime. Recently, Stan *et al.* [146] studied shock wave mediated explosion dynamics of liquid droplets and jets. They have developed a theoretical model of explosion dynamics to predict the adverse effect of the explosion on liquid samples during XEFL experiments. Apart from that, Snyder and Reitz [147] developed a new controlled atomization mechanism by focusing gas microjets from the underneath towards a liquid film, which produced secondary droplets as small as 20 μm in size. Many cutting-edge technologies such as atomization of micro-liter volume drop during liquid chromatography based on laser-induced breakdown spectroscopy (LIBS) [10] or drop shaping by laser in EUV nanolithography process [5, 148] [refer to Figure 1.7] or laser-induced forward transfer processes or laser ablation of soft tissues [129] etc., have intrigued the scientific community to explore the concerned fragmentation regimes further in a thorough manner.

TH-2590_156103041

1.3 Motivation and objectives

In view of the literature presented above, it is seen that a large portion of the microfluidics applications is based on the deformation of the liquid-vapour interface and subsequent atomization of a discrete droplet with or without an external field. In these processes, surface tension force always tries to resist the motion of the contact line or keep the interface intact. On the other hand, the externally applied potential (such as gravity, electric field, magnetic field) imparts instability to the interface and the contact line. As a result, the combined effect of substrate wettability and the magnitude and type of externally applied potential field can engender a host of interesting and complex hydrodynamic features suitable for numerous applications. Formation of the high-speed liquid jet, microjet, liquid crown, stable and unstable ejecta sheet, pinch-off, bursting, or atomization are a few most frequently observed and exhaustively studied flow morphologies in the aforementioned scenarios.

Despite the wealth of information available about the deformation dynamics of discrete liquid droplets in various scenarios enumerated above (Sections 1.2.1-1.2.4), there exists numerous unexplored areas capable of opening new avenues in microfluidics research. For instance, the growth dynamics of liquid droplets exhibit a different pattern on a wettable nozzle than that of a non-wettable solid nozzle [149]. However, the temporal evolution of the interfacial dynamics of a droplet formed on a porous, wettable nozzle has remained an open question in the literature. Similarly, the effect of increasing electric potential beyond the threshold of EWOD phenomena on the dynamics of the sessile droplet is, heretofore unknown in the open literature. Nonetheless, a complete understanding of the coupling between the external field and droplet behaviour is necessary to expand the horizon of microfluidics. The current thesis draws enormous motivation from the latter fact, wherein the central objective is to unfurl the intriguing details of some of these long-standing questions through rigorous experimentation and complementary theoretical analyses.

To address a few of the concerned open questions enumerated earlier, the following objectives have been finalized for the present thesis work.

- To study the capillary flow-mediated dynamics of liquid droplet generation from a yarn.
- To study the magnetowetting dynamics of sessile ferrofluid droplets on soft surfaces.

TH-2590_156103041

- To study the electric-discharge-mediated hydrodynamics of sessile liquid droplets.
- To study the impact dynamics of viscous liquid droplets on a soot-coated superhydrophobic surface.

Notably, we have chosen the above objectives to fit into the present thesis's central theme mentioned earlier. Herein, an honest attempt has been made to unfurl the fundamental physics of the systems under consideration in the objectives, with an expectation of furthering the existing knowledge and bridging the literature gaps in the respective systems. These microdroplet-surface-external field interactions leading to the atomization of the primary droplet governs applications ranging from condensation, frosting/icing, water harvesting, thermal management, and aerosol transport in the form of enhanced heat, mass, and momentum transfer.

1.4 Thesis overview

The remainder of the work discussed in this thesis is organized in the following chapters:

Chapter 2 presents the details of the high-speed imaging system and corresponding image-processing methods. The different components of the high-speed imaging technique, their capabilities, and corresponding calibration methods are discussed. Further, the different steps comprising the in-house image processing method are also discussed.

Chapter 3 presents a detailed appraisal of droplet growth dynamics during the capillary flow-driven droplet generation process from a yarn. The various stages of droplet growth are elucidated, and the effect of the thermophysical properties on the concerned process is also discussed. The experimental results of droplet growth dynamics are also validated with unified scaling laws.

Chapter 4 explores the effect of substrate elasticity on the magnetowetting dynamics of sessile ferrofluid droplets. The droplet's contact line exhibits different dynamics on substrates of different elasticity in a similar magnetic environment. While on the rigid substrate, the contact line experiences *stick-slip* dynamics, on the soft substrates, the contact line experiences the *pinning* effect. The substrate elasticity is also found to affect the dynamics of secondary droplets produced during magnetowetting.

TH-2590_156103041

Chapter 5 focuses on elucidating different hydrodynamic features, namely, liquid jet, crown, and bursting ejecta sheet, engendered by the deposition of discharge energy within a sessile droplet resting atop a polymer layer. Due to the dielectric discharge inside the droplet, cavitation bubbles are produced within the droplet, which subsequently undergoes expansion and collapse, resulting in acoustics pressure waves. A complex interaction of the pressure waves and cavitation bubbles drives the observed hydrodynamic features. A couple of regime maps based on several characteristics parameters are also proposed.

Chapter 6 discusses the impact dynamics of viscous droplets on a candle soot-coated superhydrophobic surface. Here, the dynamic wetting behaviour of the target surface is evaluated in terms of the spreading and retraction dynamics, droplet rebound, contact time, and liquid splashing behaviour of the liquid droplets. Additionally, the water-repelling behaviour of the bare soot-coated surface is compared and contrasted against several existing superhydrophobic surfaces.

Chapter 7 concludes the works presented in the thesis, along with the recommendations for future work.

TH-2590_156103041

TH-2590_156103041

Chapter 2

High-speed visualization and image processing

"The best and most beautiful things in the world cannot be seen or even touched. They must be felt with the heart"

- Helen Keller, *1891*

2.1 High-speed imaging system

The previous chapter highlights that the deformation of the liquid volumes in the presence of an external field is one of the crucial factors affecting the efficiency of many microfluidics applications. As such, it is essential to elucidate the intricate dynamics of the deformed liquid-vapour interface and the three-phase contact line, both qualitatively and quantitatively, in a precise and systematic way. In this regard, high-speed visualization techniques offer a systematic way to capture and analyze the concerned dynamics of liquid droplets. The basis of the aforementioned claim is much realized by looking at some of the phrases such as *making the invisible visible*, *seeing is believing*, *seeing the unseen*, or *capturing the moment* etc., coined to describe the beauty and capability of the high-speed or slow-motion movies [54]. Notably, the groundbreaking advancements in the field of high-speed visualization and image analysis algorithms, specifically the incorporation of machine learning or artificial intelligence algorithms in recent years, have contributed enormously to-

TH-2590_156103041

wards the detailed experimental realization of many complex physical systems in microfluidics. Apart from the microfluidics and bioscience applications, high-speed imagining techniques are also regularly used in several other industrial applications such as vehicle crash testing, airbag deployment, machine vision technology for packing and sorting, high-speed impact and materials testing, sport science, ballistics, and (nuclear) detonation and explosions [54]. However, in this chapter, the relevancy of these imaging techniques shall be discussed in the purview of microfluidics research. The currently adopted flow visualization techniques in the microfluidics research community primarily include *high-speed flash photography*, *shadowgraphy*, and *schlieren imaging*, *high-speed videography*, *digital holography*, *digital color interferometry*, *confocal microscopy*, *4D-confocal reference-free traction force microscopy (cTFM)* [150], *high-speed particle tracking velocimetry (2D-PTV, 3D-PTV)*, *high-speed particle imaging velocimetry (PIV, μ-PIV, or n-PIV)*, *planar laser-induced fluorescence (PLIF)*, etc., to name a few [54]. Each of the aforementioned techniques and their combinations offers a vast range of imaging capabilities starting from the motion of individual droplets or bubbles to turbulent jets [54]. Nevertheless, to cater to the demand for more comprehensive experimental realization of flow physics in the microfluidics research community, there is a continuing need to improve the current high-speed visualization techniques and identify several other potential avenues in both the visualization and image analysis domain.

Generally, high-speed photography and videography techniques are far more preferred to the other imaging tools (namely confocal or PIV imaging techniques) mentioned above, considering the complex physics and fast-paced dynamics of droplets, in analyzing most of the droplet-based and digital microfluidics systems [54, 152]. For instance, one of the most seminal contributions in the field of high-speed photography is the formation of a *milk coronet* or *milk crown* during the impact of a milk droplet on a plate covered with a thin layer of milk [see Figure 2.1(b)], was captured by *Harold Edgerton* in 1936 using flash photography [151]. This same phenomenon was initially reported in the pioneering work of Worthington in 1877, where he used a 3-μs spark plug illumination [see Figure 2.1(a)] to capture the crown formation during liquid droplet splash [29]. Notably, Edgerton is known as the father of modern flash photography. In the flash photography method, the fundamental concept is to freeze the motion of the focused object at the desired instant with the help of stroboscopic or flash lighting and simultaneously capturing the same with high-speed cameras for subsequent analyses. The frames captured at different instants

TH-2590_156103041

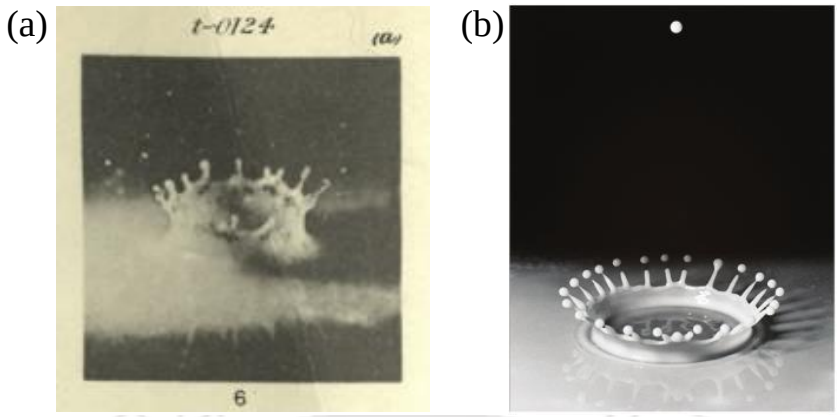


Figure 2.1: (a) Crown-shaped splash captured by Worthington [29] using spark illumination during the impact of a water droplet on a layer of milk mixed with water. (b) High-speed flash photography of a milk drop coronet captured by Edgerton [151], the pioneer of modern stroboscopic imaging. Here the milk drop impacts a thin layer of milk deposited atop a solid surface. The crown shape in both the cases, (a) and (b), is aided by the liquid surface tension.

from several reproducible events are then combined to obtain sequential images of the concerned process. As an example, Döring [153] successfully recorded sequential images of a *drop-on-demand (DOD)* drop formation event using the flash photography, and the subsequent superimposition of 100 such images revealed the key stages of the concerned process. However, the efforts failed to represent the entire event of drop formation. In a similar line, Chen and Basaran [154] carried out continuous recording of drop formation events by using an ultra-fast digital imaging system and successfully demonstrated some interesting facts such as the effects of ink properties on the ejected liquid length. Furthermore, Song *et al.* [155] have developed a drop growth monitoring and drop volume measurement system based on the *image drop analysis (IDA)* method with *charged coupled device (CCD)*, as an improvement over the already existing *drop analyzing technologies (DAT)* such as *fiber drop analyzing (FDA)* method, *capacitive drop analyzing (CDA)* method, etc., important to several industrial processes namely environmental quality monitoring, food technology, and related industries. Again, Dong *et al.* [156] developed a set-up composed of a CCD camera and short flash (pulsed laser duration 20 ns) for visualizing key stages of DOD drop formation events with a temporal resolution of 1 μs and spatial resolution of 81 μm/pixel. The latter study's most significant feature was the use of the *delay effect* for the camera and laser pulse relative to the drop generation from a printhead, which was adjusted with the help of a push-mode piezoelectric transducer

TH-2590_156103041



Figure 2.2: (a) The high-speed Photron fastcam mini UX camera, and (b) Navitar zoom lens, used in the current set-up.

attached to the printhead and a delay generator. In a related study, Hutchings *et al.* [152] employed a stroboscopic imaging technique comprised of nanosecond duration flash ($\sim$ 20 ns laser pulse), alongside an in-house image analysis code (*PEJET*), in order to explore the jet and drop dynamics near the print head of an ink-jet printing machine, specifically the spatiotemporal evolution of the shape, length and volume of jets. The image capturing techniques used in these studies successfully elucidated the key events of droplet generation from a printhead or a nozzle effectively, thereby improving the efficacy of the related industrial processes.

The existing literature reveals that the dynamics of the liquid drops or jets have mostly been investigated using stroboscopic (or flash) photography, which superimposes images taken at different instants of reproducible events of droplets or jets to analyze the associated dynamics. However, the images taken by the stroboscopic (or flash) photography method fail to show an accurate account of the temporal evolution of the entire process, specifically those involving a sudden change of flow rates or any intermediate/sudden external perturbation leading to instantaneous interface deformation of droplets or jets. In this regard, the high-speed videography technique appears to be more convenient, wherein the entire process of interest is captured in the form of a high-quality video. Subsequently, the captured video frames are restored, and quantitative data are extracted using the image processing algorithms. Most of the experimental realizations of this thesis work primarily use a high-speed *complementary metal-oxide semiconductors (CMOS)* device and a macro zoom lens to capture videos during the experiments. The high-speed camera used in the present experimental endeavours is built by *Photron®* *(Fastcam Mini*

TH-2590_156103041

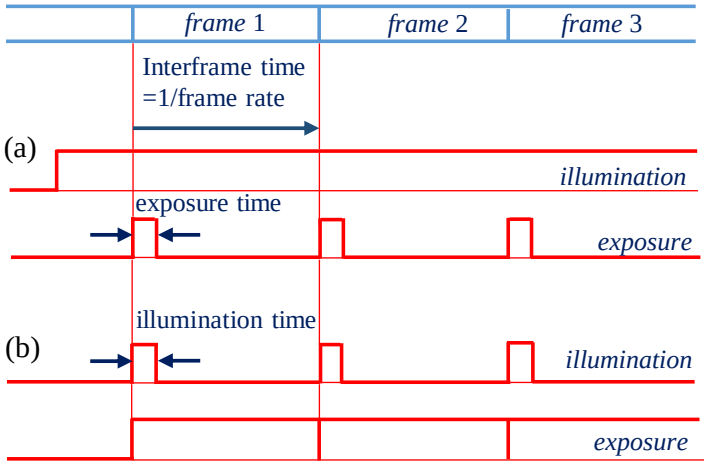


Figure 2.3: Schematic representation of the various terminologies associated with high-speed visualization techniques, namely *frame rate, interframe time, exposure time* and *illumination time* in a series of successive frames [image inspired from [54]]. (a) It shows the process of recording experiments aided by continuous illumination and an exposure time shorter than the interframe time, which helps freeze the motion of the object without motion blur. (b) Shows the process of recording high-speed events when several pulsed illuminations decide effective exposure. This video recording method allows flexibility to arbitrarily set the exposure time, up to a maximum limit equal to the interframe time.

UX100) and the macro zoom lens built by *Navitar® (18-108 mm F/2.5)* [see Figure 2.2]. Again, the background is continuously illuminated by a cold LED light source of high intensity *(Phlox®, 130000 lux)*. The external trigger for controlling the high-speed camera has been built in-house and is controlled manually during the experiments. If not mentioned explicitly, the same high-speed system will be used in all the experiments of this thesis.

It is of utmost importance to accurately define and characterize a few control parameters in order to obtain a high-speed video of excellent quality both in terms of resolution and contrast, before conducting the experiments. The control parameters considered in general are: *frame rate, interframe time, exposure time, illumination time*, which are depicted schematically in Figure 2.3 to aid the reader. Firstly, the *frame rate* is defined as the number of frames taken per unit time, and the units are generally given in frames per second (abbreviated as fps hereafter). For example, 1 Mfps represents 1 million frames per second. The Fastcam Mini UX100 high-speed camera used here can record up to a maximum frame rate of 800,000 at a resolution of 640 $\times$ 8 pixels. Also, the concerned high-speed camera is capable of recording at

TH-2590_156103041

full resolution, 1280 × 1024 pixels (equivalent to 1.3 megapixels), up to a frame rate of 4000 fps [157]. However, an increase in the frame rate is always compensated by a lower resolution of the acquired images or videos due to the limited throughput of the existing high-speed imaging systems. For example, if the frame rate is increased from 4000 fps to 40,960 fps, the screen resolution is decreased from 1280 × 1024 pixels to 1280 × 120 pixels. In this regard, the *interframe time* is defined as the time difference between two consecutive frames, and hence it can be defined as a reciprocal function of the *frame rate*. The current high-speed camera (Fastcam Mini UX 100) can have a minimum interframe time of 234 ns considering the maximum frame rate of 800 kfps. Again, the *exposure time* is defined as the time period (in seconds) for which the lens or the sensor is exposed to the object and can be controlled by varying the *shutter speed* and *aperture*. Notably, the shutter speed (exposure time) is independent of the frame rate. As a thumb rule of high-speed imaging, the exposure time is expected to be equal to or less than the interframe time to get an optimal temporal resolution and avoid motion blur. Apart from the shutter speed, by controlling the pulse length of the illumination source, i.e., the *illumination time*, the exposure time can be set in some specific high-speed cameras.

In essence, prior to choosing a high-speed imaging system for experimentation, it is essential to carry out a detailed appraisal of the system's sensitivity, actual (!) resolution, time-scale, shutter speeds, triggering options, and backlighting condition [54], in relation to the problem under study. Notably, the frame rate for capturing a fast-paced event can be determined from the relevant time-scale. Versluis [54] has mentioned the following equation for determining the optimum frame rate, f:

$$f = \frac{NU}{L}, \tag{2.1}$$

where, N is the required number of samples (≈ 5 - 10) based on the Nyquist sampling theorem, U and L are the characteristics velocity and length scale of the high-speed event, respectively. In the context of microfluidics where the characteristics length, L is very small and U is in the order of mm/ms or μm/μs, Eq. 2.1 suggests that a high frame rate, f and consequently, smaller interframe time is needed for capturing the hydrodynamics of the droplets. In nearly all the experimental works carried out as a part of this thesis work, 10000 fps to 12500 fps frame rate of the high-speed camera has been used, with a few exceptions, which shall be mentioned explicitly in the experimental methodology section of each chapter. Furthermore, the short ex-

TH-2590_156103041

posure time can be achieved by controlling the shutter speed of a high-speed camera. Notably, the Fastcam Mini UX 100 camera comes with a global electronic shutter, which can be adjusted to have a shutter speed as low as 1 µs with the associated software. For each experiment, the shutter speed is estimated from the relation, *shutter speed* $\leq \frac{1}{fps}$ (used just as a thumb rule, although shutter speed is not related to the frame rate as mentioned above) to obtain images with better spatial and temporal resolutions. The shortest shutter speed employed in this work is 80 µs while recording the phenomenon at 12500 fps. Also, to compensate for the loss in signal level due to low shutter speed and to nullify any smearing appearance of the desired object, high intensity LED backlight (130000 Lux) has been used in the experiments.

Moreover, keeping in mind that one of the main purposes of using high-speed imaging techniques in microfluidics flow visualization is to measure the dimensions too ephemeral to human eyes precisely, the aspect of magnification must be considered before experimentation, alongside the exposure settings. To elucidate the concerning dynamics of droplets, both in spatial and temporal front, a macro zooming lens is used in this work. However, too high magnification may lead to oversampling (denser spatial sampling), a shortened field of view, and lower image brightness [54]. Versluis [54] has suggested criteria for optimum magnification of a high-speed imaging system, based on the spatial Nyquist criterion, such that:

$$Magnification > 2r_p/R_s, \tag{2.2}$$

where r_p is the pixel size of the CMOS sensor located in the image plane, and R_s is the desired spatial resolution, based on Rayleigh criterion [158]. It is to note that the CMOS sensor of the high-speed camera used in this study has a 10 µm pixel pitch. Equation 2.2 suggests that the system's optimum magnification must be determined based on the spatial resolution of the object of interest and available light intensity to avoid both undersampling and oversampling. This further strengthens the previous claim regarding correct scaling for both length and velocity to obtain high contrast, high-resolution flow image.

Apart from the criteria mentioned above, triggering plays a key role during high-speed imaging experiments. Although this work completely resorted to manual triggering using a trigger switch, both *pre-triggered* and *post-triggered* acquisition techniques have been employed, depending upon the nature of the phenomena.

TH-2590_156103041

In the post-triggered acquisition method, the image frames are recorded just after the trigger button is pushed, and the trigger signal is termed as *start trigger* in this case. However, one might be interested in recording the conditions preceding the concerned event. In that situation, the pre-triggered acquisition technique is adopted, wherein the frames are already collected from the instances prior to triggering. In this triggering mode, termed as *end trigger* method, the software stores the image data in buffer memory and overrides the existing data once the trigger is pushed. The current high-speed camera facilitates both these triggering modes [157] alongside three other modes: *center*, *manual*, and *random*. Each of these modes offers different advantages and can be used according to the flow phenomena of interest. The high-speed imaging system used herein allows image data transfer conveniently, even during acquisition, to any hard drive or flash drive attached, with the help of a fast gigabit ethernet interface.

Apart from the high-speed imaging system, the microscale events having a comparatively larger temporal scale are captured using a high-quality camcorder (make: SONY) in this thesis work. Even though the camcorder offers a lower frame rate (25 fps) during the experiments compared to the high-speed cameras, the backlighting has been kept similar to that of the former. The camcorder's calibration is completed using a known length in the image to determine the relationship between the real length and image pixel, which is 0.057 ± 0.001 mm/pixel.

Overall, a systematic and high-quality image acquisition technique is an integral part of the high-speed experiments to get an insight into the many intriguing physical phenomena. As such, sincere effort has been given towards the same in this dissertation work. This has further helped in the acquisition of high-resolution and high-contrast experimental videos and images, which can be directly used in the image processing algorithms without any manipulation or beautification, a common malpractice in the scientific community [159, 160].

2.2 Image processing method

This section provides a detailed appraisal of the image processing methods and algorithms used in the current work for extracting quantitative information from the rendered high-speed videos. It is to note that the aforesaid *image processing* term bears the opposite meaning when compared with the *digital image editing* process.

TH-2590_156103041

However, both the terms are often used interchangeably among the mass, and hence it will be beneficial to distinguish between them beforehand. Digital image editing or digital imaging is the process of manipulating or beautifying digital images using an existing software program such as Adobe Photoshop or Photoscape, which is considered malpractice or misrepresentation in the scientific community [159, 160]. In contrast, image processing methods in the scientific research refers to the process of extracting quantitative information such as dimensions, coordinates, or any other measurements from the pixel values of the acquired digital images, using any available algorithms [161–163] or image processing software such as *ImageJ/Fiji* [162, 164], *MATLAB* [165], *ImageMagick* [166], among many others. These image processing softwares primarily offer comprehensive and well-documented software libraries, enabling easy and smooth implementation of the existing algorithms and synchronization with the new algorithms for the developers and scientists. One of the key features of the image processing software, which set them apart from the conventional *image editing* software, is the support for scripting in many conventional (*C/C++/Java*) and advanced (*Python/Julia*) languages. In addition, many new platforms such as *JuliaImages* [167, 168], *scikit-image* [169], *Insight Toolkit (ITK)* [170], and *OpenCV* [171], etc., are currently offering basic and advanced image processing techniques with complete flexibility of scripting and adding new algorithms.

In this thesis work, the open-source *ImageJ* (or *Fiji*) software [164] is used primarily for image processing of the experimental footage. Apart from being one of the most trusted and overly used software in scientific research since its inception, the other key features of ImageJ [164] include: (i) interactive and ready to use tools for visualizing, analyzing, editing, and image stacking; (ii) readily available plugins; (iii) availability of a macro-language interpreter, thereby enabling processing of a large block of codes over a group of images, and (iv) easy to store output data. Here, the desired image processing is completed in two stages: firstly, the digital processing of the experimental images is completed with the available tools and algorithms in ImageJ [164]. In the second stage, the extracted coordinate-pixel (X, Y, and I) data from the processed image of the first stage are used as input to an in-house C++ code. Subsequently, quantitative information has been obtained for further analyses. However, before going into the details of the current image processing method, the reason behind adopting such a detailed procedure while analyzing the dynamics of liquid drops is discussed below.

Most of the existing image processing methods for liquid droplet dynamics are

TH-2590_156103041

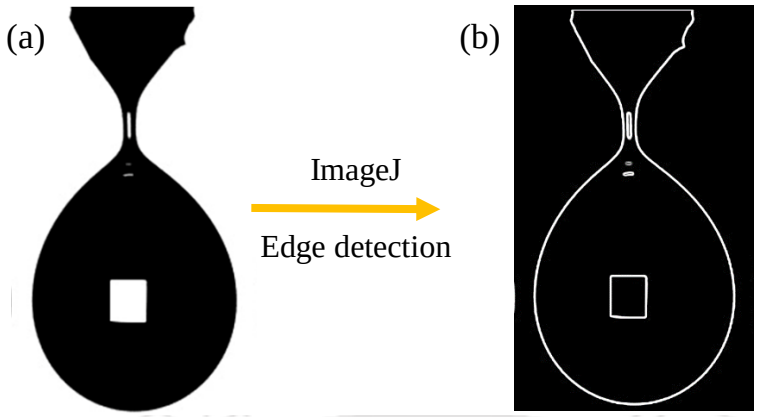


Figure 2.4: (a) Experimental image of a liquid droplet hanging from a surface. (b) The contour of the droplet after applying the *edge detection* tool in ImageJ [164].

generally useful when stroboscopic or flash photography techniques are used during the experiments. Fundamentally, in these studies, the use of flash or pulsed lighting results in a highly contrasted image quality, without any central white region [refer to Figure 2.4(a)]. As such, the *direct thresholding* algorithm of ImageJ or any other image processing software can be applied successfully for *edge detection* purpose. However, in the current situations where continuous lighting is used during high-speed videography technique, a central white region is formed in the acquired images as shown in Figure 2.4(a). The white region is formed when the bright backlight passes straight through the central drop area instead of being refracted away from the optical path [172]. This situation worsens in case of continuous LED backlighting and results in a misleading contour if not suppressed using a strong algorithm as shown in Figure 2.4(b).

The present study considers an image processing technique based on a coupling between open-source software ImageJ [164] and in-house C++ code. The videos of the time-dependent dynamics obtained experimentally, usually when converted to images, become huge in number. The macro management feature of ImageJ enables the management of such a huge number of files and processes them simultaneously. The pixel values obtained after processing the images by user-written macros are then rearranged and processed further by the in-house code in order to obtain the quantitative information of different features.

The workflow of the existing ImageJ commands used in the macros related to this thesis work is discussed below and also shown schematically in Figure 2.5.

1. **Unsharp masking**: This increases the ability to show local contrast by sup-

TH-2590_156103041

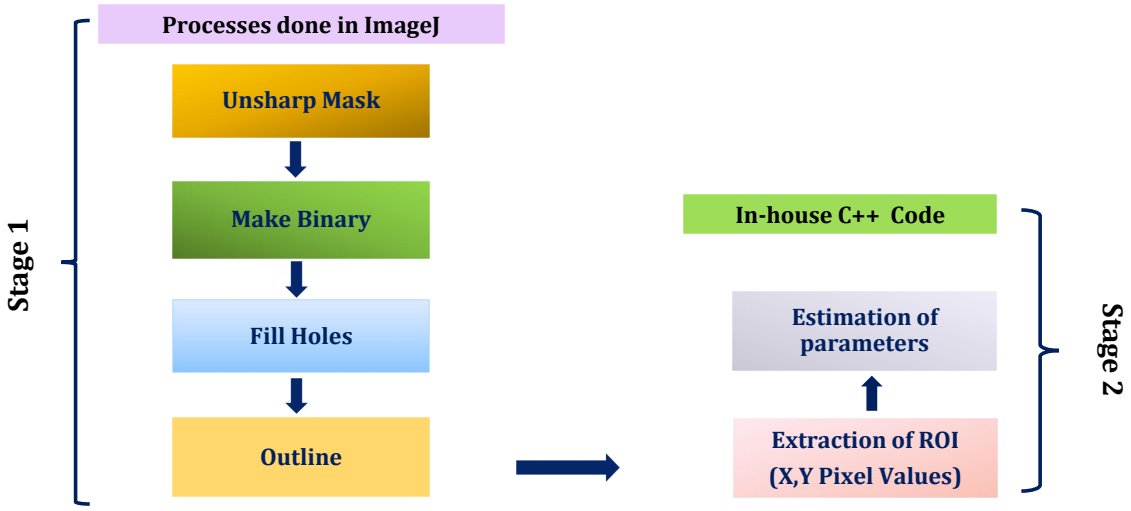


Figure 2.5: Flow chart depicting the various stages of the image processing method considered in this thesis work.

pressing the overall brightness range of the image. The suppression is done by first printing a *mask* image, slightly out of focus, onto another negative. This negative is developed and then placed on the original image to make the final print. This superposition reduces the exposure in the bright areas so that the detail can be obtained.

2. **Making binary**: The use of *Make Binary* command to a selected image or a slice of the image converts it to black and white by applying a predetermined threshold level. Making an image binary is necessary because the subsequent commands like *Fill Holes* and *Outline* are applied successfully only once it is made binary.

3. **Fill holes**: Any pixel that is part of a hole is *OFF* (i.e., part of the background) but is surrounded by *ON* pixels. For boundary representation, that means the pixel is within a boundary. For pixel representation, it means that it is not connected to other pixels that eventually form a path to the edge of the field of view. This feature enabled us to nullify the presence of bright central regions found in original images and fills it with black color, i.e., making it a part of the object, which is further useful in obtaining a proper edge of

TH-2590_156103041

the droplet.

4. **Outline**: In order to analyze the time-variant dynamics of the drops such as neck radius, length, etc., detection of the exact edge of the drop is highly desirable. This step facilitates easy tracking of the drop outline from the rest of the pixels.

5. **Crop image**: To remove unnecessary parts of an image, two commands, namely (i) *make rectangle* and (ii) *clear outside* are used in sequence. This has helped in obtaining a rectangular region of interest (ROI) around the drop and removing the undesired pixels.

6. **XY Coordinates**: For obtaining quantitative data from the black and white image files obtained from the previous step, i.e., the outline of the drop, *Save XY Coordinates...* command is used. This command writes the X and Y coordinates of each pixel of the active image file along with the intensity (I) values to a text file. Ideally, for a grayscale image, the pixel values assigned to the drop edge and the background should be 0 and 255, respectively, which may, however, deviate at some points if not made binary beforehand.

All the steps discussed above, as well as the finally obtained drop shape, is shown in Figure 2.6(a). The arrows in Figure 2.6(a) indicate the sequence of execution of the steps (1)-(6) discussed previously. Figure 2.6(a) shows the image obtained experimentally, while the final drop outline is shown in Figure 2.6(d). Notably, the present image processing method, comprised of the steps (1)-(6) mentioned above, has successfully extracted the outline of even a low contrast image. The significant contribution of the above method lies in eliminating the central white region and subsequently, extracting the actual *edge* of the droplet without detecting any internal edges arising from the white reflection unlike in Figure 2.4. As such, the method can be put forward as an alternative image processing method, specifically for applications involving high-speed videography techniques.

In the second stage of the current image processing method, the X and Y coordinates obtained in stage 1 are processed with the help of an in-house C++ code [refer to Figures 2.5 and 2.6(b)], for the calculation of concerned droplet/jet dimensions and volumes. The total volume of the droplet can be obtained from the acquired 2D image by adding the volumes of all the cylindrical cross-sections considered along the vertical axis [refer to the leftmost panel of Figure 2.6(b)]. The volume of a

TH-2590_156103041

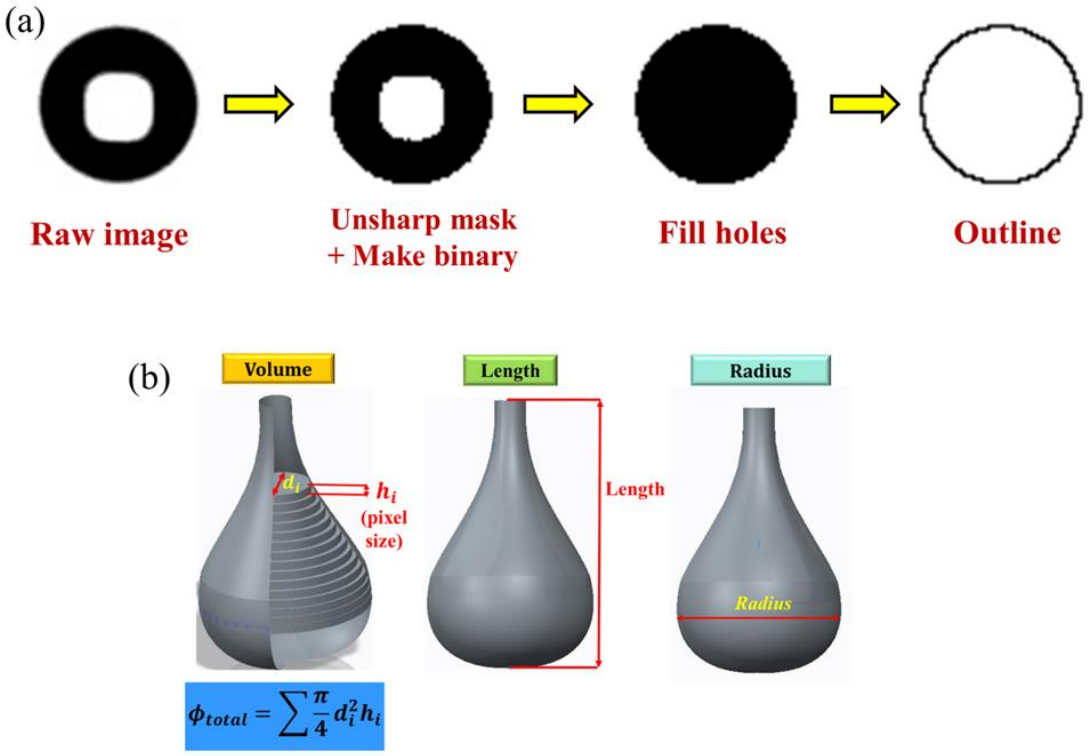


Figure 2.6: (a) Shows the different stages (in sequence) of the image-processing method adopted in this thesis work for the analysis of the high-speed events in in ImageJ [164]. (b) Shows the calculations of different quantitative parameters, namely volume, length, and radius of a deforming droplet.

cross-section having unit height, h_i (= 1 pixel in the vertical axis), and diameter (d_i) equal to the width of the slice is (calculated from the two extreme horizontal points considered along the same plane), $\phi_i = \frac{\pi}{4} d_i^2 h_i$ and as such, the total volume is calculated as shown below, i.e.,

$$\phi_{total} = \sum_{i=1}^{n} \phi_i = \sum_{i=1}^{n} \frac{\pi}{4} d_i^2 h_i, \tag{2.3}$$

where $i \in [1-n]$ indicates the number of slices considered along the vertical axis. As a result, it is possible to identify the temporal evolution of the droplet/jet volume from Eq. 2.3 within the complete time-period. Apart from the evolution of the droplet volume, the algorithm can successfully capture the disintegration of the parent droplet/jet, specifically the pinch-off phenomena, which is one of the key stages of DOD drop formation events. Further, a few other important parameters

TH-2590_156103041

associated with droplet (or jetting) dynamics, such as length of the droplet (or jet), any radial dimension [including the details of the necking event during droplet generation process as shown in Figures 2.7 and 2.8], or aspect ratio, etc. as shown in the middle and right panels of Figure 2.6(b). The aforementioned method has been employed effectively for calculating the volume of a droplet from a 2D image in many studies [152, 156]. It is to note that, if not mentioned specifically in the concerned chapter, the volume of the droplet and jets will be calculated with this method in the following experimental studies. Unlike the previous studies where the droplet volume is obtained from a spherical cap approximation, the use of the present method helps in eliminating the possible occurrence of any errors arising out of deviation in the droplet shape.

Apart from the above, the in-house code can reliably calculate the total surface area (A) of a droplet or any object of interest (up to micron-scale) from the captured experimental images. Later from the calculated surface area, it is possible to obtain the equivalent diameter of the droplet (or object) as follows:

$$d = \sqrt{\frac{4A}{\pi}}. \tag{2.4}$$

This method is successfully applied for calculating the equivalent diameter of the secondary droplets in all the studies involving droplet disintegration in the subsequent chapters. Specifically, this proposed method has been fruitful in calculating the secondary droplet size engendered by splashing in Chapter 6. However, during the measurement of the diameter of the out-of-focus droplets, additional masking is applied in the concerned areas, apart from applying the aforementioned steps (1)-(6). In the coming section, the present method will be validated through comparison with some experimental results to ensure its robustness and universality.

2.3 Validation of the image processing method

The robustness of the aforementioned image processing technique is shown with a sample experiment of droplet dripping from an orifice. The experiments of droplet dripping are among the most critical phenomena of microscale fluid flow, wherein the liquid-vapour interface experiences singularity as the dynamics approaches the pinch-off. Figures 2.7(a)-2.7(l) shows the spatiotemporal evolution of the interface

TH-2590_156103041

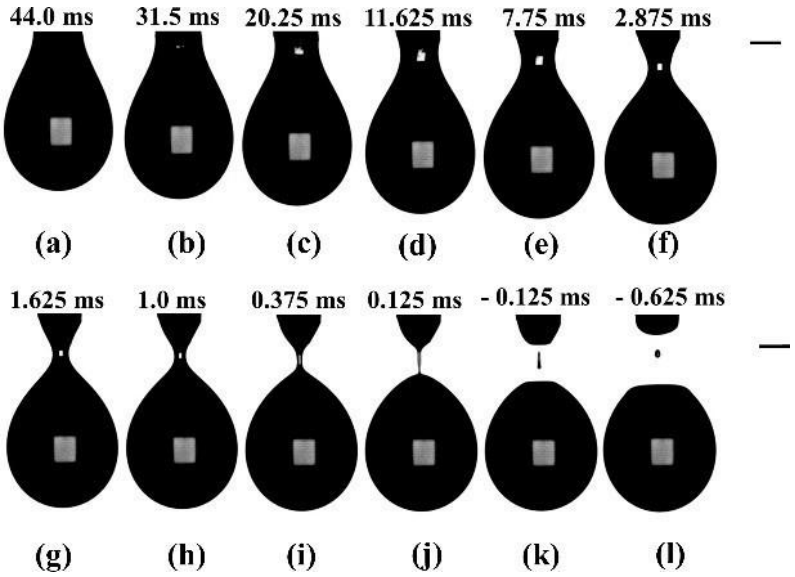


Figure 2.7: Droplet growth at the exit of an orifice near pinch-off. The scale bars shown on the right-hand side correspond to 1 mm.

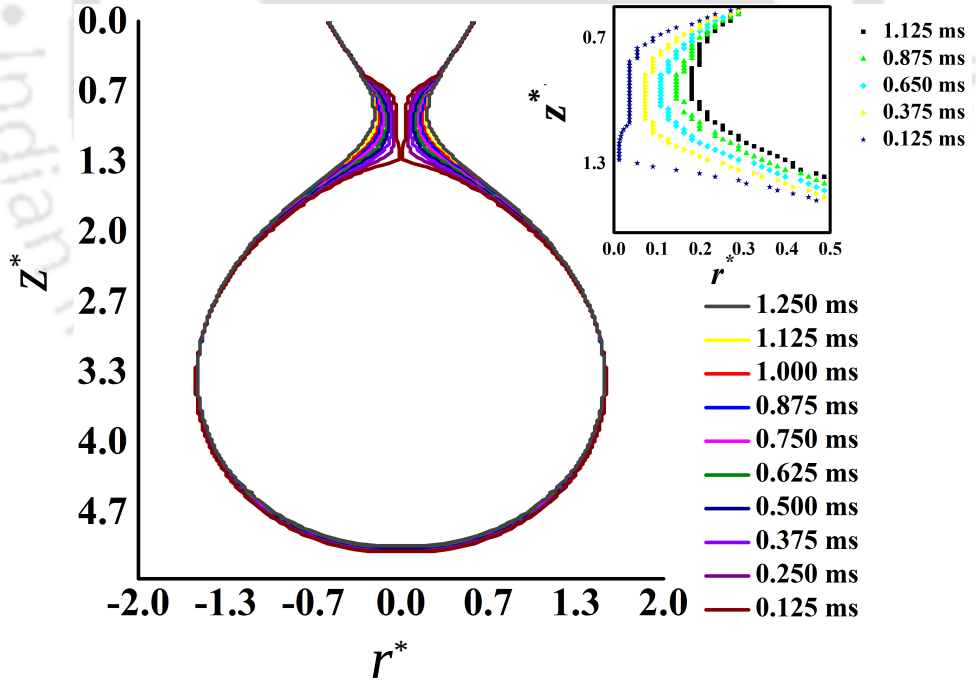


Figure 2.8: Contour of the droplet interface as extracted by using the current image processing method, corresponding to Figure 2.7. The zoomed view shows the necking phenomenon in detail.

TH-2590_156103041

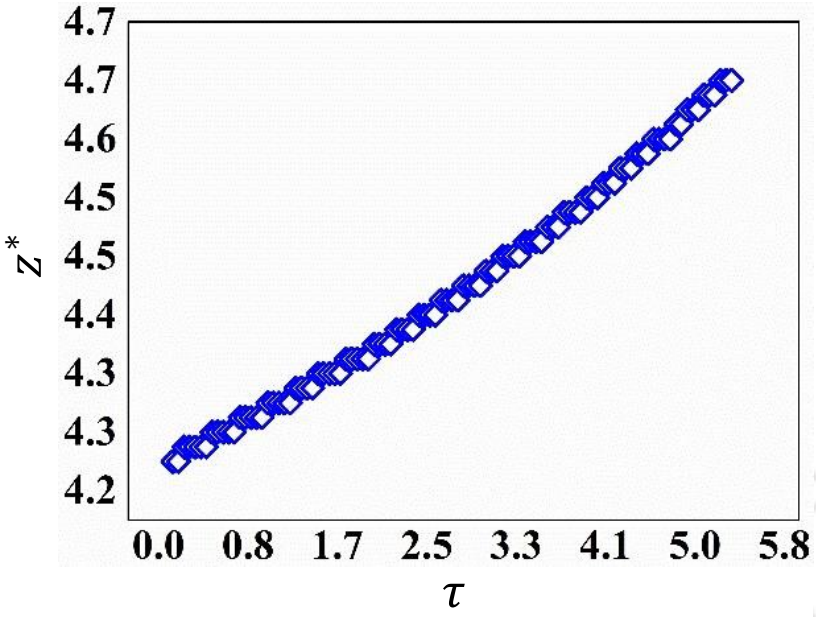


Figure 2.9: Temporal evolution of the droplet length for the events near pinch-off, corresponding to Figure 2.7.

of a water droplet hanging from an orifice or nozzle. The instant of droplet pinch-off is considered as $t = 0$ [which is expected to be in between Figures 2.7(j) and 2.7(k)], and the time post-breakup is represented in a negative scale. Interestingly, such a complex evolution of the interface, including the singularity near pinch-off, is excellently captured by the current image processing technique, as shown in Figure 2.8 [zoomed view in the inset]. In Figure 2.8, the differently coloured curves refer to different instants of droplet growth, whereas the length (z^*) and the radius r^* of the droplet is shown in the vertical and horizontal axis, respectively. Herein, the starred counterparts of the variables (z and r), i.e., $z^* = z/r_{nozzle}$ and $r^* = r/r_{nozzle}$, indicate the non-dimensional droplet length and radius, respectively, where, r_{nozzle} refers to the exit diameter of the nozzle or orifice.

Furthermore, several important facts regarding events near droplet pinch-off can be corroborated from Figure 2.8. Firstly, the spatiotemporal evolution of the droplet interface shows that the length and volume change slightly near the pinch-off. In contrast, the neck of the hanging droplet (the minimum radius along the interface) shrinks rapidly till the instant of pinch-off. Both of these observations agree strongly with that of the existing studies [154]. Again, Figure 2.9 shows the temporal variation of the droplet length corresponding to the events in Figure 2.7.

TH-2590_156103041

Here, the time-scale is expressed in the non-dimensional form, $\tau = (t - t_b)/t_{cap}$, along the horizontal axis. The term, $t - t_b$ refers to the time remaining for breakup, with t_b being the instant of breakup and $t_{cap} = \sqrt{\rho r_{nozzle}^3/\gamma}$ is the capillary time considering the properties [ρ and γ signify the density and surface tension of the droplet]. The plot reflects the meager rate of increment in droplet length, confirming the aforementioned claim.

In essence, Figures 2.7-2.9 and the corresponding discussions highlight the efficiency and accuracy of the present image processing method in extracting necessary quantitative information from the rendered high-speed images. Unless mentioned explicitly in the corresponding chapters, the aforementioned method is followed religiously in this thesis work. Also, the results obtained during the experiments in the following chapters will further strengthen the claim regarding the very high efficacy of the proposed method.

2.4 Summary

The present chapter reports the image processing technique adopted throughout the thesis for extracting quantitative information from the captured experimental images. A brief description of the different components of the high-speed visualization system considered in this thesis work and their calibration technique is also provided in this chapter. Apart from that, the use and the capability of the open-source image processing software ImageJ and the in-house C++ code is also discussed in the context of the experimental studies of this thesis work. The proposed method can capture even micron-scale resolution both in temporal and spatial front, as shown through the validation with the experimental results. The capabilities of the concerned image processing technique shall be explored in the following chapters of this thesis work.

TH-2590_156103041

TH-2590_156103041

Chapter 3

Experimental characterization of the growth dynamics during capillarity-driven droplet generation

"The science of today is the technology of tomorrow"

- Edward Teller, *1962*

3.1 Introduction

The transmission of liquids through the porous network of the naturally abundant, as well as the synthetic objects, is a ubiquitous phenomenon and has been studied extensively both by the researchers and industrialists since ages [173–179]. Specifically, the immense potential of spontaneous capillary flows (SCF) in transporting liquids through the porous networks of yarns, without the use of external pumping, have been put into use in numerous industrial and day-to-day applications, which primarily encompass textile [180, 181], and mold preparation industries

The contents in this chapter have been published as Sarma, B., Shahapure, V., Dalal, A. and Basu, D. N. (2019) "Experimental characterization of the growth dynamics during capillarity-driven droplet generation", *Physical Review E*, vol. **100**, p.- 013106.

TH-2590_156103041

[182], biomedical devices [183–185], forensic laboratories [186, 187], household drying [188, 189], coating processes, etc. The wicking ability of the constituent yarns emerges out to be one of the most influential parameters for the successful operation of these devices and processes, as has been envisaged in several experimental and analytical studies [175, 190–195].

Drop formation from a nozzle or orifice is another interesting hydrodynamic phenomenon with a wide and varied range of uses, such as inkjet printing [196, 197], spray formation [198, 199], DNA microarray deposition [200], microencapsulation [201, 202] etc. The rich underlying physics associated with the dynamics of growth and breakup of a liquid drop from a nozzle/orifice has been explored exhaustively with experimental [203–206] and computational techniques [27, 207–210] over the last few decades. Two contrasting modes of drop formation dynamics, namely dripping and jetting, [206, 211], have been identified with the help of High-speed visualization techniques and subsequent image processing [54, 212]. One of the pioneering attempts to capture the bifurcation process of pendant drops was reported by Hauser *et al.* [213] and was reproduced a decade later by Peregrine *et al.* [214]. In recent years, owing to the advancement of High-speed imaging techniques, researchers have been able to visibly explore many intricate physics of drop formation and breakup, the crucial dynamics in the vicinity of pinch-off [210, 215] in particular, which remained unfathomed only till the last decade. Such advanced experimental tools and methods have immense contributions in uncovering the relevant phenomenon, leading to some wonderful recent efforts, such as the formation of a drop from a wettable nozzle [149], tilted nozzle [216], droplet formation in dense suspension [217] etc., which has high relevancy with the industrial processes. An additional discussion on the dynamics of drop formation is given in Section 1.2.1 of Chapter 1.

In essence, it is very much evident that numerous research works have separately explored drop formation in nozzles and wicking in yarns. However, few systematic studies exist towards elucidating the rich physics of droplet generation by wicking in the porous network of a yarn. In this chapter, an honest attempt has been made to bridge this gap by unveiling the dynamics of drop formation from an unwoven yarn under varying flow conditions. A simple experimental arrangement constructed by using a yarn, as shown in Figure 3.1, serves the purpose of addressing many new aspects in the regime of drop dripping that have heretofore been unexplored. The prime focus of this chapter is a systematic experimental investigation of the dynamics of the three-phase (air-liquid-yarn) contact line during droplet growth in a yarn

TH-2590_156103041

under the effect of gravity and interfacial forces. By bringing the yarn in contact with the liquid in a reservoir, a flow field can be established owing to the continuous wicking of the liquid in the available porous network. Once the yarn is saturated, the continuously incoming liquid generates a bulb of liquid mass at the freely hanging end, which develops in volume with time. The contact line of the droplet with the yarn has distinct vertical motion during the entire growth period, which can subsequently be classified into multiple regimes. With the help of video-graphic techniques, the interfacial dynamics in each of these regimes have been captured eloquently. The subsequent image processing and data analysis of the captured videos lead to a unified description of the underlying physical phenomena in terms of the competing forces controlling the droplet contact line's dynamics. This kind of distinct vertical motion of the contact line is ubiquitously seen during the capillary rise of a liquid in a wettable tube [218] or porous material [219] or droplet sliding along a wettable surface [220] as well as in the rare case of drop formation in a wettable nozzle [149] while being a rarity during the drop generation from non-wettable nozzles [203, 221, 222].

3.2 Experimental method and materials

Figure 3.1 shows the schematic of the experimental set-up developed for this chapter, which involves a yarn hanging from an infinite liquid reservoir. A filament type yarn with an average diameter in the range of 1.5 ± 0.08 mm in the as-procured condition plays the role of the droplet generator, and a microtip of 1000 μL volume behaves as the infinite fluid reservoir, constantly supplying the fluid necessary for drop formation. The yarn consists of 4 fibers or filaments, having an average diameter in the range of 0.86 ± 0.03 mm. The surface of the yarn has been examined with the help of scanning electron microscopy (SEM) as shown in Figure 3.2, which reveals the underlying porous network facilitating liquid flow through the yarn. All the yarns are cut out at a length of 40 mm from a large roll of the same and checked for length and diameters using an optical microscope (Leica DM 2500M) before using in the experiments. For each set of experimental conditions, a separate pair of reservoir and yarn has been used. The liquid level at the reservoir has been kept constant for each experimental cycle to nullify the effect of variation in the hydrostatic pressure on the capillary flow rate. Special attention has also been given while placing the

TH-2590_156103041

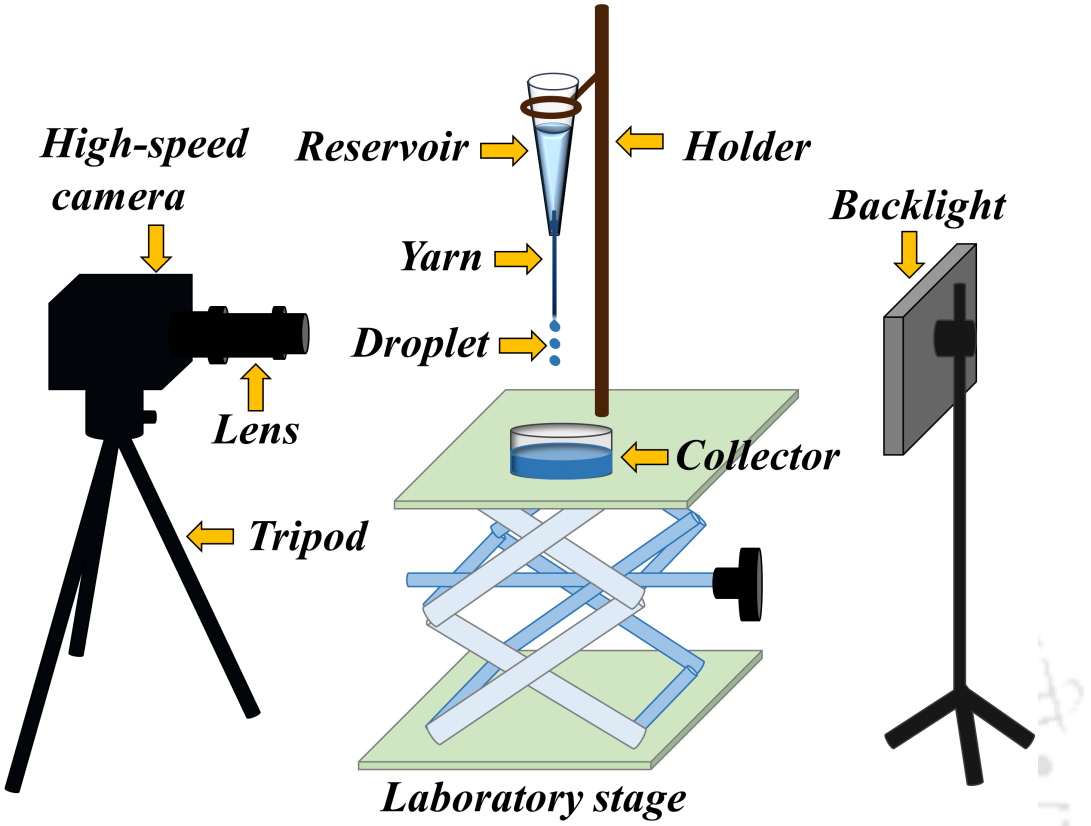


Figure 3.1: Schematic diagram of the experimental set-up with all the components.

yarn in contact with the reservoir to ensure that the capillary penetration occurs only due to the transplanar wicking mode, while the rest of the wicking modes remain suppressed [192]. Moreover, a simple knot has been provided in the yarn at the end dipped in the liquid reservoir to prohibit any sidewise leakage and obtain drop formation only due to capillary flow within the yarn.

The experiments have been carried out for four different liquids, namely DI-water (DIW, Merck Millipore, grade I, resistivity 18.2 MΩ cm at 25°C), hexadecane (Hexd), 60% glycerol (aqueous) solution (Gly60) and 2% Tween 20 solution in DI-water (Twn20). The relevant thermophysical properties, namely viscosity, surface tension, and density of each of the experimental fluids, have been measured with the help of a rheometer (PHYSICA MCR 101; Aanton Paar), tensiometer (DY-300; Kyowa), and density meter (Aanton Paar; DMA 4500) respectively and are enlisted in Table 3.1. The working fluids are chosen in such a way that the working range of viscosity and surface tension spans across a wide range.

The video recordings of the experiments have been carried out with a digi-

TH-2590_156103041

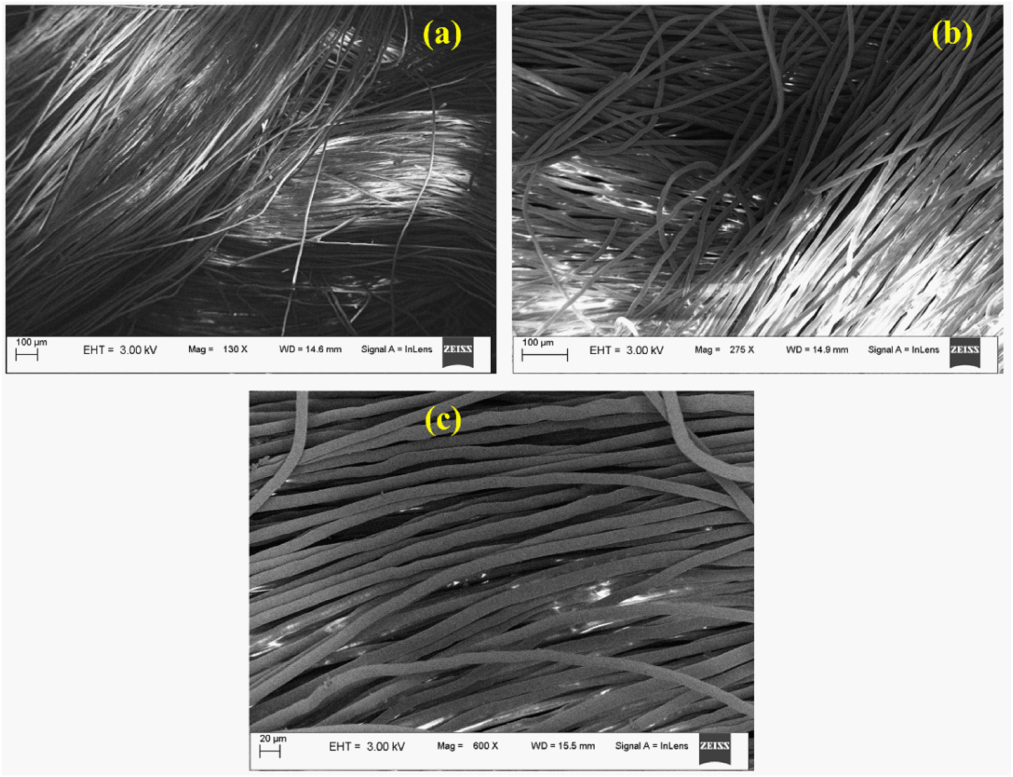


Figure 3.2: SEM images of the yarn surface with different magnifications (a) 130x; (b) 275x; and (c) 600x showing the capillary networks.

Table 3.1: Properties of experimental fluids.

Liquid	Density (ρ, kg/m^3)	Viscosity (η, mPa s)	Surface Tension (γ, mN/m)
DIW	1000.0	1.0	72.0
2% Tween 20 sol.	1000.34	1.04	36.3
40% DIW + 60% Gly.	1165.4	12.75	69.5
Hexadecane	770.0	3.0	27.0

tal camera (Cybershot DSC-HX100v, SONY Crop. Japan) at a frame rate of 25 frames per second. A bright LED Light (Phlox, 130000 Lux) placed opposite to the recorder, as shown in Figure 3.1, provides continuous back-lighting in all the experimental conditions. This arrangement ensures a sharp contrast of the interfaces relative to the background. The recorded images are then stored in a PC for subsequent image processing and analysis. An open-source image processing software ImageJ [164] has been used for the analysis of the captured experimental images.

TH-2590_156103041

Table 3.2: Experimental conditions during droplet generation from a yarn.

Flow rate	$Q\times 10^{11}$ (m^3/s)	$We \times 10^9$	$Oh \times 10^3$	$Fr \times 10^5$
Q^{DIW}	56.8 ± 5	1078.7 ± 100	4.3	375.10 ± 10
Q^{Twn20}	8.68 ± 0.3	50.31 ± 3	6.33	57.32 ± 5
Q^{Hexd}	2.06 ± 0.2	2.90 ± 0.1	24.1	13.6 ± 2
Q^{Gly60}	0.63 ± 0.07	0.16 ± 0.03	51.7	4.2 ± 0.3

The fluid properties expected to influence the dynamics of drop formation are surface tension (γ), density (ρ), and viscosity (η) of the penetrating fluid, which further can be clubbed together to form the following set of non-dimensional numbers: We, Fr, and Oh, pertinent to the physics involved in this study. Here, the Weber number, $We = \rho v_{avg}^2 L/\gamma$ signifies the relative importance of the inertia force to the capillary force, the Froude number, $Fr = v_{avg}/\sqrt{gL}$, signifies the relative importance of inertia force to the gravitational force, and the Ohnesorge number, $Oh = \eta/\sqrt{\rho\gamma L}$, expresses the relative importance of viscous force over the inertial force and capillary force. Herein, the yarn's radius, r_y, has been scaled as the characteristic length, L, and the average flow velocity, v_{avg} $(= Q/\pi r_y^2)$ has been scaled as the characteristic velocity while calculating the non-dimensional numbers. Q is the average flow rate of the penetrating fluid through the porous network, measured by the volumetric fluid measurement method. Table 3.2 enlists the values of the non-dimensional numbers along with the corresponding flow rates.

3.3 Results and discussion

This section presents a detailed appraisal of the contact line and interfacial dynamics associated with the generation of a droplet from a yarn. For the experimental conditions listed in Table 3.2, spontaneous capillary flow within the yarn's porous network engendered the formation of a droplet, which grows in time due to the accumulation of the continuously incoming mass of liquid at the free end of the yarn. This growing fluidic bulb experiences a series of changes in geometry, starting with the barrel-shaped at the beginning to the pear-shaped prior to the detachment, alongside the associated contact line movements. The plethora of events, as depicted sequentially in Figure 3.3, starts with the growth of the droplet in both radial and

TH-2590_156103041

axial directions, which is followed by the downward motion of the liquid bulb until it reaches the free end of the yarn, where it finally detaches, yielding a parent droplet and a satellite one.

In order to elicit and quantify the growth history of the droplet, the present

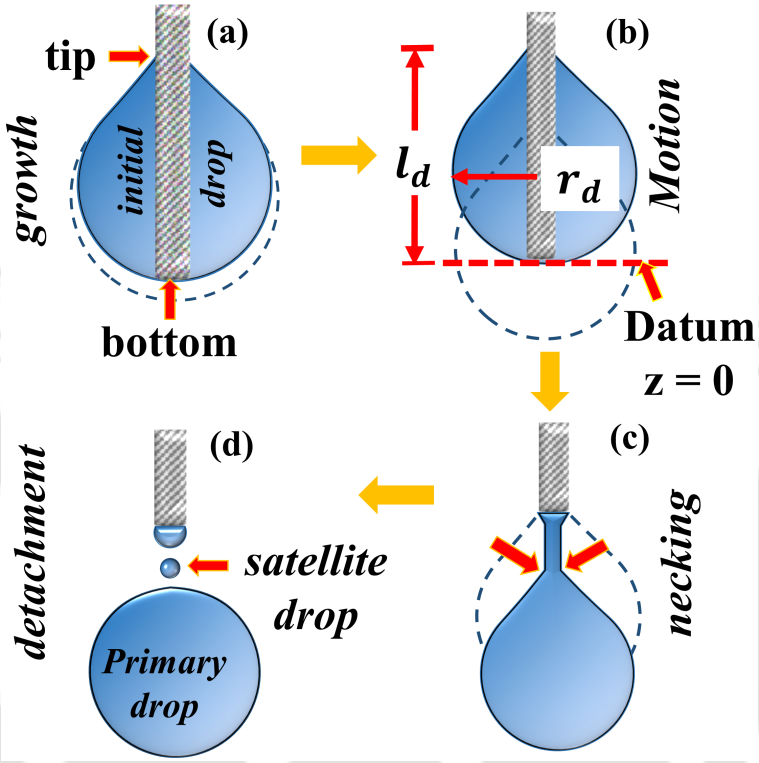


Figure 3.3: Schematic diagram of the different stages involved in drop formation from a yarn namely, (a) growth (*radial* and *axial*), (b) *motion*, (c) *necking* and (d) *detachment*. The yellow arrows show the sequence of the occurrence of the events. The two red arrows in (a) show the position of two points of interest, namely, *tip* and *bottom*, referred for describing the growth dynamics of the droplets in yarn. The variables l_d and r_d, shown in (b) with respective positions of measurements, represent the droplet's length and radius, respectively. The red dashed line drawn in the yarn's free end in (b) represents the datum's position, $z = 0$, considered for various measurements during the study.

discussion considers the spatiotemporal evolution of the trajectory of two points around the droplet, naming them as *tip* and *bottom* as shown in Figure 3.3(a). The tip, referred to as z_{tp}, corresponds to the TPCL of the droplet with the yarn, whereas the bottom-most point of the droplet along the yarn is named as the bottom (represented as z_{bt}). The relative positioning of these two points from the datum, i.e., $z = 0$, has been used to quantify the droplet's movement and location along

TH-2590_156103041

the yarn's axial direction. It is to note that the free end of the hanging yarn has been considered as the datum [refer to Figure 3.3(b)] for the ease of referencing and quantifying the trajectories. The exact location of z_{tp} has been identified in a two-step process: firstly, the raw images are converted into binary images in ImageJ software [164], which helps in marking the exact pixels representing the tip in the zoomed view of the binary images. Next, the position of the TPCL is visually tracked down, which is indicated by the change or movement in the intensity of the pixels between two consecutive images considered. Similarly, to track the dynamics of the shape change, the maximum radius of the droplet at each instant is found to be of paramount importance, and it has been identified schematically in Figure 3.3(b) by a variable r_d. Further, the length of the droplet has been deduced as the difference in position between the tip and bottom at each instant, i.e., $l_d = z_{tp} - z_{bt}$. In what follows, the temporal evolution of the trajectories of the z_{tp} and z_{bt}, as well as the droplet radius r_d, have been explored for a wide range of experimental conditions [listed in Table 3.2] to elucidate the growth dynamics of the droplet and also the different transitional regimes in Sections 3.3.1 - 3.3.5.

3.3.1 Growth dynamics of water droplets

Figure 3.4 shows snapshots of the spatiotemporal evolution of the interface and the contact line of a water droplet during its growth from a yarn. Herein, the instant of the detachment of the previous drop has been considered as $t = 0$ in the physical timescale, which acts as a reference for the subsequent snapshots. Also, the position of the tip (z_{tp}) at each instant is marked by the red arrows, a convention followed meticulously in the remainder of the chapter. It can be inferred from Figures 3.4(a)-3.4(c) that, at the onset, the contact line of the water drop, i.e., tip starts moving upward, along with the continued radial expansion of the droplet resulting in a growing bulb. The upward movement of the tip also results in augmentation in the length of the droplet. Both this radial and axial expansion leads to a consequent increment in the contact angle of the droplet, thereby changing the shape of the droplet from barrel shape at the onset to the pear shape as seen in Figure 3.4(c). However, as soon as the value of the contact angle reaches saturation (approximately 10°), the upward movement of the tip gets arrested, indicating the beginning of the second phase [refer to Figure 3.4(c)]. The delicate balance between the surface energy and the gravitational energy determines this saturation contact angle and

TH-2590_156103041

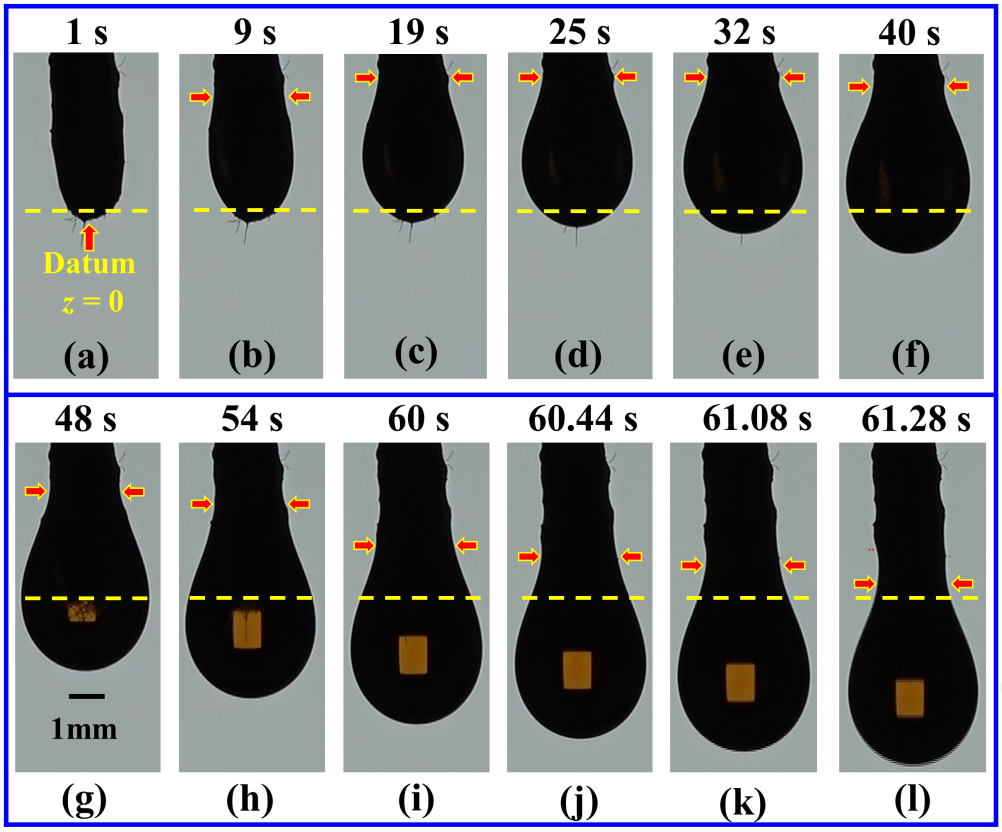


Figure 3.4: Spatiotemporal evolution of the droplet interface during the generation of a water droplet from a yarn. The corresponding experimental conditions are, $We = 1.078 \times 10^{-6}$, $Oh = 0.0043$, $Fr = 3.76 \times 10^{-3}$. The red arrows mark the position of the TPCL of the droplet (z_{tp}) at different instances, whereas the yellow dashed lines in the snapshots refer to the location of the datum. The scale bar shows 1 mm in length. The events have been recorded at 25 frames per second using a SONY camcorder.

the shape of the interface at each instant. This first stage of the droplet growth has been coined as *radial growth* stage (referred as *RG* hereafter), owing to the relatively higher rate of radial expansion in comparison to the axial expansion, which shall be discussed elaborately in the subsequent sections.

At the beginning of the second stage, the tip starts dwelling at its maximum position, whereas the bottom starts moving away from the datum, $z = 0$, as seen in Figures 3.4(d) and 3.4(e), accommodating the continuously incoming mass of liquid. The dynamics result in a significant increase in the droplet's total length, although the interface of the droplet continues to be pear-shaped. This second stage having a higher rate of expansion in the axial direction can be termed as *axial growth* stage

TH-2590_156103041

(referred to as AG hereafter). The continuous radial and the axial expansion results in a continuous enhancement in the droplet volume till the moment it attains a critical volume [discussed separately in Section 3.3.4], beyond which the gravitational pull is able to overcome the resisting forces (namely, capillary forces at the contact line). This initiates a sliding motion of the bulbous mass in the downward direction, as seen in Figures 3.4(f)-3.4(l), which persists till the detachment of the droplet from the yarn. Compared to the previous two stages, this stage has a significantly longer time span during the growth of the drop, named as *motion* stage. In one of the following subsections, it will be shown quantitatively that during this stage, the change in the droplet volume is minimal, whereas it bears the distinct sign of the movement of the contact line, which again justifies the term coined to this stage.

An account of the temporal variation in the positions of the tip (circle) and

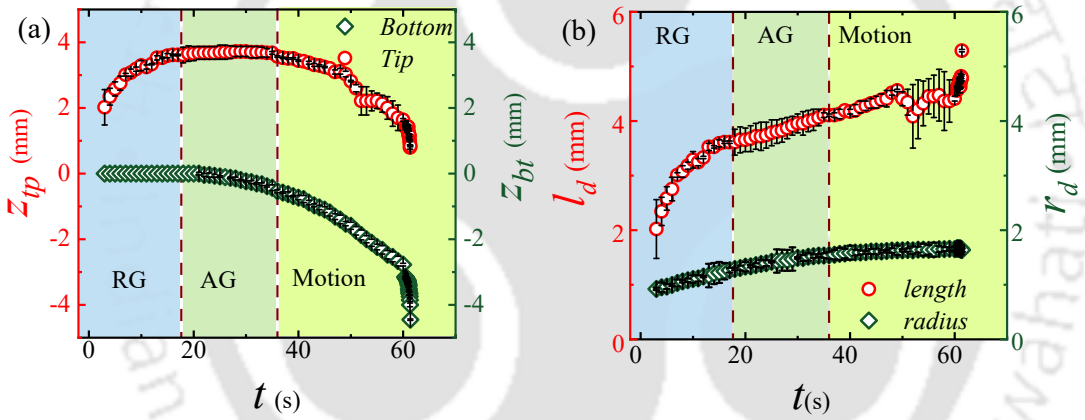


Figure 3.5: (a) The temporal variation of the position of the tip, z_{tp} and bottom, z_{bt} points during the growth of a water drop. (b) The variation of length, l_d, and radius, r_d of a water drop during its growth stage. Position of the tip and bottom below the datum, i.e., $z = 0$ (yellow dashed line in Figure 3.4), is considered negative, while the position above it has been considered as positive. The dashed vertical lines delineate the three stages of drop growth in both (a) and (b). The corresponding experimental conditions are, $We = 1.078 \times 10^{-6}$, $Oh = 0.0043$, $Fr = 3.76 \times 10^{-3}$. The uncertainties in the measurement of the position of the respective identities at each instant are marked by the error bars associated with each data point.

bottom (diamond) helps in capturing the dynamics of the contact line, as well as easy delineation of the above mentioned three stages as seen in Figure 3.5(a). Each of the three stages is found to have distinct characterizing slopes, with the corresponding points of inflection marking the transition from one stage to the other. With the tip climbing upward and the bottom of the droplet dwelling at the datum, i.e., $z_{bt} = z =$

TH-2590_156103041

0, the accumulated fluid mass expands radially in the first regime, exhibiting a time period of approximately 20 s in all the experiments done with water as the working fluid. As calculated from the experimental data plotted in Figure 3.5(a), the contact line reaches a maximum velocity of approximately 0.3 mm/s while climbing upward. Although a sharp change in the slope is present in the trajectory of z_{tp} as it enters the second stage, the transition of z_{bt} appears to be noticeably smoother [see Figure 3.5(a)]. The pinning of the tip at its maximum position (z_{tp}^{max}) is the characteristic feature of this second regime, which seems to have a time period of approximately 15 s. Figure 3.5(a) further reveals the continuous movement of the bottom, veering away from the datum during this AG stage. The depinning of the *tip* happens as soon as the weight of the continuously growing bulb overcomes the resisting forces. In Section 3.3.4, the theoretical modelling of this critical volume of the growing droplet is shown through a delicate force balance between the driving and resisting forces. Although the trajectory of z_{tp} further experiences a sudden change in the slope at the beginning of the third stage, however, it moves in a near synchronous manner with the trajectory of z_{bt} as the dynamics of the third stage evolves. The tip starts sliding towards the datum, i.e., the end of the yarn, and the bottom keeps on moving away from the yarn end as shown in Figure 3.5(a). The differently coloured zones represent the extent of a particular regime, whereas the common boundary marked by the dashed line signifies the borderline of transition between the three different regimes.

Furthermore, for a systematic investigation of the temporal evolution of the interface, the temporal variation of the radius, r_d and the length, l_d of the droplet is considered in Figure 3.5(b). Notably, both the curves hint towards the presence of three distinct regimes of droplet growth. While the different regimes are prominent along the curve of l_d due to the presence of sharp changes in its slope, the curve of r_d has a relatively smoother transition from one regime to the other. Qualitatively, both r_d and l_d increase continuously due to the incoming fluidic mass accumulation. However, the radial expansion rate slows down as the dynamics progress towards detachment, as reflected from the continually decreasing slope of the r_d curve at each stage. Interestingly, the time period of occurrence and transition of the dynamics of both the movement of the contact line and the interfacial shape change coincides with each other for all the stages during the droplet growth as seen in Figures 3.5(a) and 3.5(b). This mutual dependence between the contact line movement and shape change dynamics has further been extended for the growth of more viscous liquids

TH-2590_156103041

(than water) in the following subsection.

3.3.2 Effect of enhanced viscosity of the penetrating fluid

This section explores the effect of an increase in the penetrating fluid's viscosity on the growth dynamics of a droplet from a yarn. An increase in viscosity is achieved by allowing capillary penetration of different experimental fluids, as enlisted in Table 3.1, with viscosity ranging from 1.04 mPa s to 12.75 mPa s. As confirmed by Washburn's law of wicking [173, 223] as well as its modified versions for different porous structures [195], viscosity is a key parameter that affects both the saturation limit and the wicking rate, and even the slightest increase in viscosity of the penetrating fluid can slow down the rate of wicking to a great extent owing to the increment in the viscous drag within the capillary network [195]. The reduction in flow rate further delays the growth rate of the droplet. The spatiotemporal evolution of the liquid-air interface along with the movement of the contact line during the growth of a viscous droplet is shown in Figure 3.6. The representative snapshots of Figures 3.6(A)-3.6(L) in row (i) correspond to the generation of a droplet of tween 20 solution, whereas the snapshots 3.6(A)-3.6(L) in row (ii) show the growth of a hexadecane droplet on a yarn. The red arrows mark the tip of the droplet in Figure 3.6. The movement of the tip along the yarn for both the liquids suggests the presence of all the three regimes encountered previously in the case of water droplets. However, a one-to-one comparison of the snapshots reveals that the onset of each regime and the transition from one regime to another is significantly delayed in the physical timescale, as the viscosity of the imbibing fluid is increased even by a marginal amount.

Figure 3.7 shows the time-varying trajectories of z_{tp} and z_{bt} during the growth of both the droplets shown in Figure 3.6. The two different colors (magenta and blue) of the corresponding symbols (circle and diamond) signify the two different experimental fluids tween 20 solution (Twn20) and hexadecane (Hexd), respectively. It can be discerned that even with the slightest increase in the viscosity value, the incipience of each stage of droplet growth is delayed, thereby further delaying the transition from one regime to the other, as claimed previously. For example, in case of tween 20 solution, the end of the RG stage and transition to the AG stage takes place approximately at 50 s, whereas for, hexadecane the corresponding instant marks only the beginning of the RG stage in the physical timescale. The interfa-

TH-2590_156103041

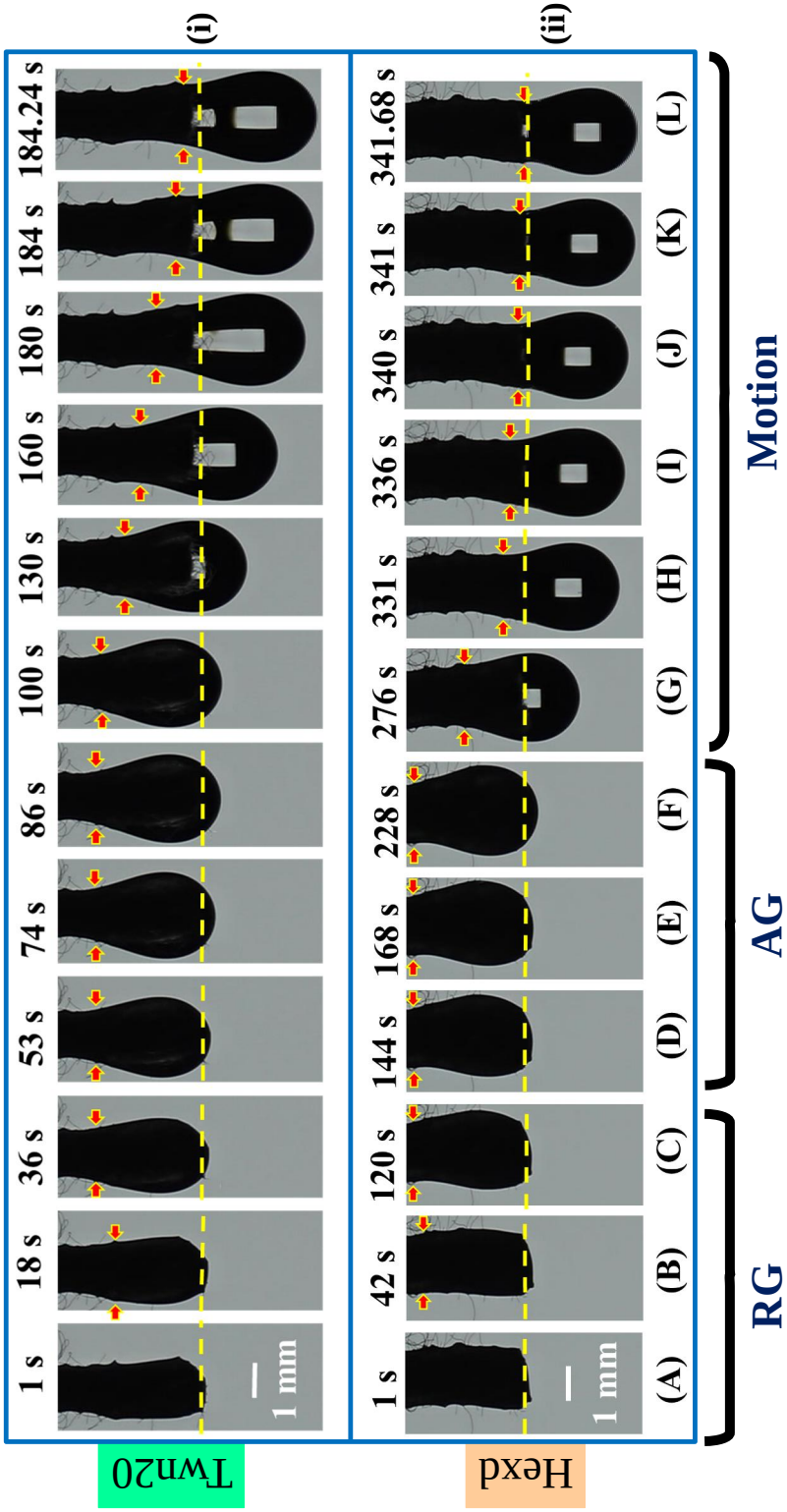


Figure 3.6: (a) Spatiotemporal evolution of the interface during the growth of (i) tween 20 and (ii) hexadecane droplets from a yarn. The red arrows mark the position of the TPCL at different instants. The scale bar shows 1 mm in length. The corresponding experimental conditions are listed in Table 3.2. The yellow dashed lines in the snapshots of rows (i) and (ii) show the datum.

TH-2590_156103041

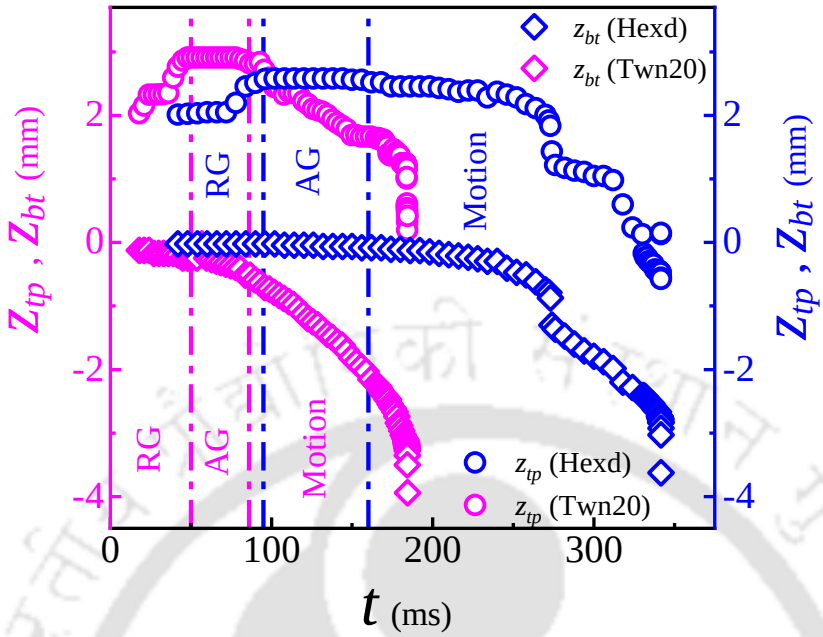


Figure 3.7: The temporal variation of z_{tp} and z_{bt} for two experimental fluids (marked by different colours), namely, Tween20 and Hexadecane, during droplet growth in a yarn [corresponding to Figure 3.6]. The differently colored dotted vertical lines delineate all the three stages seen during the drop growth period.

cial shape change of the droplet is also expected to follow the delayed transition regimes. Notably, the droplet's shape in all the experimental conditions follows the Young-Laplace equation, as shown in Section B.1 of Appendix B.

3.3.3 Self-similar contact line and interface profile evolution

A cumulative appraisal of the dynamics of the contact line during the growth of the droplet encompassing all the experimental conditions can be drawn by representing the trajectory in a non-dimensional framework of z_{tp} as shown in Figure 3.8(a). The non-dimensionalization of both z_{tp} and t has been done with the help of the maximum value of the corresponding identities, i.e. $z^*_{tp} = z_{tp}/z^{max}_{tp}$ and $t^* = t/t_{total}$, wherein t_{total} is the total time taken for the generation of one drop in each experimental cycle and z^{max}_{tp} is the maximum value of z_{tp} within that time period, t_{total}. It is to note that t_{total} signifies the total time span observed for each experiment calculated from the beginning of the RG stage to the final detachment of the droplet from the yarn. This kind of unique non-dimensionalization helps in extracting information regarding the rate of evolution of each dependent variable over a unit

TH-2590_156103041

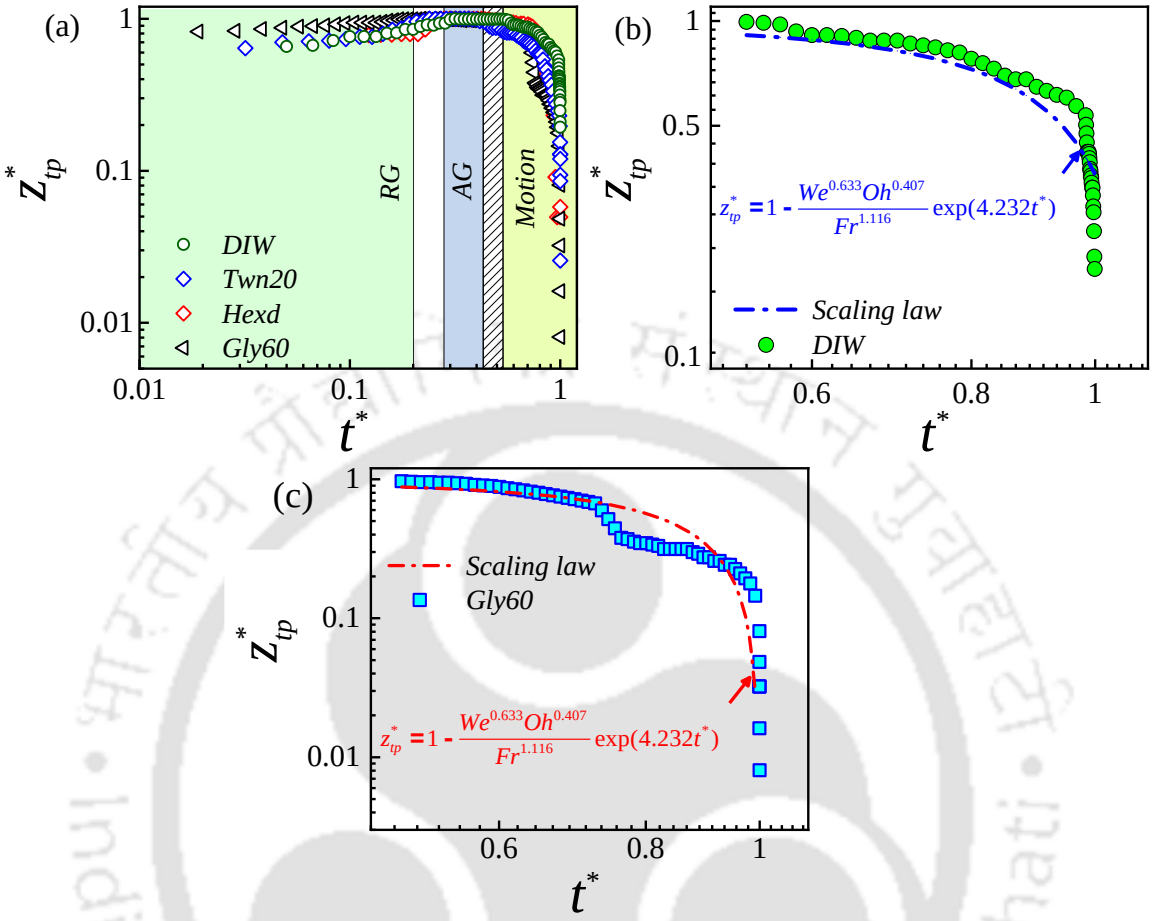


Figure 3.8: (a) The variation of the non-dimensional tip position, z^*_{tp} with non-dimensional time t^* is plotted in a log-log scale for all the experimental conditions. The vertical shaded regimes correspond to the transition regimes separating the three stages of drop growth. Plots (b) and (c) compare the experimental data of z^*_{tp} with the derived asymptotic relation (dashed-dotted line), Eq. 3.5, for water (DIW) and 60% glycerol (Gly60) solution, respectively.

time span and one-to-one comparison of each relevant quantity in different experimental conditions. Figure 3.8(a) shows the variation of z^*_{tp} with t^* in a log-log scale for all the experimental conditions studied herein. The presence of three distinct regimes during the droplet growth becomes evident from Figure 3.8(a), wherein all the non-dimensional profiles of z^*_{tp} collapsed to a single trajectory, despite starting from different initial instants. This hint towards self-similarity in the contact line profile evolution in the later stages of the droplet growth period, specifically in the motion stage, irrespective of the initial conditions. Another important observation from Figure 3.8(a) is the presence of two shallow windows for the transition of the

TH-2590_156103041

contact line dynamics from one regime to another, marked by two differently hashed zones. A qualitative assessment of the data reveals that the *RG-to-AG* transition of the contact line dynamics takes place within the first 20-30% of the total time span for the experimental conditions studied herein. The second transition window appears in 45-55% of the total time taken for droplet growth, where the dynamics transform from the AG stage to the motion stage.

The self-similarity between the temporal dynamics of the contact line during the motion stage can be modeled by considering the competing forces during the period, namely, capillary force, viscous drag, and gravity. The capillary force at the tip can be expressed as [224], $F_c = 2\pi\gamma r_y \cos\theta_c$, whereas the viscous force on the droplet appears as, $F_v = -2\pi\eta l_{wt}\frac{v}{\ln\left(\frac{r_d}{r_y}\right)}$ [149, 225]. Herein, v, θ_c, and l_{wt} signify the vertical velocity of z_{tp}, contact angle, and wetted length of the yarn, respectively. The viscous drag has been derived after solving the momentum conservation equation in cylindrical coordinates for the droplet, subjected to the boundary conditions of zero vertical velocity (v_z) along the outer surface of the yarn ($r = r_y$) and equals to the velocity of the drop at its interface ($v_z = v$ and $r = r_d$), and deriving the shear-stress term as, $\eta\frac{dv_z}{dr}|_{r=r_y} = -\frac{\eta v}{r_y \ln\left(\frac{r_d}{r_y}\right)}$, where $\frac{dv_z}{dr}$ is the velocity gradient along the radial direction (r). The shear stress acts over the surface around the cylindrical yarn, $2\pi r_y l_{wt}$, resulting in the viscous friction force, F_v during the movement of the droplet. Considering the gravitational force as, $F_g = mg$, where m is the instantaneous mass of the liquid drop, the governing equation can be written in the following form:

$$\frac{d(mv)}{dt} = 2\pi\gamma r_y \cos\theta_c \pm 2\pi\eta l_{wt}\frac{v}{\ln\left(\frac{r_d}{r_y}\right)} - mg. \tag{3.1}$$

The mass of the drop can be expected to increase linearly with time, i.e. $m = \dot{m}(t - t_0)$, where $\dot{m}$ is the mass flux and t_0 refers to the beginning of the RG stage. However, qualitative analysis [refer Section 3.3.4] of the experimental data clearly shows that the change in the mass of the droplet is negligible in the motion stage, and as such, the droplet mass is considered to be constant in this stage. By introducing the following dimensionless characteristic variables;

$$l^*_{wt} = \frac{l_{wt}}{L}, t^* = \frac{t}{\tau}, m^* = \frac{m}{\rho L^3}, v^* = \frac{v}{v_{avg}} = \frac{v}{\frac{L}{\tau}}, \tag{3.2}$$

TH-2590_156103041

where, $L = r_y$ and $\tau = t_{total}$ are the characteristic length and time scale, respectively. Substituting the dimensionless characteristic variables from Eq. 3.2, Eq. 3.1 can be converted to the following non-dimensional form:

$$\frac{d(m^*v^*)}{dt^*} = \frac{2\pi\cos\theta_c}{We} \pm \frac{2\pi}{Re\ln\left(\frac{r_d}{r_y}\right)}v^*l^*_{wt} - \frac{1}{Fr^2}m^*. \tag{3.3}$$

Here, the Weber number, We and Froude number, Fr bears the same definition as discussed in Section 3.2. The Reynolds number, Re signifies the balance between the inertia force and the viscous force and defined as, $Re = \rho v_{avg}L/\eta$ with v_{avg} being the characteristic velocity scale as seen in Eq. 3.2. Interestingly, Eq. 3.3 bears the same form of the governing equation as mentioned in Chang *et al.* [149] for droplet formation in a wettable nozzle. Substituting $Oh = \frac{We^{1/2}}{Re}$, in Eq. 3.3, Eq. 3.4 is obtained in terms of the non-dimensional numbers considered herein, as:

$$\frac{d(m^*v^*)}{dt^*} = \frac{2\pi\cos\theta_c}{We} \pm \frac{2\pi}{\frac{We^{1/2}}{Oh}\ln\left(\frac{r_d}{r_y}\right)}v^*l^*_{wt} - \frac{1}{Fr^2}m^*. \tag{3.4}$$

Equation 3.4 shows the important non-dimensional groups, namely We, Fr and Oh, necessary for determining the scaling law for z^*_{tp} with respect to time, t^* during the downward movement of the drop. A regression analysis [see detail in Section B.2 of Appendix B] of all the experimental data sets suggests the following co-relation between z^*_{tp} and t^*:

$$z^*_{tp} = 1 - \left(\frac{We^{0.633}Oh^{0.407}}{Fr^{1.116}}exp(4.232t^*)\right). \tag{3.5}$$

An account of the exponents of the non-dimensional groups of Eq. 3.5 reflects that the gravity force dominates the temporal dynamics of the contact line, z_{tp} in this third regime. Although surface tension tries to resist the droplet motion, its effect appears to be weaker than the weight of the droplet as soon as it starts descending along the yarn. The asymptotic relation between z^*_{tp} and t^* gives a good agreement with the experimental data as seen in Figures 3.8(b) and 3.8(c), which shows the temporal evolution of z^*_{tp} in the motion stage for water and 60% glycerol solution, respectively. The scaling law reported above (Eq. 3.5) has a good resemblance with the asymptotic relation proposed by Chang *et al.* [149]. However, the latter

TH-2590_156103041

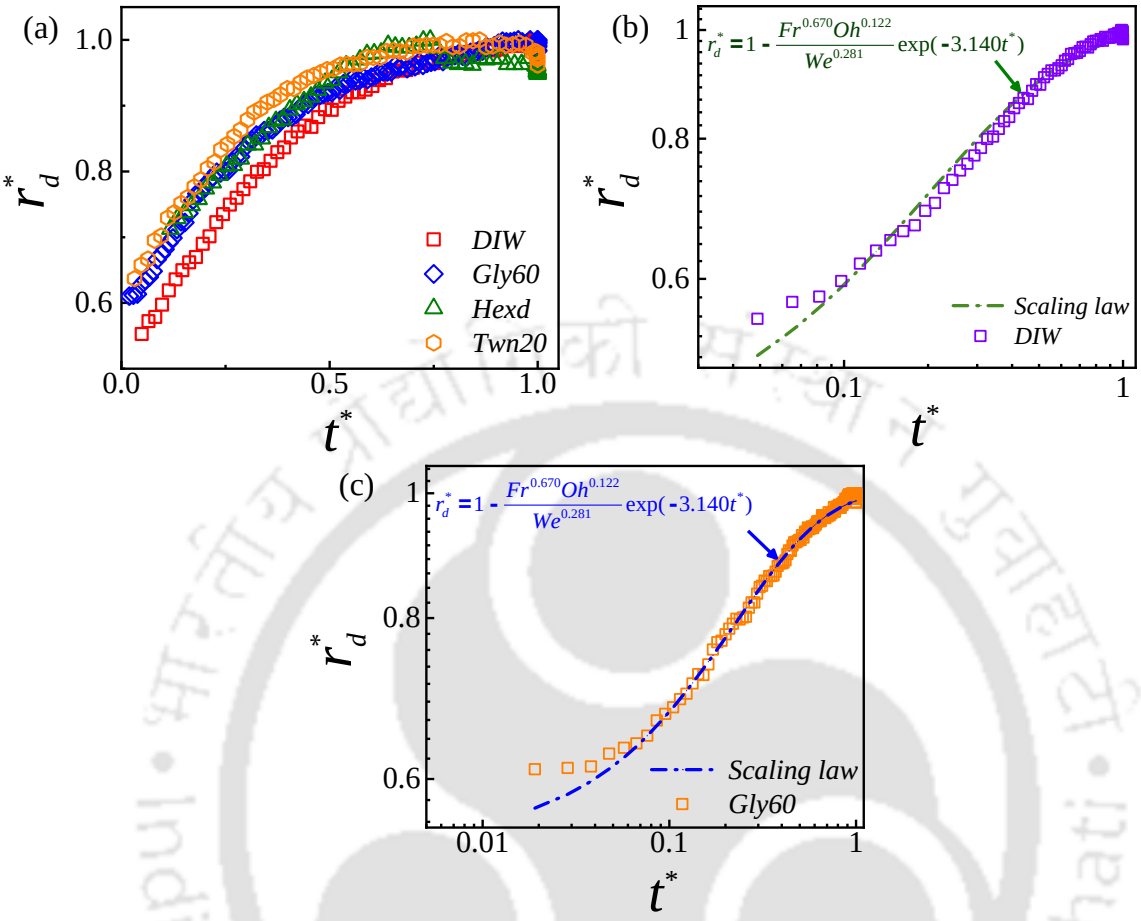


Figure 3.9: (a) Linear plot of variation of non-dimensional radius, r_d^* with non-dimensional time, t^* of a continuously growing droplet at different experimental conditions corresponding to Table 3.2. Logarithmic plots of r_d^* with t^* exhibit the good agreement between the derived scaling law (dashed-dotted line), Eq. 3.6, and the experimental data for (b) water and (c) 60% glycerol solution, respectively.

has shown a parabolic fit of the position of the contact line of the droplet while it descends along a wettable nozzle, whereas an exponential decrease of z_{tp}^* has been observed in this study.

Furthermore, the spatiotemporal evolution of the interface of the droplet during its growth can be well understood by plotting the variation of the non-dimensional radius, r_d^* with time, t^* as shown in Figure 3.9(a). Herein, the physical timescale has been non-dimensionalized as discussed previously, whereas the maximum values of the droplet radius, r_d^{max} over the considered time span, t_{total} has been used as the scale for non-dimensionalization of the radius. Figure 3.9(a) clearly shows that, irrespective of the experimental conditions, all the profiles of r_d^* follow a similar kind

TH-2590_156103041

of asymptotic trajectory during the growth period. However, the vertical shift of the profiles can be attributed to the variations in their thermophysical properties. Also, the initially-separated profiles converge beyond a specific time instant, as seen in Figure 3.9(a). A quantitative assessment of the experimental data reveals that the profile converges approximately at 55% of their total time period, which is also, coincidentally, the transition point of the contact line dynamics from the AG stage to the motion stage. Till this transition point, the radius of the droplet grows to nearly 90%-95% of its final value. Hence the third stage involves very little change in the radius as well as the droplet volume, which also strengthens the previous claim that the mass of the droplet remains nearly constant during that period.

Again, the claim regarding the universal droplet growth dynamics can further be strengthened by proposing a scaling law for r_d^*, specifically in the first two stages of growth dynamics in terms of the non-dimensional groups: We, Oh and Fr. The regression analysis [see detail in Section B.2 of Appendix B] of the experimental data of r_d^* suggests the following asymptotic scaling law:

$$r_d^* = 1 - \left(\frac{Fr^{0.670} Oh^{0.122}}{We^{0.281}} exp(-3.410 t^*) \right). \tag{3.6}$$

The inversely proportional relationship between the We and r_d^* in Eq. 3.6 signifies the logical trend of a fluid with higher surface tension trying to hold a droplet of greater radius. The asymptotic relation of Eq. 3.6 also suggests that the capillary force dominates the gravity force during the first stages of growth, and this results in the upward movement of the *tip*, as well as higher radial expansion in the initial period, as discussed previously. As per Eq. 3.6, the rate of change of the droplet radius will be more in the initial periods, which eventually slows down, and finally, the radius of the droplet will remain nearly constant, which coincides with the observation in Figure 3.9(a). The good agreement between the experimentally measured data and theoretical prediction can be seen in Figures 3.9(b) and 3.9(c) plotted for two fluids, water, and 60% glycerol solution, respectively. It is to note that the scaling relation [Eq. 3.6], differs greatly from the scaling law, $D_d^* = (4 + 6t^*)^{(1/3)}$ obtained in case of generation of a droplet from an orifice under constant flow condition [27]. The latter takes care of the growth of a spherical droplet constantly adhering to a nozzle exit, in contrast to this study where the droplet undergoes changes from the barrel to pear-shape, and is never spherical. Equation 3.6 has been derived in the

TH-2590_156103041

purview of this difference in basic assumption, considering the contributions of the thermophysical properties of the experimental fluids.

3.3.4 Estimation of critical volume required for sliding

The critical volume, ϕ_{sl}^{cr}, of the droplet, which is nothing but the maximum volume attained by the droplet prior to the beginning of downward sliding from its maximum position, has a direct effect on the final volume of the detached droplet. The instant of occurrence of ϕ_{sl}^{cr} is the point of transition between the second and the third stage. As estimated previously, r_d attains nearly 90-95% of its final radius, whereas l_d reaches nearly 80% of its total length till the end of the second stage. Approximating the droplet shape with an annular cylinder, i.e., $\phi_{sl}^{cr} \sim ZR^2 \sim l_d^{cr}(r_d^{cr})^2$, it can be estimated that the droplet volume nearly attains 70%-80% of its total volume (i.e., the volume of the detached primary droplet) just before initiating the downward motion in each experimental conditions. Here, r_d^{cr} and l_d^{cr} represents the critical radius and the length of the droplet at the instant of measurement of ϕ_{sl}^{cr}, respectively.

By considering the delicate balance between the driving and the resisting forces, ϕ_{sl}^{cr} can be estimated theoretically. Along with the driving force, F_g and the resisting force, F_c, mentioned in Section 3.3.3, the capillary force due to the presence of a liquid film along the yarn, F_{fc}, has also been considered as another resisting force while estimating ϕ_{sl}^{cr}. However, the viscous drag, F_v, has not been considered herein due to the negligible velocity of the interface at the onset of sliding motion. The *AG-to-motion* stage transition occurs once F_g just overcomes the static friction offered by F_c and F_{fc} for a droplet of volume ϕ_{sl}^{cr}. Notably, both the resisting forces are larger when the surface tension is higher. The resisting force due to the liquid film also depends upon the droplet wetting length, l_{wt}, and becomes large with higher film thickness.

The discussed force balance, shown schematically in Figure 3.10, can be written as;

$$F_g = F_c + F_{fc}. \tag{3.7}$$

The gravitational force experienced by the drop can be rewritten as, $F_g = \rho g \phi_{sl}^{cr} = \frac{4\pi}{3}(r_d^{cr})^3 \rho g$ assuming the droplet to be spherical in shape for simplifying the calculations. The capillary force due to the liquid film [226] can be written as,

TH-2590_156103041

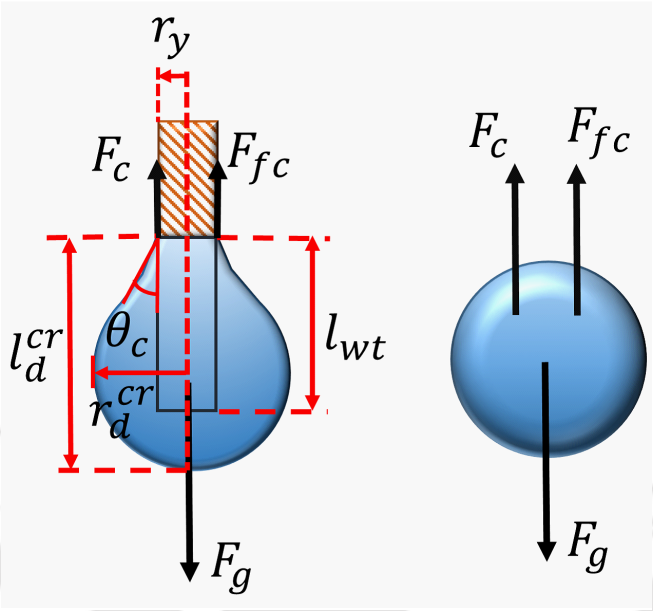


Figure 3.10: Force balance in case of a drop continuously growing on a yarn just prior to the initiation of sliding motion. The different geometrical parameters of the drop considered in the force balance are shown with dimensional arrows. F_g is the gravitational pull experienced by the droplet due to its weight, F_c is the capillary force along the contact line, and F_{fc} is the capillary force due to the liquid film acting along the wetting length l_{wt}.

$F_{fc} = \gamma l_{wt}$, where, the wetting length, is $l_{wt} = 2\zeta_l^{sl} r_d^{cr}$, with ζ_l^{sl} as the fitting parameter that takes into account the deviation of the droplet shape from the spherical shape. The final form of the Eq. 3.7 can be found as follows;

$$\frac{4\pi}{3}(r_d^{cr})^3 \rho g - 2\gamma\zeta_l^{sl} r_d^{cr} - 2\pi\gamma r_y \cos\theta_c = 0. \tag{3.8}$$

The cubic equation, Eq. 3.8 with positive polynomial discriminant has the single real solution as follows,

$$r_d^{cr} = \sqrt[3]{\frac{3L_{cap}^2 r_y \cos\theta_c}{4} + \sqrt{\left(\frac{3L_{cap}^2 r_y \cos\theta_c}{4}\right)^2 - \left(\frac{\zeta_l^{sl} L_{cap}^2}{2\pi}\right)^3}} + \sqrt[3]{\frac{3L_{cap}^2 r_y \cos\theta_c}{4} - \sqrt{\left(\frac{3L_{cap}^2 r_y \cos\theta_c}{4}\right)^2 - \left(\frac{\zeta_l^{sl} L_{cap}^2}{2\pi}\right)^3}}, \tag{3.9}$$

TH-2590_156103041

where $L_{cap} = \sqrt{\gamma/\rho g}$ is the capillary length. Based on the value of the critical radius, r_d^{cr}, obtained from Eq. 3.9, the theoretical critical volume, $\phi_{sl}^{cr} = \frac{4\pi}{3}\zeta_\phi^{sl}(r_d^{cr})^3$ can be calculated where ζ_ϕ^{sl} is a geometric pre-factor taking into account the deviation of ϕ_{sl}^{cr} from its actual drop volume [226]. A critical comparison of the experimental data with the theoretical volume data shows that irrespective of the different thermophysical properties of the experimental fluids, the value of ζ_ϕ^{sl} is fixed at, $\zeta_\phi^{sl} = 0.7 \pm 0.15$. Also, the fitting parameter, ζ_l^{sl} accounting for the wetting length comes out to be close to each other for different experimental conditions and found to be in the range of, $\zeta_l^{sl} = 0.57 \pm 0.13$. The consideration of the geometric pre-factor and fitting parameter nullifies the deviation in the ϕ_{sl}^{cr}, appearing as a result of considering the droplet to be spherical in shape.

3.3.5 Dynamics of droplet detachment: Static pinch-off

The dynamics of the growth stage comes to an end as soon as the tip reaches the end of the yarn and the detachment phase of the droplet begins. Owing to the low flow rate of the penetrating fluid through the capillary network of the yarn, i.e., extremely small We conditions (of the order of 10^{-9}), the dynamics of detachment adheres to the laws of the *static pinch-off* regime, wherein, the subsequent outcomes such as the size of the detached primary droplet (ϕ^{pin}), the volume of the remnant fluid after the breakup, etc. solely depends on the competition between the gravitational force and the capillary force ($2\pi\gamma r_y$) [227]. As reported by Harkins and Browns [227], in the static-pinch-off regime, the detached primary droplet volume, ϕ^{pin}, can be determined as follows:

$$\phi^{pin} = \zeta^{pin}\left(\frac{2\pi\gamma r_y}{g\rho}\right), \tag{3.10}$$

where, the *Harkins-Brown compensation factor*, ζ^{pin} is defined as the ratio of the volume of the primary droplet detached from the nozzle, ϕ^{pin}, to the maximum volume of the liquid balanced by the capillary force at the nozzle exit (the term within bracket in the R.H.S. of Eq. 3.10). Conventionally, expressed as, $\zeta^{pin} = f(r/(\phi^{pin})^{1/3})$, the compensation factor assumes different forms and numerical values depending upon the nozzle and the liquid pair and thereby ensuring that post-detachment, a fraction of the total volume remains attached to the nozzle exit.

Figure 3.11 shows the experimentally measured drop volumes for four different liquids listed in Table 3.1, which are being designated by the corresponding We as

TH-2590_156103041

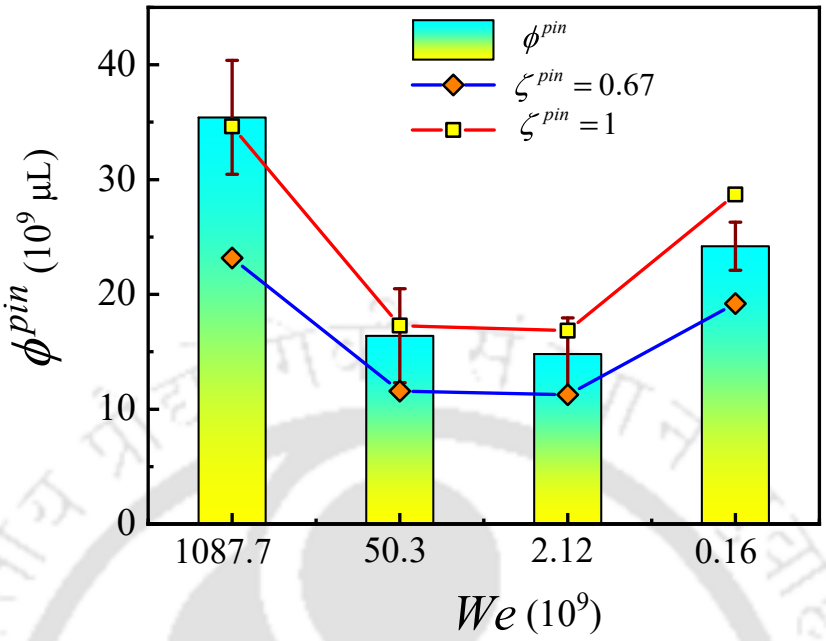


Figure 3.11: Comparison between the experimentally and theoretically (obtained from the correlation, Eq. 3.10, proposed by Harkins and Browns [227]) measured primary droplet volume.

listed in Table 3.2. The volume of the released drop decreases sharply with a decrease in We, as seen in Figure 3.11, which demonstrates that higher surface tension force can hold a larger drop volume prior to pinch-off. A suitable fitting method shows that $\zeta^{pin} = 0.67$ allows us to adhere to the lowest limit of experimentally measured volumes for the entire range of We explored in this study, as shown by the lowermost solid line (with symbols) in Figure 3.11. The uppermost curve corresponds to the maximum volume of the hanging drop that the yarn can support, i.e., $\zeta^{pin} = 1$, which is nothing but the weight of the *ideal drop* as determined by Tate's law [228]. In the absence of a unique value of ζ^{pin} in literature, the current approach of representing the measured data via a range of parameters (0.67-1.0) seems to be the only viable option and hence has been adopted in the present analyses. If the surface tension of fluid is known beforehand, the reported values of the compensation factor may help in predicting the final volume of a droplet detached from a yarn.

TH-2590_156103041

3.4 Summary

This chapter reports a novel qualitative assessment of the dynamics of the generation and detachment of a droplet from a yarn under different experimental conditions. A simple drop generation facility has been engendered by the continuous capillary flow within the yarn, facilitating a comparison of the present system with the existing methods of drop formation from a capillary tube. Depending on the relative positioning of the contact line, the complete growth cycle of a Newtonian droplet on a yarn can be divided into three distinct regimes, namely *radial growth*, *axial growth* and *motion*. The contact line dynamics during the *motion* stage are found to be self-similar irrespective of the initial experimental conditions, which can be described by an asymptotic scaling relation based on the combined effect of driving and resisting forces. The scaling relation suggests that gravity force dominates upon the capillary forces during the third stage. Another asymptotic relation has been proposed for the evolution of the radius of the droplet during its growth. By using a number of fluids spanning across a wide range of viscosity, it is found that for the macroscale contact line dynamics occurring over a physical time scale, viscosity plays the role of rate limiter. Furthermore, the meager flow rates during the experiments directed the dynamics of drop formation in the *static-pinch-off* regime. This chapter's findings may stimulate further investigations on the dynamics of growth of a droplet generating from a yarn with different chemical and physical textures.

TH-2590_156103041

Chapter 4

Magnetowetting dynamics of sessile ferrofluid drops on soft surface

"...by the help of microscopes, there is nothing so small, as to escape our inquiry; hence there is a new visible world discovered to the understanding.."

- Robert Hooke, *1665*

4.1 Introduction

With the advent of the droplet microfluidics [3, 229, 230], ferrofluid (FF) based technologies [103, 115, 116, 231–234] have garnered remarkable appreciation as a wireless mechanism of droplet manipulation over its conventional counterparts (e.g., mechanical, electrical, optical, acoustic) owing to a list of prodigious advantages, specifically precise and smooth control of discrete liquid volumes as well as no unnecessary heat generation, exhibited by the former, thereby making it a suitable host for numerous cutting-edge technologies. In general, the interface of a sessile FF

The contents in this chapter have been published as Sarma, B., Shahapure, V., Dalal, A. and Basu, D. N. (2020) "Magnetowetting dynamics of sessile ferrofluid drops on soft surfaces", *Soft Matter*, vol. **16**, pp.- 970-982.

TH-2590_156103041

droplet, submitted to a magnetic field acting in a specific direction, exhibit remarkable deformation as explored in several studies [114, 122, 235–239], succeeding the pioneering work of Cowley and Rosensweig [98, 240]. A detailed discussion on the instability and subsequent deformation dynamics of ferrofluid/paramagnetic droplets in the presence of a magnetic field is already presented in Section 1.2.3 of the thesis. Notably, the deformations often alter the wetting behaviour of the magnetic droplets depending upon the direction of application of the magnetic field as well as the wettability of the underlying surface [114, 241–243]. Recently, Banerjee and Sen [243] experimentally demonstrated the decrease of the apparent contact angle of a FF droplet, engendered by the significant interfacial deformation, eventually leading to the bifurcation of the parent droplet in a vertically varying non-uniform magnetic field.

In this regard, most of the existing reports on the aforementioned magnetowetting behaviour of sessile droplets are primarily restricted to rigid substrates. In contrast, a sessile droplet dispensed atop a soft, deformable surface inherently induces a capillary deformation, popularly called a *wetting ridge* [21, 244–249]. The kind of deformation emanates from the combined influence of the unbalanced normal component of the capillary force and the Laplace pressure distribution within the droplet, with an inherent length scale, h_{wr}, dependent upon the ratio of the surface tension of the liquid (γ_{lg}) to the elastic modulus (E) of the underlying surface [21, 244–249], i.e., $h_{wr} \sim (\gamma_{lg} \sin\theta_{eq})/E$. However, for a small substrate thickness-to-droplet length scale ratio, one can neglect the effect of Laplace pressure on the deformation of the film [245–247]. In such a scenario, the presence of a wetting ridge near to the TPCL intrinsically modifies the macroscopic spreading /dewetting behaviour of the drops on a viscoelastic surface, by incorporating some complex dynamics such as *inertial spreading*, *viscoelastic braking*, *stick-slipping*, *stick-breaking* as reported previously [247, 250–252]. Interestingly, the aforementioned modified wetting dynamics of a sessile droplet on viscoelastic surfaces can be manifested to acquire desired applicability in numerous processes or technologies, including droplet evaporation [253, 254], droplet impact [255], electrowetting [256], droplet transportation [257], durotaxis [258], adhesives [259], highly stretchable synthetic materials [260] etc. to name a few. For example, Lopes and Bonaccursor [253, 254] reported that the enhanced softness of the underlying substrate accelerates the evaporation of both water and nano-suspension drops, thereby changing the particle deposition pattern in the latter event. Again, Dey *et al.* [256] experimentally characterized the

TH-2590_156103041

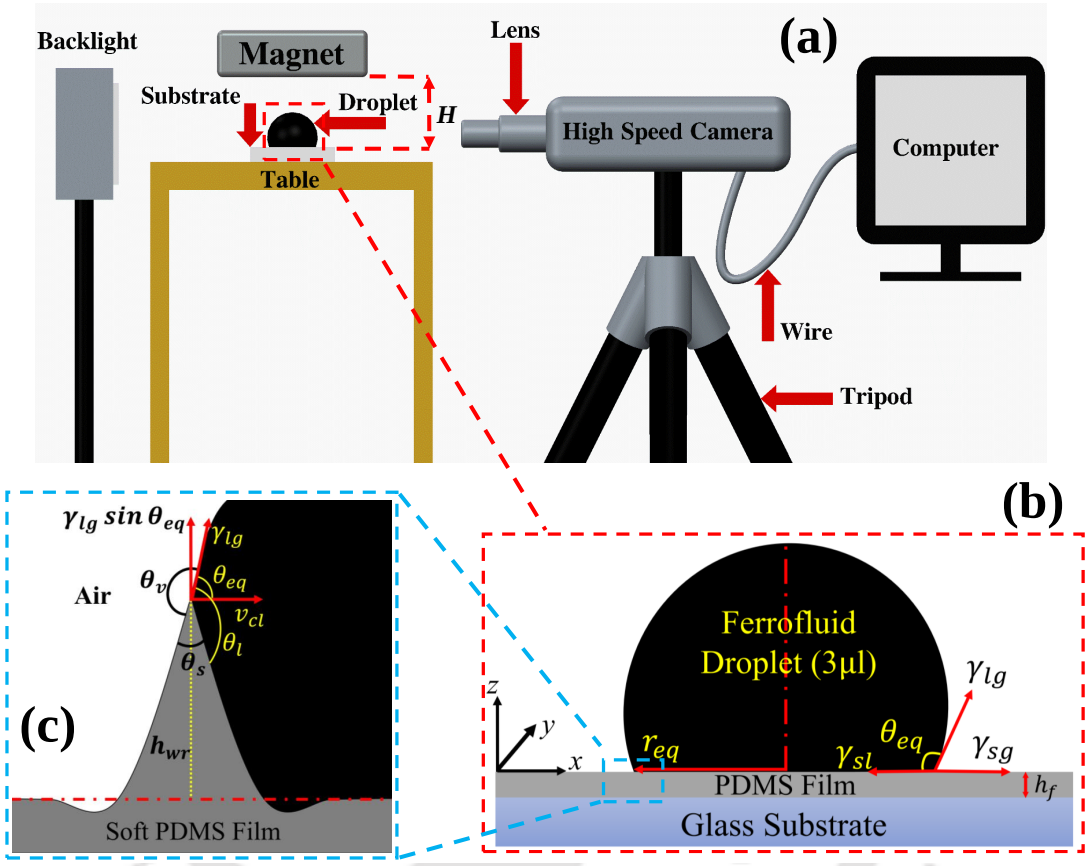


Figure 4.1: (a) Schematic of the experimental set-up for investigating the magnetowetting behaviour of sessile ferrofluid (FF) drops dispensed atop a PDMS coated glass substrate. The magnet and the drop are positioned co-axially to avoid any lateral deformation. (b) shows a zoomed view of the FF droplet along with all the components of the surface tension (γ_{ij}) and equilibrium parameters (radius, r_{eq} and contact angle, θ_{eq}) in the absence of a magnetic field. Here, i, j signify the solid (s)-liquid(l), liquid-vapour(g) and solid-vapour components of the surface tension. (c) Schematic of the surface deformation near the TPCL on a soft surface. The red dashed-dotted line indicates the position of the solid-liquid-air interface prior to the deposition of the liquid drop, whereas the vertical yellow dotted line shows the height of the wetting ridge (h_{wr}) formed above the free surface.

TH-2590_156103041

slower electrospreading dynamics of the contact line of a sessile droplet triggered by substrate deformation. Recently, Biswas *et al.* [257] demonstrated magnetic field-mediated propulsion of non-magnetic droplets in a soft deformable platform impregnated with magnetic beads. The prime focus of the aforementioned work revolves around the topography induced propulsion of droplets of different volumes, whereas the effect of the wetting ridge on the motion was in hindsight.

As observed, the mutually inclusive relationship between the magnetic field induced spreading/dewetting of a drop, and the surface deformation induced interfacial interactions on a soft elastomer film, has heretofore been unexplored. Emulating the magnetowetting set-up of Banerjee and Sen [243], as shown in Figure 4.1, the dynamics of the continuously evolving interface as well as the three-phase contact line near to the solid substrate have been explored by performing a set of experiments on different substrates. Specifically, the prime concern is to bring out the change in the magnetowetting behaviour of a paramagnetic sessile drop as the elastic nature of the underlying substrate changes. Nonetheless, understanding is crucial for paving a new way for the yet unexplored paradigm of elastocapillarity mediated magnetowetting dynamics.

4.2 Experimental section

4.2.1 Materials

A water-based FF, EMG 408, purchased from Ferrotec (USA), has been used in this study. The concentration of the magnetite (Fe_3O_4) nanoparticles (average diameter $\sim$ 10 nm) is 1.2% by volume (5.4% by weight) and the initial magnetic susceptibility (χ) is 0.5. The thermophysical properties of the FF are: density (ρ) = 1070 kg/m^3, surface tension (γ_{lg}) = 60 mN/m, and viscosity (η) = 2.0 - 5.0 mPa.s [as per the product data-sheet given]. The magnetization of the ferrofluid saturates at a flux density of 6.6. mT. The PDMS (Polydimethylsiloxane, Sylgard 184) and hexane (analytical grade) are procured from Dow Corning (Wiesbaden, Germany) and Sigma-Aldrich, respectively. The rectangular rare earth Neodymium magnets (N52) (dimensions: 10 mm $\times$ 20 mm $\times$ 2 mm) are purchased online. The glass slides are purchased from JSGW, India (Micro slides). Milli-Q grade water has been used for all the cleaning processes during the experiments.

TH-2590_156103041

4.2.2 Methods

4.2.2.1 Surface preparation.

The elastomeric hydrophobic substrates are prepared by coating the plain glass slides (dimension: 12 mm × 12 mm × 1 mm) with thin films of PDMS having different elastic modulus (E). Prior to coating, the glass micro-slides are cleaned following a standard procedure discussed in Section A.2 of Appendix A. The stiffness of the films is varied by mixing the base (oligomer) and the curing agent (cross-linker) in three different weight ratios, namely 10:1, 30:1, and 50:1. It is well known that an increase in the oligomer content results in a decrease in the stiffness of the thin films, which in the present case varies from 1.5 MPa to 0.02 MPa [253, 254, 256] [see Table 4.1]. The degassed prepolymer mixture is further mixed with the solvent (hexane) in the ratio of 110:10:1. Subsequently, the final solution is spin-cast on the previously cleaned glass slides with a spin coater (SPIN NXG P1, Apex. India. Pvt. Ltd.). The coated glass slides, when allowed to cure overnight in a vacuum oven (Spac-N-Service Pvt. Ltd., India) at 100 °C, result in a thin transparent PDMS film. The spin coating of the substrates has been carried out in two steps: after pouring the prepolymer, the substrate is rotated at 500 rpm for 30 s initially and later on at 5000 rpm for 70 s with an intermediate acceleration of 2500 rpm/s^2. The thickness of the films (h_f) thus prepared are measured with the help of a surface profilometer (Dektak 150 surface profiler, Veeco Instruments), which is shown in Table 4.1. Also, the prepared surfaces exhibit an average surface roughness of 1 ± 0.5 nm when measured in atomic force microscopy (Bruker, Innova). Furthermore, the wetting behavior of the fabricated surfaces, in the absence of a magnetic field, has been examined by measuring the equilibrium (θ_{eq}), as well as advancing/receding (θ_A/θ_R) contact angles in a contact angle goniometer (Apex India) [see Table 4.1]. It is to note that the values of different parameters in Table 4.1 represent an average value derived from 5 different measurements corresponding to each elastic modulus. The cured substrates are preserved in the vacuum desiccators if not used immediately in experiments.

4.2.2.2 Magnetowetting experiments.

The schematic of the experimental set-up is shown in Figure 4.1(a), where a FF droplet resting atop a PDMS coated glass substrate is experiencing a vertical mag-

TH-2590_156103041

Table 4.1: Properties of differently crossed-linked elastomer films: Young's Modulus (E) and thickness (h_f) (row (i) and (ii)]; equilibrium contact angles (θ_{eq}), advancing (θ_A) and receding contact angles (θ_R) of a 3 μL ferrofluid droplet on polymeric films of different elasticity in the absence of magnetic field [row (iii)-(v)].

Properties	Sylgard (10:1)	Sylgard (30:1)	Sylgard (50:1)
E[253, 254, 256] (MPa)	1.5	0.06	0.02
h_f (μm)	2.1 ± 0.2	2.8 ± 0.15	1.6 ± 0.3
θ_{eq} (°)	108 ± 1.1	112 ± 1.5	114 ± 2.1
θ_A (°)	103.2 ± 3.5	109.5 ± 2.1	116.5 ± 1.8
θ_R (°)	61.1 ± 3.5	45.2 ± 4.5	35.2 ± 3.9

netic pull. In the first step, a FF droplet of known volume is dispensed, ϕ_0, on the PDMS prepared substrate with the help of a micropipette. Subsequently, the permanent magnet is placed directly above the droplet at a known height (H), measured from the surface of the underlying substrate. The vertical movement of the magnet to a specific height is facilitated by a movable arm protruding from a fixed stand and a scale attached to the stand. Again, the droplet and the magnet are placed co-axially to avoid any asymmetric deformation in the droplet shape, in all the experiments. Herein, the behaviour of a FF droplet of initial volume, ϕ_0 = 3 (± 0.2) μL, on PDMS coated substrates with different stiffness (E = 1.5, 0.06, and 0.02 MPa) is observed and analyzed, while the magnet is placed at the height of, H = 4.7 mm from the substrate surface. Figure 4.2 shows the variation of the applied magnetic field along the vertical axis indicating a non-uniform behaviour. The dynamics of shape evolution are recorded by a video-graphic technique which is discussed in detail in the next section. Also, the identical experiments have been performed at least five times to ensure the repeatability of the observed phenomena and analyzed data in each experimental condition.

4.2.2.3 Video-graphic and image processing technique.

The complete shape evolution of the droplet is recorded with a digital camcorder (SONY) at a frame rate of 25 fps. The background is continuously illuminated by a high intensity LED light (Phlox, 130000 lux) that further enhances the quality of the captured videos by enhancing the contrast. Additionally, the fast events of droplet splitting are captured in a high-speed camera (FASTCAM Mini UX100

TH-2590_156103041

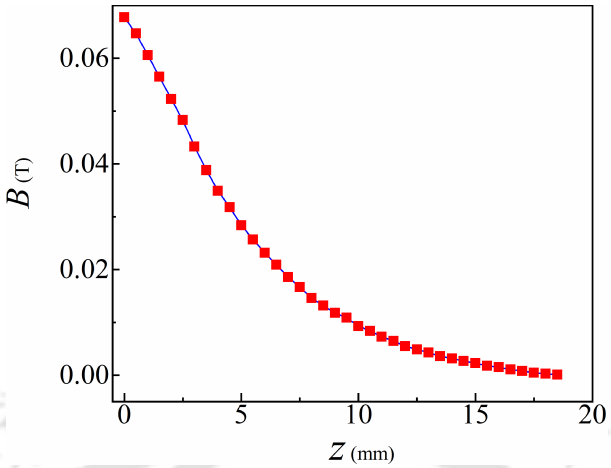


Figure 4.2: Magnetic flux density (B) as a function of the vertical gap (H, also denoted as z here) between the magnet and the PDMS coated glass substrate.

model, Photron, USA, Inc.) fitted with a zoom lens (Navitar Macro zoom, 18-108 mm F/2.5). By using a shutter speed of 0.2 ms, the high-speed events are recorded at 2000 frames per seconds, achieving a resolution 1280 × 1084 pixels. The positions of both the camera and light are shown schematically in Figure 4.1(a).

Further, the captured videos and images are analyzed for deciphering the temporal dynamics of the droplet with the help of an open-source image processing software ImageJ [164] and an in-house image processing code. The image processing method is discussed in detail in Chapter 2.

4.3 Results and discussion

In this section, a detailed appraisal of the dynamic wetting behaviour of FF droplets, experiencing a vertical magnetic pull, on PDMS surfaces with different stiffness is presented. Considering the smaller volume of the sessile droplet ($\phi_0 = 3$ µL) the effect of gravity can be neglected with convenience, as $L < L_{cap}$, leading to $Bo_g << 1$. Here, $L = r_{eq}$ (≤ 1 mm) is the characteristic length scale, r_{eq} is the equilibrium radius of the dispensed droplet, L_{cap} ($= \sqrt{\gamma_{lg}/\rho g}$)$= 2.73$ mm is the capillary length scale, and Bo_g ($= \rho g L^2/\gamma_{lg}$) is the gravitational bond number signifying the balance between the gravity force and surface tension force. On the other hand, to signify the dominance of the driving magnetic force over the resisting surface tension force, the *magnetic Bond number* defined as, $Bo_m = (\chi_m \phi_0 |\overrightarrow{\nabla} B^2|)/(\mu_0 \pi \gamma_{lg} L)$ ($= 131$) is

TH-2590_156103041

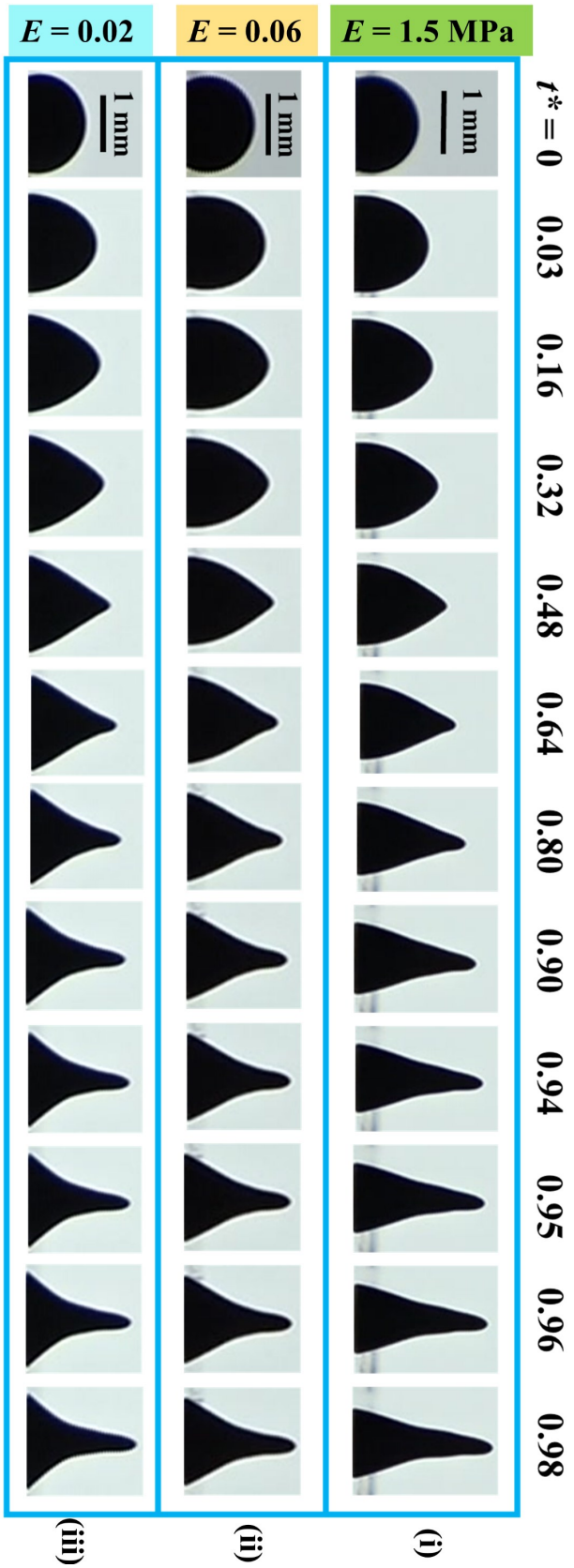


Figure 4.3: Shape evolution of ferrofluid droplets during magnetowetting on the three different PDMS coated glass substrates with elastic moduli (E) (i) 1.5, (ii) 0.06, and (iii) 0.02 MPa, respectively. The other experimental parameters are, $\phi_0 = 3$ µL, $B = 450$ mT, and $Bo_m = 131$. The volume concentration of the nanoparticles is 1.2%. A non-dimensional time scale, t^*, has been considered to show the progress of the dynamics, where $t^* = 0$ corresponds to the moment of introduction of the magnetic field. The scale bars are shown in the first image of each row.

TH-2590_156103041

considered herein. Here, χ_m is the initial magnetic susceptibility, B is the induced magnetic flux density (corresponding to $H = 4.7$ mm), μ_0 ($4\ \pi \times 10^{-7}$ N/A^2) is the permeability of free space. The higher value of Bo_m in comparison to Bo_g, further strengthens our previous claim regarding negligible effect of gravity.

On the other hand, by considering the microscopic *softness parameter*, γ_{lg}/ER [261, 262], the prepared elastomeric surfaces of different stiffness can be divided in two categories: rigid and soft surface. Assuming, R to represent any macroscopic length scale ($\sim$ mm), preferably, $R = r_{eq}$, for a substrate with $E = 1.5$ MPa $= O[10^6 Pa]$, $O[\gamma_{lg}/ER] \sim 10^{-6}$, thereby placing it in the limit of (apparently) *rigid surface* [261, 262]. However, as we lower the stiffness of the substrates by two orders, i.e., $E \sim O[10^4 Pa]$, $O[\gamma_{lg}/ER] \sim 10^{-3}$, indicating their enhanced softness. The latter surfaces with reduced stiffness are popularly known as *soft surfaces* in literature [261, 262]. The aforementioned distinctions shall be referred frequently in the subsequent discussions.

4.3.1 Shape evolution of a FF droplet during magnetowetting: The macroscopic events

Figure 4.3 depicts the temporal evolution of the shape of FF droplets dispensed atop substrates of different stiffness while experiencing a similar magnetic environment. Each row of the image sequence corresponds to the events associated with substrates of different elasticity arranged in decreasing order from top to bottom. As mentioned previously, the rectangular magnet positioned at a height, H= 4.7 ($Bo_m = 131$, $B = 450$ mT) mm from the solid surface, engenders a non-uniform magnetic field in the axial direction (B) as shown in Figure 4.2. Notably, due to the magnet's physical dimensions, the magnetic field in the radial direction across the width of the droplet (B_x, B_y) can be considered uniform. The beginning of the physical time scale, $t = 0$ is considered just before introducing the magnet. Again, the dynamics of shape evolution are considered to be accomplished when the parent droplet bifurcates itself to generate a daughter droplet, designated as splitting time, t_s. The deformation dynamics of the FF droplet in Figure 4.3 are shown in a non-dimensional time-scale, t^* ($= t/t_s$) to facilitate one to one comparison of the concerned events in different experimental conditions.

The image sequence shown in Figure 4.3(a-l) in row (i) corresponds to the tem-

TH-2590_156103041

poral evolution of interfaces of a sessile FF droplet during magnetowetting on a rigid surface (E =1.5 MPa). The corresponding time period, t_s of evolution, is approximately 13.6 min. It can be discerned that the droplet continuously elongates in the direction of increasing magnetic flux density (B) till the moment of bifurcation. The sessile spherical drop evolves through a plethora of intermediate shapes, including cusp formation at the apex in the initial moments [Figures 4.3(e) and 4.3(f)] till the spiked cone-type formation at the final instants [see Figure 4.3(i-l)] engendered by the magnetic field. Notably, this journey of shape evolution leading to the splitting of the droplet is accompanied by the continuous reduction of the (apparent) dynamic contact angle, θ_d (or θ_d^*) and the contact diameter, d_c (or d_c^*) as depicted clearly in Figures 4.4(a) and 4.4(b). The equilibrium value of the contact angle, θ_{eq} [refer to Table 4.1], and contact diameter, d_{eq} are considered as a scale to non-dimensionalize θ_d and d_c, respectively, while the standard deviations from repeated experiments are shown as error bars. As seen in Figure 4.4(a), θ_d^* approximately reduces by 35% of its initial equilibrium angle (θ_{eq}) during magnetowetting on an apparently rigid surface. Interestingly, Banerjee and Sen [243] also reported a similar trend of θ_d^* during magnetowetting on a substrate with a similar elastomeric composition (10:1 mixing ratio of base and cross-linker). However, contrary to the linearly decreasing trend observed in Figure 4.4(b), they reported that the contact diameter d_c^* remains constant throughout the time period of evolution while using a FF with similar thermophysical properties (EMG 408).

Further, while following the trajectory of θ_d^* corresponding to $E = 1.5$ MPa, it is found to exhibit three different slopes comprising of initial sharp decrease, followed by a nearly constant period and finally the zone of linear decrease just prior to the bifurcation. The distinct transitions mentioned above clearly hint towards the possible existence of different driving mechanisms in all three regimes that shall be unfolded in the subsequent sections. Although not apparent in Figures 4.3 and 4.4, the θ_d remains constant when the dynamics of deformation approach splitting, as discussed separately in Section 4.3.3.

Next, The deformation history of a FF droplet dispensed atop soft surfaces ($E < 1.5$ MPa) is shown through the time-lapse image sequence of row (ii) and (iii) in Figure 4.3. It is to note that the imposed magnetic field is identical to the experimental realization described in the previous paragraphs, i.e., $Bo_m = 131$ (B = 450 mT). Figure 4.3(a-l) in row (ii) corresponds to the soft surface having elastic modulus, $E = 0.06$ MPa, whereas, the elastomeric substrate corresponding to image

TH-2590_156103041

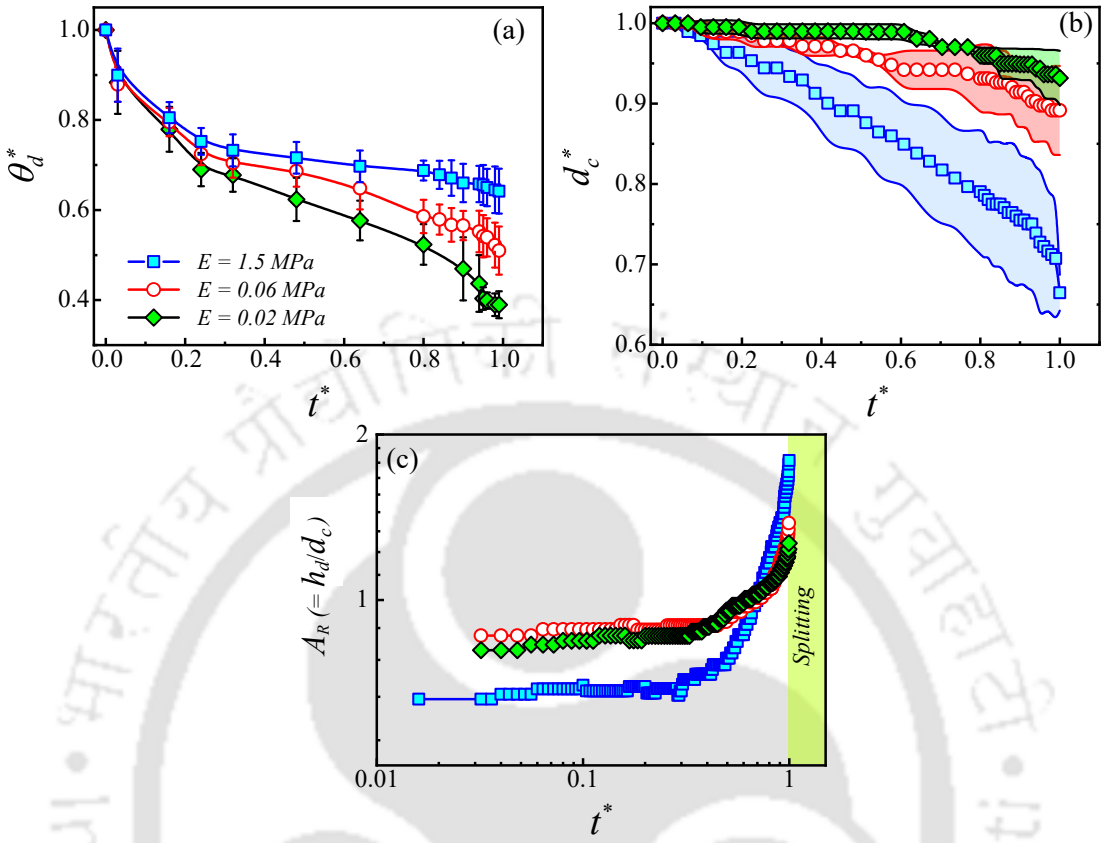


Figure 4.4: Time-averaged behavior of different parameters related to the deformation of a FF droplet of 3 µL volume when dispensed atop three substrates of different elasticity (E) and subjected to an axial magnetic field $B = 450$ mT ($Bo_m = 131$). Plot (a) corresponds to the change in dynamic contact angle, θ_d^*, whereas plot (b) corresponds to the change in the contact diameter, d_c^* of the droplet. The colored regimes around the trajectory in plot (b) corresponds to the error bars derived from repeated events. (c) Variation of the temporal variation of the aspect ratio, A_R, corresponding to the events of Figure 4.3. The non-dimensional scale for time is the splitting time, t_s, whereas the equilibrium value of the contact angle, θ_{eq}, and diameter d_{eq}, before the introduction of the magnetic field have been used as a scale for non-dimensionalizing the concerning quantities.

sequence (a-l) in row (iii) has elastic modulus, $E = 0.02$ MPa. The time periods of splitting, t_s, are found as 14.6 min and 14.2 min for the events of rows (ii) and row (iii), respectively. As seen clearly, the evolution of the interface goes through a similar passage of elongation and shape deformation, leading to the splitting of the parent droplet even for the soft substrates. However, an individual comparison of the droplet shape in row (i), (ii), and (iii) at each instant reveals a few interesting observations. For example, within the initial 30% of t_s, the droplet transforms into

TH-2590_156103041

an elliptical shape from the initial spherical shape for rows (i) and (ii), whereas, for the softest substrate in row (iii), the droplet attains a dome shape within the same time, succeeded by the formation of pyramidal shape for a small duration as seen in Figure 4.3(e). Again, for $t \geq 0.5t_s$, a cusp-like formation is observed in the apex of the droplet, which further elongates with time in all the experimental conditions of Figure 4.3. However, the extent of this elongation decreases with the decreasing stiffness of the underlying substrate.

Figure 4.4(a) further depicts the gradual decrement of θ_d^* during magnetowetting on soft substrates. However, the concerned trajectories (for $E = 0.06$ and 0.02 MPa) are devoid of any distinct transition in slopes as one moves along the temporal scale. Notably, the extent of reduction of the θ_d^* (or θ_d) within the complete cycle of magnetowetting is maximum ($\approx 70\%$) for the softest substrate ($E = 0.02$ MPa). On the other hand, as seen in Figure 4.4(b), d_c^* (or d_c) remains nearly constant or pinned for most of the time period ($t \approx 0.8t_s$) of evolution, as the softness of the underlying substrates is increased. These newly found aspects of FF droplets' dynamic wetting behaviour on soft substrates further indicate that the reduction of substrate stiffness can be a great tool for enhancing the wettability of elastomeric surfaces in the presence of a magnetic field.

Another interesting observation that can be made from Figures 4.4(a) and 4.4(b) is that both θ_d^* and d_c^* behave in a near synchronous manner for the soft substrates, whereas the temporal evolution dynamics of the concerned quantities are different on an apparently rigid substrate. The noticeable collapse of the time-varying trajectories of the aspect ratio, $A_R = h_d/d_c$, in Figure 4.4(c) for both soft surfaces further strengthens our claim. Interestingly, the trajectory of A_R exhibits an opposite trend during magnetowetting in the rigid surface, as evident in Figure 4.4(c). Intrigued by the aforementioned differences, a thorough investigation has been carried out in the following sections to explore the driving mechanisms of the contact line motion and shape evolution under the influence of substrate elasticity.

However, prior to elucidating the events near TPCL, a brief note on the macroscopic forces dominating the events of shape deformation and splitting in the presence of a magnetic field is worth mentioning. As the applied magnetic field is higher than the saturation magnetization (M_s) of the FF ($B > \mu_0 M_s = 6.6$ mT), all the magnetic dipoles reorient themselves in a direction parallel to the magnetic field within a very short time-scale [263]. Subsequently, the suspended magnetic nanoparticles migrate towards the high magnetic intensity region, which is countered only

TH-2590_156103041

by thermal diffusion [98]. Although not apparent due to the high concentration of magnetic nanoparticles in the present image sequence of Figure 4.3, Banerjee and Sen [243] in their study has brilliantly shown that the paramagnetic beads prefer to move towards the apex of the droplet and get accumulated in due course of time. The same can be corroborated from the initial cusp like formation in Figures 4.3(e) and 4.3(f), similar to that reported by Tokarev *et al.* [264] in case of magnetic nanorods. The magnetic interaction increases as more particles migrate towards the apex, continuously deforming the interface. This elongated cluster of nanoparticles bounded by a liquid-gas interface finally develops necking, leading to the splitting of the droplet once the magnetic stress ($p_n = \mu_0 M_n^2/2$) across the interface overcomes the resisting surface tension force, which is shown schematically in Figure 4.5 [also refer to Section C.1 of Appendix C]. Here, p_n is the normal magnetic traction dependent on the normal component of magnetization, M_n. By combining the contribution of this normal magnetic pressure, p_m, along with the capillary pressure ($p_c = 2\kappa\gamma_{lg}$), acting at an interface of curvature κ, between the magnetizable drop and non-magnetizable surrounding medium [also refer to Section C.1 of Appendix C], an augmented *magnetic Bernoulli equation* [98, 240, 241] can be formulated as shown below:

$$p^* + \rho g h_{intf} + \frac{\rho v_{intf}^2}{2} - p_m = const. \tag{4.1}$$

subjected to the boundary condition,

$$p^* + p_n = p_0 + p_c. \tag{4.2}$$

Here, v_{intf}, h_{intf} and n represents velocity, elevation, and unit vector normal to the interface, respectively. Also, the additional pressure terms from Eqs. 4.1 and 4.2 are: fluid magnetic pressure, $p_m = \mu_0 \int_0^H M dH$, pressure of the surrounding non-magnetic fluid, p_0, and modified pressure, p^* $(= p(\rho, T) + p_m + p_s)$ representing the combined effect of thermodynamic pressure ($p(\rho, T)$), magnetorestrictive pressure (p_s) as well as the fluid magnetic pressure (p_m). A further simplification of Eq. 4.1 [also refer to Section C.1 of Appendix C] clearly indicates the continuous elongation of a water-based FF droplet in a non-uniform magnetic field.

Again, the total energy, E_t, of a FF droplet in a magnetic field receives an additional contribution from the magnetic energy (E_m) along with the surface energy ($E_s = \sum \gamma_{ij} dA_{ij}$). Here, i, j represents the three different components of surface

TH-2590_156103041

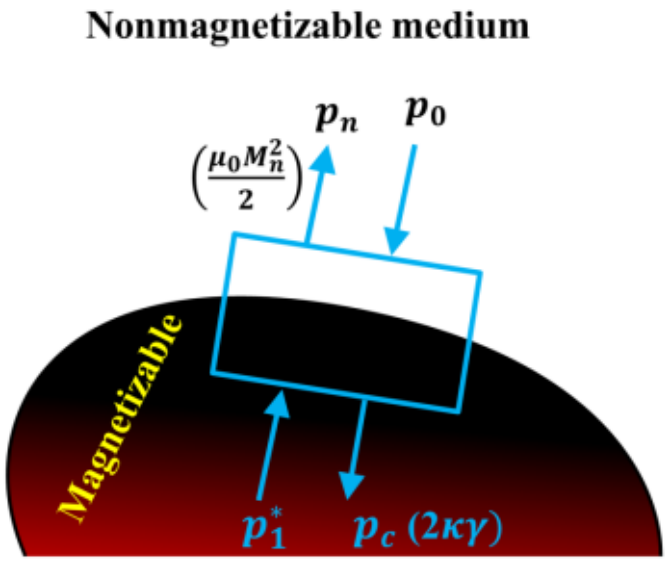


Figure 4.5: Schematic representation of the force balance at the interface between the magnetizable liquid medium (1) and non-magnetizable surrounding (2). The same has been written as FHD boundary condition in Eq. 4.2.

tension, and dA is the interfacial area under consideration. In general, for a continuously deforming droplet, the magnetic energy, $E_m = -\frac{\mu_0 \phi_0 MH}{2}$, also gets modified at each time instant, where M is the effective magnetization, and H is the effective magnetic field. Taking the demagnetization coefficient (D) into account, the effective magnetization, $M = \frac{\kappa H}{(1+\kappa D)}$ behaves as a geometry dependent parameter. However, in the process of maintaining a minimum Gibbs free energy state of the system, the droplet responds to the change in the E_m by lowering the apparent contact angle, θ_d [243]. A detailed appraisal on the dynamics of contact angle and contact radius of a continuously deforming droplet on different soft surfaces is presented in the following sections.

4.3.2 Dynamics of the three-phase contact line: Stick-slip vs pinned state

4.3.2.1 Stick-slip dynamics.

In the process of unveiling the mechanisms at work near the TPCL during magnetowetting on substrates with different stiffness, the temporal variations of the dynamic contact angle, θ_d (or θ_d^*), and contact radius, r_c (or r_c^*) corresponding to

TH-2590_156103041

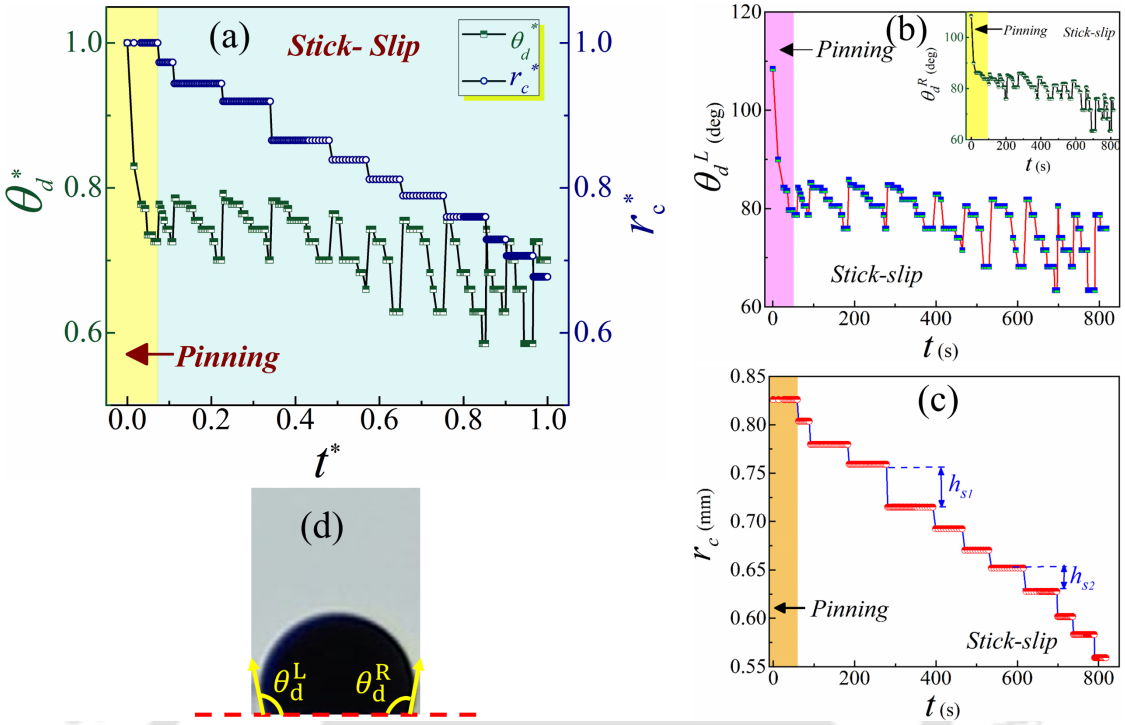


Figure 4.6: (a)-(c) Variation of contact angle (θ_d or θ_d^*) and contact radius (r_c or r_c^*) at a higher temporal resolution shows distinct *stick-slip* pattern during magnetowetting of a sessile FF droplet on an apparently rigid substrate (E =1.5 MPa). The other experimental conditions are, ϕ_0 = 3 µL, Bo_m = 131, B = 450 mT. The non-dimensional time scale is derived using the splitting time, t_s. (d) Shows position of measurement of left (θ_d^L) and right (θ_d^R) contact angles for this study.

the events of Figure 4.3 are considered again. Figure 4.6 depicts a detailed appraisal of the concerned parameters associated with the phenomena shown in row (i) of Figure 4.3. It can be discerned that on an apparently rigid substrate (E = 1.5 MPa), the contact line recedes in a *stick-slip* fashion during the complete cycle of deformation and splitting. The r_c (or r_c^*) varying with steps and terraces at regular intervals whereas, discrete jumps in the θ_d (or θ_d^*) within the same intervals can be observed clearly in Figure 4.6(a), identified as the characteristic feature of stick-slip motion in literature [252, 265]. The overall dynamics of the TPCL can further be demarcated in two distinct zones as follows: initially, the contact angle decreases gradually, whereas the radius remains pinned at its equilibrium value, r_{eq}, while experiencing the vertical magnetic pull. During this initial *pinning* phase of short duration of nearly 50 s (t_p = $0.08t_s$), θ_d decreases approximately by ($\Delta\theta_d$) 30° [calculated from Figure 4.6(b)] attaining the receding contact angle, θ_R, while

TH-2590_156103041

the radius remains pinned at 0.74 mm as derived from Figure 4.6(c). This *primary pinning* phase is analogous to the *constant contact radius (CCR)* evaporation mode observed during droplet evaporation on soft substrates [253, 254]. Further, this initial sticking phase is followed by a *slip-phase* with a sudden decrease in r_c (Δr_c = 0.022 mm), whereas θ_d (or θ_d^*) initially stagnates and increases slightly afterwards approximately by 6° ($\Delta\theta_d$). The contact angle tries to recover the initial equilibrium configuration (θ_{eq}) with this jump, however, reaches a new equilibrium state instead. Shanahan and Sefiane [266] earmarked that this new equilibrium arises as the surface has previously been in contact with the liquid drop during the *stick phase* and may have retained some molecules of the liquid either by physical retention or adsorption, thereby altering the wettability of the surface. Notably, during the successive stick-slip cycles, the CL tries to recover this new equilibrium contact angle during each jump, thereby further strengthening the claim of Shanahan and Sefiane [266]. Also, after each jump, θ_d approximately decreases to the receding angle, θ_R. However, for the initial cycles, $0.08t_s \leq t \leq 0.50t_s$ (or 58 s $\leq t \leq$405 s), the jump in θ_d ($\Delta\theta_d \approx 7°$ -10°) is comparatively smaller than the rest of the cycle, $t > 0.50t_s$ ($\Delta\theta_d \approx 14°$ -17°). These characteristic stick-slip cycles, periodic with a time period, $\tau \approx 100$ s, are distinctly present during the magnetowetting cycle, except for the last few cycles.

A few distinguishing features of the stick-slip cycles on apparently stiff surface are as follows: the *slip distance* in all the cycles is approximately same, i.e., Δr_c = 0.018-0.022 mm [except for the 4^{th} slip in Figure 4.6]. Secondly, the slip events occur coherently throughout the cycle of magnetowetting. The same becomes evident after comparing the instants of occurrence of jump in the main plot of Figure 4.6(b), showing the time evolution of left contact angle, θ_d^L and the plot in inset showing the evolution of right contact angle, θ_d^R [refer to Figure 4.6(d) for measuring positions]. The observations corroborate the fact that the contact line remains pinned across its entire perimeter (i.e., no local pinning) and recedes smoothly during the complete deformation cycle. Further, these stick-slip dynamics of the CL, delineated with all the transition zones [pinning → stick-slip (small $\Delta\theta_d$) → stick-slip (large $\Delta\theta_d$)] have successfully been reproduced during all the experimental realizations with identical experimental conditions. Also, approximately same slip distance (0.018-0.024 mm) is observed for different experimental realizations, which comprehends the robustness of the experimental arrangements and ensuing magnetowetting dynamics. Notably, the stick-slip events of the CL on a PDMS coated (apparently) stiff surface

TH-2590_156103041

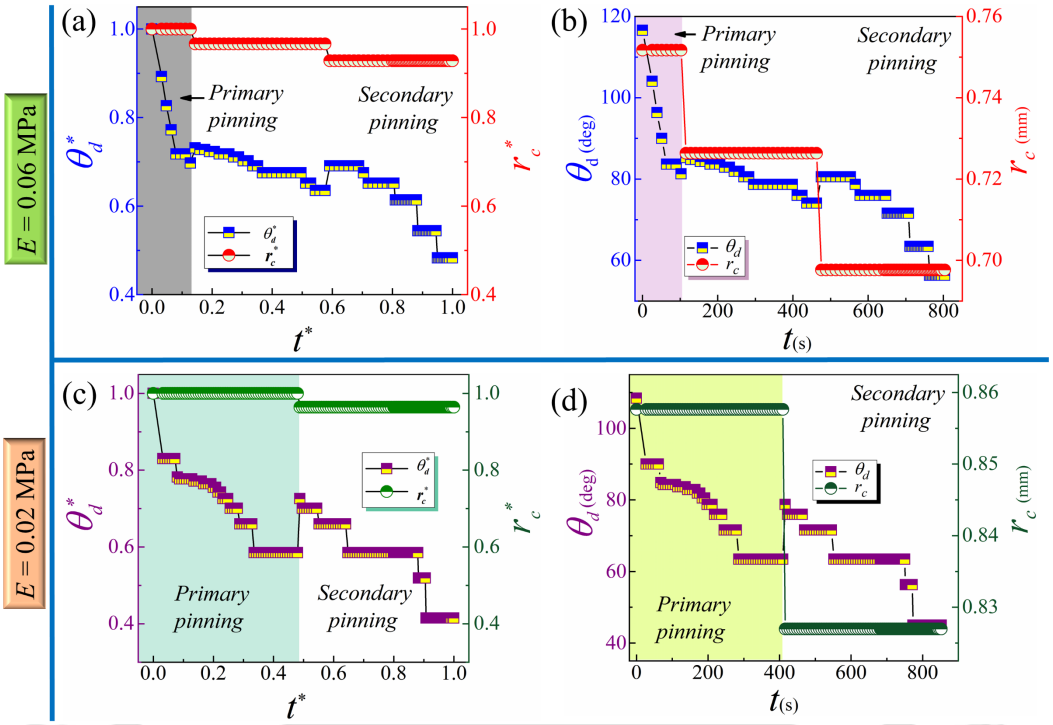


Figure 4.7: Variation of contact angle (θ_d or θ_d^*) and contact radius (r_c or r_c^*) of a FF droplet as a function of time for soft solids in presence of magnetic field. Plots (a and b) and (c and d) correspond to two soft substrates of elastic moduli, E = 0.06 MPa, and E = 0.02 MPa, respectively. The other experimental conditions are, ϕ_0 = 3 µL, Bo_m = 131, B = 450 mT.

are analogous to the events of receding contact line on rigid textured surfaces or chemically heterogeneous surfaces [267].

4.3.2.2 Pinning dynamics.

On the other hand, replacing the apparently rigid substrate with a soft one results in a transition from the stick-slip motion to a nearly *pinned* motion of the CL as depicted in Figure 4.7. Figures 4.7(a) and 4.7(b) show the temporal variations in θ_d (or θ_d^*) and r_c (or r_c^*) during magnetowetting on a soft substrate with elastic moduli, E = 0.06 MPa, whereas, Figures 4.7(c) and 4.7(d) show the dynamics of TPCL on the softest substrate (E = 0.02 MPa). The rest of the experimental parameters correspond to that of Figure 4.2 and relevant discussions. It can be discerned that the propensity of stick-slip is greatly suppressed, while the extent of the primary pinning phase increases remarkably with a decrease in the stiffness of the underlying

TH-2590_156103041

substrate. Figures 4.7(a) and 4.7(b) show that for an soft surface with $E = 0.06$ MPa, the initial pinning phase has time period, $t_p \approx 100$ s ($0.13t_s$), accompanied by a sharp decrease (increase) in θ_d ($\Delta\theta_d \approx 35°$). However, the dynamic contact angle does not reduce to the receding contact angle, θ_R at the end of the primary pinning regime, unlike the case of an apparently rigid substrate as mentioned in Section 4.3.2.1. The relation between the θ_R and substrate stiffness shall be explored separately in Section 4.3.2.3. Further, a subsequent increase in the contact angle, ($\Delta\theta_d \approx 3°$) as well as a step decrease in, r_c (or r_c^*) by 0.025 mm also indicates a slip-like behaviour. Interestingly, once the first slip is over ($t > 0.13t_s$), the dynamics enter in the *secondary pinning* regime, which extends over the rest of the evolution period of drop deformation up to droplet splitting. Although, another slip event is observed in between two prolonged pinning phases in this second regime [refer to Figures 4.7(a) and 4.7(b)], however, this is not evident in a few other experiments with identical conditions. The aforementioned characteristics mark the transition from stick-slip dynamics to a new pinning mechanism of the CL engendered by the reduced stiffness of the substrate.

A further reduction in the stiffness of the underlying soft substrate to $E = 0.02$ MPa, significantly enhances the time period of primary pinning, which may even extend up to half of the total droplet deformation cycle ($t_p = 410s \approx 0.5t_s$) as seen in Figures 4.7(c) and 4.7(d). This prolonged pinning of the CL is also accompanied by a greater reduction of the associated contact angle, $\theta_d = 60°$ ($\Delta\theta_d \approx 45°$). Subsequently, an instantaneous jump in the contact angle ($\Delta\theta_d \approx 15°$) and a slip in radius ($\Delta r_c \approx 0.030$ mm) is seen, thereby indicating a slip-like behavior of the CL, succeeded by a secondary pinning phase extending up to the splitting of the FF droplet. Notably, the larger jump in θ_d confirms the presence of a larger pinning force or obstacle hindering the motion of the CL. In a few different experimental realizations (not reported herein), the CL is found to be in the pinned state throughout the deformation cycle, whereas a more gradual decrease in θ_d is observed. Interestingly, the intermediate slip events in the less elastic substrates are accompanied by a larger slip distance ($\Delta r_c \approx 0.030$-0.035 mm). Further, the decrease in the contact radius, r_c, is found to be only 4% of the initial equilibrium radius (r_{eq}), as also seen in Figure 4.4(b). When compared with a completely rigid surface like glass, where the r_c reduces nearly by 70% within the time period of splitting [refer to Figure 4.8(a)], the aforementioned observations bear the characteristics of strong pinning of the CL on the soft substrates. Interestingly, this greater reduction in the r_c during

TH-2590_156103041

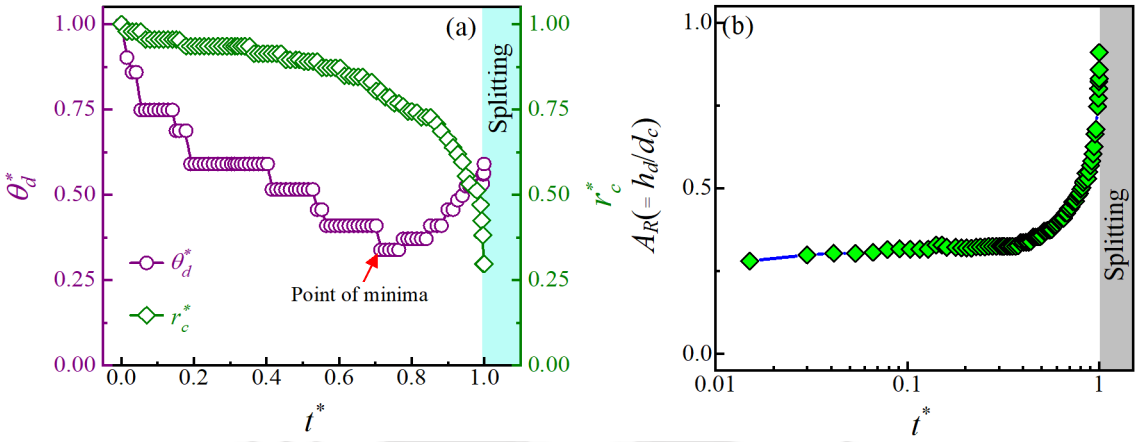


Figure 4.8: Temporal evolution of the (a) apparent contact angle and contact radius, (b) aspect ratio, during magnetowetting on a rigid glass substrate.

magnetowetting on a completely rigid glass surface is analogous to an apparently rigid PDMS surface ($E = 1.5$ MPa). However, the trajectory of the dynamic contact angle, θ_d, depicts a different temporal evolution on glass with a point of minima, as shown in Figure 4.8(a), unlike polymeric PDMS surfaces. It can be anticipated that the higher surface energy, leading to higher wettability of the glass surface, is responsible for the presence of a minimum point during magnetowetting on the former. The variation of the aspect ratio, A_R, follows a similar trend to that of polymeric surfaces as apparent from Figure 4.8(b). The magnetowetting of a FF droplet on a rigid glass surface is shown for comparison with soft surfaces and shall not be discussed further. The stronger pinning of the CL on soft substrates shall be argued in the next section.

4.3.2.3 Multiscale aspects of contact line transition.

The foregoing discussion regarding the changing dynamics of the CL with the stiffness of the underlying substrate, thereby affecting the ensuing magnetowetting response of a FF droplet, can be assessed in the purview of elastocapillary mediated wetting dynamics of droplets on soft substrates. In general, soft surfaces promote the growth of wetting ridge in comparison to apparently rigid surfaces [21, 244–249]. As a result, the extent of elastocapillary deformation on the former ($O[\gamma_{lg} \sin\theta_{eq}/E] \sim 10^{-6}$ m) is much higher than the latter ($O[\gamma_{lg} \sin\theta_{eq}/E] \sim 10^{-9}$ m). Apart from favouring the growth of large size wetting ridge, soft surfaces further accommodate cusp bending, thereby facilitating enhanced pinning in many physical

TH-2590_156103041

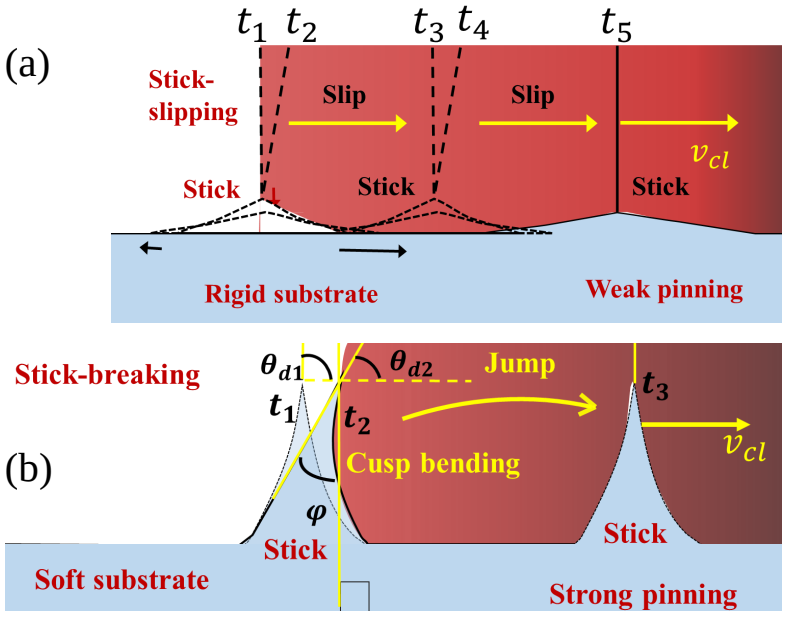


Figure 4.9: Schematic representations of (a) stick-slip and (b) stick-break mechanisms during elastocapillary mediated magnetowetting events [252].

scenarios [252].

The aforementioned critical aspects suggest that the repeated stick-slip cycles observed in Figure 4.6 is an artifact of weak pinning of the CL to the wetting ridge [252] on apparently rigid surfaces. Park *et al.* [252] demonstrated through direct visualization that the weak pinning of the CL is a consequence of moderate growth of the wetting ridge, thereby promoting early depinning. The CL slips from its non-equilibrated position and subsequently forms a new wetting ridge within a *pinning-depinning* cycle as depicted schematically in Figure 4.9(a). The ease of pinning and depinning of the CL from the wetting ridge further facilitates many such stick-slip cycles as seen in Figure 4.6. In contrast, the prolonged pinning dynamics on soft surfaces, as seen in Figure 4.7, is a manifestation of strong pinning of the CL to the wetting ridge [252]. The depinning event in such situations is generally accompanied by a large jump in the contact angle. Such large jumps are commonly present in all the experimental realizations of magnetowetting on substrates with E = 0.02 MPa. Subsequent to the depinning, as the CL initiates the formation of a new wetting ridge, the secondary pinning begins, a phenomenon known as *stick-breaking* [252]. The prolonged pinning regimes, along with the larger reduction in the θ_d, are further boosted by the enhanced cusp bending in the case of large wetting ridges

TH-2590_156103041

on soft surfaces as reported previously [252, 268]. A schematic representation of the same is shown in Figure 4.9(b).

In a different perspective, the depinning events are always associated with an in-

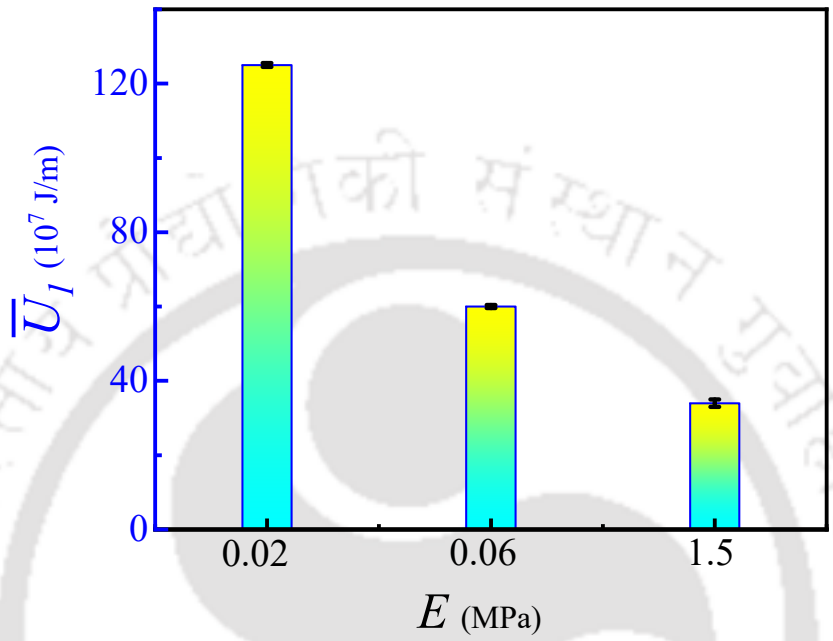


Figure 4.10: Average values of first potential energy barrier, $\overline{U_1}$, derived using Eq. 4.4 for PDMS coated glass substrates with different elastic moduli, E.

trinsic energy barrier ($\overline{U}$) determined by the extent of pinning of the CL, as explored in the context of numerous spreading [256, 265, 269] or receding events [253, 254] on soft substrates. During the magnetowetting, the droplet elongates in response to the non-uniform magnetic field, which in turn is compensated by a decrease in the contact angle, thereby minimizing Gibbs free energy (G) [243]. However, on elastomeric substrates where the CL is pinned to a wetting ridge, the decreasing contact angle further modifies the liquid angle, θ_l [refer to Figures 4.1 and 4.9], thereby disturbing the capillary equilibrium. This lack in capillary equilibrium is the source of excess free energy, $\delta\overline{G}$ (expressed as per unit length of the TPCL). Shanahan [270] proposed that for a spherical cap-shaped droplet evaporating in stick-slip mode, as soon as $\delta\overline{G}$ overcomes the potential energy barrier, $\overline{U}$ (expressed as per unit length of TPCL), the triple line jumps to a new equilibrium position. Later, the same theory has been validated by Shanahan and his co-workers for nanosuspension drop evaporation [271], and evaporation of droplets strongly pinned to substrates [272]. As derived by Shanahan [270], the excess Gibbs free energy per unit length of the

TH-2590_156103041

TPCL can be written as:

$$\delta\overline{G} = \frac{\gamma_{lg} r (\delta\theta)^2}{2(2 + \cos\theta_{eq})} \tag{4.3}$$

where, r is the radius of the droplet just prior to the jump, θ_{eq} is the equilibrium contact angle, and $\delta\theta$ is the jump angle during the slip phase. Equation 4.3 can be used for obtaining the maximum free energy ($\overline{\delta G_{max}}$) required to overcome the energy barrier ($\overline{U}$) associated with each stick-slip cycle. To have a more reliable account of ($\overline{\delta G_{max}}$), recently Oksuz and Erbil [273] modified Eq. 4.3 in terms of known contact angles, i.e. $\delta\theta = \theta_{eq} - \theta_{min-1}$, which calculates the first potential energy barrier, $\overline{U_1}$ as shown below:

$$\overline{U_1} = \overline{\delta G_{max}} = \frac{\gamma_{lg} r_0 (\theta_{eq} - \theta_{min-1})^2}{2(2 + \cos\theta_{eq})} \tag{4.4}$$

where, $r_0 (= r_{eq})$ is the equilibrium contact radius, and θ_{min-1} is the dynamic contact angle at the end of primary pinning phase. By considering the droplet to be nearly spherical, the value for the first potential energy barrier, $\overline{U_1}$ (expressed as per unit length of TPCL), can be roughly estimated for all the three surfaces from the available experimental data corresponding to Figures 4.6 and 4.7. For the surfaces with elastic moduli, E = 1.5, 0.06 and 0.02 MPa, the value of $\overline{U_1}$ comes out to be 39.6×10^{-7}, 45×10^{-7}, and 100×10^{-7} J/m, respectively. Again, for all the repetitions in each experimental condition, the average value of the first potential energy barrier is found as, $\overline{U_{1,1.5}} = 34(\pm 8) \times 10^{-7}$ J/m, $\overline{U_{1,0.06}} = 60(\pm 15) \times 10^{-7}$ J/m, and $\overline{U_{1,0.02}} = 125(\pm 25) \times 10^{-7}$ J/m, where the corresponding surfaces are indicated by the 2^{nd} subscript in $\overline{U_{1,E}}$. The aforementioned values, shown graphically in Figure 4.10, comprehend that the CL requires higher energy to overcome the first pinning regime on soft surfaces, thereby indicating a stronger pinning on the same. It further strengthens our claim regarding the prolonged primary pinning phase observed in the softest substrate [refer to Figure 4.7 and corresponding discussion].

Furthermore, the evolution of the first potential energy barrier ($\overline{U_1}$) with the substrate stiffness is also inherently associated with the receding contact angle, θ_R. As depicted in Figures 4.6 and 4.7, the different receding contact angles lead to different transition times from the initial pinning phase to the subsequent phases. On the apparently rigid substrate (PDMS 10:1) $\theta_R \approx 63^\circ$ (circle) as shown in Figure 4.11(a) and once the dynamic contact angle, θ_d attains θ_R, the dynamics enter in the stick-slip regime preceded by a depinning from the wetting ridge. In contrast,

TH-2590_156103041

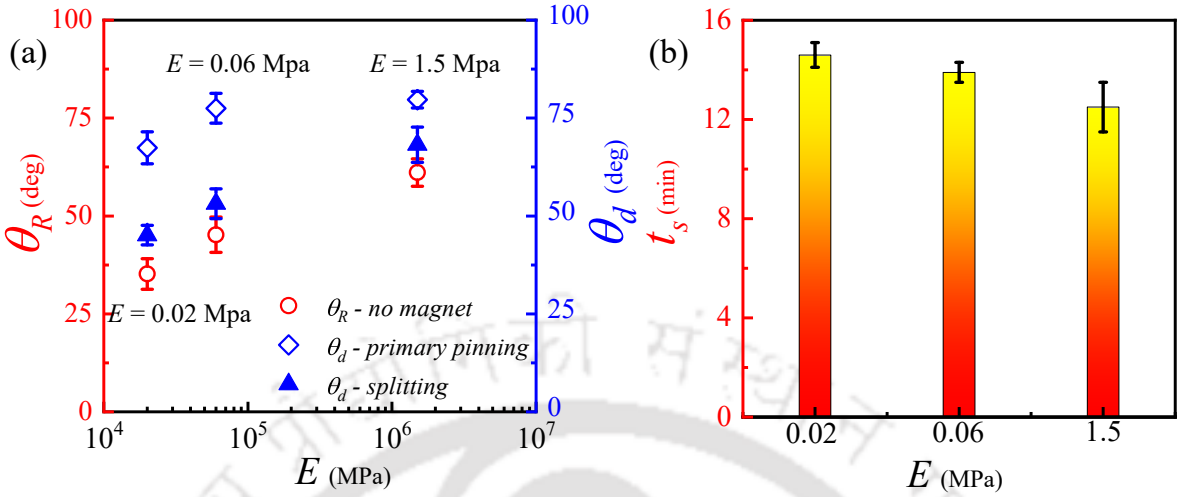


Figure 4.11: (a) Variation of receding contact angle (circle), dynamic contact angle at the end of primary pinning phase (diamond) as well as just prior to splitting (filled triangle) with the substrate stiffness (E). (b) Droplet splitting time, t_s, corresponding to different elastic moduli (E) of the underlying substrate.

for the softest substrate ($E = 0.02$ MPa), the θ_R ($\approx 35°$) is found to be the smallest from the contact angle measurements done in the absence of a magnetic field. However, unlike the dynamics on apparently rigid surfaces, the θ_d does not reduce to θ_R at the end of the primary pinning phase for the soft substrates. This statement is comprehended by the substantial difference between the θ_R (circle) and the θ_d at the end of the primary pinning phase (diamond) for the soft substrates as shown in Figure 4.11(a). This difference can be attributed to the early depinning of the CL from the wetting ridge. Karpitscha *et al.* [268] reported that there is a critical bend angle, φ ($= \theta_{eq} - \theta_d$) associated with the formation of wetting ridge, where the former is inversely proportional to the substrate elasticity [268]. Once the θ_d reaches the saturation angle of wetting ridge, φ_{crit}, triggered by the magnetic pull, any further forcing enables the dynamical depinning of CL. However, as the CL starts forming a wetting ridge in the new equilibrium position, a gradual decrease of the θ_d is observed from its new equilibrium value. Interestingly, for the soft substrates, θ_d attains (filled triangles) the value of θ_R as the dynamics progress towards splitting [refer to Figure 4.11(a)]. The outcomes signify that the θ_R plays a major role in the dynamics of the splitting of the FF droplet. The θ_d reduces to the θ_R through multiple depinning events in soft substrates, thereby increasing the time period of droplet splitting as seen in Figure 4.11(b). In contrast, for rigid surfaces,

TH-2590_156103041

the θ_d reaches the θ_R in a very early stage resulting in the smallest splitting time, t_s as shown in Figure 4.11(b).

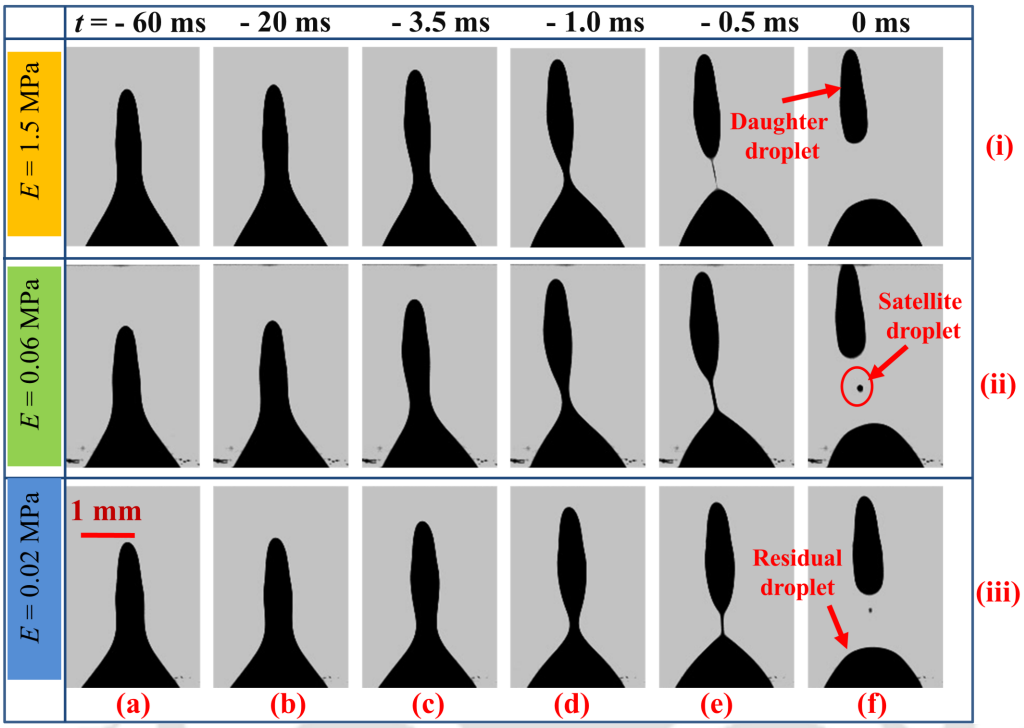


Figure 4.12: The temporal evolution of the interface of a FF droplet prior to splitting in the presence of a magnetic field. Images (a)-(f) in row (i), (ii) and (iii) show the necking dynamics associated with different substrate having elastic moduli, E = 1.5, 0.06, and 0.02 MPa, respectively. The other experimental conditions are, ϕ_0 = 3 µL, B = 450 mT, and Bo_m = 131. The beginning of time, t = 0, is considered the instant of droplet splitting, whereas the frames before that have been shown as negative in the time scale for convenience. The images are captured at a frame rate of 2000 fps.

4.3.3 Effect of substrate elasticity on droplet splitting dynamics.

As discussed previously, the continuous elongation of a FF droplet in a non-uniform magnetic field further leads to the splitting of the parent droplet. In this section, the effect of the substrate stiffness on the dynamics of the splitting of a FF droplet is explored. The corresponding events in the vicinity of splitting are recorded with a high-speed visualization system, as mentioned in Section 4.2.2.3. Figure 4.12 shows

TH-2590_156103041

the temporal evolution of the interface of a FF droplet on three different surfaces with elastic moduli, $E = 1.5$, 0.06, and 0.02 MPa in row (i), (ii), and (iii), respectively. The other experimental parameters correspond to Figure 4.3. The instant of splitting is considered $t = 0$ ms, whereas the instants prior to it have been shown on a negative scale for the reader's convenience. The image sequence in Figure 4.12 clearly shows that, as the dynamics approach splitting, the initially elongated spike develops necking [see columns (d) and (e)], which connects the parent droplet to the to be formed daughter droplet. Any further shrinkage of the neck subsequently splits the parent droplet to a daughter droplet, a satellite droplet, and a residual volume of FF as depicted in the final column of Figure 4.12. The break-up of the neck in this study is analogous to the *end-pinching* dynamics observed during drop impact phenomena [38]. As evident from Figure 4.12, the dynamic contact angle remains constant at, $\theta_d = 68.2° \pm 4.5°$, $53.13° \pm 3.8°$, and $45.1° \pm 2.5°$ on substrates with elastic moduli, $E = 1.5$,0.06, and 0.02 MPa respectively when the dynamics approach splitting during magnetowetting. Figure 4.12 also hints about the possible size variation of the daughter droplet with decreasing stiffness of the underlying substrate, which shall be discussed in the next paragraph.

In order to elicit and quantify the effect of substrate softness on the splitting

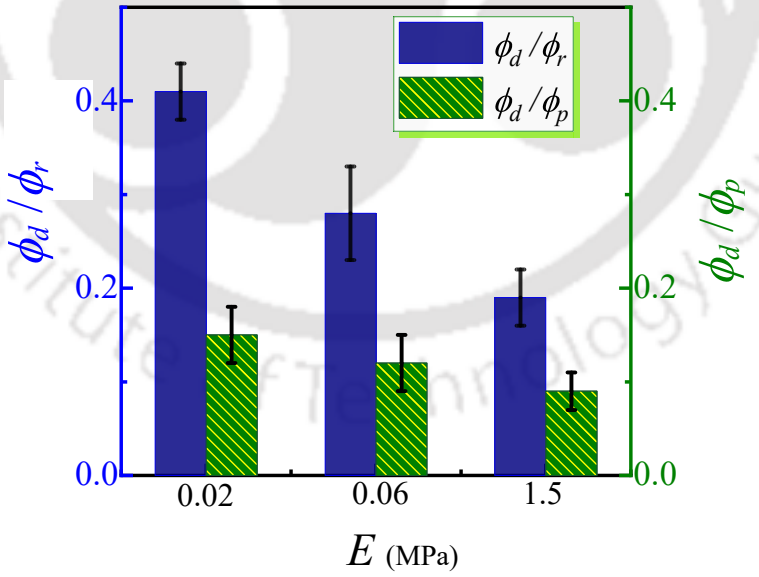


Figure 4.13: Variation of splitting ratio, $S.R$ [= volume of daughter droplet (ϕ_d)/ volume of residual droplet (ϕ_r)] with the substrate elasticity (E). The plot also shows the variation of the ratio of the daughter droplet volume to the volume of parent droplet (ϕ_r) along the right-hand side axis.

TH-2590_156103041

dynamics, the variations in the ratio of the volume of the daughter droplet (ϕ_d) to that of the residual droplet, ϕ_r, i.e., splitting ratio, $S.R$ ($= \phi_d/\phi_r$) with the substrate elasticity are analyzed, and the results are presented in Figure 4.13. It can be discerned that the splitting ratio, $S.R$, decreases with an increase in the substrate's stiffness, considering the other experimental parameters are the same. The effect of the stiffness on the ratio of the volume of the daughter droplet (ϕ_d) to that of the parent droplet (initial volume), ϕ_p is also analyzed and shown in Figure 4.13. The results indicate that for a fixed initial volume (ϕ_0 or ϕ_p), the size of the produced daughter droplet increases with an increase in the underlying substrate's softness during magnetowetting of FF droplets provided the magnetic field is identical in each case. Again, it has been observed that for a fixed initial volume and identical magnetic field, the magnetic interaction is predominant on an apparently rigid substrate as compared to that for a softer substrate. On the other hand, the prolonged pinning of the CL in the soft substrates promotes greater deformation of the interface resulting in a larger curvature near the neck region as apparent from Figure 4.12. As such, the surface tension generates a greater resistance to *pinch-off* or *splitting* in soft substrates. Possibly, the competition between the two aforementioned dominating factors results in a larger drop size with decreasing stiffness of the substrate for a fixed volume of the parent droplet. Notably, the volume of the satellite droplet is much lesser in comparison to the volume of the parent or daughter droplet, and hence the mass loss arising out of it during the magnetowetting cycles can be neglected easily. Furthermore, the secondary droplet volume corresponding to the ϕ_d and ϕ_r is measured using the in-house image processing method discussed in Chapter 2. It is to note that, in measuring the ϕ_r, the present image processing method is preferred to the conventional spherical cap approximation of sessile liquid droplets, thereby nullifying the possible occurrence of any errors arising out of deviation in the droplet shape.

Notably, in this study of magnetowetting, the effect of evaporation on the magnetowetting dynamics of the FF droplet is not considered, as the time scale of evaporation is much higher than the time-scale of deformation and splitting. Some additional comments regarding evaporation of FF droplet has been provided in Section C.2 of Appendix C. Furthermore, all the PDMS coated surfaces used in this study have approximately similar surface energy values [see discussion in Section C.3 of Appendix C], thereby indicating that the observed dynamics are engendered by the surface elasticity and magnetic field interactions.

TH-2590_156103041

4.4 Summary

The magnetowetting behaviour of sessile ferrofluid droplets on elastomeric surfaces with different stiffness is investigated in this chapter. The non-uniform magnetic field engenders deformation and splitting of the ferrofluid droplet, which is greatly influenced by the substrate's softness. It is found that the decrease in the dynamic contact angle is maximum on the softest substrate, while the contact line remains pinned. Again, for an apparently rigid substrate, the contact radius decreases almost linearly, whereas the decrease in the contact angle appears to be lower than that of soft substrates. The contact line experiences transition from stick-slip on rigid surfaces to pinned motion on soft surfaces, favoured by the presence of a large wetting ridge and smaller receding contact angle on the latter. Again, the splitting time and splitting ratio (the ratio of the daughter droplet volume to that of the residual droplet) increases with an increase in the softness of the underlying substrate. In the long run, the study unfurls a few interesting aspects of static magnetowetting behaviour of sessile FF droplets mediated by the substrate stiffness, which is expected to foster the research in the burgeoning field of solid capillarity and also to identify the most important new avenues for future investigations.

TH-2590_156103041

TH-2590_156103041

Chapter 5

Electric-discharge-mediated jetting, crowning, bursting, and atomization of a droplet

"It is, indeed an incredible fact that what the human mind, at its deepest and most profound, perceives as beautiful finds its realization in external nature....What is intelligible is also beautiful."

- Subrahmanyan Chandrasekhar, *1979*

5.1 Introduction

Electric field discharge during lightning [274] or generation of the electric arc at the contact of a charged insulator with a conductor [275] has been among the very intriguing natural phenomena that fascinated researchers for ages. Over the years, a great deal of attention has been given to comprehend such phenomena because they can be useful in various applications such as triboelectric energy harvesting [276], mixing [277, 278], gas-discharge lamps, or ionizing tubes [279], among others.

The contents in this chapter have been published as Sarma, B., Kumar, S., Dalal, A., Basu, D. N., and Bandyopadhyay, D. (2021) "Electric-Discharge-Mediated Jetting, Crowning, Bursting, and Atomization of a Droplet", *Physical Review Applied*, vol. **15**, p.-014005.

TH-2590_156103041

Interestingly, confining an electric discharge inside a microfluidic system may convert the electrical energy into the mechanical one to emerge a number of fascinating fluid dynamical phenomena such as splashing, crowning, jetting, or bursting. In similar lines, of late, extensive research activities have been observed in exploring the physics associated with the deformation and disintegration of droplets with the help of various external fields such as the electric, magnetic, or laser excitations [5, 280, 281].

The studies on the splashing, crowning, jetting, or bursting of fluids have started long back [32, 38, 282]. For example, the pioneering contributions from Worthington [29] have uncovered the possible flow morphologies assumed by an impacting liquid droplet on a solid surface. Later, the jetting or splashing during the impact of a liquid or solid object on a fluid medium is found to accompany the formation of a crown or umbrella flow morphologies [38, 53, 61]. Subsequently, in recent years, with the development of characterization facilities [54], the physics associated with the formation of a jet, crown [9, 38, 283], or fragmentation of a droplet [284] have been extensively explored. Importantly, in the present era of microscale devices, the fragmentation of the droplets, jets, or crowns into the miniaturized forms have shown their relevance in enhancing mass, momentum, and heat transport [141, 285]. Such explorations have contributed significantly in the developments of cutting-edge applications such as superhydrophobic surfaces [286], droplet microfluidics [82], spray painting, atomization of propellants [287], nebulizers, sprinklers [288], distributors [289], and inkjet printing [19].

However, the field-induced splashing, crowning, jetting, or bursting are found to be very different from the similar phenomena observed during the impact of an object on a liquid surface. In this direction, recently, such phenomena have been explored under the influence of various external triggers such as electric field [136], photonic excitations [5], thermal gradient [290], or shock waves [139]. For example, the expansion and collapse of a vapour bubble produced by an electric spark in an electrolyte solution are found to generate a pulsed liquid micro-jet of 30 μm diameter having a peak velocity of 90 m/s, aiming its use as an intravascular injection during microsurgeries [132]. Similarly, the cavitation bubbles generated during electric discharge inside a macroscopic droplet in a microgravity environment have been found to induce jetting and splash [136]. Again, Karri *et al.* [291] showed that an oscillating and collapsing cavitation bubble positioned near a liquid surface and co-axially to a cylindrical hole engenders jetting and sprays via breakup of

TH-2590_156103041

the jets. The advancement in the imaging techniques has enabled a more effective characterization of these events of drop-shaping or drop breakup to the jet, crown, and atomized droplets using laser pulse or x-ray pulse [60, 145, 146]. Importantly, the miniaturization of the droplets during laser-induced breakdown spectroscopy (LIBS) [10], lithography [148], or laser ablation [129] is among the already existing commercial processes.

Fundamentally, the origin of diverse flow morphologies during the drop impact, splashing, or breakup can be attributed to various factors, which include the surface and bulk properties of the impacting object [283, 292], velocity, and angle of attack of the impacting object [293], and the texture and roughness of the surface on which the impact takes place [294]. Despite their diversified origin, the crowns or jets are ejected during the impact of a solid or liquid object in a bulk fluid due to a substantial axial pressure gradient created at the crown- or jet-base [48, 50, 60]. For example, the transfer of the inertial force of the impacting droplet in the liquid medium is the primary reason for forming axial columnar jets on a deformable liquid-air interface [37, 38]. The progress in the domains of stability analysis [295, 296] and computational fluid dynamics [293, 297] in the past few decades have also helped in unfurling several critical aspects of flow dynamics associated with crown formation, crown-sealing, buckling, ejecta-sheet formation, or pinch-off.

In view of this background, it is proposed that the confinement of electric-discharge inside a sessile droplet can be one of the very simple but interesting ways for splashing, crowning, jetting, or fragmentation of the same. The experiments are performed in a set-up resembling the electrowetting-on-dielectric (EWOD) [6, 298] in which a droplet has been placed on an electrode-isolator pair while a pointed electrode is inserted into the drop from the top to confine the discharge inside the droplet, as schematically shown in Figure 5.1(a). A series of experiments have been performed to identify the pathways to control the electric field discharge location by tuning the electrode distance, the magnitude of the externally applied electric field, viscosity, electrical conductivity, and surface tension of the droplet. Both the experiments and simulations uncover that the location of the pointed anode in the droplet, alongside the separation distance of electrode from the base of the droplet, can be some crucial factors in varying the location of discharge, which eventually leads to the metastable liquid jets, crowns, microthreads or microdroplets. The roles of the electric field, inertial, viscous, and surface tension forces in predicting the experimentally measured time scales along with the energy conversion efficiencies of

TH-2590_156103041

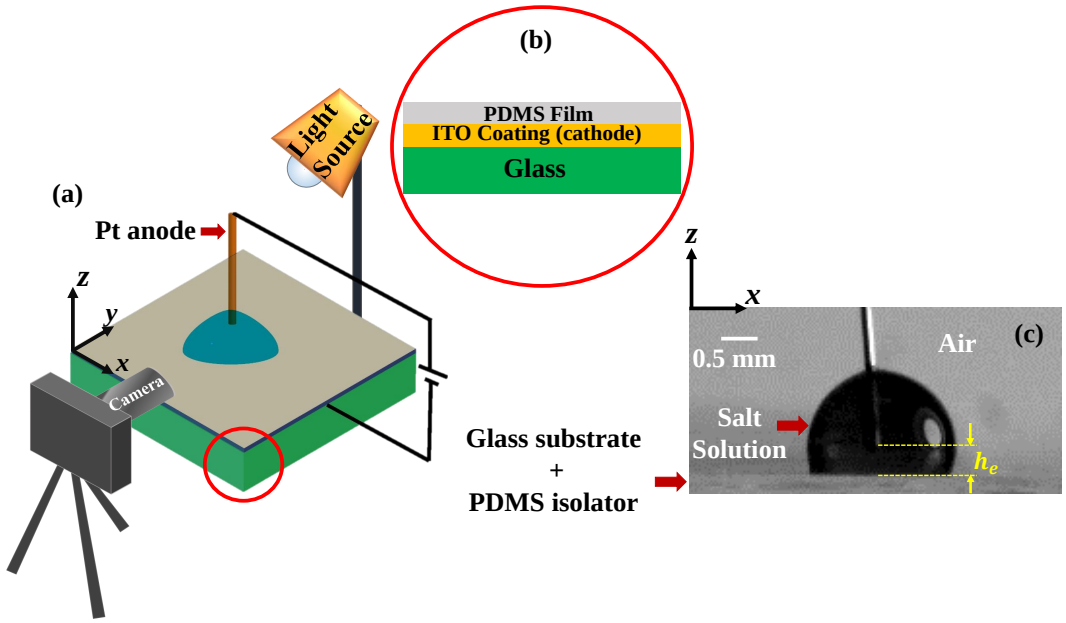


Figure 5.1: Schematic diagram of the experimental set-up. Image (a) shows an isometric view where a droplet is dispensed upon a thin PDMS film coated on an ITO-glass substrate. A pointed Pt wire connected from the top of the droplet acts as the anode. The different layers of the isolator-cathode-isolator substrate composed of PDMS-ITO-glass are shown as an inset in the image (b). (c) Shows the photographic side view of an experiment from which the position of the droplet and Pt anode can be visualized. The notation h_e indicates the distance between the droplet base and anode. A high-speed camera has followed the spatiotemporal evolution of the concerned hydrodynamic features, and a light source provides the illumination positioned opposite the camera.

the different processes have also been reported. The proposed methodology can be employed as an alternative technique to disintegrate the macroscopic droplets into the microscopic ones for improved heat, momentum, and mass transport in various microfluidic applications including, but not limited to, inkjet printing [19], electrospraying [219], tissue ablation [299], or electroporation [300] etc.

5.2 Experimental method and materials

5.2.1 Experimental procedure

The experimental procedure is schematically shown in Figure 5.1(a). In this set-up, with the help of a micropipette, a 5 μL droplet is placed on a PDMS (poly-

TH-2590_156103041

dimethylsiloxane, Dow Corning, India, SYLGARD® 184 kit) coated ITO-glass surface (Indium-tin oxide, MG Super Lab, dimension: 12.5 mm × 12.5 mm × 1.1 mm). The PDMS layer acts as the dielectric isolator between the ITO cathode and conducting droplet, while the glass layer acts as a bottom isolator, as shown in Figure 5.1(b). The droplet is connected to the electric field with the help of a platinum (Pt) wire anode (dia. 150 μm, Surgeon Sons, India) from the top, as shown in Figures 5.1(a) and reffig:1(c). The electrodes are connected to a DC power source (SES Instruments Pvt. Ltd., range: 0 - 1500 V) to generate the electric field (Ψ) across the electrodes placed at a distance h_e apart. Here, a high voltage is directly supplied to the electrodes instead of slowly ramping of voltage. Notably, along with the applied potential (ψ), the anode's location is another critical parameter affecting the strength of the discharge and the ensuing hydrodynamics. The gap between the anode and dielectric is maintained with a vertically moving platform, thereby generating an electric field of desired intensity. Besides, to maintain symmetry, special care has been taken to place the electrode near the central portion of the droplet with respect to the horizontal XY-plane, as shown in Figure 5.1(a). The repeatability of the results under varied conditions has confirmed the robustness of the proposed experimental set-up. It may be noted here that the Pt-anode is cleaned after each experiment to enhance the repeatability of the results. Further, to control the variations in the initial volume (ϕ_0) of the dispensed droplets, the microtips attached to the micropipette are replaced after dispensing every drop. The dynamics of atomization are captured with a high-speed camera for subsequent analysis, as discussed in Section 5.2.4. Unless stated otherwise, the electric discharge is generated across a 5 μL droplet of electrical conductivity 13.18 mS/cm with the help of a 500 V electric field potential applied through the electrodes.

Table 5.1: Properties of DI water and PDMS [301].

Liquid	DI-water	PDMS
Density (ρ, kg/m^3)	997.05	970
Viscosity (η, mPa s)	0.890	3500
Conductivity (σ_s, mS/cm)	5.6×10^{-5}	2.5×10^{-13}
Surface tension (γ, mN/m)	72.1	21
Dielectric Constant (ϵ)	80.0	2.65

TH-2590_156103041

5.2.2 Dielectric substrate preparation

The PDMS film is spin-coated on the ITO-glass to prepare the isolator-cathode-isolator (PDMS-ITO-glass) base substrate, as shown in Figure 5.1(b). For this purpose, initially, the ITO-coated glass slides are cleaned following the standard procedure [refer to Section A.1 of Appendix A]. Simultaneously, the pre-polymer is prepared by mixing the PDMS (properties in Table 5.1) and the curing agent in the weight ratio of 10:1 before degassing the mixture. The resulting solution is then mixed with hexane (analytical grade, Sigma-Aldrich) in the ratio of 110:10:1. Following this, the solution is spin-casted with a spin coater (SPINNXG - P1, Apex India Pvt. Ltd.) on the ITO coated glass substrate. After that, the films are cured overnight at 100°C in the vacuum oven (Spac-N-Service Pvt. Ltd., India). Spin coating at 2500 rpm with an acceleration of 5 m/s^2 and duration of 120 s resulted in a thin polymer film of thickness, $h \sim 1$ ($\pm$ 0.1) μm, on the ITO glass [302]. The thickness of the films and the surface roughness are measured with the help of a surface profilometer (Dektak 150 surface profiler, Veeco Instruments Inc.) and atomic force microscopy (Bruker, Innova), respectively. The transparent dielectric films thus prepared has a surface roughness in the nanometer range ($\sim 2 \pm 0.5$ nm). The hydrophobic nature of the surfaces is confirmed by measuring the equilibrium contact angle, θ_{eq} [see Table D.1 of Appendix D] of DI-water droplets in a goniometer (Apex India). The dielectric substrates are preserved in the vacuum desiccators if not used immediately in experiments.

5.2.3 Droplet preparation

Different types of fluids are used to prepare the droplets for the experiments, as listed in Table 5.2. The base fluid is chosen to be the de-ionized (DI) water (Merck Millipore, grade I, resistivity 18.2 MΩ cm (at 25°C) and the physical properties of the same is shown in Table 5.1. The viscosity of the droplet is tuned by mixing glycerol (Merck, 98% pure), while the electrical conductivity of the droplet is varied by mixing KCl (Sisco Research Laboratories Pvt. Ltd., Mumbai) into the solutions. In order to prepare droplets of the glycerol-water mixture with a known electrical conductivity, salt solutions of glycerol and water are prepared separately beforehand and then mixed at different volumetric ratios, as per the requirement of the experiments. The concentrations of the salt solutions (C_s) for different samples are listed

TH-2590_156103041

Table 5.2: Composition and properties of the experimental solutions ([a][303], [b][304]).

Soln.	Composition (C_s)	Viscosity (η, mPa s)	Conductivity (σ, mS/cm)	Surface Tension (γ, mN/m)	Density (ρ, kg/m^3)
1	0.01 M KCl + DIW	0.890[a]	1.33	72.12[b]	997.35[a]
2	0.05 M KCl + DIW	0.890[a]	6.74	72.19[b]	998.55[a]
3	0.1 M KCl + DIW	0.889[a]	13.18	72.27[b]	1000.41[a]
4	0.5 M KCl + DIW	0.887[a]	64.20	72.96[b]	1018.29[a]
5	1.0 M KCl + DIW	0.886[a]	111.70	73.82[b]	1041.25[a]
6	0.1 M KCl + 50% Gly. + 50% DIW	6.88	13.18	70.1	1128.7
7	0.1 M KCl + 65% Gly. + 35% DIW	18.25	13.18	68.7	1168.3
8	0.1 M KCl + 70% Gly. + 30% DIW	26.96	13.18	66.5	1181.5
9	0.1 M KCl + 80% Gly. + 20% DIW	66.90	13.18	65.3	1207.9

TH-2590_156103041

in Table 5.2. The solutions are categorized as low ($\eta \leq 1$ mPa s), moderate (1 mPa s $< \eta \leq 10$ mPa s), and high viscosity ($\eta > 10$ mPa s), depending upon the volumetric ratio of glycerol and DI water present in the droplet. Table 5.2 enlists the values of viscosity, surface tension, density, and conductivity of the solutions used in the experiments. These are measured by using rheometer (PHYSICA MCR 101; Aanton Paar), tensiometer (DY-300; Kyowa), density meter (Aanton Paar; DMA 4500), and conductivity meter (Orion 3-star conductivity benchtop model, Thermo Scientific), respectively. The conductivity meter has been calibrated against the standard solution of 0.1 M KCl each time before the measurements are made.

5.2.4 Imaging and experimental analysis

The dynamics of fast-paced atomization events are reordered using the high-speed videography technique, which is deemed more reliable than conventional flash photography methods. The dynamics of the droplet during and after the electric discharge are captured with a high-speed video camera (Photron, FASTCAM Mini UX100) fitted with a zoom lens (Navitar Macro zoom, 18-108 mm F/2.5) with a recording speed ranging from 4000 to 10000 frames per second (fps). The shortest shutter speed employed is 80 μs while the phenomenon is captured at 10000 fps. The frame speed and resolution are optimized based on the inherent time and length scales of each phenomenon reported. A high-intensity LED light (Phlox, 130000 lux) continuously illuminates the background, which enhanced the quality of the captured videos by boosting the contrast. Images are analysed with the help of open-source software ImageJ [164]. The other details of imaging and subsequent analysis can be read in Chapter 2.

5.3 Results and discussion

The experimental set-up described previously in Section 5.2.1 [refer Figure 5.1(a)] ensures the formation of a charging multilayer capacitor when a DC electric field is generated across the droplet with the help of the Pt anode and ITO cathode. The magnitude of the capacitance due to the presence of the approximately 1 μm PDMS film is determined to be about, $C = \epsilon_0 \epsilon_p A/h = 5.28$ nF, where ϵ_0, ϵ_p, and A denote the permittivity of free space, dielectric constant, and area of the PDMS film, re-

TH-2590_156103041

spectively. In such a scenario, when the electric field intensity is increased beyond a threshold value ($\Psi \geq \Psi_{cric}$), the dielectric barrier of the PDMS film breaks down, leading to an electric field discharge through the droplet. This critical electric field, Ψ_{cric}, for this discharge, is found out after performing a series of experiments, as discussed separately in Section 5.3.7.1. The electric discharge is facilitated by the sub-millimetric gap between the electrodes ($h_e \leq 1$ mm), while the electric potential (ψ) has been varied between 400 - 1200 V. Interestingly, the dielectric breakdown is analogous to the flash produced in the high voltage electricity supply wires in the presence of water droplets (pollutants) due to the degradation of the electrical insulation [305, 306]. The phenomenon is also comparable to the useful dielectric barrier discharges (DBDs), routinely used in the ozone generation, incoherent excimer ultraviolet sources, greenhouse gas recycling, and synthetic jet actuation [307, 308].

Importantly, the experimental parameters and thermophysical properties, which are of paramount importance for the present experiments, are electric field potential (ψ), initial radius (r_d), surface tension (γ), density (ρ), and dynamic viscosity (η) of the droplet. These parameters can further be clubbed together to form the following set of non-dimensional numbers: *Capillary number*, $Ca = \dfrac{\eta V}{\gamma}$, *Ohnesorge number*, $Oh = \dfrac{\eta}{\sqrt{\rho \gamma L}}$, and *Electric field Bond number*, $Bo_E = \dfrac{\epsilon_0 \epsilon_p r_d \Psi^2}{\gamma}$. The Ca signifies the relative strength of the viscous over surface tension force, Oh signifies the relative strength of the viscous force over the combined influence of inertial and surface tension forces, and Bo_E signifies the dominance of the electric field force over the surface tension force. In this study, the radius of the droplet, r_d, is considered as the characteristic length scale, L, whereas the maximum velocity of the corresponding hydrodynamic feature (namely, crown, jet, or bursting) has been considered as the characteristic velocity, V. The maximum velocity has been estimated by considering the first few frames (roughly four) of the evolution of the respective hydrodynamic features just after their emergence. Here, in all the experimental realizations, $t = 0$ is assigned to the frame just prior to discharge, a convention followed throughout the chapter. It is to note that the effect of the initial contact angle (or equilibrium contact angle, θ_{eq}) of the droplet on the hydrodynamics observed has not been considered in this study. A separate discussion on the same given in Section D.1 of Appendix D.

Further, in Section D.2 of Appendix D, an order of magnitude analysis of the different forces for a sessile droplet deforming under the influence of the electric field

TH-2590_156103041

is shown in detail. The study reveals that, during the electric-discharge, the magnitude of the gravitational force is significantly smaller than the capillary and electric field forces under the proposed experimental conditions [309]. Thus, the dimensionless numbers associated with the gravitational force have not been considered in the present study. In what follows, the salient features of the post-discharge electrohydrodynamic behaviours with the variations in the electric field intensity alongside the viscosity, surface tension, and the electrical conductivity of the droplet are discussed thoroughly.

5.3.1 Initial dynamics of discharge and generation of cavitation bubbles

5.3.1.1 Dielectric barrier discharge

The electric field discharge due to the local breakdown of the dielectric film, beyond a critical intensity ($\Psi \geq \Psi_{cric}$), helps in confining a significant amount of energy inside the droplet fluid. Such discharges are supplemented by the production of *plasma channels* in the droplet with the occurrence of visible flashes, as shown in Figure 5.2(a). In a way, the intensity of flash can be treated as an indicator of discharge strength. However, the exact location of discharge is not only difficult to trace, but also the sequence of events after the discharge does not show up the same degree of repeatability even when the experimental conditions remain similar. Interestingly, a series of experiments and simulations uncover that the initial positioning of the anode is one of the crucial factors in fixing the location of discharge. Post-discharge, the plasma channels manifest within a brief time span (t_{disc}) before expanding either to a critical size to form a local nucleus or bridge the gap between the electrodes. Notably, the discharge and plasma formation have a timescale much lower than the hydrodynamics of droplet actuation. Thus, during the experiments, multiple discharge cycles are also a possibility within the droplet in contrary to the events of spark discharges [136, 310]. An evaluation of the specific input energy for discharge, E_d/m, can be compared with the specific energy of the ejected mass (E_k/m) to calculate the mechanical energy conversion efficiency of the reported hydrodynamic phenomena.

TH-2590_156103041

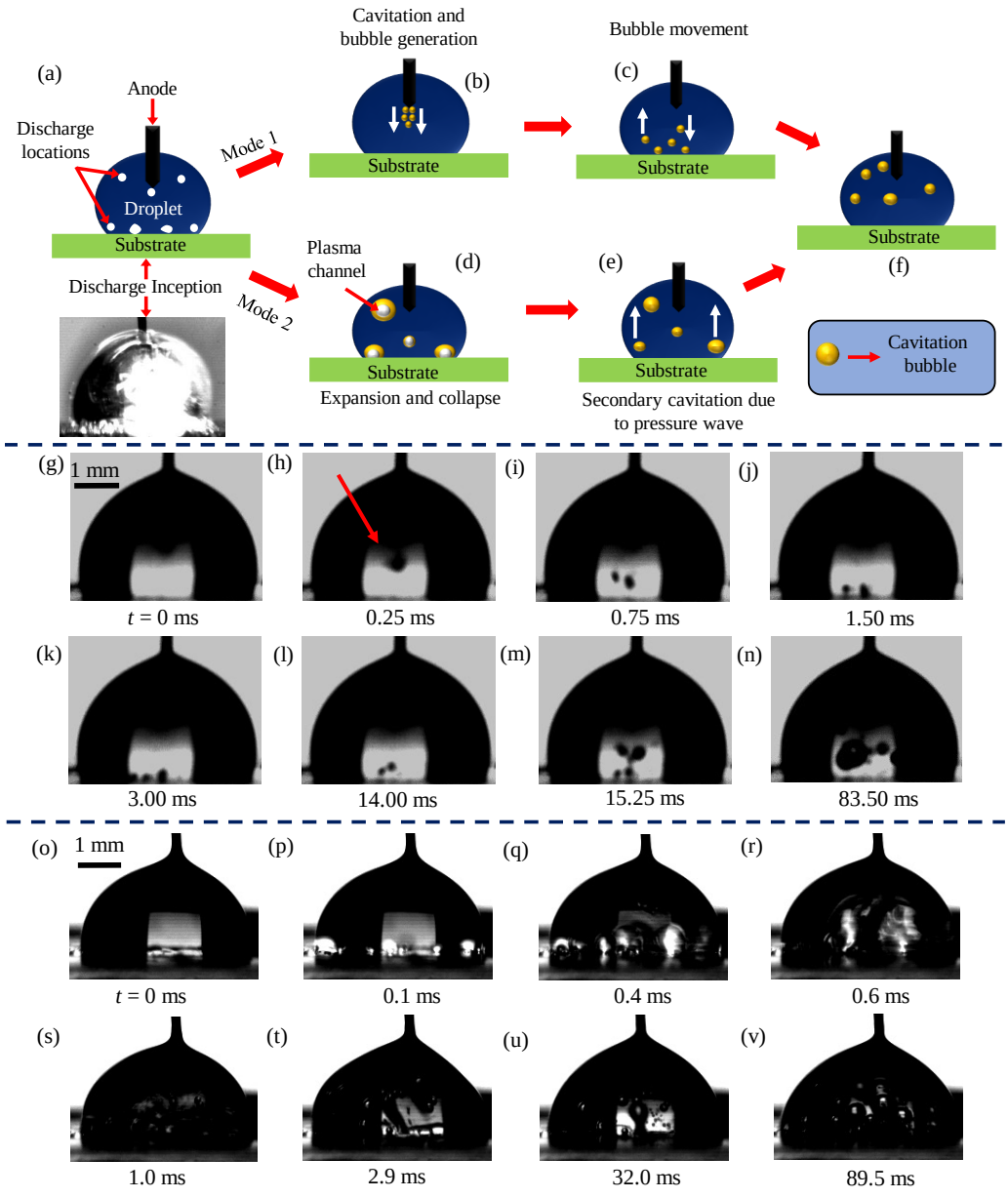


Figure 5.2: (a)-(f) Schematics of the *mode 1* and *mode 2* of bubble formation after discharge in the droplet. (a) also showing the experimental footage of the discharge covering the droplet. (g)-(n) experimental snapshots of bubble formation inside a DI-water droplet (solution 4, Table 5.2) in mode 1. The red arrow on the image (h) marks the onset of bubble formation. (o)-(v) show the bubble formation inside a droplet of glycerol (65%) and water (35%) mixture (solution 7, Table 5.2) in mode 2.

TH-2590_156103041

5.3.1.2 Dynamics of bubble formation

Previous studies indicate that such dielectric breakdown by electric field discharge favours the formation of single or multiple cavitation bubbles inside the droplet [136, 311]. However, the origin of the cavitation bubbles in the discharge cycles host a complex physics, as argued by several existing literature [311, 312]. In particular, the *thermal model* is found to be most relevant to the present experimental observations [136, 312], which suggests that the bubbles are generated by the localized heating of the liquid volumes through the rapid flow of electrical current near the discharge hot-spots. The intensely localized electric field of large power density at the tip of the sharp anode, as well as the microscale asperities in the cathode, generate discharge channels, which in turn facilitates local heating of liquid to nucleate several bubbles of high thermal energy [312] and subsequently the multiple hot-spots. Consequently, the thermally simulated bubbles trigger observed hydrodynamic phenomena. This is in stark contrast to the situations that arise with the use of pulsed laser [5, 145] or thermal excitation [313], or electric spark [136, 310], which facilitate the formation of a single isolated bubble within a sessile or suspended droplet.

Notably, the experiments conducted for the present study show two distinct modes of discharges and subsequent cavitation bubble formations, (i) from the tip of the *anode* or (ii) from the physical or chemical heterogeneities of the *cathode* as depicted schematically in Figures 5.2(a)-5.2(f). In the *mode 1*, the bubbles are ejected as a cluster from the sharp tip of the anode and pushed towards the cathode at a velocity of approximately 1 m/s. After hitting the cathode, the cavitation bubbles randomly bounce back to the liquid-gas interface, often after coalescing, to cause the reported hydrodynamic phenomena. The path in the schematic images, $a \rightarrow b \rightarrow c \rightarrow f$, depicts this mechanism wherein the arrows mark the direction of the movement of bubbles and their coalescence within the droplet. The corresponding experimental visuals are shown in Figures 5.2(g)-5.2(n), where the electric discharge is generated within a 5 μL conducting droplet (solution 4, Table 5.2) at an electric field intensity, $\Psi = 13.2$ kV/cm. The red arrow on Figure 5.2(h) indicates the onset of bubble ejection. In this mode, the discharge cycle is completed within, $t_{disc} =$ 13 ms [up to Figure 5.2(m)]. Figure 5.2(n) shows a collection of coalesced bubbles within the droplet after multiple discharge cycles in the case of droplets with high electrical conductivity.

On the other hand, the *mode 2* has been schematically depicted by the path

TH-2590_156103041

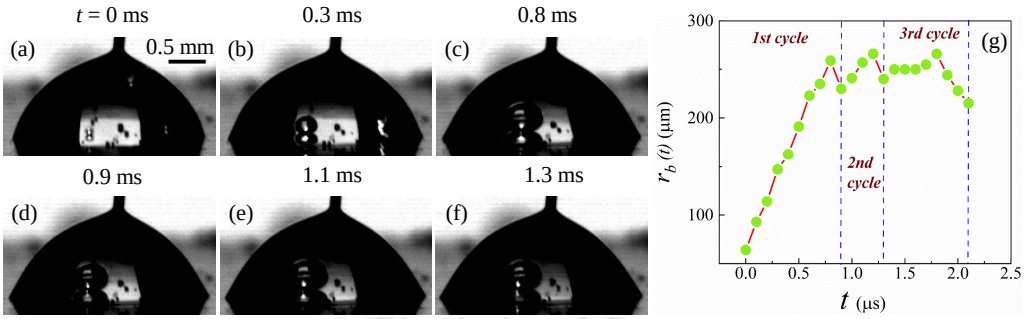


Figure 5.3: (a)-(f) Show growth dynamics of a cavitation bubble after discharge inside a highly viscous drop of glycerol (80%)-water (20%) mixture (solution 9, Table 5.2) post-discharge. The droplet volume is 5 μL, whereas the electric potential applied is $\psi = 500$ V ($\Psi = 16.98$ kV/cm). Plot (g) shows the temporal variation of the cavitation bubble radius (r_b) oscillating inside a highly viscous liquid.

$a \rightarrow d \rightarrow e \rightarrow f$, in Figure 5.2, wherein the bubbles are preferably generated near the cathode before they undergo expansion and collapse. The experimental snapshots in Figures 5.2(o)-5.2(v) show such bubble formation after discharge in a 5 μL droplet of glycerol (65%) and water (35%) mixture (solution 7, Table 5.2) when, $\Psi = 13.51$ kV/cm. The discharge hot-spots can be identified by the bright flashes in Figure 5.2(p). The expansion and collapse of the cavitation bubbles can be followed in Figures 5.2(p)-5.2(s). Prior art suggests that the case shown in Figure 5.2(s) can cause release of *acoustic pressure waves (APW)* or *shock waves* [136, 137, 313, 314], which reflect back and forth inside the liquid volume to stimulate the phenomena exhibited. Previous studies also indicate that such confined movements of the pressure waves result in the *secondary cavitation*, as seen in Figure 5.2(t) [136, 313]. In a way, *microbubbles* or *secondary cavitation bubbles* are generated via the multiple excitations of the pre-existing nuclei, e.g., dissolved gas and/or impurities, in the liquid volume, as the APW redistribute their energy after reflecting at boundaries [146, 315]. The multiple reflections of APWs further facilitate the formation of a large cluster of these secondary bubbles within one discharge cycle in the droplet [136, 315]. This is marked by the comparatively darker interior of the droplet [comparing Figures 5.2(o) and 5.2(v)] after 3 discharge cycles at $t = 89.5$ ms.

The lifetime of the secondary cavitation bubbles (t_{osc}^{sec}) is higher than the lifetime of primary ones (t_{osc}^{pri}). This can be found out by considering the Rayleigh collapse time [316], t_{coll}^{pri}, of the latter, defined as the time required for a bubble at maximum

TH-2590_156103041

radius, r_b^{max}, to shrink to its next minimum, r_b^{min} (= 0), in a liquid of density ρ under the static pressure, P_{stat}. Thus, for a water vapor bubble, the collapse time is as follows:

$$t_{coll}^{pri} = 0.915\ r_b^{max}\sqrt{\frac{\rho}{P_{stat} - P_v}}, \tag{5.1}$$

where, P_v is the non-negligible water vapor pressure opposing the outer static pressure, P_{stat}. Considering, P_{stat} = 100 kPa under atmospheric conditions and P_v = 3.2 kPa, water vapor pressure at 25 °C, the time-period for the collapse of a, r_b^{max} = 1 mm, bubble is, $t_{coll}^{pri} \sim 0.11$ ms, leading to $t_{osc}^{pri}(= 2t_{coll}^{pri}) \sim 0.22$ ms, a value closer to the experimentally observed values ($\approx$ 1.0 ms) in Figures 5.2(p)-5.2(s). However, the difference in the magnitude of both experimentally and theoretically observed values of t_{osc}^{pri} arise from not considering the effect of viscosity and multiple bubble interaction during the analysis of the concerned phenomena. In contrast, the secondary cavitation bubbles are seen to have a lifetime, $t_{osc}^{sec} \sim O[10^2$ ms], for the highly viscous case shown in Figures 5.2(o)-5.2(v). It may be noted here that r_b^{max} of the microbubbles are in the range of 0.1 mm to 1 mm, whereas the primary cavitation bubbles can expand to a size equivalent to the droplet.

Further, for highly viscous droplets (solution 9, Table 5.2), the primary cavitation bubble is not able to shrink to, $r_b^{min} = 0$, after one oscillation cycle [see Figures 5.3(a)-5.3(d)]. This can be linked with the lower discharge energy and enhanced viscous dissipation within the droplet. However, the bubble radius reaches new maxima in the next few cycles, as can be seen in Figure 5.3(g). Figure 5.3(g) clearly shows a damping behaviour as the bubbles oscillate in the viscous surrounding. The $r_b(t)$ is tracked only up to three discharge cycles beyond which the spatial resolution of the experimental images makes it difficult to track. Interestingly, similar behaviour has been reported recently for cavitation bubbles in an elastic matrix [317].

The discussions above also highlight the limits of the present experimental set-up to provide a comprehensive picture of the underlying physical processes associated with the discharge cycles and subsequent oscillatory behaviour of the cavitation bubbles [318]. This is because, the proposed experimental set-up is equipped to capture the time scales of hydrodynamics features (t_{hydro}), which is much larger than the discharge or oscillatory ones, $t_{disc} < t_{osc}^{pri} \ll t_{hydro}$. Thus, it has become possible to elucidate several characteristic features of discharge-mediated jetting or crowning or bursting dynamics, as discussed in the following sections.

TH-2590_156103041

5.3.2 Overview of the fragmentation regimes

The EHD features reported here, namely, *jetting*, *crowning*, and *bursting*, have been engendered by electrical discharge in the liquid droplet. In the "jettin" regime, a series of smaller volumes of the liquid masses are ejected from the main droplet matrix. On the other hand, "bursting" of the sessile droplet is an intense and fast phenomenon, which completely disrupts the cohesive forces of the droplet to eject the entire mass in the form of fine sprays of liquid droplets in a split-second. The "crowning" can be considered as an intermittent regime with the formation of metastable liquid sheets from the drop-matrix during ejection, followed by the ejection of droplet masses before the collapse. Importantly, during the multiple discharge cycles, there exists a possibility of witnessing a combination of the EHD features when the other experimental conditions are kept similar. The experiments reveal that the droplet volume, viscosity, electrical conductivity, and field intensity are crucial factors to fine-tune the thermodynamics and kinetics of such jetting, crowning, bursting, and mixed regimes. For example, one can manifest all the regimes simply by tuning the intensity of the applied electric field while keeping other parameters the same [detailed discussion in Section 5.3.7.1]. Further, the kinetics of such phenomena can be tuned by changing the viscosity of the droplet. In what follows, it is shown that even the location of the anode [expressed in terms of the vertical distance between the electrodes, $h_e^* = h_e/r_d$] plays a crucial role in deciding the type of EHD pattern that emerges.

For this purpose, in order to anticipate the post-discharge EHD scenario, some simulated results are shown in Figures 5.4 and 5.5, on the distribution of electric field at the instant of application, before discharge. The details of the geometry, meshing, governing equations, boundary conditions, and solution procedure of the simulations have been provided in Section D.3 of Appendix D. In particular, the simulations uncover the distribution of the equipotential lines and field vectors at different locations of electrode-droplet geometry. It is worth noting here that the droplet's conducting nature favours the formation of a capacitor-like configuration with the dielectric layer sandwiched between the electrode pairs to concentrate the EHD stress mostly across the former. The contours with vectors in Figures 5.4(a)-5.4(d) show such electric field distribution in the entire droplet-electrode set-up. Further, the magnified pairs of contours at the bottom show the same in the dielectric layer under the anode and the TPCL (identified with the help of differently coloured

TH-2590_156103041

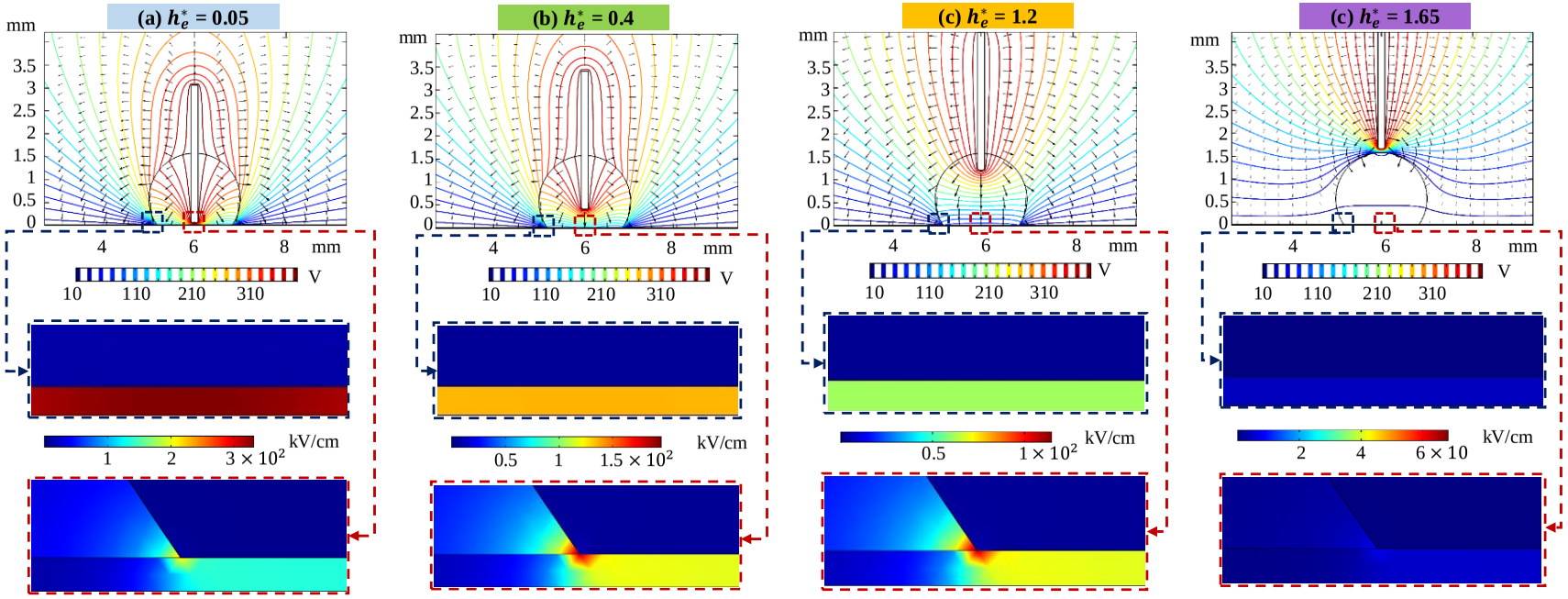


Figure 5.4: Distribution of the electric field vector and equipotential lines when a potential, $\psi = 400$ V is applied to a droplet of radius, $r_d = 1$ mm, for different position of the electrode, $h_e^* =$ (a) 0.05, (b) 0.4, (c) 1.2, and (d) 1.65. The colored plots underneath each column represent the enlarged view of the two boxed areas (in each plot), which show the electric field distribution (surface plot) within the dielectric layer. The non-dimensional electrode distance is, $h_e^* = h_e/r_d$.

TH-2590_156103041

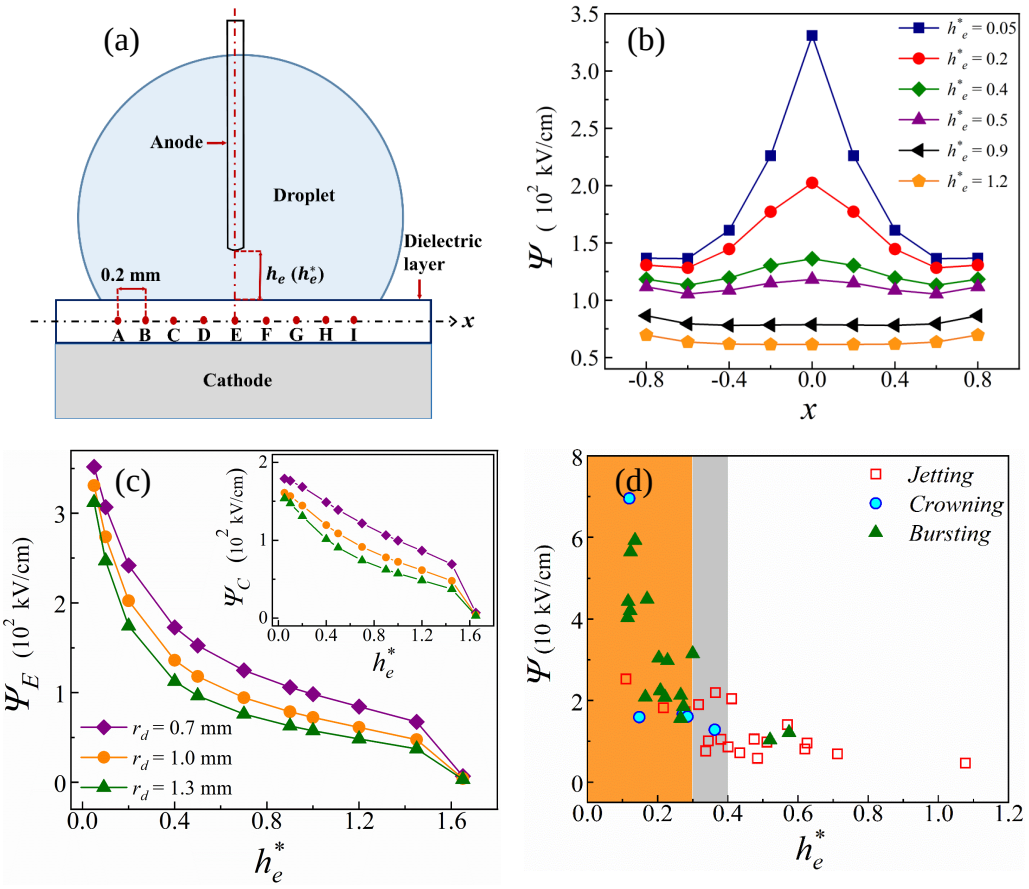


Figure 5.5: (a) Schematic diagram showing the locations (A-I) in the dielectric layer, which is considered for the other plots. (b) The resulting field intensity (Ψ) inside the dielectric layer at the locations indicated in the image (a) when $\psi = 400$ V and the location of the electrode (h_e^*) is varied. (c) The variation of field intensity at location E, Ψ_E, (and C in the inset, Ψ_C) with h_e^* for liquid droplets of different radius (r_d), while the electrode diameter is kept same (0.150 mm). (d) Experimental points showing different regimes, namely, jetting, crowning, and bursting, at the different applied electric fields, Ψ, with the variation in h_e^*.

boxes). Figure 5.4(a) shows that when the anode tip is very close to the cathode, the field intensity is highest at the dielectric layer just under the tip. On the other hand, Figures 5.4(b,c) show that, with the increase in the gap between the electrodes, not only the effective intensity of the electric field within the dielectric layer decreases but also the zone of maximum field intensity shifts towards the TPCL. Importantly, Figure 5.4(d) shows that if the electrode is placed outside the droplet, the field intensity at the thin dielectric layer decreases drastically both under the anode as well as at the TPCL.

TH-2590_156103041

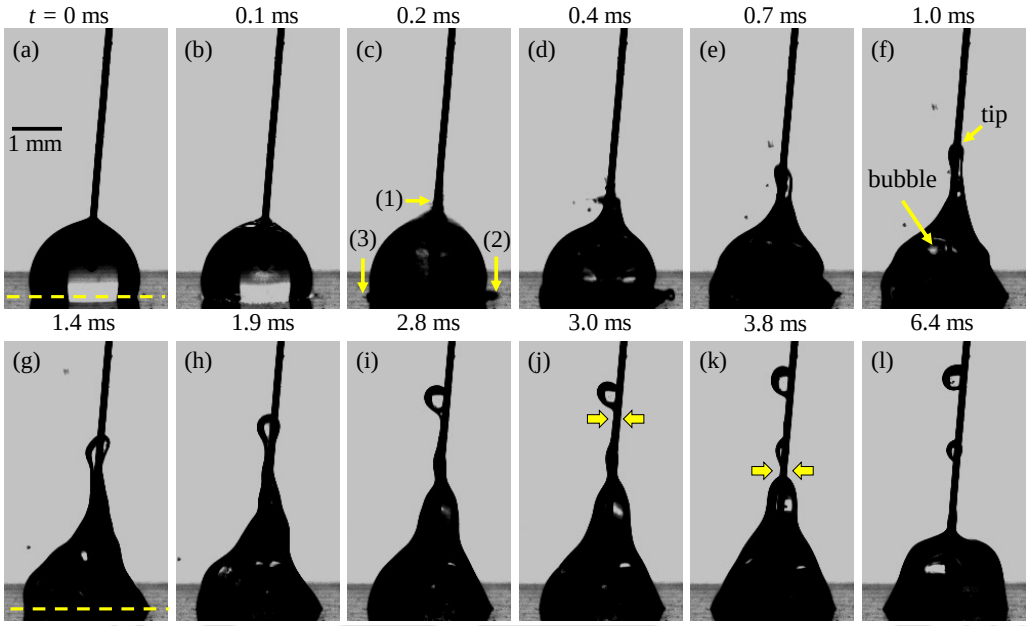


Figure 5.6: Sequence of jet formation due to the electric discharge inside a droplet (solution 5, Table 5.2) and subsequent breakup of the jet ejecting secondary droplets. Images (a)-(j) show the growth of the jet, in which image (j) shows the pinch-off region, the area marked between the arrows indicating neck formation phenomena. Images (k) and (l) show the second pinch-off event along with the separated secondary droplets. The other experimental conditions are, $\psi = 1000$ V, $\Psi = 20.86$ kV/cm, $\phi_0 = 5$ µL, $C_s = 1.0$ M, and $\eta = 0.886$ mPa s. The broken yellow line shown in image (a) has been considered as datum during the jet height and velocity measurement.

The results shown in Figure 5.4 are further extracted for a better analysis in Figure 5.5, wherein Figure 5.5(a) schematically shows the locations A–I at the dielectric layer at which the data are extracted. Figure 5.5(b) shows the variation in the field intensity at some of these different locations (x) at different electrode distances, h_e (or h_e^*). The figure suggests that for $h_e^* = 0.05$, the field intensity (Ψ) is highest under the anode (location E), whereas, beyond $h_e^* = 1.0$, the field intensity becomes highest at the TPCL. The plots in Figure 5.5(b) speak about the presence of two distinct regimes. For $h_e^* < 0.3$, the electric field is concentrated at the center of the droplet footprint (location E), which favours the formation of a strong discharge channel between the electrodes originating from a single discharge hot-spot. Such a discharge may favour the bursting of the droplet, as depicted in Figure 5.5(d). Further, Figure 5.5(d) shows that for $h_e^* > 0.4$, the electric field distribution may favour the formation of multiple discharge hot-spots in the wetted

TH-2590_156103041

area of the droplet, which may lead to the jetting regime. In the intermediate zone, $0.3 < h_e^* < 0.4$, one can observe both crown and jet formation, as depicted in Figure 5.5(d). In essence, the results from the simulation and experiments show a strong correlation between the pre-discharge electric field distribution and the observed EHD regimes, as summarized in Figure 5.5(d). Furthermore, the size of the droplets also affects the effective electric field at different positions of the electrode. The electric field strength at two locations of the dielectric layer, Ψ_C and Ψ_E, for different droplet sizes, are shown in Figure 5.5(c). The plots clearly show that as the droplet size decreases, the electric field's strength increases at all the locations, thereby facilitating the bursting or liquid crown formation events.

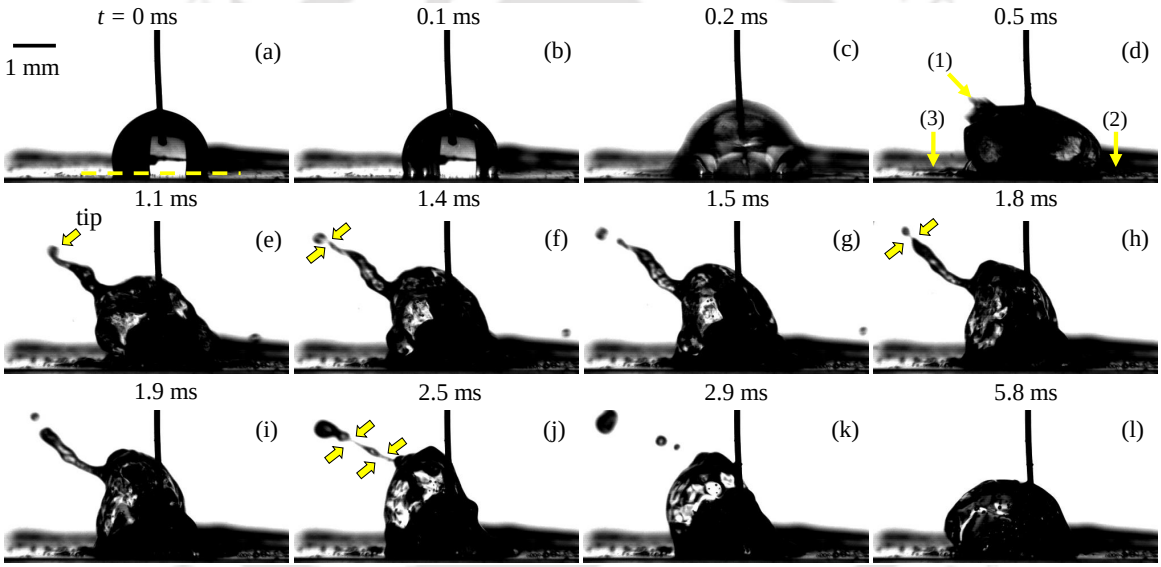


Figure 5.7: (a)-(l) Sequence of liquid jet formation due to the electric discharge inside a droplet (solution 4, Table 5.2) and subsequent breakup of the jet ejecting secondary droplets after discharge. The first pinch-off event is marked by the arrows in image (e), while the pair(s) of arrows in images (g,i) mark(s) different breakup events of the liquid jet. The other experimental conditions are, $\psi = 800$ V, $\Psi = 13.51$ kV/cm, $\phi_0 = 5$ µL, $C_s = 0.5$ M, and $\eta = 0.887$ mPa s. The broken yellow line on image (a) represents the datum.

5.3.3 Jetting regime

The discharge mediated spatiotemporal evolution of a liquid jet originating from the free surface of a droplet (solution 5, Table 5.2) is presented in Figure 5.6. The results suggest that the mechanism of formation of such liquid jets are markedly

TH-2590_156103041

different from the ones observed due to the collapse of surface waves in atomization experiments [319]. However, the dynamics of the jet breakup are much akin to that of the reported work. Figure 5.6(b) shows that post-discharge, bubbles are generated at the hot-spots (small white regions) immediately under the air-water interface of the droplet. The expansion and subsequent collapse of the bubble(s) stimulate the upward motion of the liquid jet [133, 136, 137]. Interestingly, the issuance of three jets is shown in Figure 5.6(c) marked by numbers 1 – 3, out of which two are growing along the cathode surface, while the other being released vertically along the anode, marked as 1. The experimental conditions ensure that multiple discharge locations are generated within the droplet, which in turn generate multiple bubbles with a lifetime of $t_{osc}^{pri} < 100$ µs, as indicated by the frames of Figure 5.6. While the rapid expansion of these hot-bubbles helps in creating the jets in all the directions, the anode helps one of the jets (1) to climb against gravity, as shown in Figures 5.6(c)-5.6(j). The maximum upward velocity of the jet has been found out as $v_j \sim 2.5$ m/s (suffix j refers to jetting phenomena). The jet simultaneously develops a bulbous tip [refer Figure 5.6(f)] while climbing up the electrode. The size of the tip increases until the jet reaches the maximum height [Figure 5.6(j)] before it separates from the body of the primary jet as a result of *end-pinching* (marked by arrows) to form an isolated bulbous secondary droplet. After the bulbous secondary droplet is pinched-off, the remainder of the jet traces back towards the liquid surface under the action of the capillary force. Subsequently, another pinch-off is also seen near the jet base in Figure 5.6(k), giving birth to an additional secondary droplet [Figure 5.6(l)].

However, it will not be appropriate to assume that these discharge mediated jets always ascend along the anode while moving upward. Even though the positioning of the anode is critical, the emergence of the jet is dependent on the location of the discharge [see Section 5.3.7.2] and subsequent cavitation bubble dynamics [see Section 5.3.1]. In Figure 5.7, a situation is presented wherein the jet is not following the anode. Here discharge is generated within the droplet (solution 4, Table 5.2) with the help of an electric field, $\Psi = 13.51$ kV/cm. Again, post-discharge, the formation of multiple jets, numbered as 1 - 3, are shown in Figure 5.7(d). The distinguishable primary jet, numbered as 1, has similar characteristics to that of the same shown in Figure 5.6, with *capillary pinch-off* [refer to Figures 5.7(e) and 5.7(g)] being the predominant mechanism droplet generation from an upward-moving jet. However, in later instances, after the generation of a couple of secondary droplets, the retracting jet is further disintegrated into multiple droplets, as shown in Figures

TH-2590_156103041

5.7(i)-5.7(l). The jet breakup locations are marked with arrows. The maximum jet velocity for this case is found to be $v_j \sim 1.5$ m/s.

The breakup of the liquid thread during the jet formation follows the end-pinching mechanism identified by Stone *et al.* [320] and Vukasinovic *et al.* [319]. The similarity in the order of magnitude of the Ca ($\eta v_j/\gamma \approx O[10^{-3}] \times O[10^{0}]/O[10^{-1}] \sim 10^{-2}$) also allows us to make an analogy with this already proposed mechanism. Briefly, the impulse from the cavitation bubbles collapsing inside the droplet pushes the liquid-air interface with a high momentum to form the jet. The fluid near the liquid-air interface ascends faster than the fluid near the jet base or contact line due to less frictional resistance. Subsequently, the growing bulbous front moves away from the remainder of the jet at a much faster rate causing a gradual reduction in the neck radius and eventual pinch-off to form the secondary droplet. In this scenario, the necking of the jet grows further since the higher capillary pressure in the regions of smaller radius forces the fluid to move towards the bulbous tip with a lower capillary pressure, as explained previously by Stone *et al.* [320]. The time scale for the post-discharge jet breakup $\sim$ 1.5-3 ms matches with the theoretical capillary timescale, $t_{cap} \sim \sqrt{\rho r_j^3/\gamma} \sim O[10^{-3}$ s], where r_j is the radius of the jet [23]. Considering the jets to be near-cylindrical one, the mass of the jets prior to secondary droplet generation can be evaluated as, $m_j = 1.4 \times 10^{-7}$ kg, and 1.2×10^{-7} kg, corresponding to Figures 5.6 and 5.7, respectively. Accordingly, the maximum (average) kinetic energy of the jets is found to be, $E_k^j = m_j v_j^2/2 \sim 4.7 \times 10^{-4}$ mJ (3.13×10^3 mJ/kg) and 9.0×10^{-5} mJ (7.5×10^2 mJ/kg) respectively, depicting an (average) energy conversion efficiency of, $\sim$ 0.35-0.6%, for the electric discharge mediated jet formation.

The size of the secondary droplets is found to be in the range of 0.2 - 0.5 mm. One significant observation for the jet breakup is the deviation from the *Plateau-Rayleigh instability* through the magnification of the capillary waves [321]. In a way, the elongated liquid jet generated after discharge breaks via the end-pinching mechanism to form the secondary droplets while the remaining part of it recoils back towards the primary droplet. It is well known that for the capillary instability to grow, the wavelength (λ) of disturbance has to be more than the circumference ($2\pi r_j$) of the jet, i.e., $\lambda/r_j \geq 9$ [322, 323]. The liquid jets shown in Figures 5.6 and 5.7 have aspect ratio, $A_R = L/r_j = O(6) - O(9)$, where L is the maximum length of the liquid jet. Thus, the length scale is found to be much smaller than the length required for the growth of the conventional Plateau-Rayleigh modes.

TH-2590_156103041

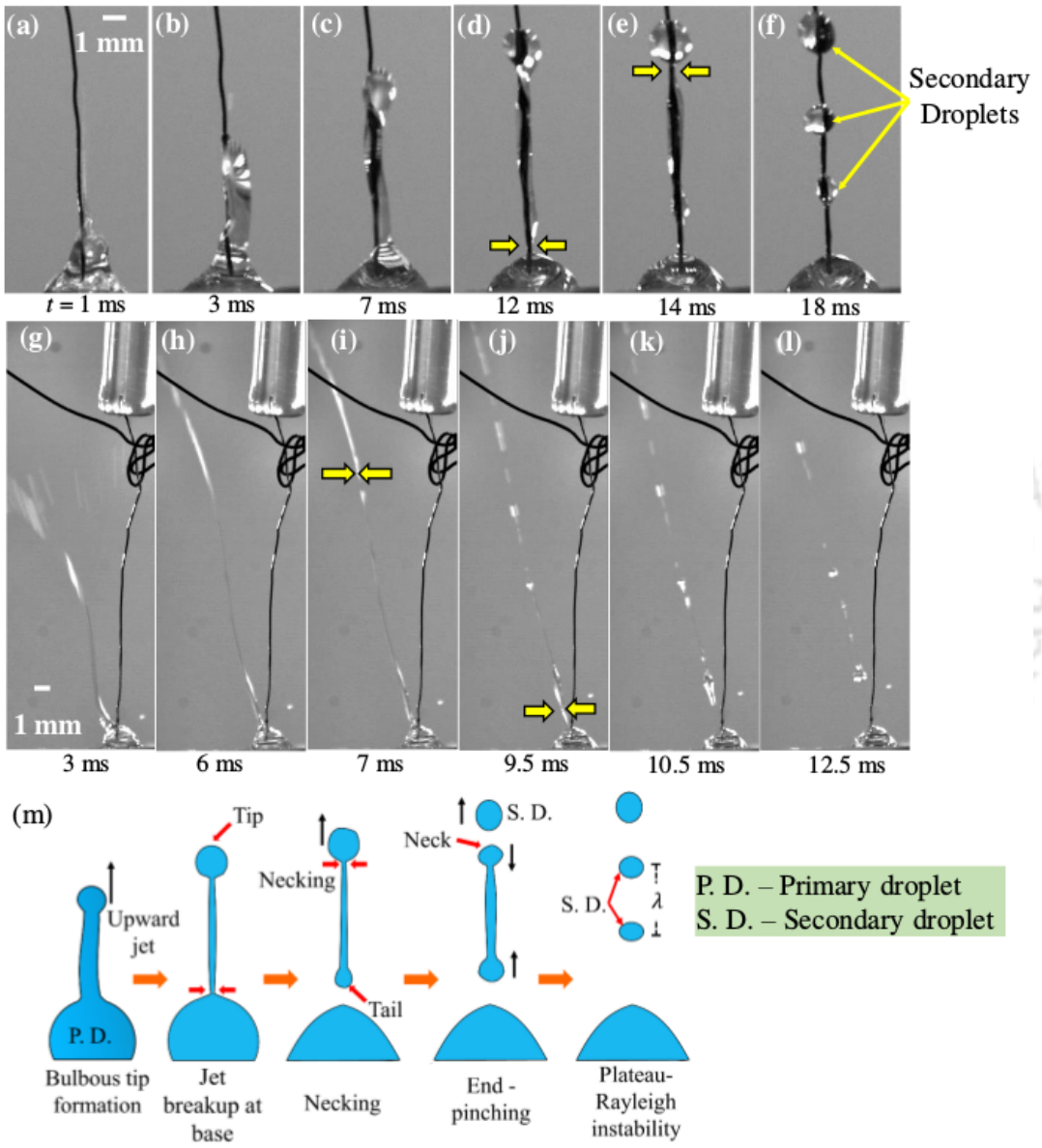


Figure 5.8: Continued on the following page.

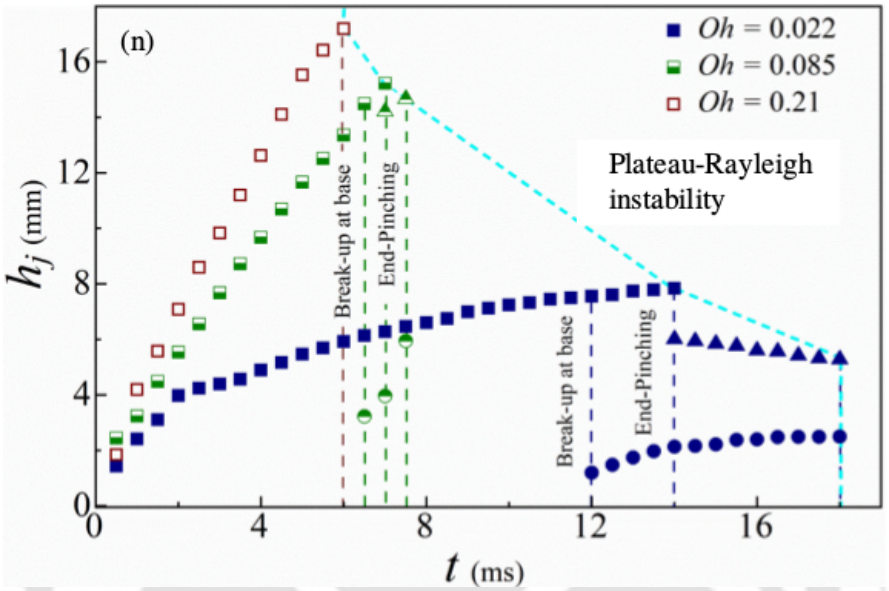


Figure 5.8: Images (a)-(f) show the time evolution of a jet originating from a droplet with moderate viscosity subjected to an electric discharge. Experimental conditions are, $\psi = 500$ V ($\Psi = 7.06$ kV/cm), $\phi_0 = 5$ µL, $C_s = 0.1$ M, and $\eta = 6.88$ mPa s. Images (g)-(l) show the time evolution of the jet formed when a very high viscosity droplet is subjected to an electric discharge. The experimental conditions are, $\psi = 500$ V ($\Psi = 9.19$ kV/cm), $\phi_0 = 5$ µL, $C_s = 0.1$ M, and $\eta = 66.96$ mPa s. The arrows mark the position of jet breakup at different instants. Image (m) schematically describes the underlying mechanism of the breakup of a viscous jet and subsequent formation of secondary droplets from the jet. Image (n) shows characteristic trajectories of three different positions of a viscous thread, namely, the tip of thread (■), the tail of unbroken thread (●), and neck (▲) for droplets of different viscosity (represented by different colours as well as symbols). The broken lines differentiate the time of occurrence of events.

TH-2590_156103041

Importantly, apart from the formation of the regular jets, an array of *microjets* also appears along the liquid-air interface after the discharge, which has a significant contribution towards the effective atomization or mass loss. A dedicated section [see Section 5.3.6] is presented later to discuss the dynamics of microjets during electric discharge mediated atomization.

5.3.3.1 Dynamics of viscous jets

Figure 5.8 shows that the dynamics of the jets can be significantly affected by the viscosity of the droplet. The high-viscosity droplet electrowets in the pre-discharge phase before forming the jet after the discharge. Figures 5.8(a)-5.8(f), and 5.8(g)-5.8(l) show the evolution of liquid jets of two different viscosities (solution 6 and solution 9, Table 5.2). The cylindrical jets, for $Oh = 0.022$ and 0.21, move upward for a considerably longer time as compared to the previously shown less viscous jets in Figures 5.6 and 5.7. However, for $Oh = 0.022$, the liquid jet continuously develops a bulbous tip until about 12 ms, as shown in Figure 5.8(d). The stages are composed of jet ascending, bulbous tip formation, jet breakup at the base, capillary thinning (necking), end-pinching, and Plateau-Rayleigh instability, as schematically described in Figure 5.8(m). The arrows shown in Figure 5.8(d) indicate the first breakup of the liquid jet at its base. Figure 5.8(e) shows the separation of the bulbous tip from the jet through capillary pinch-off before moving upward, while the separated jet in the middle [neck to tail, Figure 5.8(m)] retracts downward. It develops a dumbbell-shaped intermediate structure to relax the high surface curvatures generated near the breakup points. Finally, the intermediate dumbbell-shaped flow morphology undergoes disintegration to form two more secondary droplets due to the Plateau-Rayleigh instability. The size of the secondary droplets is in the range of 0.4 - 0.6 mm, which helped in estimating the mass of the liquid jet to be $\sim 1.34 \times 10^{-6}$ kg. The maximum kinetic energy of the jet is found to be $\sim 2.5 \times 10^{-3}$ mJ (1.90×10^{3} mJ/kg), yielding an energy conversion efficiency of $\sim 1.44\%$ for an input energy, $E_d \approx 1.32 \times 10^{5}$ mJ/kg.

Again, increase in the viscosity by an order ($Oh = 0.21$), results in the formation of a long but slender jet, as seen in Figures 5.8(g)-5.8(l). The jet thins while moving upward and subsequently disintegrate into parts, as shown in Figure 5.8(i). The absence of the bulbous tip in a highly viscous jet is a substantial difference from the previous experimental realizations. In this case, the highly viscous jet attains

TH-2590_156103041

a maximum velocity of $\sim$ 4.7 m/s. The arrows in Figure 5.8(j) mark the point of detachment of the jet from its base. The secondary drop formation due to Plateau-Rayleigh instability becomes more prominent after this point, as shown in Figures 5.8(k) and 5.8(l). The typical size of the secondary droplets is found to be $\sim$ 0.2-0.35 mm.

Notably, Vukasinovic *et al.* [319] have previously shown that the first breakup point for an upward moving viscous jet appears at the base of the jet before undergoing various instabilities to form secondary droplets. The same phenomenon has been observed in Figures 5.8(a)-5.8(f). The Plateau-Rayleigh instability has been found to dominate once the thread is detached from the base. However, a further increase in the viscosity by an order (Oh = 0.022 to 0.21) accelerates the thinning of the emerging cylindrical jet from the base, which in turn favours the growth of the capillary instabilities from the very beginning owing to the very high aspect ratio of the latter ($A_R \sim 100$). As a result, the first breakup of the jet takes place simultaneously with its detachment from the base, before multiple equally spaced secondary droplets are generated within a few milliseconds. Figure 5.8(n) traces the trajectories of three characteristic points during the shape evolution of the viscous liquid jets, namely, the tip, tail, and neck, as indicated in the schematic, Figure 5.8(m). In this plot, the point, $t = 0$, marks the instant prior to discharge while the surface of the isolator is considered as $h_j = 0$, to make the distance absolute. The three different colours depict three cases with different viscosity values whereas, the different symbols, namely square box (■), circle (●), and triangle (▲) refer to the tip of the thread, the tail of the unbroken thread, and neck positions, respectively. The vertical broken lines demarcate the aforementioned events observed during the shape evolution of the viscous jets after discharge.

Figure 5.8(n) exhibits a few exciting observations for the discharge mediated jet formation. Firstly, the initial slopes ($t < 2$ ms) of the trajectories indicate an early acceleration of the jets. This also hints about the inertia-dominated jet dynamics immediately after the discharge. For the high viscosity solutions ($Oh \geq 0.1$), the acceleration continues until the first breakup point, and Plateau-Rayleigh instability takes place immediately after its detachment from the base. Also, the rapid thinning of the jet facilitates the growth of unstable wavelengths to generate a greater number of secondary droplets. However, for moderate viscosity of the droplet ($Oh = 0.022$), the slope of the jet trajectory decreases after the initial inertia dominated phase ($t < 2$ ms), indicating slower jet dynamics and thinning. Comparing the dynamics

TH-2590_156103041

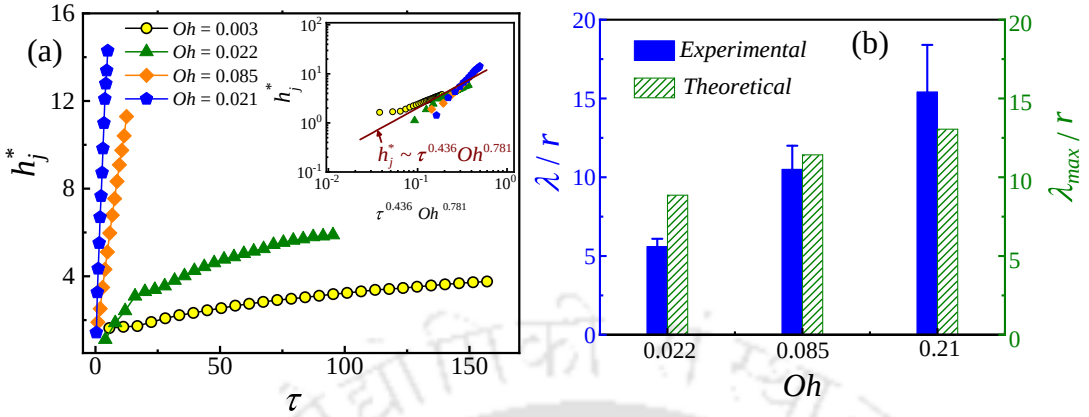


Figure 5.9: The plot (a) shows the variation in the non-dimensional jet height (h_j^*) before the first breakup with time ($\tau = t/t_{vis}$) when electric discharge is instigated inside the droplets of different viscosity (solutions 5, 6, 8, and 9, Table 5.2). Here, $t_{vis} = \eta L/\gamma$ is the viscous time-scale corresponding to the experimental conditions. The plot in the inset shows the merging trend of the experimental data points following a unified scaling law, $h_j^* = a\tau^b Oh^c$, with coefficients: $a = 20.169 \pm 1.582$, $b = 0.436 \pm 0.047$, and $c = 0.781 \pm 0.060$. The plot (b) shows the variation in the normalized spacing of the secondary droplets - experimental (λ/r) and theoretical (λ_{max}/r) with Oh, where λ and r are the average spacing and radius of secondary droplets, obtained from experiments, while λ_{max} is obtained from the theoretical analysis. Here, λ_{max} signifies the wavelength of the fastest-growing disturbance responsible for the breakup of the thread. The Oh number is calculated based on the initial equilibrium radius of the primary droplet (r_d). The experimental conditions are $\psi = 500$ V (all three cases, except for solution 5, where $\psi = 1000$ V), $\phi_0 = 5$ µL, and $C_s = 0.1$ M.

of jets for the less viscous (see Figures 5.6 and 5.7) and more viscous (see Figure 5.8), it can be inferred that the electric discharge can generate thinner and longer liquid jets in the latter situation. Also, as observed, the propensity of the generation of both high aspect ratio jets, $A_R \geq O(15)$, and secondary droplets increases with the increase in viscosity of the droplet. The broken line demarcates the region of Plateau-Rayleigh instability for jets of different viscosity in Figure 5.8(n). Herein, the results from a single experimental realization are shown to give a qualitative overview of the viscous jet dynamics.

The experiments further confirm that the increase in the experimental solution's viscosity kinetically stabilizes the liquid jet, which in turn facilitates its elongation in the vertical direction. Consequently, the elongated jets favour the growth of capillary waves to form multiple secondary droplets after the first one is formed following

TH-2590_156103041

the end-pinching mechanism. Importantly, for the systems under consideration, a pair of jetting regimes can be elucidated from the magnitude of the Ca to differentiate the underlying mechanism of secondary droplet formation. For example, when $Ca \ll 1$, for the experiments shown in Figures 5.6 and 5.7, fast-moving jets can generate bulbous secondary droplets through capillary pinch-off, indicating the dominance of inertia over the surface tension force. In comparison, an increase in the viscosity of the droplet prompts the appearance of the other regime corresponding to $Ca \geq 1$, where the jets initially detach from the base before the dominance of the capillary force over the inertia helps in breaking them into multiple secondary droplets via Plateau-Rayleigh instability.

The temporal variations in the jet height, h_j, until the instant of the first breakup for solutions having different viscosity is shown in Figure 5.9(a). Here, τ is the non-dimensional time scale derived as, $\tau = t/t_{vis} = t/(\eta L/\gamma)$, with t_{vis} being the visco-capillary time-scale [324] and $h_j^* = h_j/r_d$ is the non-dimensional jet height. The figure confirms that, with an increase in the solution viscosity, the resulting liquid jets become faster, accompanied by continuous thinning. Interestingly, all the non-dimensional plots collapse into a single curve as shown in the inset of Figure 5.9(a) following the unified power law, $h_j^* \propto a\tau^b Oh^c$. The regression analysis of the experimental data gives the coefficients as: $a = 20.169 \pm 1.582$, $b = 0.436 \pm 0.047$, and $c = 0.781 \pm 0.060$. Notably, the strong dependency of the jet height on the Oh is reflected from the magnitude of the coefficient c, which further explains the reason behind the elongated jets observed in high viscosity. Again, Figure 5.9(b) shows the variation in the normalized spacing of the secondary droplets, λ/r, with Oh in which the experimental and theoretical values are plotted in blue and olive, respectively. The details of the theoretical treatment to calculate the most unstable wavelength (λ_{max}) have been provided in Section D.4 of Appendix D. The plot suggests that λ/r increases monotonously with an increase in viscosity of the primary droplet, which is in good agreement with the theoretical predictions from the Plateau-Rayleigh instability of viscous jets [96, 325].

5.3.4 Crown formation regime

Figure 5.10 shows a sequence of images of liquid crown formation when a 5 μL droplet of 0.5 M KCl solution (solution 4, Table 5.2) is exposed to a discharge of energy, $E_d \approx 5.28 \times 10^5$ mJ/kg. The figure suggests three stages of crown forma-

TH-2590_156103041

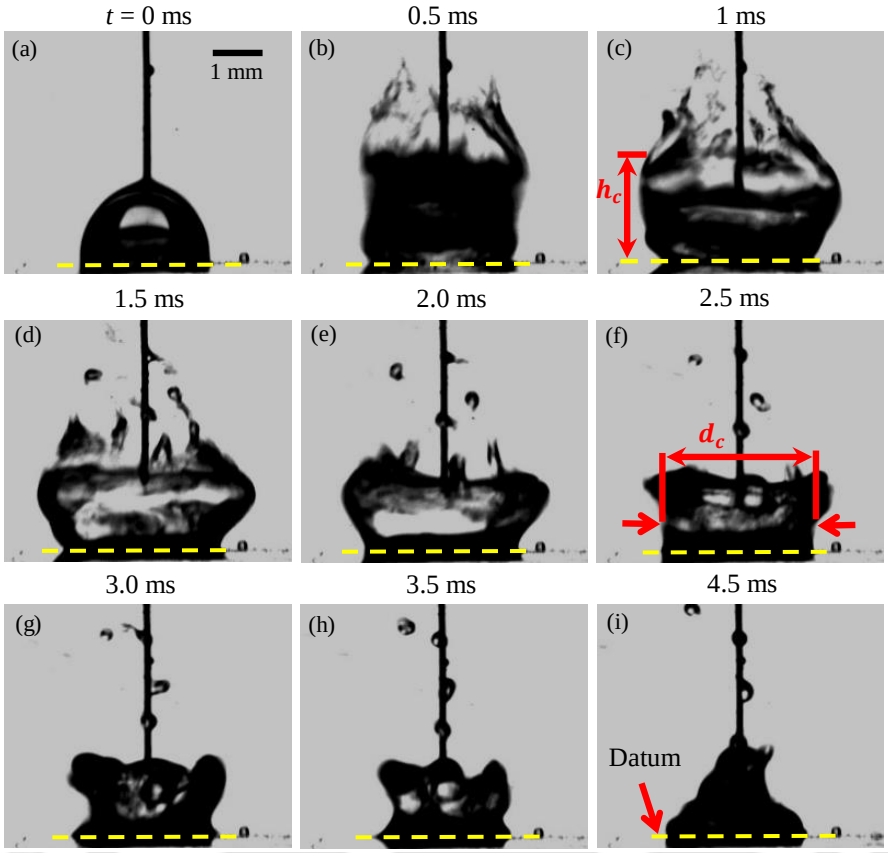


Figure 5.10: Images (a)-(i) show the time evolution of the interface of a drop of KCl solution (solution 4, Table 5.2), subjected to an electric field discharge, leading to the formation of a liquid crown. Experimental conditions are, $\psi = 1000$ V, $\Psi = 9$ kV/cm, $\phi_0 = 5$ µL, $C_s = 0.5$ M, and $\eta = 0.887$ mPa s. Images (c),(f) show the positions of measurement of the crown height, h_c, with respect to a datum marked by the broken yellow line, and neck diameter (or radius), d_c (or r_c), respectively.

tion, (i) onset with a cohesive failure of the droplet after discharge, (ii) formation and expansion of liquid-sheet to form a crown, and (iii) secondary droplet generation from the rim of the crown before complete sealing and collapse. In the first stage, the cavitation bubble formed due to the discharge is expected to undergo a rapid expansion to cause a cohesive failure of the droplet, as observed in Figures 5.10(a) and 5.10(b). Here, it can be intuitively argued that the rupturing of the liquid-vapor interface takes place at a later stage of bubble expansion, thus creating a lower pressure difference between the bubble interior and surrounding air at the time of rupture. This further favours the formation of a crown, analogous to the phenomenon reported by Avila and Ohl [145] in their work on laser-induced droplet

TH-2590_156103041

fragmentation.

In the second stage, the cylindrical liquid sheet stretches vertically as well as expands in a radially outward direction, as seen in Figures 5.10(b)-5.10(d). The liquid sheet expands until 1.5 ms, which is continually opposed by the capillary forces. While stretching, the sheet progressively develops a liquid rim as well as thin ligaments due to continuous accumulation of fluid mass, as visible in Figures 5.10(b) and 5.10(c), in a similar fashion to that of liquid splash events [31]. The liquid rim grows in size with time before experiencing capillary instability leading to the formation of an array of ligaments at the periphery, as seen in Figure 5.10(d). The ligaments further generate secondary droplets via capillary pinch-off, which are ejected away from the rim. The experiments uncover that the maximum velocity of the liquid sheet during the early expansion phase reaches $v_c^e \sim 0.8$ m/s.

In the third stage, the sheet starts collapsing or shrinking towards a common centre under the effect of surface tension, as shown in Figures 5.10(e)-5.10(i). One significant observation of this collapsing phase is the formation of a *necking regime*, which continuously shrinks till the total collapse of the crown, marked by the red arrows in Figure 5.10(f). Figures 5.10(c) and 5.10(f) indicate the definitions of the height (h_c) and diameter (d_c) of crown (also referred as *neck diameter*) as it approaches sealing phase. The temporal variations in the neck radius further reflect the characteristics of the collapsing phase of the crown, which shall be discussed in the context of Figure 5.12. The maximum shrinking velocity of the liquid sheet is $\sim$ 1 m/s. Experiments uncover that the typical time scale for the expansion phase, $\approx$ 1.5 ms $\approx 0.3t_{sheet}$, is substantially lesser than the collapsing phase, $\approx$ 4 ms $\approx 0.7t_{sheet}$, indicating the dominance of capillary forces over the inertial force within the lifetime of the liquid sheet (t_{sheet}) forming the crown. The aforementioned features have also been reported during crown formation by laser irradiation or thermal exposure [145, 326].

The experimental timescale associated with the crown formation can be obtained from the balance of driving electric field force and restoring viscous and capillary forces. For example, the theoretical time scale, $t_{exp} = \left(\frac{\epsilon_0 \epsilon_p r_d \Psi^2}{\gamma}\right)\left(\frac{\eta L}{\gamma}\right) = Bo_E\ t_{vis} =$ 3.25 ms, is found to be in close agreement with the experimentally observed time period of the inertia driven expansion phase (1.5 ms) of the crown regime. Here t_{vis} is the visco-capillary time scale related to the initial expansion of the crown. Similarly, the timescale for the collapse of the crown is obtained from the interplay between the driving inertial force to the restoring surface tension force. The timescale for

TH-2590_156103041

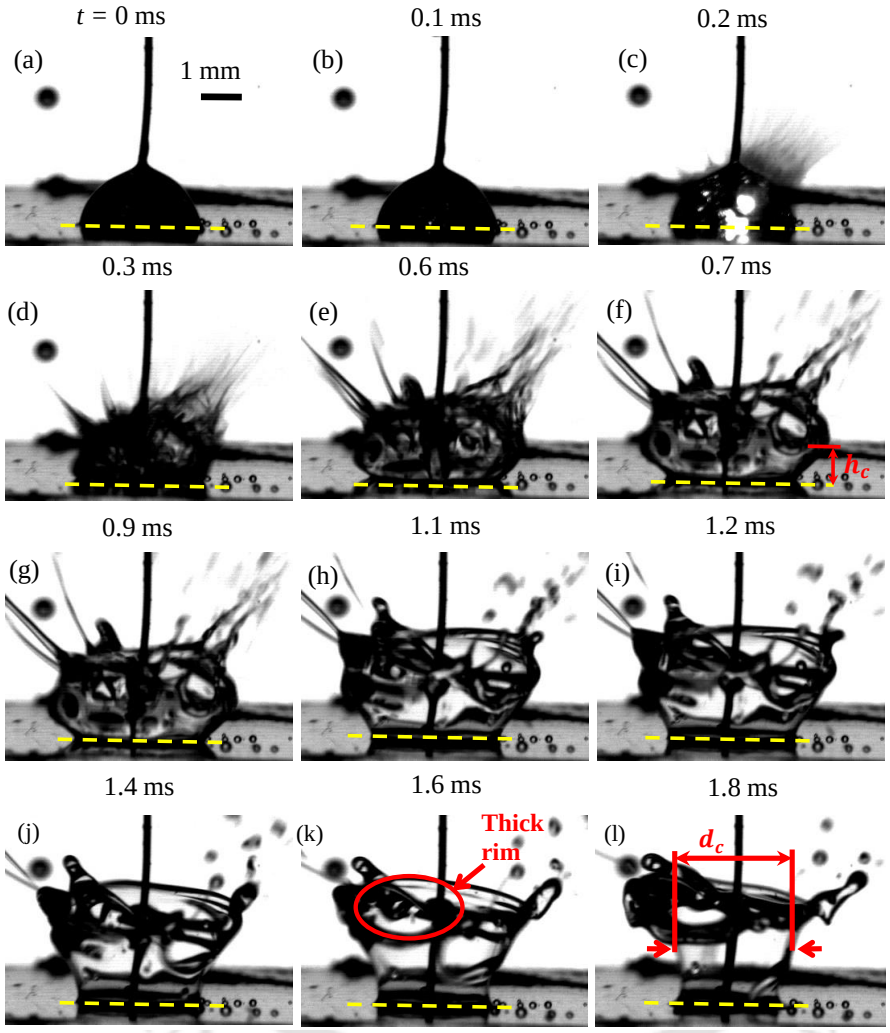


Figure 5.11: Images (a)-(l) show the spatiotemporal evolution of a high-viscosity droplet of aqueous KCl solution and glycerol mixer (solution 7, Table 5.2) subjected to an electric discharge. Experimental conditions are, $\psi = 800$ V, $\phi_0 = 3$ µL, $C_s = 0.1$ M, and $\eta = 18.25$ mPa s. Image (a) shows the initial shape of the drop prior to discharge, images (b),(c) show propagation of discharge within the drop and initiation of crown formation, images (d)-(g) show the expansion of the crown, and images (h)-(l) show the sealing and collapse of the crown. Images (f),(l) show the positions of measurement of the crown height, h_c, with respect to a datum marked by the broken yellow line, and neck diameter (or radius), d_c (or r_c), respectively.

TH-2590_156103041

such a process is evaluated as [145], $t_{cap} = \sqrt{1/6}(\rho r_c^3/\gamma)^{1/2}$, where t_{cap} corresponds to the time required for a fluidic crown of neck radius, r_c to retract itself towards a common centre, thereby converting the surface energy to the inertial one. Substituting the necessary values, t_{cap} is obtained as ($\approx$) 2 ms, which agrees closely with the experimental value (2.5 ms). In addition, the typical dimensions and physical properties of the droplet, $L = O[10^{-3}$ m], $v = O[10^{0}$ m/s], $\rho = O[10^{3}$ kg/m^3], $\gamma = O[10^{-1}$ N/m], $\psi = O[10^{3}$ V] and $\eta = O[10^{-3}$ Pa s] lead to, $Bo_E = O[10^{3}]$, and $Ca = O[10^{-2}]$, which endorses the dominance of electric field and surface tension forces over the inertial one in this breakup regime.

In the experiment shown in Figure 5.10, the average height of the liquid sheet composing the crown wall, h_c is $\sim$ 2 mm, at the end of expansion stage [refer Figure 5.10(d)]. Again, the velocity of retraction of the liquid sheet, v_c^r is found to be $\sim$ 0.9 m/s, which helps in obtaining the thickness of the sheet, $\delta \approx$ 0.2 mm, from the force balance expression proposed by Taylor [327], $v_c^r = \sqrt{2\gamma/\rho\delta}$. Therefore, the mass of the crown can be evaluated as, $m_c \sim 2\pi\rho\delta h_c r_c \sim 4.95 \times 10^{-6}$ kg, where r_c is the hollow-radius of the crown [43]. The kinetic energy corresponding to the maximum expansion velocity of the crown ($v_c^e \sim$ 0.8 m/s) is found to be, $E_k^c \sim m_c(v_c^e)^2/2 \sim 2.08 \times 10^{-3}$ mJ (4.16×10^{2} mJ/kg), which is $\sim$ 0.1% of the discharge energy, $E_d = 5.28 \times 10^{5}$ mJ/kg. Furthermore, the average diameter of the secondary droplets generated through this breakup mode is $\sim$ 0.3 mm, which is $\sim$ 10% of the initial drop diameter. The experiments suggest that the electric discharge within a liquid droplet can disturb the restoring influence due to the surface tension force to develop a crown morphology with a higher surface to volume ratio and irregular shape. Even such irregular crown can be made more regular by enhancing the droplet viscosity, as shown in Figure 5.11 in the following Section 5.3.4.1.

5.3.4.1 Crown dynamics at higher viscosity

The shape evolution of a droplet with higher viscosity, for a discharge energy of, $E_d \approx 4.82 \times 10^{5}$ mJ/kg (solution 7, Table 5.2) is presented in Figure 5.11. The enhancement in viscosity from 0.887 mPa s to 18.25 mPa s is achieved by adding glycerol to the aqueous solution of KCl while maintaining the conductivity identical to the base solution (σ_s = 13.18 mS/cm). The experiments suggest that the overall dynamics of the aforementioned three stages remain very similar regardless

TH-2590_156103041

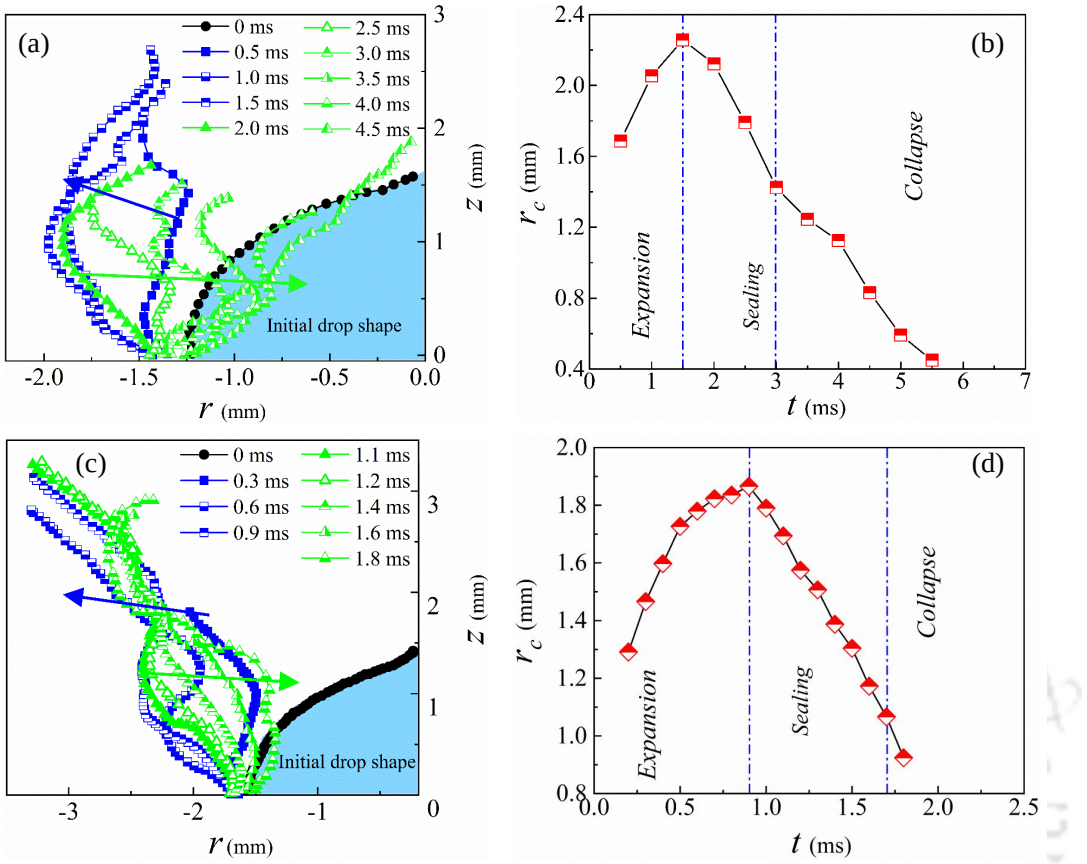


Figure 5.12: Images (a),(c) represent the contour of the liquid-air interface of the crown for a low ($Oh = 0.003$) and a high ($Oh = 0.056$) viscosity droplet, respectively. Here, a set of different symbols, namely, circle, square, and triangle filled and bordered with black, blue, and green colour, respectively, are used to depict the previously mentioned three distinct stages of crown evolution, namely, the droplet before electric discharge, the crown formation, and expansion, and finally the sealing and collapse of the crown, with the help of contours. The blue arrow pointing towards the left indicates the direction of expansion of the crown, while the green arrow pointing rightward indicates the direction of crown sealing. Plots (b) and (d) show the rate of change of the neck radius, r_c, corresponding to the crown formation events shown in Figures 5.10 and 5.11, respectively.

of the viscosity of the droplet. The phenomenon initiates with a cohesive failure of the droplet due to discharge [see Figures 5.11(a)-5.11(c)] before the formation and expansion of crown with a rim decorated with spikes [see Figures 5.11(d)-5.11(g)] takes place. Such elongated spikes are characteristics of the *Richtmyer-Meshkov instability*, observed during large initial acceleration of a liquid sheet [328]. Early ejection of liquid mass is also observed due to the breakup of some of these spikes

TH-2590_156103041

via capillary instability of threads [see Figures 5.11(e) and 5.11(f)].

The expansion of the crown up to ~ 0.9 ms also favours the formation of a rim, as shown in Figures 5.11(d)-5.11(g). The unstable rim subsequently generates thick ligaments, which again undergo capillary breakup to generate secondary droplets during the expansion stage. The size of the secondary droplets generated by the stable viscous sheet ranges from 0.1 to 0.4 mm. Further, a quantitative analysis of the frames from the early expansion stage of Figure 5.11 indicates that the maximum velocity of expansion of the crown, v_c^e, is ~ 2.0 m/s. The sheet starts retracting at ~ 0.9 ms, indicating the onset of the sealing and collapse stage, accompanied by the movement of the TPCL towards the anode, as shown in Figures 5.11(h)-5.11(l). Notably, this movement of the contact line is not prominent during the collapse of less viscous liquid sheets [refer to Figure 5.10]. However, such TPCL retraction for more viscous droplets favours the formation of a *necking region* below the thicker rim, as shown by the red circle and arrows in Figures 5.11(k) and 5.11(l). Here, a prolonged sealing and collapsing phase ($\approx 0.8 t_{sheet} \approx 3$ ms) is observed, owing to the significant viscous resistance against the fluid motion for these activities. Although not shown in Figure 5.11, beyond 1.7 ms, the crown collapses progressively due to the influence of the surface tension force [145].

It may be noted here that, neglecting any loss of liquid mass during the early expansion phase, the calculated velocity of crown expansion (v_c^e, is ~ 2.0 m/s) corresponds to an average kinetic energy of 2.01×10^3 mJ/kg, which is $\sim 0.45\%$ of the total discharge energy from the electric field. Thus, a strong viscous force confines more discharge energy to develop a more stable crown, as shown in Figure 5.11. More importantly, an increase in the magnitude of the viscosity ($\eta \sim O[10^{-3}] \rightarrow \eta \sim O[10^{-1}]$) of the droplet raises both Ca (approximately $O[10^0]$) and Oh (approximately $O[10^{-1}]$) by two orders of magnitude as compared to the less viscous case, which corroborates the dominant role of viscosity on the hydrodynamics and the presence of a kinetically controlled crown formation.

Figures 5.12(a) and 5.12(c) show the contours of the outer wall of the liquid-air interface of the initial droplet and the crown after the electric discharge, extracted from the time-resolved images presented in Figures 5.10 and 5.11, respectively. For brevity and clarity, only half cross-section of the droplet is shown in the concerned plots. Here, a set of different symbols, namely, circle, square, and triangle filled and bordered with black, blue, and green colour, respectively, are used to depict the previously mentioned three distinct stages of crown dynamics with the help of contours.

TH-2590_156103041

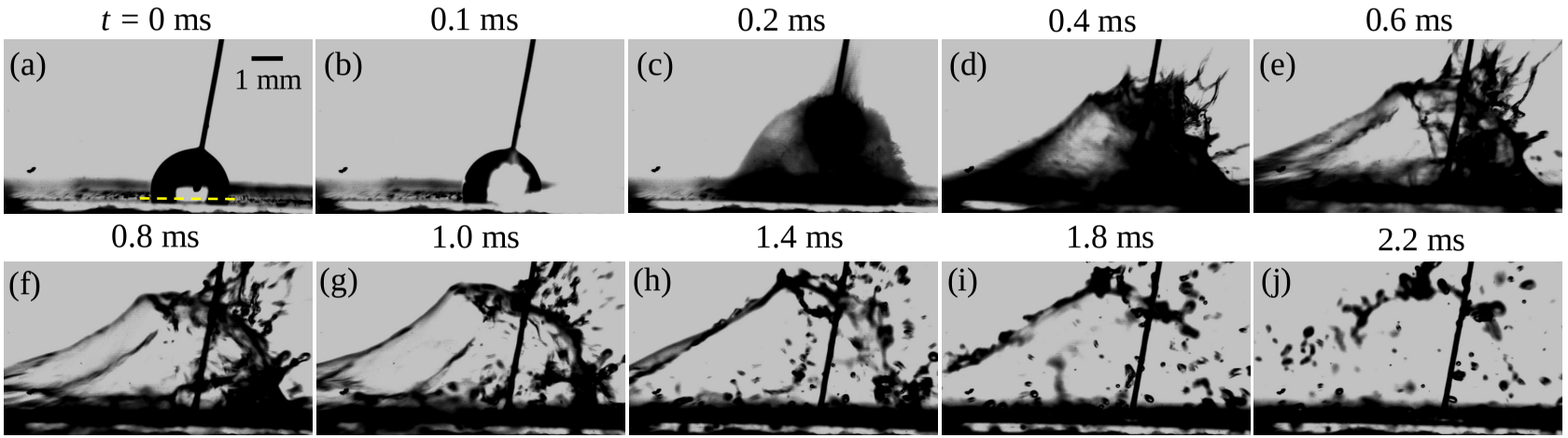


Figure 5.13: The snapshots show the spatiotemporal evolution of a liquid drop of high electrical conductivity (1 M) and low viscosity ($\eta = 0.886$ mPa s) subjected to an electric field discharge. The other experimental parameters are, $\psi = 1200$ V, $\Psi = 60$ kV/cm, and $\phi_0 = 5$ µL. The yellow broken line on image (a) shows the position of the datum. The frames are captured at a rate of 10000 frames per second.

TH-2590_156103041

The plots 5.12(a) and 5.12(c) suggest that in the post-discharge phase, the crown grows in all the three radial (r), vertical (z), and azimuthal directions (considering the liquid sheet as an annular cylinder, the angular direction is termed as azimuthal, θ). The contours in Figure 5.12(c) distinctly exhibit the motion of TPCL for the highly viscous liquid sheet. The TPCL is forced to move away from the centre of the droplet in the expansion phase, whereas it retracts itself back to the centre in the sealing phase under the effect of surface tension force. Interestingly, this kind of distinct contact line motion is absent in less viscous liquid sheet, as shown by the contour in Figure 5.12(a). The various stages of crown dynamics can further be deciphered by the distinct change of slope in the trajectory of neck radius, r_c in Figures 5.12(b,d). For example, the maximum value of the necking regime indicates the end of the expansion stage at 1.5 ms for the less viscous case. Also, for the high viscosity droplet, it is not possible to measure the neck-radius beyond 1.7 ms as the neck merges with the rim. However, it has a substantially larger time scale for the sealing and collapsing phase (approximately 3 ms) in comparison to the expansion phase.

5.3.5 Bursting regime

Apart from the crown formation and jetting, the liquid droplets can also *burst* into numerous smaller ones under the influence of an intense electrical discharge. Notably, a droplet with higher electrical conductivity ($C_s \geq 0.5$ M) can promote such catastrophic bursting mode under a high field intensity discharge. Importantly, similar fragmentation of a droplet has previously been observed only for high-intensity pulsed laser or x-ray exposures [142, 145, 146].

Figure 5.13 shows the spatiotemporal evolution of the droplet during a discharge mediated bursting. The discharge is confined within a 5 μL droplet of 1 M KCl solution (solution 5, Table 5.2) by applying a field of intensity, $\Psi = 60$ kV/cm, having a specific discharge energy, $E_d \approx 7.60 \times 10^5$ mJ/kg. Figures 5.13(a) and 5.13(b) show that in a timespan of $t < 1$ ms the discharge is translated into rapidly expanding cavitation bubbles, which in turn cause the bursting of the droplet, as shown in Figure 5.13(c). The bursting is indicated by the production of a fine mist along with unstable liquid sheet(s), which eventually ejects an array of minuscule secondary droplets. The liquid sheet is also found to accelerate radially outward with an expansion velocity of approximately 20 m/s along with the formation of

TH-2590_156103041

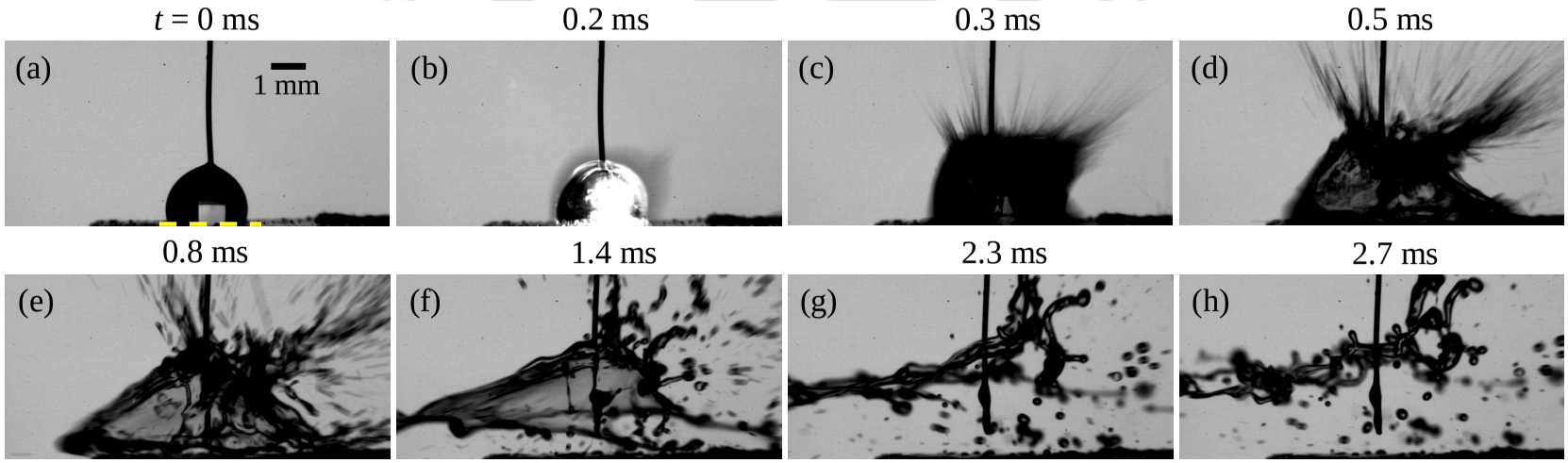


Figure 5.14: The snapshots show the spatiotemporal evolution of a liquid drop of moderate viscosity (solution 6, Table 5.2) and low electrical conductivity (0.1 M) subjected to an electric field discharge. The other experimental parameters are, $\psi = 800$ V, $\Psi = 16$ kV/cm, and $\phi_0 = 5$ µL. The yellow broken line on image (a) shows the position of the datum. The frames are captured at a rate of 10000 frames per second.

TH-2590_156103041

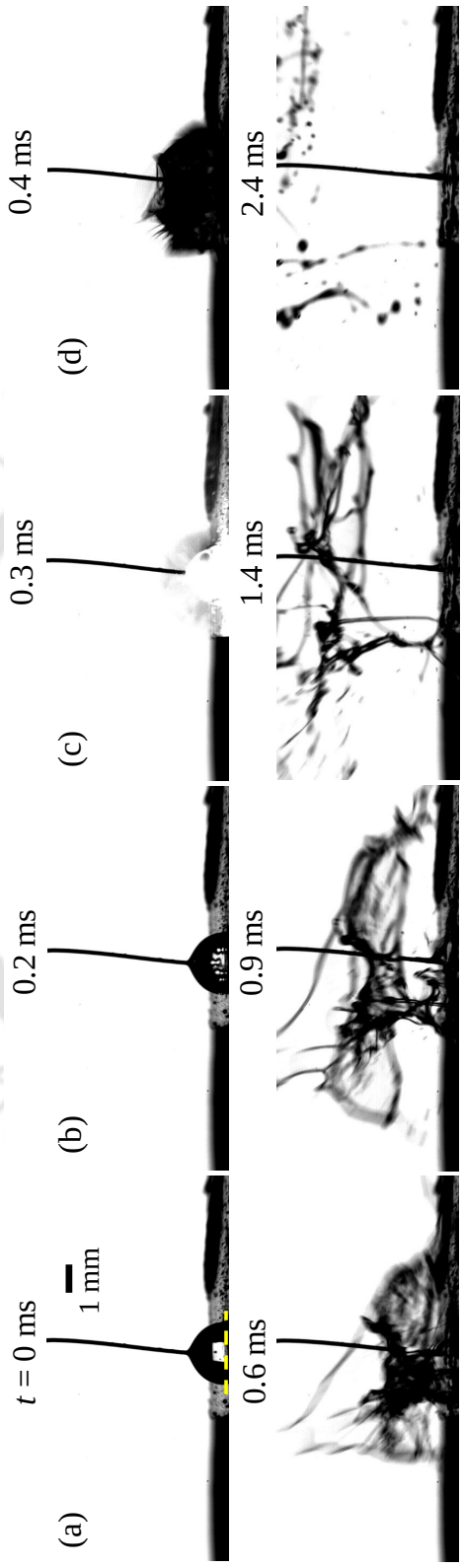


Figure 5.15: The snapshots show the spatiotemporal evolution of a liquid drop of high viscosity (solution 9, Table 5.2) and low electrical conductivity (0.1 M) subjected to an electric field discharge. The other experiment parameters are, $\psi = 500$ V, $\Psi = 18.9$ kV/cm, and $\phi_0 = 5$ µL. The yellow broken line on image (a) shows the position of the datum. The frames are captured at a rate of 10000 frames per second.

TH-2590_156103041

thin ligaments of fluid attached to a growing rim, as shown in Figures 5.13(d) and 5.13(e). Figure 5.13(f) shows that the thin liquid sheet and fluid ligaments eventually rupture and eject secondary droplets of size ranging from 0.1 mm to 0.5 mm. After formation, the secondary droplets are ejected away radially at an average speed of approximately 4 m/s. The average kinetic energy of the bursting ejecta sheet is found to be approximately 1 mJ for this less viscous droplet of mass, 5.21×10^{-6} kg, leading to the efficiency of approximately 27.5%.

Figure 5.14 shows the bursting dynamics of a moderately viscous liquid droplet (solution 6, Table 5.2) at an applied field intensity of, $\Psi = 16$ kV/cm. The initial dynamics of discharge generation and subsequent unstable sheet formation for the viscous droplets are analogous to the previously discussed less viscous (DI-water) case in Figure 5.13. Briefly, for the moderately viscous case in Figure 5.14, the liquid sheet moves radially outward at an (maximum) expansion velocity of approximately 10 m/s when the $E_d \approx 3.01 \times 10^5$ mJ/kg. Notably, the liquid spikes generated along the growing rim of the liquid sheet are more prominent in this case than in the less-viscous situation. With the progress in time, the liquid droplets are ejected in the form of fine sprays from the sheet, while the liquid rim becomes much thicker, as shown in Figures 5.14(b)-5.14(f). Importantly, a larger viscous resistance also increases the lifetime of the unstable liquid sheet to 1.5 ms.

Subsequently, the unstable sheet collapses into the liquid rim [see Figures 5.14(g) and 5.14(h)], which finally disintegrates into an array of secondary droplets undergoing a Plateau-Rayleigh instability, as seen for the less-viscous droplet. Considering the expansion velocity of $\sim$ 10 m/s, a discharge efficiency approximately 18% is found in this case, while observing a complete disintegration of the parent droplet into secondary droplets with a size range of approximately 0.05 mm-0.5 mm. Figure 5.15 shows the bursting dynamics of a high viscosity liquid droplet (solution 9, Table 5.2) at an applied field intensity of, $\Psi = 18.9$ kV/cm, having $E_d \approx 1.09 \times 10^5$ mJ/kg. While the initial dynamics of sheet formation and breakup remain similar to the previous two cases (Figures 5.13 and 5.14), the fluid ligaments are found to be prominent for a much longer period until 2.4 ms. The viscous resistance kinetically stabilizes the liquid sheet and the rim to delay the growth of large-scale perturbations and subsequent disintegration into the secondary droplets. Further, Figures 5.13 - 5.15 suggest that the diameter of the fluid ligaments reduces with the increase in the viscosity of the liquid droplet. The discharge efficiency for the present scenario is found to be approximately 30% by considering the maximum expansion velocity

TH-2590_156103041

of the liquid sheet, approximately, 9 m/s and ignoring any early mass loss.

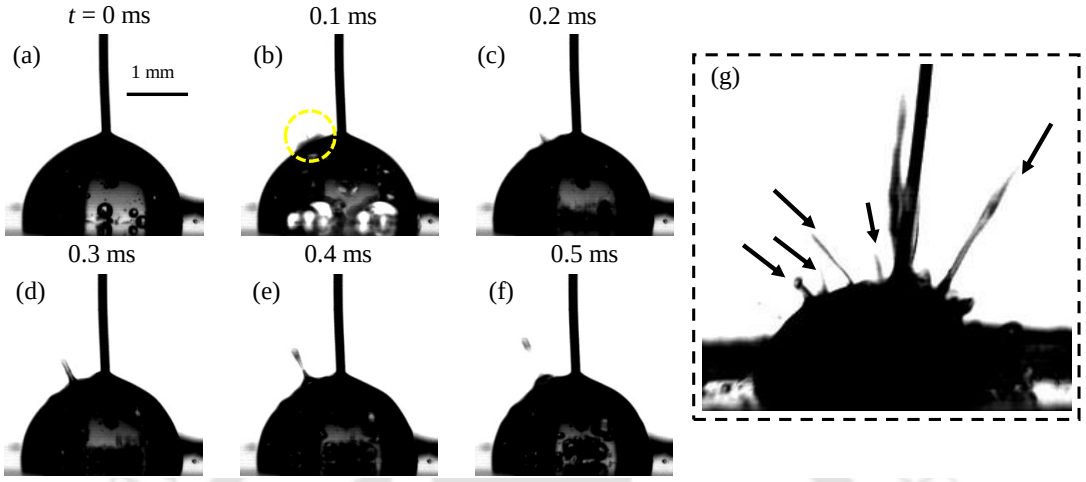


Figure 5.16: (a)-(f) Dynamics of microjetting for a DI-water droplet (solution 3, Table 5.2). The yellow broken circle in image (b) indicates the incipience of microjet formation. (g) Dynamics of microjetting for a droplet of glycerol (50%)-water (50%) mixture (solution 6, Table 5.2).

5.3.6 Dynamics of microjetting

Apart from the jetting, crowning, and bursting of droplets, the formation of *microjets* is also seen in the post-discharge scenario, as shown in Figure 5.16. Previously, Thoroddsen *et al.* [43] have reported the formation of microjets in the context of laser-droplet interaction, when the focal point of the laser pulse has been well inside the liquid phase. Figure 5.16(b) shows that confining an electric discharge in a droplet can also engender such liquid jets from the top of the droplet, as marked by the yellow broken circle. Such jets are expected to form as a result of the interaction of the pre-existing thermal bubbles [see Figure 5.16(a)] with the APWs immediately after discharge. This proposed mechanism can be backed by several experimental observations from the present study as well as drawing an analogy with the microjets reported by Thoroddsen *et al.* [43]. Firstly, these fine jets often emerge from the apex area of the liquid-air interface, where the probability of finding smaller bubbles is maximum [see Figures 5.16(a) and 5.16(b)]. These pre-existing bubbles act as nuclei of microjet generation after absorbing the energy of the high-pressure waves released during the discharge [refer to Figure 5.16(b)]. As such, the underlying mechanism of these microjets generation is markedly different from those regular jets

TH-2590_156103041

discussed in Section 5.3.3, where the latter is produced by the pressure waves from the collapse of cavitation bubbles. Interestingly, these microjets disappear during discharge in a fresh droplet or if the bubbles are removed with a syringe prior to discharge [43]. Although, the development of one single microjet is shown in Figures 5.16(a)-5.16(f), they can appear in large numbers, as shown in Figure 5.16(g), from a more viscous droplet (solution 6 Table 5.2). The experiments uncover that the velocity of such microjets ranges from 5 m/s to 30 m/s, where the velocities of the viscous jets are comparatively higher. Further, these microjets can generate droplets as small as 10 μm. In a way, the APW mediated microjets contribute towards the effective atomization of the droplets during dielectric discharge. A detailed characterization of these microjets with the help of experiments is kept as future scope of research.

5.3.7 Characterization of hydrodynamics

5.3.7.1 Effects of electric field intensity and salt concentration

Figure 5.17 shows the possibility of different electric discharge induced flow morphologies, namely, jetting *(square-red)*, crown formation *(circle-blue+cyan)*, bursting *(triangle-olive)*, and *jetting + bursting (diamond-purple)*, with the variation in the electric field intensity, expressed in terms of the electric bond number (Bo_E) and the molar concentration of KCl in the solutions (C_s). Here, jetting+bursting is the mixed regime, where both the phenomena have been observed during discharge cycles. The plot suggests that for $Bo_E > 0.7$, the droplet undergoes bursting at all concentrations, as indicated by the blue dashed line. Further, the propensity of droplet bursting at lower electric fields, $Bo_E < 0.7$, increases with the salt concentration beyond 0.1 M. In contrast, a lower salt concentration ($C_s < 0.1$ M) and field intensity $Bo_E < 0.35$) is seen to favour jetting phenomena. The regimes can be understood clearly from the right-hand side plot, which is the enlarged view of the dashed rectangular regime.

Further, in the intermediate field intensity, $0.35 < Bo_E < 0.7$, the *crown formation* regime can be seen at 0.1 M, 0.5 M, and 1.0 M salt loading. For 0.1 M concentration, the transition from crowning to bursting is marked by a blue-coloured-hatched rectangular zone, while the transition from jetting to crowning is marked by a white-coloured regime in the right-hand side plot. Importantly, the

TH-2590_156103041

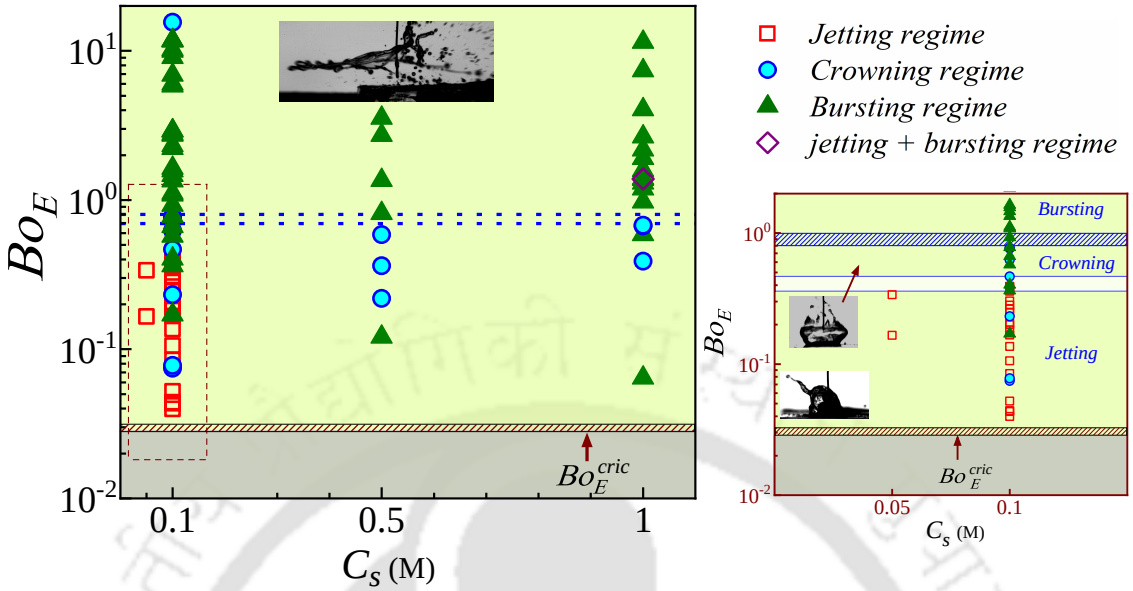


Figure 5.17: Different regimes of electric-discharge-induced droplet atomization, namely, jetting (square-red), crown formation (circle-blue+cyan), bursting (triangle-olive), and jetting + bursting (diamond-purple) with the variation in the electric field intensity, expressed in terms of the electric bond number (Bo_E) and the molar concentration of KCl in the droplet (C_s). The rectangular dashed region marked is shown in an enlarged view in the right-hand side plot. The approximate borders are indicated with broken lines and coloured/hatched regions.

plot also shows that for $C_s = 0.1$ M, all the flow morphologies can be obtained simply by tuning the electric field intensity, Ψ (or Bond number, Bo_E), while keeping other parameters constant. The plot also highlights that the drops with 0.1 M salt loading may exhibit all the flow morphologies with the variation in the electric field intensity (or Bo_E), whereas the droplets with more than 0.5 M salt are akin to bursting only. It is also observed that all the phenomena are absent below $Bo_E = 0.032$ ($\Psi \leq 3$ kV/cm), which ensures the necessity of critical electric field intensity (Ψ_{cric} or critical bond number, Bo_E^{cric}) to cause the dielectric breakdown of the PDMS layer and subsequent electric discharge. The shaded brown regime marks the boundary of Bo_E^{cric} for different experimental fluids, which has been obtained with the help of control experiments. Furthermore, for the experimental solution with salt concentration, $C_s = 0.01$ M (solution 1, Table 5.2), none of the discussed hydrodynamic features are observed within the range of electric potential studied herein. Instead, the droplet with the aforementioned conductivity is seen exhibiting general EWOD dynamics, which further illustrates the role of solution conductivity

TH-2590_156103041

in the dielectric-discharge-induced droplet deformation process.

5.3.7.2 Effect of the position of occurrence of electric discharge

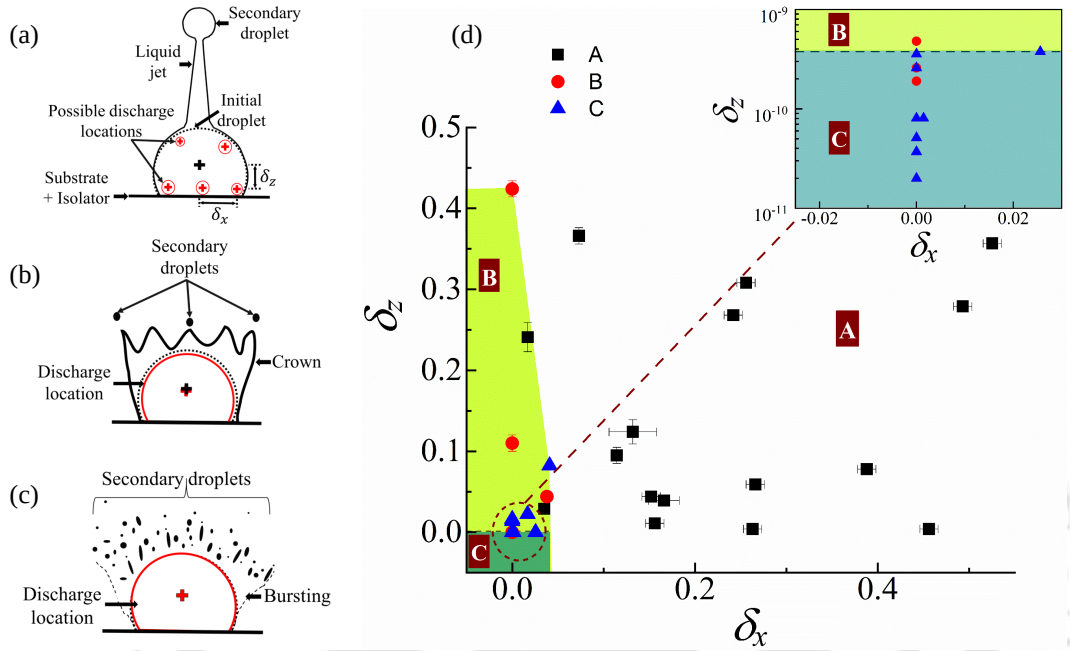


Figure 5.18: Schematics (a)-(c) show the different locations of electric field discharge observed (zone with a red circle with a "+" sign at the centre) with respect to the geometric centre of the droplet (zone with a black circle with a "+" sign at the centre) during the experiments. The dimensionless distances between these two points in the vertical and horizontal planes are denoted as δ_z, and δ_x, respectively. The plot (d) shows the occurrence of liquid jetting (A), crown formation (B), and bursting (C) in the (δ_x, δ_z) plane. The broken line between the regions B and C divides the two regimes. The error bars are due to the uncertainty in determining the centre for both the electric discharge and droplet. The red broken circle marks the area shown in the inset.

Apart from the electrical conductivity, viscosity, and field intensity, the position of occurrence of the electric discharge appears to be another critical parameter, directly influencing the formation of a liquid jet (A), liquid crown (B), or bursting (C) phenomena, as shown in Figure 5.18. For this purpose, initially, the best 30 experiments are selected in which the geometric center of the droplet and the center of the discharge are identified from the experimental snapshots, along x and z axes, with the help of the image-processing software ImageJ [329]. Thereafter, the normalization of the distances is done by the radius of the droplet prior to discharge (r_d).

TH-2590_156103041

Combining all these parameters into the dimensionless parameters in space (δ_x, δ_z), each of the performed experiments has been assigned to one of the three categories (A, B, or C), as shown in Figure 5.18. Figures 5.18(a)-5.18(c) schematically depict the probable positions of the electric field discharge observed (zone with a red circle with a '+' sign at the center) during the experiment with respect to the geometric center of the droplet (zone with a black circle with a '+' sign at the center). The normalized distances between these two points in the vertical and horizontal planes are denoted as δ_z and δ_x, respectively. The experimental results suggest that a superimposition of the electric field discharge center and the droplet's geometric center always results in the formation of the crown or bursting ejecta sheet. In contrast, the deviations in the discharge locations from the droplet's geometrical center lead to the jetting phenomenon. The probability of jetting is enhanced with the increase in the distance between the discharge and the droplet center in either direction, as shown in Figure 5.18(a), where the probable discharge locations are marked with a red circle. The aforementioned claim can be correlated with the multiple discharge hotspots along the cathode, as discussed previously in Sections 5.3.1 and 5.3.2. The region $\delta_x > 0.035$ is found to be the possible region of jetting dynamics, while for the region $0 < \delta_x \leq 0.035$, it is difficult to distinguish between the crown formation and droplet bursting, as shown by the inset in Figure 5.18(d).

5.3.8 Comparison with existing methods and target applications

In the current study, the sessile droplet exhibited the formation of liquid jets when exposed to a lower intensity discharge. Similar studies have been carried out in the recent past to engender liquid jet from a free surface initially at rest by creating overpressure at the jet base. In this regard, Fletcher and Palanker [132] report the formation of liquid jets created by electric discharge induced vapour bubble, which is then successfully used for incision of soft tissues. The study suggests that a jet of 30 μm diameter can reach a velocity of 90 m/s at an energy conversion efficiency of $\sim 10\%$, about an order of magnitude higher than the one proposed herein. Similarly, Avila *et al.* [330] have shown the formation of high-speed microjets mediated by the spark-induced cavitation bubble at an efficiency of approximately 2%-5%, much closer to the efficiency reported by us ($\sim$ 0.35%-2%). Further, Tan *et al.* [331] could

TH-2590_156103041

Table 5.3: Comparison between the current study and recent experimental studies for liquid-jet generation.

Study.	Method of jet generation	v_j (m/s)	E_k (μJ)
Tomita [332]	Ultrasound	0.48 - 2.2	$\sim$ 0.02 - 0.08
Avila *et al.* [330]	Spark energy	up to 400	up to 15
Delrot *et al.* [338]	Laser pulse	4 - 7	NA
Onuki *et al.* [339]	Impulsive force	2 - 15	NA
Current study	Dielectric discharge energy	1.5 - 4.8	1.35 - 11

form liquid jets by accelerated Rayleigh waves, while Tomita [332] has shown the characteristics of the jetting using an ultrasound source of intensity, $I = 220$ W/cm^2 with an exposure time of 3 - 5 ms, at an efficiency of $< 1\%$. Notably, the velocity of the liquid jets reported by the latter study (0.48-2.2 m/s) matches closely to that of this study [see Table 5.3]. Apart from the above examples, several other studies have reported the dynamics of the liquid jets emanating from a free surface by using pulsed laser [136, 137], shock waves [291, 310] or blast waves [333]. In Table 5.3, different parameters of the jetting events of this study are compared with that of a few recent literatures, wherein the reported jet velocity or the kinetic energy is much closer to that of the former. Notably, the creation of overpressure beneath the free surface enables liquid jetting in the absence of nozzles or any liquid reservoirs as discussed above, which is in stark contrast to the jetting observed in electrospinning, electrospraying, or gas dynamic virtual nozzles (GDVN) [4, 12, 13, 334–337]. Also, the latter methods [4, 12, 13, 334–337] have been used extensively for continuous production of secondary droplets from an emerging liquid jet, unlike the proposed method.

The prior art also reports that the dielectric breakdown of a discrete liquid volume can lead to interesting hydrodynamic features such as jet, counter jet, crown, ejecta sheet, or plumes, to name a few [5, 43, 136, 145, 340]. In this regard, Obreschkow *et al.* [136] have reported that the confinement of an electric spark induced cavitation bubble inside a centimetric droplet can produce jets, counter jet, and splash, which is similar to that of this study. The study shows that the microjet speed can go beyond 50 m/s with an efficiency of 30% - 50%. A disruption efficiency of $> 30\%$ for the bursting mode has also been discussed for the present study on a similar note. Further, Thoroddsen *et al.* [43] have studied the formation of spray

TH-2590_156103041

and microjets from sessile liquid droplets mediated by intense 30 mJ/pulse laser energy for approximately 7 ns. They report that the tip of the disruption sheet can acquire a speed of approximately 1400 m/s leading to the formation of *laser crown* at an efficiency of approximately 20%, again similar to that of the present study. Furthermore, Avila and Ohl [145] have reported the fragmentation of acoustically levitated water droplets exposed to a single laser-induced cavitation bubble. The dynamics of the *rapid atomization* and the *unstable sheet formation* regimes mentioned in the concerned study [145] have a striking similarity with the bursting mode discussed in this study. The corresponding energy conversion efficiency (laser energy $\rightarrow$ bubble energy) is approximately 0.35% for the rapid atomization mode and approximately 7% for the *coarse fragmentation regime*, as shown in the study [145]. Again, the *stable sheet fragmentation* mode of Avila and Ohl [145] has similar dynamics to that of the crown-formation regime in this study, which is reported to have an energy efficiency of nearly 1%-3%, a value much closer to this study. Interestingly, Vogel *et al.* [340] have previously reported the maximum energy conversion efficiency of 10% for nanosecond laser pulses. Furthermore, Klein *et al.* have observed drop deformation and fragmentation by using a plasma propulsion tool to accelerate the flow in a levitated liquid droplet [5, 341], a set-up specifically designed for EUV nanolithography applications. In another unique study, James *et al.* [48] have reported the formation of a polydisperse spray from a sessile droplet of volume 100 μL due to its exposure to substrate vibration near resonance.

Thus, from the aforementioned discussion, it is apparent that the efficiencies of the various processes reported for the present method are rather competitive, if not similar or superior to the processes available so far. However, such comparative studies are to be explored under the perspective of the differences in the underlying mechanisms involved with the methodologies associated with light, sound, electric field, or others.

5.4 Summary

In this chapter, bursting, crown or jet formation, and atomization phenomena are observed when electric-discharge is confined at the base of a sessile droplet. Emulating an EWOD set-up, a hemispherical droplet is placed on a cathode-isolator platform while a pointed anode from the top stimulates the discharge inside the drop.

TH-2590_156103041

Beyond a critical intensity of the applied electric field, the dielectric layer under the droplet suffers breakdown to generate the discharge. Within a few milliseconds, the electric-discharge stimulates crown or jet formation or bursting of the droplet. A lower (higher) salt loading in the droplet at lower (higher) field intensity leads to the jetting (bursting). The crown formation happens only for an intermediate window of salt loadings and electric field intensities. The energy conversion efficiency is found to be approximately 25% - 30% for droplet bursting, while the same is approximately 1% for jet or crown formation. The experiments and simulations uncover that the location of pointed-electrode in the droplet and the separation distance of electrodes can be among the crucial factors in varying the discharge location, leading to the aforementioned flow morphologies. Further, the interplay between surface tension, viscous, and electric field forces inside the droplet plays a crucial role in engendering the flow patterns. The set-up transiently shows up the formation of end-pinching of jets, microjets, high-aspect-ratio liquid threads, upward-moving jet, liquid spikes riding on a crown-rim, and the capillary breakup of jets. Such electric discharge mediated droplet disintegration resembles closely the previously reported laser or plasma induced phenomena. In the near future, alongside exploring the complex but interesting fundamental aspects of such discharge mediated EHD of drops, the possibility of applications of the same in inkjet printing [19], electro-spraying [219], droplet miniaturization, tissue ablation [299], electroporation [300] or biomedical devices [132] can also be explored.

TH-2590_156103041

Chapter 6

Interfacial dynamics of viscous droplets impacting a superhydrophobic candle soot surface: Overview and comparison

"Those who dedicate their actions to God, abandoning all attachment, remain untouched by sin, just as a lotus leaf is untouched by water"

- Bhagavad Gita, *Chapter: 5, Verse: 10*

6.1 Introduction

The extremely water repelling behavior of the lotus leaves (Nelumbo nucifera) [342], elephant ear leaves (Colocasia affinis) [343], or cicada wings [344] have been intriguing the researchers for a long time due to their inherent abilities such as self-cleaning [344–346], de-icing, anti-fogging [347], antimicrobial activity [348, 349], and anti-reflectivity [350]. Fundamentally, the embedded micro-/nano-structures in these natural surfaces favor the formation of a thin air cushion between the liquid volume and the surface, thereby maintaining a critical contact, known as *Cassie-Baxter*

The contents in this chapter is under review in *Langmuir*.

TH-2590_156103041

state (*CB* state henceforth), between the two [14, 351, 352]. However, depending upon the spatial configurations of the structures, the initial conditions, and the thermophysical properties of the liquid volume, the liquid-vapor interface may penetrate the air-gap between the structures, thereby marking a transition to a new wetting state, known as *Wenzel* (*W* state henceforth) configuration [15, 351, 352]. This fundamental knowledge has further been extended to engineer numerous synthetic superhydrophobic surfaces (*SHPs*) targeting specific applications which include, but not limited to, self-cleaning [344, 346], anti-icing [353–355], anti-sticking [356], marine fouling [357], drag reduction [358], oil-water separation [359], fog-harvesting [20, 360], sensory devices [361], and green engineering [362, 363].

Notably, there exist several standard methods based on photolithography, spray coating by non-wetting chemicals, template methods, wax solidification, polymerization, sublimation, electrospinning, sol-gel processing, electrochemical methods, hydrothermal synthesis, layer-by-layer deposition, and one-pot reactions, etc., to impart extreme water-repelling properties to an otherwise regular flat surface [364–366]. Although each of the above methods has several advantages such as uniform coating, durability, and robustness, they also exhibit a certain number of limitations such as the requirement of sophisticated instruments, multistep procedures, applicability to specific materials, etc. [366]. Interestingly, a recent analytical report published by Mordor intelligence in 2018 has projected an increase in the demand for superhydrophobic coatings at the rate of 25.6% of the compound annual growth rate (CAGR) in the period 2019-2024 [367]. Also, for regular outdoor/household activities, one generally prefers low-cost and extremely durable superhydrophobic surfaces. The latter two sentences, when considered together, hint towards the necessity of developing some cost-effective and rapid fabrication techniques for producing robust and durable superhydrophobic surfaces.

The facile fabrication methods, such as flame deposition of carbon soot nanoparticles (CSNPs), resulting from the incomplete combustion in a burning paraffin candle [368–374] or lamp wick soaked in rapeseed oil [375], have been found effective in converting a smooth surface to a superhydrophobic surface. The soot particles agglomerate to form a fractal network on the top of the glass slide upon deposition, thereby imparting the roughness favoring superhydrophobicity [368, 370, 375–378]. However, the fractal networks are fragile in nature in these bare soot-coated SHPs due to weak inter-particle interactions and thus suffer from durability and robustness issues in self-cleaning applications [368, 370, 375–378]. The aforementioned limita-

TH-2590_156103041

tions are tackled by using additional coatings [368], calcination processes [376], or binder layers [377, 378]. For example, Deng *et al.* [368] coated the soot particles with a silica shell by chemical vapor deposition (CVD) of tetraethoxysilane (TES) in the presence of aqueous ammonia solution and subsequently removing the CSNPs via calcination at 600°C, before the deposition of semi-fluorinated silane atop the hollow silica shells using CVD. Similarly, Liu *et al.* [376] prepared a transparent, robust, and thermally stable PDMS-derived soot-coated SHPs by exposing it to calcination in a muffle furnace. While the additional processes increase the durability of the SHPs and favor the target applications, they also add complexity and increase the overall cost and production time [refer to Table 6.1]. Most recently, Iqbal *et al.* [379] have introduced an easy, cost-effective, facile technique of carbon-soot coated superhydrophobic surface preparation [379]. Instead of using the soot as a template for surface roughness, authors have brilliantly used bare soot particles after embedding them in a PDMS layer to achieve desired robustness, stability, and superhydrophobicity [379]. However, only the physicochemical [379], and static wetting characteristics (in terms of the equilibrium contact angle, θ_{eq}) have been analyzed in the concerned study [379]. The aforementioned discussions highlight two important aspects in the case of low-cost soot-based SHPs: firstly, although there exists a huge number of soot-based non-wetting surfaces, the majority of them need a complex fabrication technique to achieve durability and robustness. Secondly, due to the latter fact, bare soot coated SHPs have remained poorly understood regarding the dynamic wetting behavior, unlike the multifunctional/structured SHPs [368–374], thereby limiting their use in self-cleaning applications. In this chapter, an honest attempt has been made to bridge the gap mentioned above by exploring the dynamic wetting behavior of a bare soot-coated surface. To complete the task at hand, the non-wetting surface prepared by Iqbal *et al.* [379] has been chosen from the lot, as it fits strongly to the proposed criteria of a low-cost and durable SHPs.

Notably, for a long time *liquid drop impact* method is considered as an effective method to elucidate the dynamic wetting characteristics of a superhydrophobic surface [37, 114, 381, 382]. With the use of appropriate experimental conditions, the aforesaid method can unravel several crucial aspects of the SHPs, including impalement resistance [37, 114], *CB-to-W* state transition [352], dynamic contact angle hysteresis (*CAH*) [383], *zipping effect* [384], and slip length [385], to name a few. The aforementioned critical insights obtained from droplet impact studies further help in design optimization and operation of a host of cutting-edge applications

TH-2590_156103041

Table 6.1: Comparison of different candle soot-based superhydrophobic surfaces in terms of the fabrication method, fabrication time, static equilibrium contact angle (θ_{eq}), and roll-off angle (θ_{roll}).

Study	Fabrication time	Fabrication method	θ_{eq}	θ_{roll}
Deng *et al.* [368]	> 1 hour	1) CVD of TES catalyzed by ammonia. 2) Calcination. 3) CVD coating of semifluorinated silane.	165° ± 1°	~ 1°
Deng *et al.* [369]			165° ± 1°	~ 1°
Zhao *et al.* [370]			161° ± 1°	~ 1°
Guo *et al.* [371]			>150°	<10°
Lin *et al.* [372]			165° ± 1°	~ 1°
de Goede *et al.* [373]			165° ± 1°	~ 1°
Yu *et al.* [374]			165° ± 1°	~ 1°
Liu *et al.* [376]	> 1 hour	1) PDMS layer coating. 2) Candle soot deposition. 3) Heat treatment in muffle furnace.	~ 163°	<1°
Seo *et al.* [377]	> 1 min	Paraffin wax-fixed candle soot (PFCS) coating.	~ 162°	~1°-2°
Qahtan *et al.* [380]	>10 min	Spray coating with candle soot dispersion.	163° ± 2°	< 2°
Iqbal *et al.* [379]	~5 min	1) Spin-coating of PDMS solution. 2) Flame deposition of candle soot. 3) Removal of loose particles with high-speed water jet.	160° ± 1°	< 2°
CSNPs coated SHPs				

TH-2590_156103041

such as ink-jet printing [19, 386], spray painting, and spin-coating [38, 387], DNA microarray deposition [388, 389], pesticides deposition [390, 391], bloodstain pattern analysis [392, 393], and surfactant selection [394], to name a few. In this regard, extensive research has been done on the impaction dynamics of liquid droplets on different superhydrophobic surfaces by experimental [369, 383, 395–407], numerical [408, 409], and analytical [38, 405, 410] methods. Briefly, a liquid droplet with an initial diameter, D_0 (or radius, R_0) starts spreading immediately after impacting a non-wettable solid surface at an impact velocity, V_0, thereby redistributing its kinetic energy partly to interfacial energy and, subsequently, retracts itself back after reaching a maximum extent (r_{max}) [38, 369, 383, 395–410]. A plethora of regimes can be observed during the retraction phase, including *deposition*, *complete rebound*, *partial rebound*, *bubble entrapment*, *splashing*, or *sticking*, depending upon the impact parameters and thermophysical properties of the liquid droplets [38, 369, 383, 395–410]. Furthermore, depending upon the topography and roughness of the prepared SHPs, *CB-to-W* state transition can be observed in certain impact conditions, which, in turn, favors the transition between the aforementioned events of the retraction phase. The outcomes of these spreading and retraction phases can be expressed in terms of a few desirable parameters, namely, coefficient of restitution (ε), spreading factor (β), contact time (t_c), and secondary droplet size (d).

Herein, the impact dynamics of viscous liquid droplets on the CSNPs coated superhydrophobic surface is studied in a simple experimental set-up, as shown in Figure 6.1. The present study makes a humble attempt to elucidate two primary aspects through rigorous experimentation: (i) detailed appraisal of the impact dynamics of different liquids on the target surface in terms of key parameters and (ii) quantitative comparison of these dynamics with some existing and widely used superhydrophobic surface. These aforementioned objectives are taken care of by considering droplets with thermophysical properties spanning across a wide range [see Table 6.2] and a large set of impact velocity. The impact dynamics are evaluated by considering the variations in different spreading and retraction parameters ($\varepsilon, \beta, t_c, d$) with experimental conditions, expressed in terms of relevant non-dimensional numbers, namely, Weber (We), Reynolds (Re), and Ohnesorge (Oh) number. Here, the Weber number, We ($= \rho V_0^2 R_0/\gamma$), signifies the relative strength of the inertia force to the surface tension force, and the Reynolds number, Re ($= \rho V_0 R_0/\mu$), signifies the relative importance of the inertial force to the viscous force. Again, the effect of liquid viscos-

TH-2590_156103041

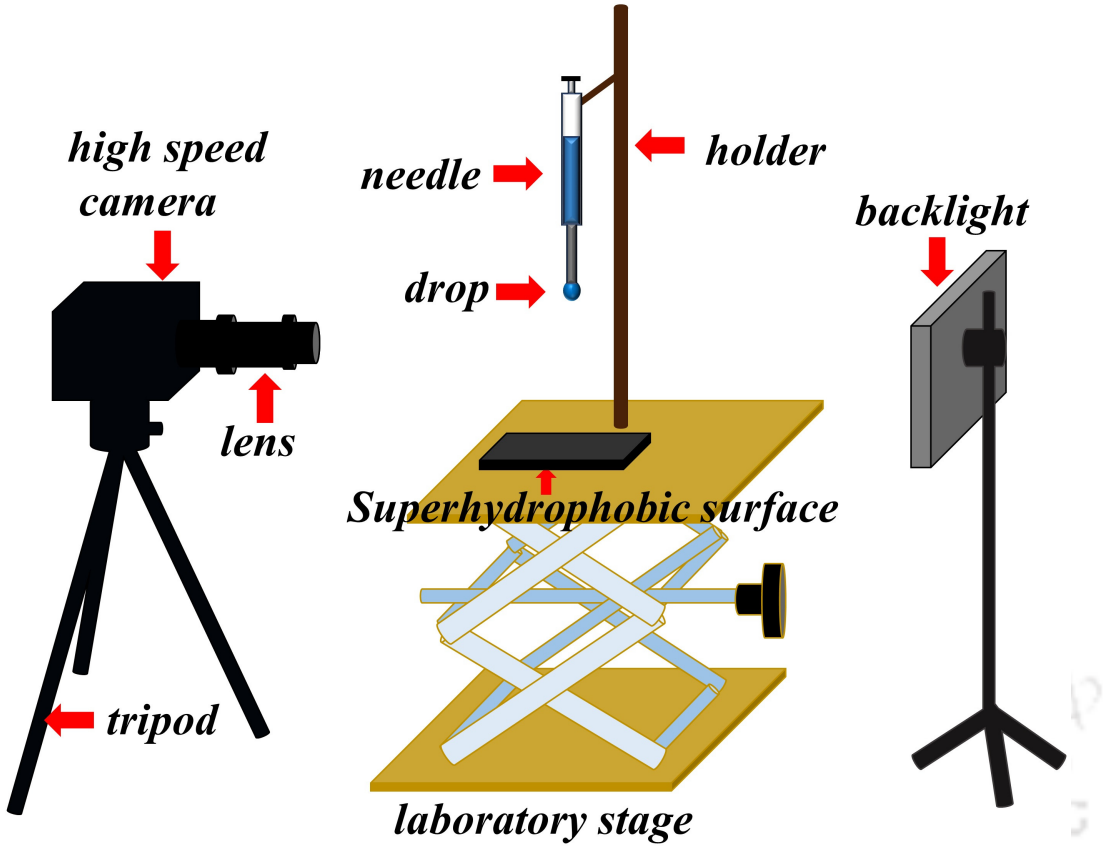


Figure 6.1: Schematic diagram of the experimental set-up.

ity is expressed in terms of the Ohnesorge number, Oh $(= \sqrt{We}/Re = \mu/\sqrt{\rho R_0 \gamma})$, which indicates the relative importance of the viscous force over the surface tension and inertial forces, with γ, μ, and ρ denoting surface tension, viscosity, and the density of the droplet, respectively. We finally complete the characterization by carrying out a quantitative comparison of a few crucial parameters $(\varepsilon, \beta, t_c)$ on the present CSNPs based surface to that of a few existing superhydrophobic surfaces [369, 383, 395–403] in similar experimental conditions. Interestingly, in the case of the impact of water droplets, the CSNPs coated surface does not exhibit the *partial pinning/partial rebound* regime, unlike the silica-coated SHPs [369–374], which is one of the most significant contributions of this study. Further, the proposed surface exhibit splashing for moderately viscous solutions (up to 8 fold higher viscosity than that of DI-water) at high impact velocity. These results and corresponding discussions highlight the strength of the present candle soot coated, cost-effective, superhydrophobic surfaces.

TH-2590_156103041

6.2 Experimental methods and materials

6.2.1 Experimental set-up

The experimental set-up is shown schematically in Figure 6.1, wherein liquid droplets engendering from a needle are allowed to hit freely on a superhydrophobic surface kept underneath, from different heights (h). The drops ($D_0 = 2.1 \pm 0.3$ mm) are generated at the free end of the needle (size 24G) of a syringe attached to a vertically movable arm. The distance, h, between the superhydrophobic surface and the needle is adjusted by displacing the movable arm of the vertical stand to explore a range of impact velocities ($V_0 = 0.19$-3.2 m/s) during the experiments. Notably, four different experimental fluids; namely, DI-water (DIW), 50% glycerol solution (Gly50), 65% glycerol solution (Gly65), and 80% glycerol solution (Gly80), have been used in this study to get a detailed appraisal of the effect of liquid viscosity on the impact dynamics. The complete details of the thermophysical properties are listed in Table 6.2, which also shows the corresponding experimental conditions in terms of the Weber number (We), Reynolds number (Re), and Ohnesorge Number (Oh). The broad range of the We ($\approx$ 0.64-221) and Re ($\approx$ 13.7-4187.5), as enlisted in Table 6.2, ensures a detailed wetting characterization of the concerned superhydrophobic surface in this study.

6.2.2 Superhydrophobic surface preparation

The specified CSNPs based superhydrophobic surfaces are prepared following the protocol similar to Iqbal *et al.* [379]. The glass micro-slides are initially cleaned following the protocol mentioned in Section A.2 of Appendix A. In the next step, the pre-polymer is prepared by mixing the PDMS [properties in Table 5.1 of Chapter 5] and the curing agent in the weight ratio of 10:1 and subsequently degassed using a vacuum pump. The resulting solution is then mixed with hexane (analytical grade, Sigma-Aldrich) in the ratio of 110:10:1 and degassed again to remove any residual bubble. Afterward, the solution is spin-casted on the glass slides with a spin coater (SPINNXG-P1, Apex India Pvt. Ltd.). A frequency of 1500 revolutions per minute and a duration of 20 s is chosen for operating the spin-coating instrument to obtain a thin film of PDMS on the glass slides [thickness of the film $\sim 3.5 \pm 1$ μm]. Subsequently, the coated glass slide is exposed to a candle flame (for approximately 3

TH-2590_156103041

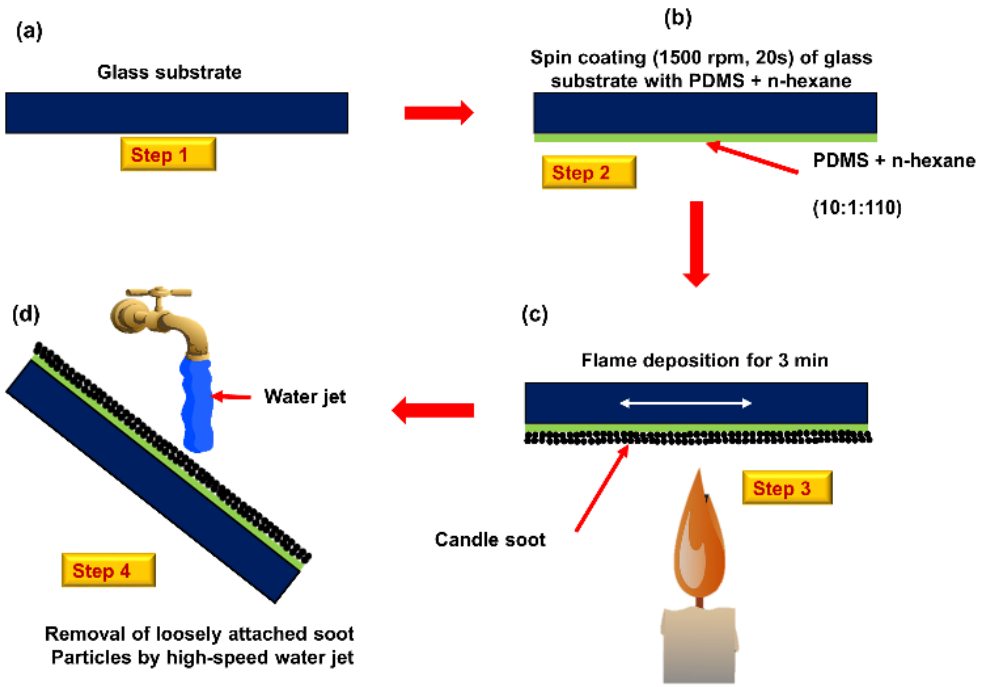


Figure 6.2: (a)-(d) Schematics of different steps involved in the surface preparation method by flame deposition of candle soot.

min) to deposit the CSNPs on the top of the PDMS thin film. While a fraction of the nanoparticles is embedded into the PDMS film, the loosely attached CSNPs are removed from the substrate with the help of a high-speed water jet once the flame deposition is over. The fresh CSNPs coated glass slides are then stored in vacuum desiccators if not used immediately. The different stages of the superhydrophobic surface preparation are shown schematically in Figures 6.2(a)-6.2(d).

It is to note that the hexane ratio, spin-coating rpm, and duration have been changed slightly from the reference study [379], keeping in mind the in-house fabrication capability. Despite the differences mentioned previously, a static contact angle of $\theta_{eq} > 155^{\circ}$ [measured using a contact angle goniometer (Apex India)] and a roll-off angle of $\theta_{roll} \sim 1 - 2^{\circ}$ for all the viscous liquids is observed on the surface at hand [See Table 6.2]. Furthermore, Figures 6.3(a) and 6.3(b) suggest that the resulting surface morphology, obtained from the field emission scanning electron micrograph (FESEM), of the soot coated surface at hand, resembles entirely even at the nanometer length scale with that of the Iqbal *et al.* [379]. Fundamentally, the carbon soot forms a uniform coating over the surface with aggregates visible on the nano-scale. The cohesive forces in the soot molecules tend to drive the carbon atoms

TH-2590_156103041

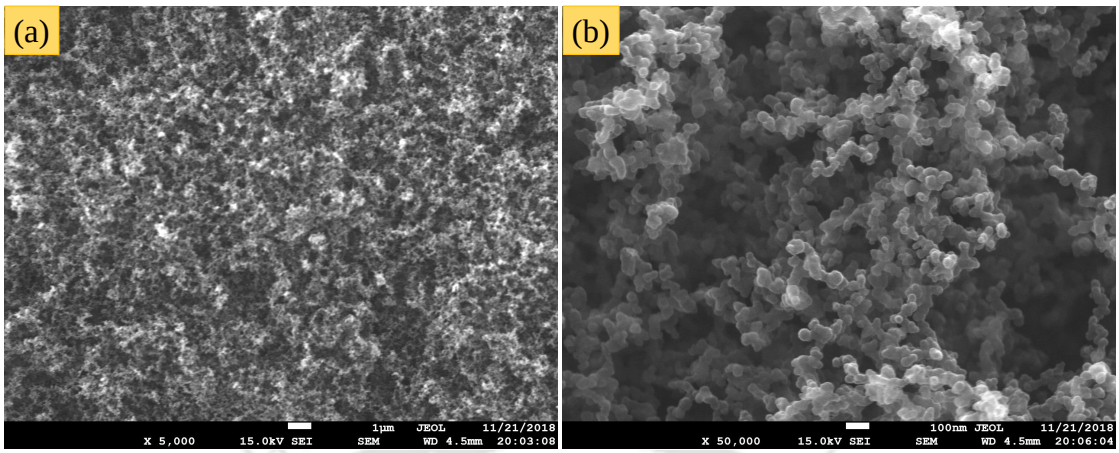


Figure 6.3: The surface morphology of the superhydrophobic surface prepared from candle soot nanoparticles as viewed in scanning electron microscopy (SEM) at (a) 5000 x and (b) 50000 x. The scale bars in (a) and (b) represent 1 μm and 100 nm, respectively. The morphology of the surface is similar to the Iqbal *et al.* [379], indicating a similar nanometric roughness.

Table 6.2: Thermophysical properties of the experimental fluids, equilibrium contact angle, and experimental conditions.

Soln.	DIW	Gly50	Gly65	Gly80
ρ (kg/m^3)	997.05	1128.7	1168.3	1207.9
η (mPa s)	0.890	6.88	18.25	66.90
γ (mN/m)	72.1	70.1	68.7	65.3
θ_{eq} (°)	160 ± 1	159.1 ± 1.1	158.4 ± 1.2	157 ± 1
V_0 (m/s)	0.2 - 3.2	0.2 - 3.2	0.2 - 3.06	1.88 - 3.31
We	0.64-169	1.0-175	0.74-178.42	70.27-221
Re	261.39-4187.48	43.36-558.53	0.74-178.42	36.5-65.07
Oh	0.003	0.023	0.062	0.23

to form agglomerates with free-hanging structures [see Figure 6.3(b)], which is similar to the fractal network of CSNPs reported in previous studies [368, 379]. Hence, it can be concluded that once the similar roughness level is assured through adequate deposition of the CSNPs on a target surface, the amount of hexane initially used for spin-coating of the PDMS film becomes unimportant. The other physicochemical characteristics of the surface can be read elsewhere [379].

TH-2590_156103041

6.2.3 Imaging technique

The impact dynamics are studied with the help of a high-speed videography technique, as discussed in Section 2.1 of the thesis. A framing rate of 12500 frames per second and a shutter speed of 80 μs are used during the experiments to obtain high-definition videos. The desired quantitative information is extracted from the captured images through a novel image processing technique described in Sections 2.1 and 2.2 of Chapter 2. Notably, during the size measurement of secondary droplets, a background subtraction process is performed in ImageJ to obtain a sharpened version of the original image, thus minimizing the size error. Afterward, the surface area (A) of the secondary droplet is measured to obtain the radius of the same, as $d = \sqrt{\frac{4A}{\pi}}$. The method has successfully measured droplet sizes within the pixel limit (greater than 25-40 μm pixel^{-1}). Also, the counting of the produced secondary droplets is performed by visual inspection in a side-view set-up (marginally tilted to reduce projection error).

6.3 Results and discussion

6.3.1 Overall temporal dynamics post impact

In this section, a summary of the characteristic events during droplet impact on the superhydrophobic surface has been presented. The interfacial dynamics of droplets of three specific experimental solutions (DIW, Gly65, and Gly80) on impacting the SHPs at different velocities (V_0) is shown in Figure 6.4. After touching the surface at $t = 0$ ms, the droplet spreads upto r_{max} in all the experimental conditions [see Figure 6.4(a)]. The shape of the droplet in the late spreading stage can be approximated by a puddle at small V_0 or a liquid sheet bounded by a thick rim at high V_0 [405]. Immediately, from its maximum spreading state, the droplet retracts itself back and consequently, either lifts itself up completely [complete rebound, Figure 6.4(a)] or partially [partial rebound, Figure 6.4(b), $V_0 = 2.50$ m/s] or even may stick to the surface [complete pinning, Figure 6.4(c)], depending upon the impact conditions. In the spreading regime (or *R1 regime*), r_{max} is determined by the balance between the competing energies namely, kinetic energy (E_k) and capillary energy (E_s) [406]. As a result, nearly similar spreading dynamics of the droplet have been observed in all the experimental conditions as shown in Figures 6.4(a)-

TH-2590_156103041

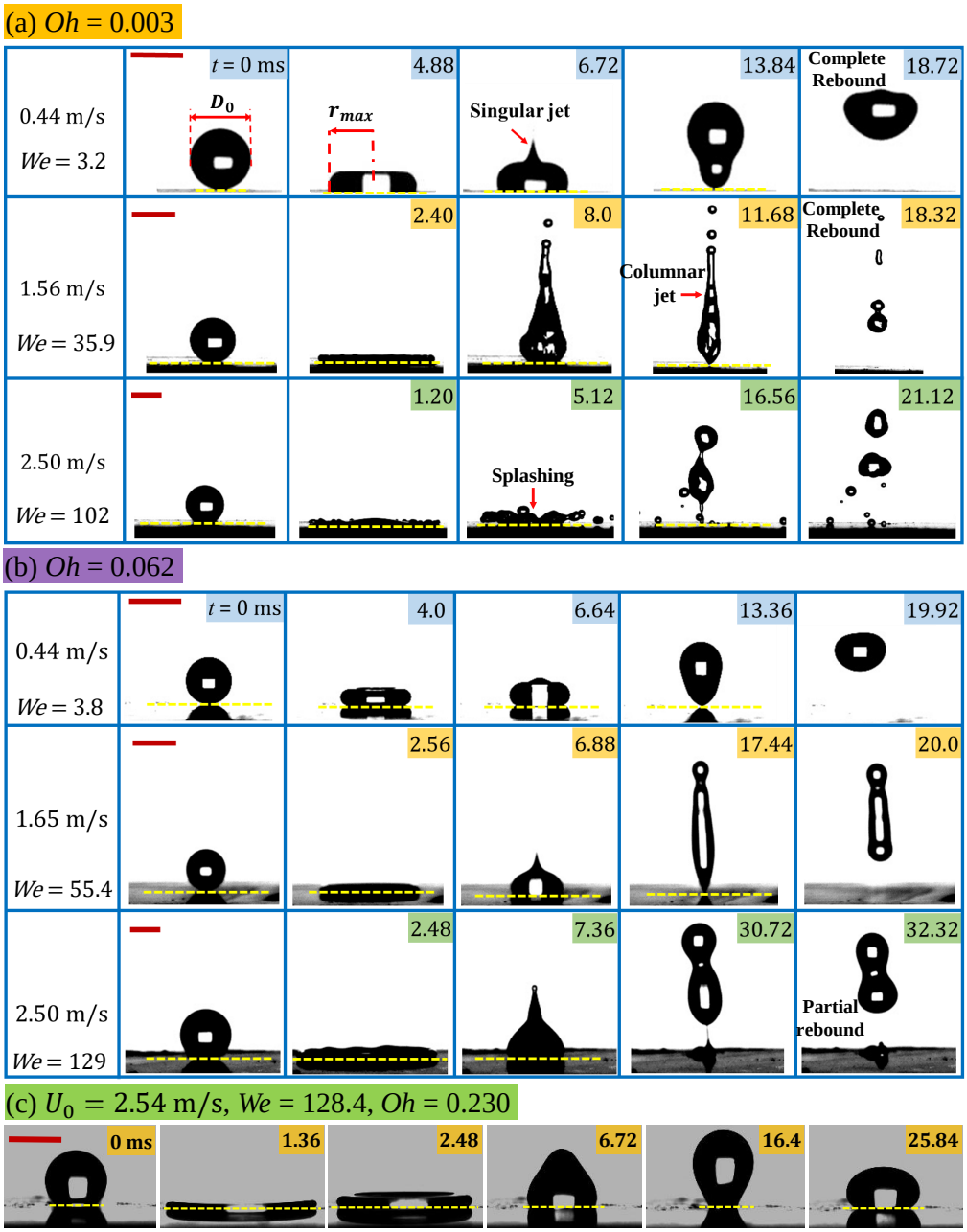


Figure 6.4: Spatiotemporal evolution of the interface of droplets of (a) DIW (Oh = 0.003) (b) Gly65 (Oh = 0.062), and (c) Gly80 (Oh = 0.23) solutions after impacting the superhydrophobic surface with different velocities mentioned in the first column. The second column shows the instants just before droplet impact, referred to as t = 0 ms, whereas the subsequent columns show the interface's evolution post-impact. The scale bars represent 1 mm in all the images.

TH-2590_156103041

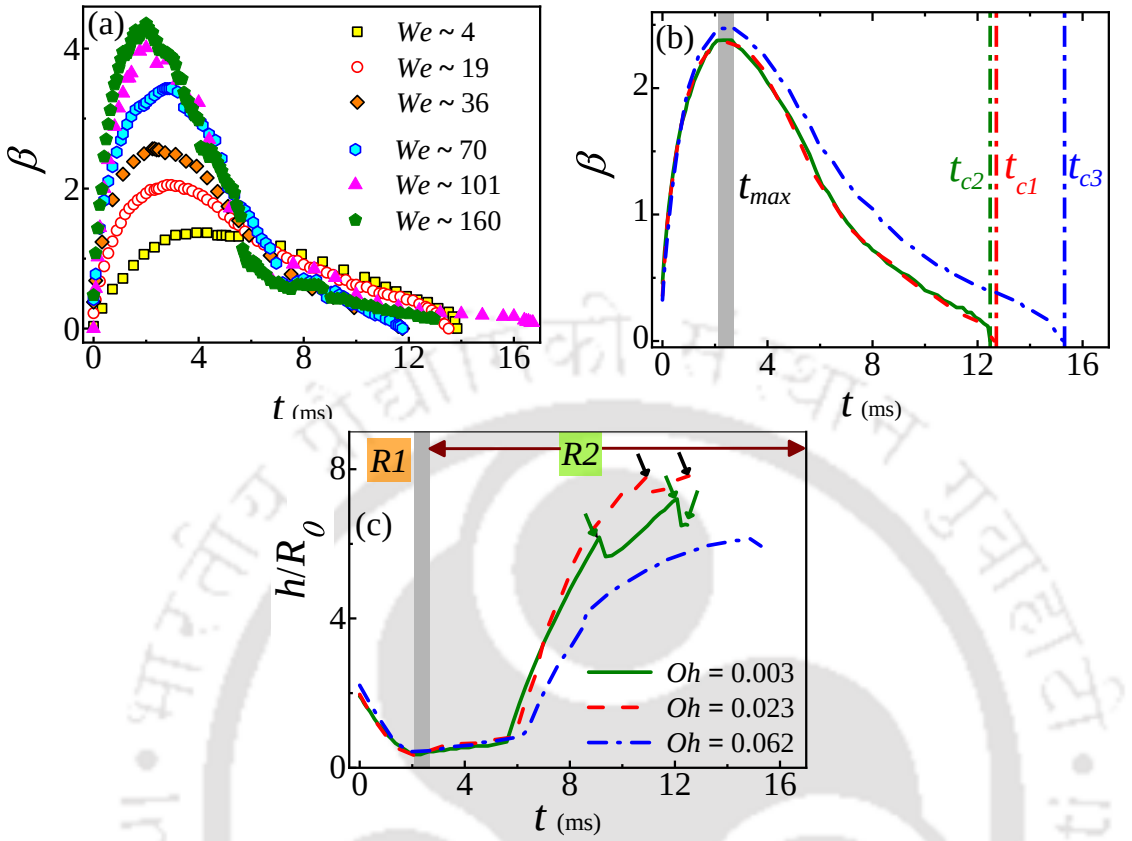


Figure 6.5: (a) Temporal evolution of the spreading ratio, $\beta = r(t)/R_0$, in the case of a water droplet ($Oh = 0.003$) impacting the surface at $We \approx 4$, 19, 36, 70, 101, and 160. (b) Spreading ratio, β, and (c) non-dimensional droplet height, h_d/R_0, as a function of time for different viscosity droplets ($Oh = 0.003$, 0.023, and 0.062) impacting the surface at $We \approx 36$. The colored rectangular regions in (b) and (c) mark the transition zones between the spreading and retraction regime for different events considered. The dash-dotted lines in (b) mark the contact time for different events. The arrows in (c) mark the point of pinch-off.

6.4(c), although the spreading extent, r_{max}, can vary with the liquid viscosity and the impact velocity as shown in Figures 6.5(a) and 6.5(b). Figure 6.5(a) shows the temporal evolution of the contact radius, $r(t)$, in terms of the instantaneous spreading factor, $\beta = r(t)/R_0$, for a droplet impacting the SHPs at the initial conditions: $We \in [4 - 160]$, $Re \in [12 - 5000]$, $Oh = 0.003$. It can be discerned that, as We increases, the droplet spreading extent $\beta_{max} = r_{max}/R_0)$, increases monotonically for a specific liquid [e.g., $\beta_{max}|_{(We=160)} = 4 \times \beta_{max}|_{(We=4)}$]. Figure 6.5(a) also shows that an increase in the impact We, substantially reduces the maximum spreading time, t_{max} [e.g., $t_{max}|_{(We=160)} = t_{max}|_{(We=4)}/3$]. Again, Figure 6.5(b) shows the vari-

TH-2590_156103041

ation of β in time for different droplet viscosity (Oh = 0.003, 0.023, and 0.062) and $We \approx 36$, which suggests that at a specific impact velocity, β increases with an increase in the liquid viscosity. Notably, the height of the liquid droplet, h_d, exhibits a decreasing trend with an increase in the liquid viscosity as shown in Figure 6.5(c), complementing the observations in the latter sentence.

On the other hand, in the retraction regime (or *R2 regime*), the capillary force

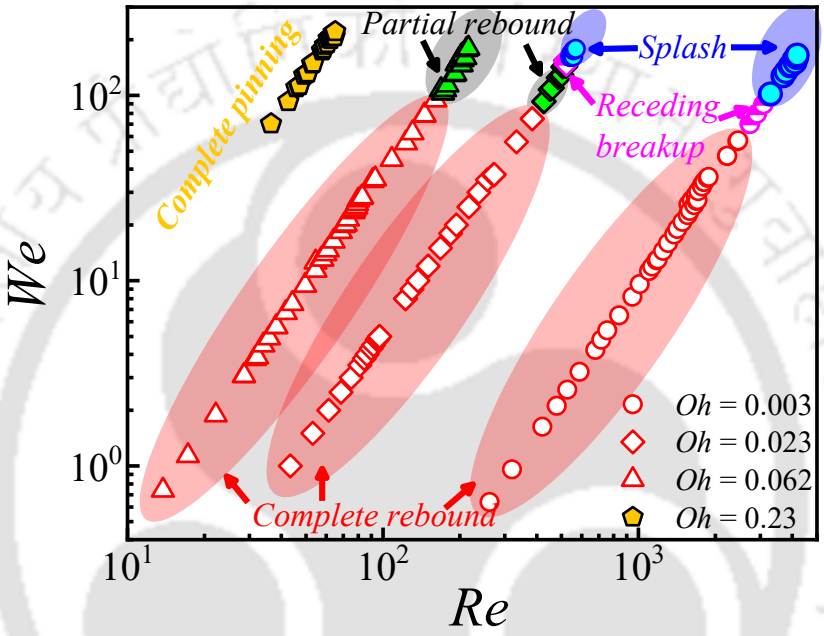


Figure 6.6: $We - Re$ map showing different regimes during the impact of viscous droplets on a superhydrophobic surface. The various experimental liquids are represented with different symbols, whereas the colored zones depict different hydrodynamic features, namely, complete rebound, partial rebound, receding breakup, splashing, and complete pinning.

imparts the motion to the contact line of the droplet, thereby enabling depinning of the latter from the micro-/nano-gaps between the heterogeneous structures of the surface. However, this dewetting event of the TPCL is also greatly influenced by the viscous dissipation (E_v) within the droplet, which, in turn, affects the hydrodynamics of the metastable phases, such as cavity formation, singular jet formation, columnar jet formation, splash, etc. For example, at low V_0 (= 0.44 m/s) and low η (Oh = 0.003), the formation of *singular jet* and subsequent, symmetric droplet rebound is observed [refer to Figure 6.4(a)]. In contrast, for high η (and V_0 = 0.44 m/s), the formation of singular jet is suppressed [refer to Figure 6.4(b)]. Similarly, for a low viscosity droplet, liquid *splashing* appears at V_0 = 2.5 m/s as shown in

TH-2590_156103041

Figure 6.4(a), which is completely suppressed at higher viscosity (for $Oh = 0.062$ and 0.23), while keeping other experimental conditions similar to the above.

Notably, the aforementioned plethora of transitions in hydrodynamic features during the retraction phase can be well described by a non-dimensional regime map of $We - Re$ as shown in Figure 6.6. Herein, the transition between different metastable phases with the We, for a specific liquid and the Oh, is marked by different symbols and color codes. Furthermore, the transitions from the "CB" (total rebound) state to the "W" (partial rebound or complete pinning) state is also demarcated in Figure 6.6. One of the interesting observations corroborated from this regime map is the absence of the partial rebound regime for water droplets impacting the soot-coated surface in the range $15 \leq We < 60$, which is contrary to the previous observations of Deng *et al.* [369] on the similar fractal surface. This aspect has been discussed in detail in Section 6.3.7 later. Similarly, the regime map also successfully demarcates the transition from the rebound regime to the splashing regime via the *receding breakup* regime. Notably, a similar kind of $We - Re$ based regime map has rarely been reported for droplet impaction on bare soot-coated SHPs, previously.

In essence, the deformation of the droplet in both the R1 and R2 regime are primarily governed by the conversion between the kinetic energy (E_k) and surface energy (E_s) [396, 406]. Assuming, $\dot{r}$ as the velocity of the TPCL, $\rho\dot{r}^2/2$ and $k\gamma r^2/\phi_0$, represent the E_k and E_s per unit volume, with k being the geometric constant. Hence, the total energy per unit volume, $E_t (= E_k + E_s)$, is

$$E_t = \frac{1}{2}\rho\dot{r}^2 + \frac{k\gamma r^2}{\phi_0}, \tag{6.1}$$

where, ϕ_0 is the initial volume of the impacting droplet. Assuming a negligible energy loss in the R1-regime, energy minimization leads to,

$$\ddot{r} + \frac{2k\gamma r}{\rho\phi_0} = 0. \tag{6.2}$$

Equation 6.2 represents the simple harmonic oscillator, whose angular frequency of the oscillation (ω) is,

$$\omega = \sqrt{\frac{2k\gamma}{\rho\phi_0}} = \sqrt{\frac{2k\gamma}{m}}, \tag{6.3}$$

TH-2590_156103041

where m ($= \rho\phi_0$) is the mass of the droplet. Therefore, the corresponding harmonic timescale (t_h) of oscillation is, $t_h \sim \sqrt{m/\gamma}$. Notably, t_h has been found to represent the key impact dynamics more comprehensively in both the spreading and retraction phase [406]. If not mentioned exclusively, the t_h scaling will be used religiously in the rest of the text, with the pre-factor being adjusted from the experimental data.

6.3.2 Dynamics of droplet spreading

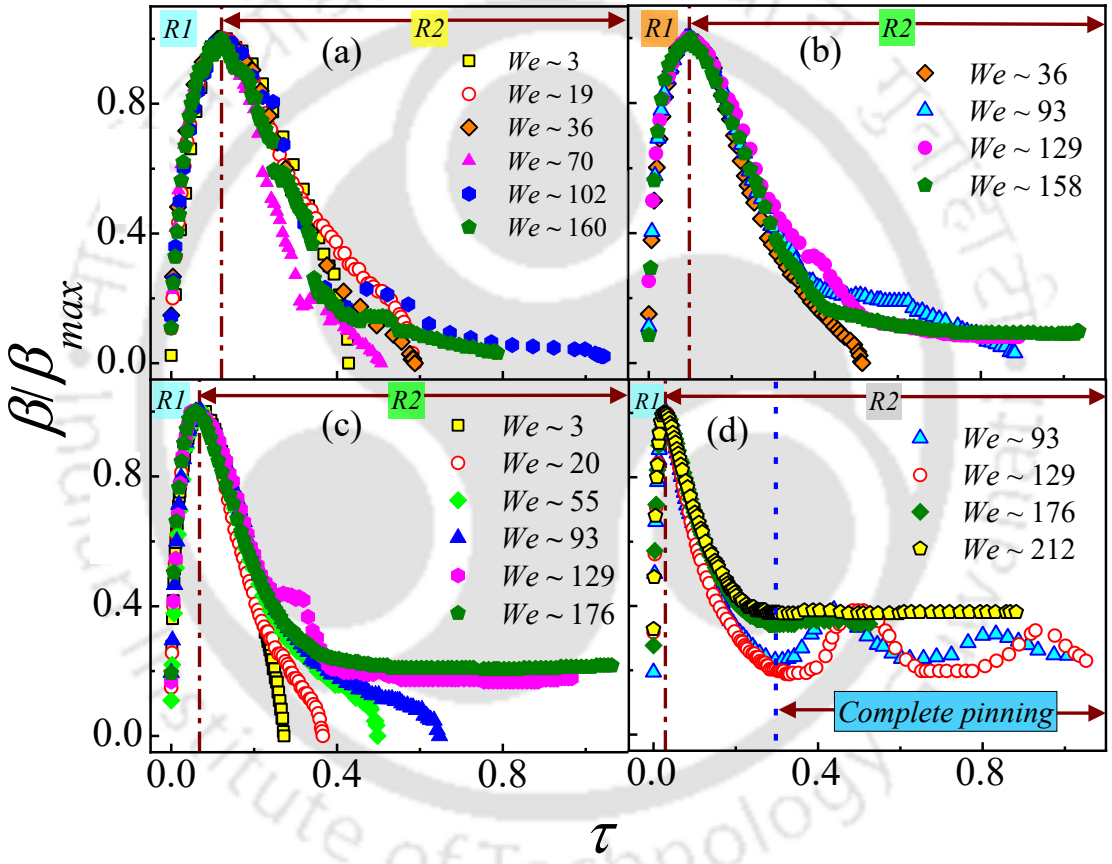


Figure 6.7: Temporal evolution of the spreading ratio, β/β_{max} of (a) DIW ($Oh = 0.003$), (b) Gly50 ($Oh = 0.023$), (c) Gly65 ($Oh = 0.062$), and (d) Gly80 ($Oh = 0.23$) droplets for different impact We.

Figures 6.7(a)-6.7(d) show the temporal evolution of the normalized spreading ratio, β/β_{max}, for different viscosity droplets, at specific impact conditions (We). Interestingly, upon normalizing the physical time-scale (t) with the t_h, i.e., $\tau = t/t_h$, the trajectories of β/β_{max} collapse to a single curve in the spreading stage for all the We

TH-2590_156103041

at a specific viscosity ($Oh = 0.003$). Also, the spreading and retraction regimes can be well demarcated (dashed-dotted line) upon using the appropriate scaling (t_h). The aforementioned observations further strengthen the previous claims that the dynamics are primarily governed by the energetics of E_k and E_s.

Notably, the maximum spreading radius, r_{max}, and the corresponding ratio,

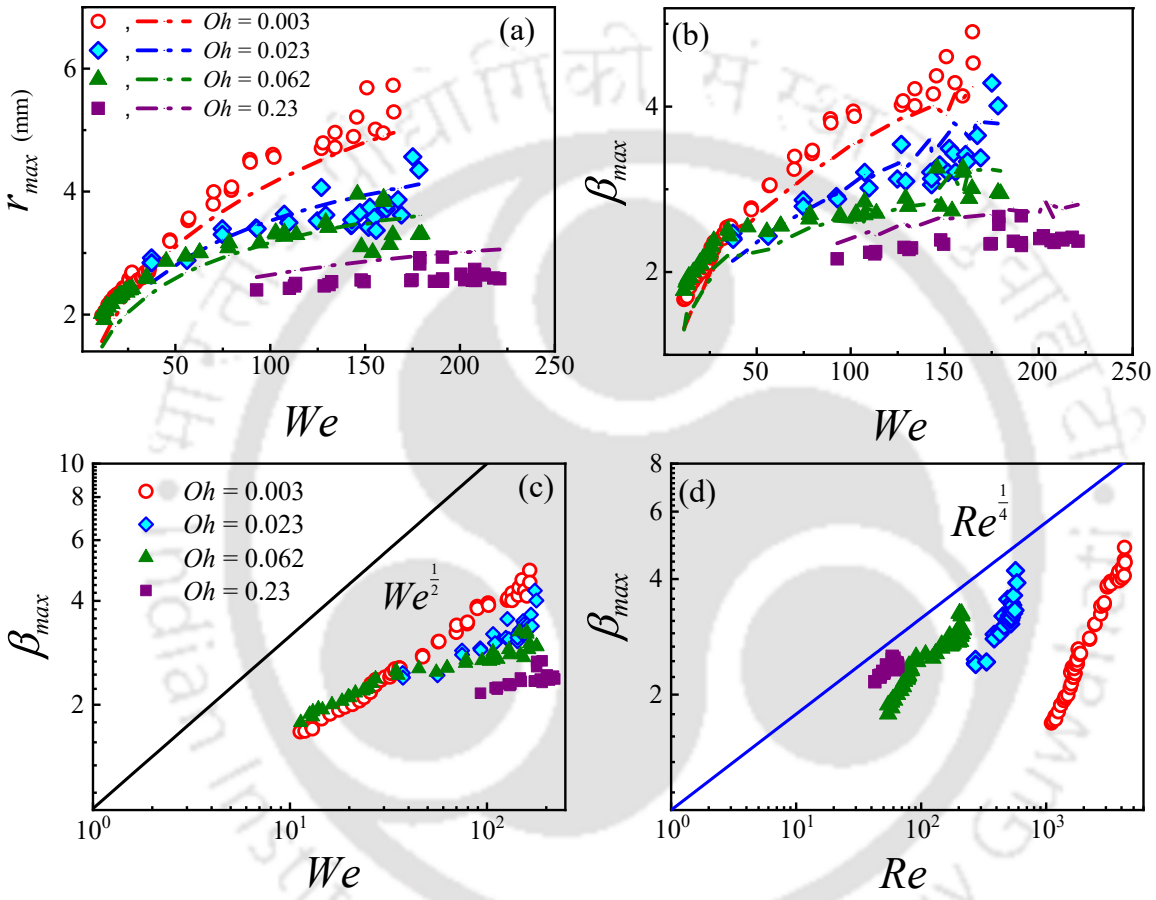


Figure 6.8: Variation of the (a) maximum spreading radius (r_{max}), and (b) maximum spreading ratio (β_{max}) with the impact We for different viscosity liquids. Variation of the maximum spreading ratio, β_{max} (c) with the impact We, when the theoretical scaling law, $\beta_{max} = We^{\frac{1}{2}}$ is applied and (d) with the impact Re, when the theoretical scaling law, $\beta_{max} = Re^{\frac{1}{4}}$ is applied.

β_{max}, have been established as one of the crucial parameters to study impact dynamics of droplets on solid surface[38, 369, 396–410], which appears to be a function of the We, as shown in Figures 6.8(a) and 6.8(b). Although, previous studies have shown that, $\beta_{max} = We^{\frac{1}{2}}$ or $We^{\frac{1}{4}}$ (in the capillary regime) or $\beta_{max} = Re^{\frac{1}{4}}$ or $Re^{\frac{1}{5}}$ (in the viscous regime), these independent correlations haven't been able to fit the

TH-2590_156103041

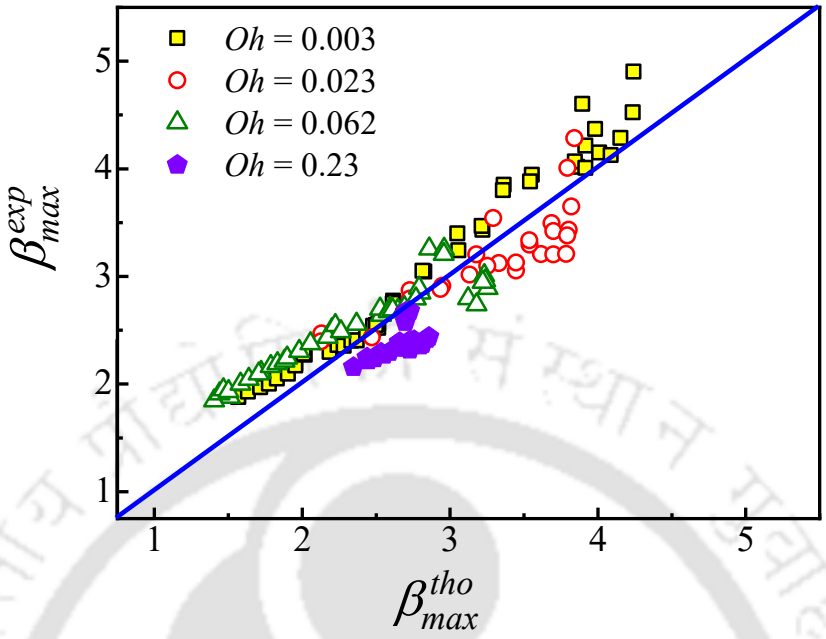


Figure 6.9: Comparison of the experimental data (β_{max}^{exp}) of maximum spreading for different viscosity droplets to the theoretical data (β_{max}^{tho}) obtained from Eq. 6.4.

present experimental data convincingly, as shown in Figures 6.8(c) and 6.8(d) [however, some of the scalings, such as, $Re^{\frac{1}{4}}$ might follow the experimental data in the very high viscosity limit as shown by Zhao *et al.* [370], see the discussion in Section E.1 of Appendix E]. Instead, Figures 6.8(a) and 6.8(b) show that the scaling of r_{max} and β_{max} with the We, religiously follows the correlation proposed by Gordillo *et al.* [405], represented as:

$$2\ We^{-1}\ r_{max}^2 + 0.45\ \lambda\ Re^{-\frac{1}{2}}\ r_{max}^{\frac{5}{2}} - 0.45 = 0, \tag{6.4}$$

where λ (= 0.4) is a free constant signifying the friction factor between the droplet and the superhydrophobic surface and additionally accounts for slip length in the case of SHPs. The value of λ has been adjusted experimentally to absorb all the assumptions in deriving Eq. 6.4 [405]. Notably, $\lambda = 0$ represents the Leidenfrost conditions [405]. Interestingly, Eq. 6.4 is equivalent to the widely accepted theoretical framework of Laan *et al.* [392], based upon the spreading parameter, $P \equiv f(We\ Re^{-\frac{2}{5}})$ [405]. The strong correlation between the experimental data (β_{max}^{exp}) and the theoretical prediction (β_{max}^{tho}) of Eq. 6.4 is apparent from Figure 6.9. It is worth mentioning that Eq. 6.4 has been derived based on the mass, and the

TH-2590_156103041

momentum conservation for a spreading liquid sheet [405]. Figure 6.9 also suggests that the proposed formulation sightly underestimates the experimental data in the low We regime ($We < 30$). This difference originates from the initial assumption by Gordillo *et al.* [405] in which a lamella is considered to be formed at the base of the droplet at $t = t_e$. However, for the low We regime, the elastic deformation of the droplet leads to a puddle-like shape during spreading, rather than a liquid sheet. Again, the model has successfully predicted the spreading extent of viscous liquids even at high We. This stems from the fact that Gordillo *et al.* [405] assumed a boundary layer flow within the lamella considering the shear affected thickness, δ as, $\delta = \sqrt{t/Re}$, instead of considering δ to be equal to the sheet thickness or its half as that of many existing studies. Also, the presence of the factor λ, representing slip conditions, makes Eq. 6.4 a robust theoretical formulation, suitable across a vast range of surface conditions and liquid properties.

6.3.3 Dynamics of droplet retraction

During droplet impact on a superhydrophobic surface, the retraction regime can exhibit a plethora of hydrodynamic features, such as air cavity formation, singular and columnar jet ejection, splashing and droplet fragmentation, etc., as seen in Figure 6.4. These characteristic features are greatly influenced by continuous depinning of the TPCL from the inner spaces of the micro-/nano-structures of the superhydrophobic surface [406]. Such behavior of the contact line can be well understood from the retraction rate, $\dot{\beta}$ (negative values), as well as the retraction velocity, v_{rec} as shown in Figure 6.10.

In Figures 6.10(a)-6.10(d) the normalized retraction rate, $\dot{\beta}R_0/V_0$, is plotted as a function of time, τ, for different impact velocities and liquid viscosity (the negative values of $\dot{\beta}$ indicates the retraction rate). Notably, the concerned time evolution of $\dot{\beta}$ reveals a few characteristic features of the retraction dynamics of the deformed droplets on a superhydrophobic surface: firstly, while for the lower impact speeds $\dot{\beta}$ suddenly increases towards the end of dynamics, for higher impact speeds ($\sim We \geq 60$), the trajectory of $\dot{\beta}R_0/V_0$ goes upward (towards, $\dot{\beta} = 0$) after reaching a point of minima. This trend has been observed for all the liquid viscosities as seen in In Figures 6.10(a)-6.10(d), which can be attributed to the *CB-to-W* transition at higher impact speed [406]. Secondly, the retraction rate is much higher (negative values of $\dot{\beta}$ in Figure 6.10) for low ($Oh \leq 0.003$) and moderate viscosity

TH-2590_156103041

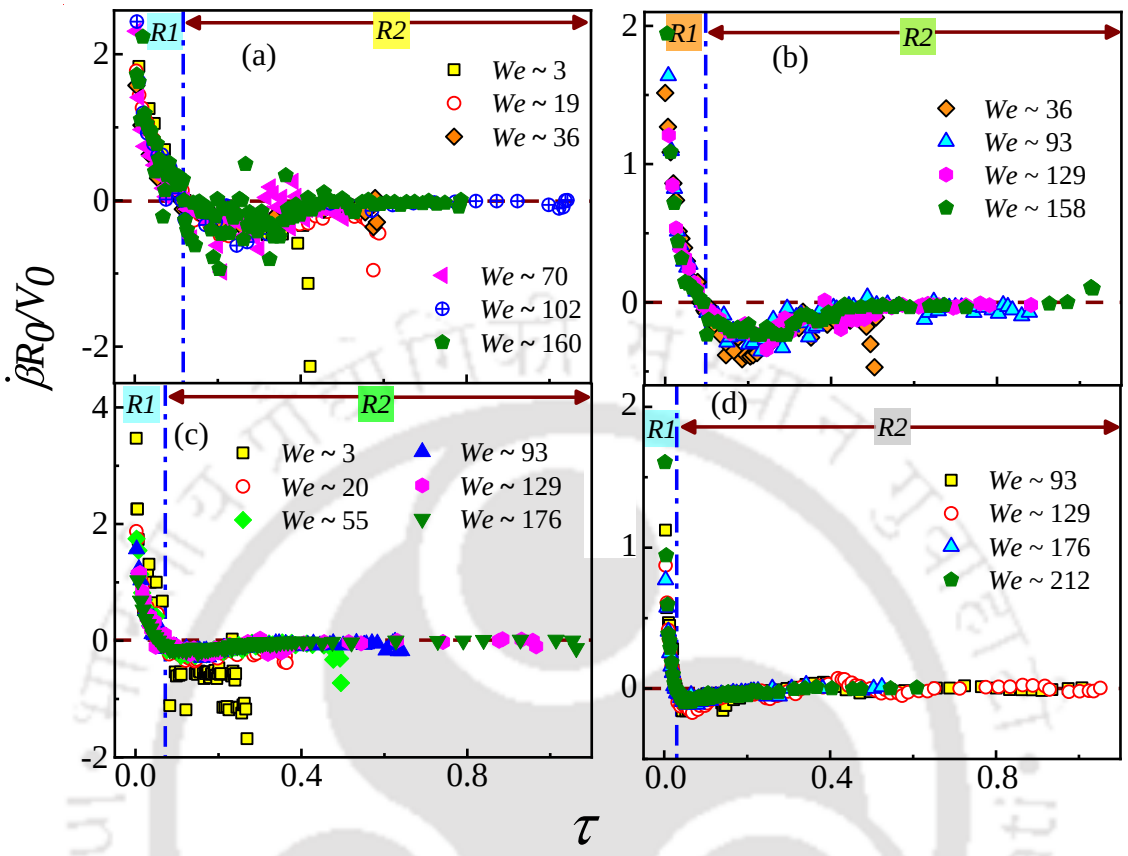


Figure 6.10: Temporal evolution of the normalized retraction rate [negative values of $\dot{\beta}R_0/V_0$] of (a) DIW ($Oh = 0.003$), (b) Gly50 ($Oh = 0.023$), (c) Gly65 ($Oh = 0.062$), and (d) Gly80 ($Oh = 0.23$) droplets for different impact We.

droplets ($0.003 \geq Oh \leq 0.05$) than that of the high viscosity solutions ($Oh \geq 0.1$) [407, 411]. The aforementioned characteristics hint towards the existence of two different regimes based on liquid viscosity: inertial regime and viscous regime, as discussed by Bartolo *et al.* [411].

Furthermore, the retraction of a deformed droplet from its maximum position, r_{max}, can be compared to the retraction of a thin liquid sheet with a velocity, v_{rec}, following the Taylor-Culick law, i.e., $v_{rec} = \sqrt{2\gamma/\rho h_f}$ [412, 413]. Here, h_f is the thickness of the liquid film at $r = r_{max}$. As such, the velocity of retraction is inversely proportional to thickness of the film at $t = t_{max}$, i.e., $v_{rec} \sim (h_f)^{-1/2}$. Figure 6.11(a) reflects the strong agreement between the experimental retraction velocity of the TPCL and the $h_f^{-1/2}$ law, where v_{rec} is defined by $v_{rec} \equiv avg[\dot{r(t)}]$. A slight deviation of the experimental v_{rec} from the proposed theory at low h_f (i.e., high V_0),

TH-2590_156103041

can be attributed to the disintegration of the sheet during splashing.

Interestingly, substituting h_f from the mass conservation (i.e., $\pi h_f r_{max}^2 \approx \frac{4}{3}\pi R_0^3$)

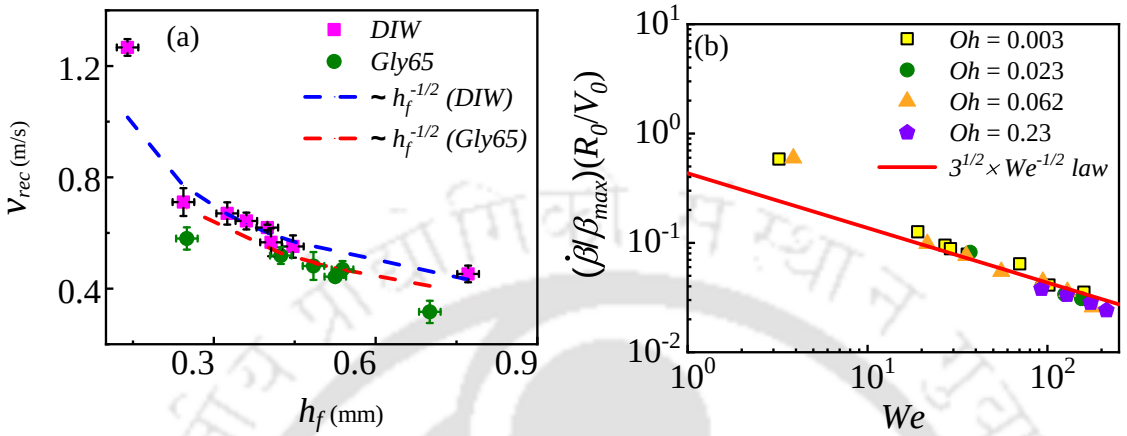


Figure 6.11: (a) Retraction velocity, v_{rec}, of the contact line V/S height of the liquid film, h_f, at maximum spreading. (b) Normalized retraction rate, $(\dot{\beta}/\beta_{max})$ (R_0/V_0), V/S the We, following the Taylor-Culick law (red-solid line) [412, 413].

in the Taylor-Culick law results in:

$$v_{rec} = \sqrt{\frac{3\gamma}{2\rho R_0^3}} r_{max} \Longrightarrow \frac{v_{rec}}{r_{max}} = \sqrt{\frac{3}{We}} \frac{V_0}{R_0}. \tag{6.5}$$

Equation 6.5 expresses the retraction rate as a function of the We. Substituting, the retraction rate, $v_{rec}/r_{max} = \dot{\beta}/\beta_{max}$ in Eq. 6.5, Eq. 6.6 is obtained as follows:

$$\left(\frac{\dot{\beta}}{\beta_{max}}\right)\left(\frac{R_0}{V_0}\right) = \sqrt{\frac{3}{We}}. \tag{6.6}$$

The normalized retraction rate from Eq. 6.6 strongly agrees with the present experimental results as shown in Figure 6.11(b), where $\dot{\beta}/\beta_{max}$ is defined as $\dot{\beta}/\beta_{max} \equiv avg[\beta(\dot{t})]/\beta_{max}$. This inverse dependency of the retraction rate on the We is a characteristic of the inertial regime of retraction [411]. The integral relationship of the spreading and retraction dynamics with We further hints towards the dependency of the resulting hydrodynamic features on the We, as discussed in the following sections.

TH-2590_156103041

6.3.4 Contact time dynamics

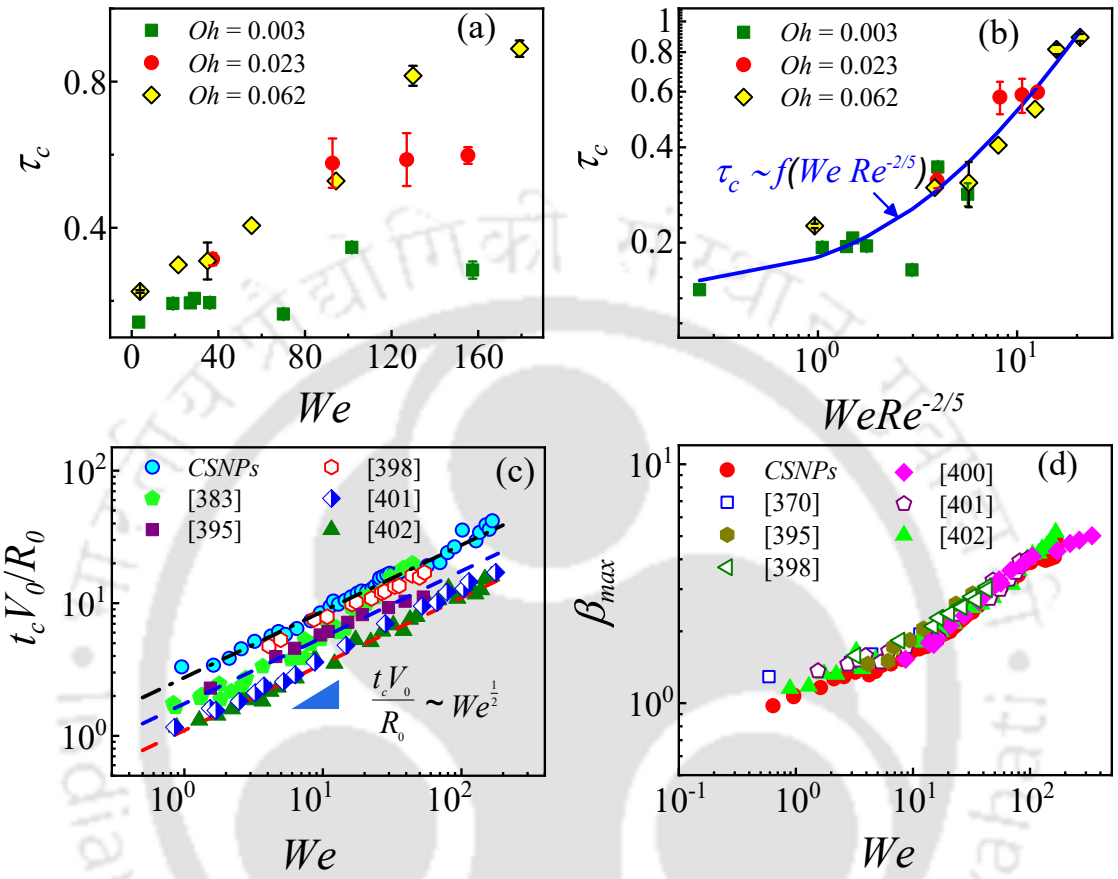


Figure 6.12: Variation of the (a) normalized contact time, τ_c, with the We for different liquids. (b) Normalized contact time, $\tau_c(= t_c/t_h)$, as a function of We and Re. (c) Contact time, t_cV_0/R_0 as a function of We for different superhydrophobic surfaces. (d) Maximum spreading ratio, β_{max} V/S We for different superhydrophobic surfaces.

Analysis of contact time (t_c) during droplet impact is very important for industrial processes, specifically those involving cooling and nucleation dynamics [414]. The contact time, t_c, is defined as the time period from $t = 0$ to the instant of lift-off of the droplet from the surface and hence, $t_c = t_{max} + t_{rec}$, where, t_{rec} is the total time-period of retraction dynamics. Figure 6.12(a) shows the variation of the non-dimensional contact time $\tau_c(= t_c/t_h)$ with the impact We for liquids of different viscosity. It can be discerned that with an increase in the We, τ_c increases monotonically for all the liquid viscosities. For instance, during the impact of a viscous droplet ($Oh = 0.062$) on the candle soot coated surface τ_c increases nearly by four

TH-2590_156103041

folds as the We increases from $We \sim 4$ to $We \sim 179$ [i.e., $\tau_c|_{(We\approx179)} = 4\times\tau_c|_{(We\approx4)}$]. Again, at a specific impact We, τ_c increases with an increase in the liquid viscosity (Oh), which can be attributed to the slower retraction rate of the TPCL along the surface as discussed in the previous section. Notably, a regression analysis of the experimental data by considering the effect of both We and Re results in a total collapse of the data from Figure 6.12(a) to a single master curve as seen in Figure 6.12(b), following the unified scaling, $\tau_c \sim f(P)$, wherein, $P \equiv f(WeRe^{-\frac{2}{5}})$, bears the previous definition of spreading parameter P [392]. Here, most of the data points correspond to the viscous regime, i.e., $P >> 1$, considering the definition of P by Laan *et al.* [392]. The spreading parameter, P, dependent form of the contact time further infers to the We and Re dependent spreading and retraction dynamics and the veracity of the harmonic time-scale (t_h). Interestingly, by considering the inertial time scale R_0/V_0 to non-denationalize the contact time, Xie *et al.* [415] has shown that for the impact of viscous nanodroplets the contact time follows a scaling based on the We and Re as, $f(We^{\frac{2}{3}}Re^{\frac{-1}{3}})$, which is quite similar to the scaling obtained above for the impact of viscous microdroplets.

Figure 6.12(c) shows a comparison of the contact time for impact of water droplets (DIW) on different superhydrophobic surfaces [369, 383, 396–399, 401]. For the sake of brevity and clarity, the convective time scale (R_0/V_0) of the previous studies is used in Figure 6.12(c) instead of the t_h. The figure suggests that, for a specific set of thermophysical properties, the non-dimensional contact time $\frac{t_cV_0}{R_0}$ increases monotonically with the We for all the surfaces similar to that shown in Figure 6.12(a), and can be approximated by,

$$\frac{t_cV_0}{R_0} \sim aWe^{\frac{1}{2}}, \tag{6.7}$$

where, a is the fitting constant equal to 2.75 ± 0.1 for the CSNPs coated current surface [black dashed-dotted line in Figure 6.12(c)]. Notably, Eq. 6.7 can be extended for all the surfaces as seen in Figure 6.12(c), however, with different empirical constants [e.g., $a = 1.75 \pm 0.03$ (blue line), and 1.15 ± 0.1 (red line)]. This difference in the empirical constant of Eq. 6.7 is, however, a bit unexpected as the variation of the maximum spreading factor, β_{max}, is nearly the same for all these surfaces, as shown in Figure 6.12(d). On the other hand, the difference in the contact line's retraction rate on the CSNPs coated surface from that of the other textured/irregular

TH-2590_156103041

SHPs can be a probable cause of the lacuna mentioned above. Interestingly, the contact time during the impact of a water droplet on the current CSNPs coated surface closely resembles that of the Leidenfrost impact [396] as shown in Figure 6.12(c), thereby indicating a higher degree of superhydrophobicity of the former.

6.3.5 Droplet rebound dynamics

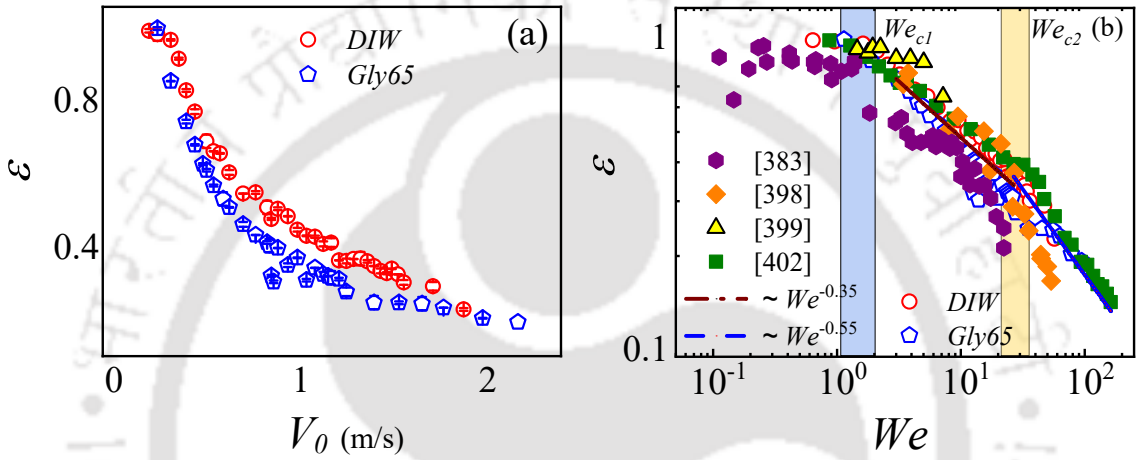


Figure 6.13: Variation of the (a) coefficient of restitution, ε with the impact velocity, V_0 for liquids of different viscosity. (b) Comparison of the rebound coefficient, ε, for different superhydrophobic surfaces as a function of impact We.

Droplet rebounding from a superhydrophobic surface is another interesting phenomenon, which occurs if the droplet's initial kinetic energy is sufficient to compensate for the dissipated energies (surface friction and viscous dissipation) during retraction. As such, there exists a threshold velocity of rebound defined as [370], $v_{re}^{cr} = \frac{9\eta}{8\rho R_0}$ ($\approx O[10^{-3} - 10^{-1}]$ m/s), in order to overcome the pinning (partial and complete) of the TPCL. The rebound dynamics is usually characterized by the coefficient of restitution (ε) [370], defined as the ratio of the velocity after the droplet impact to the initial impact velocity, i.e., $\varepsilon = v^{'}/V_0 = \sqrt{h^{'}/h}$ (discarding both mass loss and drag). Here, $h^{'}$ is the height reached by the primary rebounding droplet after its first rebound. Figure 6.13(a) shows the variation of the ε with the V_0 for two experimental fluids namely, DIW ($Oh = 0.003$), and Gly65 ($Oh = 0.062$). As seen, for all the rebound events, $\varepsilon < 1$, thereby indicating energy dissipation during contact line retraction. Apparently, the ε decreases with the increase in the V_0, which can be attributed to the enhancement in the droplet deformation and

TH-2590_156103041

vibration, leading to higher loss at the high impact velocity [370]. Furthermore, the viscous dissipation increases with an increase in the viscosity of the droplet, and as such, ε should be less for a high viscosity droplet, even at the same V_0 as shown in Figure 6.13(a).

Again, for comparing the performance of the current CSNPs coated superhydrophobic surface, the variation of the ε with the We is plotted for different superhydrophobic surfaces [369, 383, 396–399, 401] in Figure 6.13(b). Surprisingly, the present surface exhibits a higher value of the ε for all the We, in comparison to other SHPs. This difference in the magnitude of ε is more prominent in the moderate and the high We regime as apparent from Figure 6.13(b). The closeness (slightly higher) in the magnitude of the rebound coefficient on differently textured/disordered SHPs in similar experimental conditions further infers to the competitive or at par [when compared to SC-CNT coated surface [402]] water-repelling behavior of the current CSNPs coated surface.

Figure 6.13(b) also hints towards the presence of three distinct transition regimes as the impact velocity increases, marked by the patterned zones at $We = We_{c1}$ and $We = We_{c2}$. Apparently, for $We < We_{c1}$, $\varepsilon \sim 1$, thereby indicating a completely elastic collision between the droplet and the surface and meager deformation. As the We increases beyond We_{c1}, the deformation of the droplet increases, resulting in the Worthington jet and, in turn, secondary droplets. The ε in this regime ($We_{c1} < We < We_{c2}$) varies according to the scaling: $\varepsilon \sim bWe^{-0.35}$, where, $b = 1.17 \pm 0.03$ is the fitting coefficient. Again, in the third regime, $We > We_{c2}$, the ε varies as per the scaling law $\varepsilon \sim cWe^{-0.55}$ as shown by the blue dashed line in Figure 6.13(b). Here the fitting coefficient $c = 2.75 \pm 0.07$. In this regime, the momentum before impact is distributed among the secondary droplets, generated either from a columnar jet or splashing. As a result, one observes low ε due to substantial deformation of the droplet post-impact. The aforementioned scaling laws match closely to the ones proposed by Aria and Gharib [402] for CNT-based SHPs.

6.3.6 Splashing dynamics

The splashing of a droplet impacting a dry/wet surface is one of the most sought-after modes of droplet atomization. A brief introduction of this regime has previously been put forward in the context of Figures 6.4(a) and 6.6, which sheds light on two prime aspects: (i) there exists a critical impact velocity, v_{sp}^{cr} (or We_{sp}^{cr}) beyond which

TH-2590_156103041

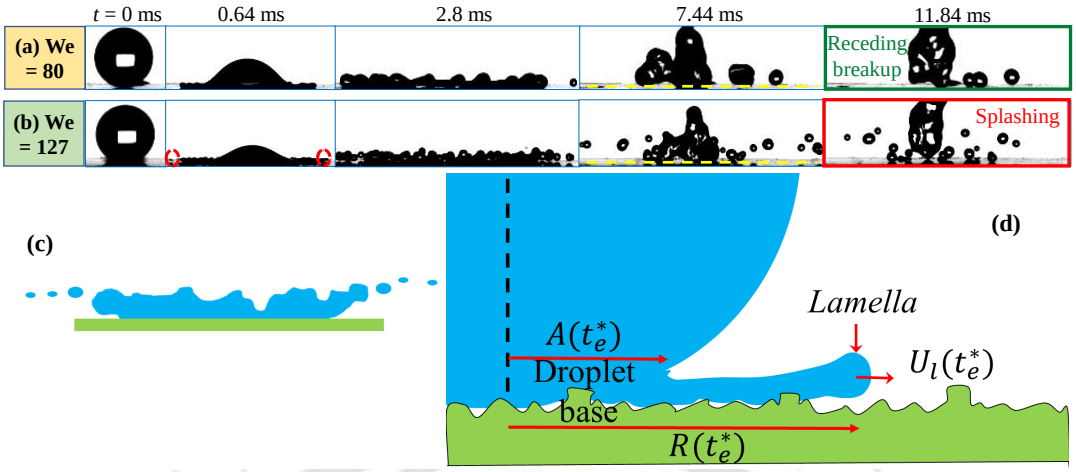


Figure 6.14: Sequential snapshots depicting the dynamics of (a) receding breakup and (b) splashing during the impact of water droplets on the CSNPs coated superhydrophobic surface. The dashed yellow line marks the datum's position, while the broken red circle in (b) shows the generated secondary droplets as the droplet is spreading. The impact velocities in (a) and (b) are 2.2 and 2.8 m/s, respectively. Schematic of (c) prompt splash and (d) lamella ejection event.

splashing regime is observed, (ii) for high viscosity droplets splashing is suppressed. However, before indulging in further details, it will be better to define the splashing and non-splashing behaviors for brevity and clarity. Previous reports have divided the splashing event on solid surfaces into two major categories: (a) prompt splash and (b) corona splash. In the prompt splash event, secondary droplets are generated from a lamella, ejected from the droplet base at time t_e [lamella ejection time; see the schematic in Figures 6.14(c) and 6.14(d)]. Again, during corona splash, secondary droplets are ejected from a vertically displaced lamella, wherein the aerodynamic lift force is dependent on the surrounding gas pressure [38, 403, 416]. Notably, corona splash is prominent during liquid droplets' impact on partially wetting smooth surfaces. In contrast, the rough surfaces, similar to the surface at hand, are expected to promote the prompt splashing dynamics [38, 403, 416]. Apart from the prompt splash, nonwetting surfaces also exhibit receding breakup, in which as the liquid sheet retracts from r_{max}, the liquid fingers that have already been formed at the outer rim disintegrates themselves from the rim and engenders several secondary droplets [38]. Figure 6.14(a) and 6.14(b) show the event of receding breakup and prompt splashing to clarify the picture further, wherein secondary droplets are seen at a much later stage after the generation of the lamella during the receding breakup

TH-2590_156103041

mode. In this study, as the impact velocity increases for water droplets, it passes through the receding breakup stage (60< We <100) to enter the prompt splashing stage [see Figures 6.6 and 6.14]. Here onward, the focus is shifted on analyzing the characteristics of the prompt splash event, and following the logic of the above discussion, the receding breakup mode of a droplet during impact is identified as the non-splashing behavior.

Inline to the above discussions, there exist several splashing criteria for droplets impacting rough surfaces [38], which aims to unfurl the critical velocity needed for splashing, i.e., v_{sp}^{cr} (or We_{sp}^{cr}). The most generalized formulation regarding the splashing threshold during the vertical impact on a rough surface is $We\sqrt{Re} = K$, where the parameter K is to be found empirically from the experimental data [38]. For similar impact parameters, the threshold value of K is generally lesser for rough surfaces, indicating more splashing. Most recently, Quintero *et al.* [416] discussed that the splashing criteria can be derived by considering the time evolution of the thickness of the rim bordering the lamella, after its ejection at time t_e^*. Here, t_e^* is the non-dimensional lamella ejection time, defined as, $t_e^* = t_e/(R_0/V_0)$ [416]. Notably, in the limit of $Re^{\frac{1}{6}}Oh^{\frac{2}{3}} < 0.25$, the ejection time, t_e^* can be predicted as, $t_e^* = 1.05We^{-2/3}$ [416]. In the current experiments, splashing is observed for the impact of water and 50% glycerol solutions (gly50) at experimental conditions, $We_{sp}^{cr} > 100$ and $We_{sp}^{cr} > 160$, respectively, which satisfies the condition, $Re^{\frac{1}{6}}Oh^{\frac{2}{3}} < 0.25$. As such, the theoretically obtained lamella ejection time, $t_e \approx$ 0.01-0.02 ms, matches closely with the experimental data ($t_e <$ 0.08 ms) for both water and 50% glycerol solutions. The rim of this ejected lamella further experiences capillary instabilities as the droplet spreads along the rough surface, consequently generating numerous secondary droplets at the same time. In the coming section, the variation of these secondary droplets' size and number with the impact conditions will be discussed, which are of utmost importance in pathogen removal or self-cleaning processes.

6.3.6.1 Size of the secondary droplets

Numerous small droplets or *secondary droplets* are generated due to splashing, whose size (d) spans across a wide range, as shown in Figure 6.4(a) (V_0 = 2.5 m/s). Figures 6.15(a)-6.15(d) show the normalized size distribution (d/D_0) of the secondary droplets for different impact velocities. As shown in the figure, the distribution can be fitted with a log-normal function, whose corresponding probability distribution

TH-2590_156103041

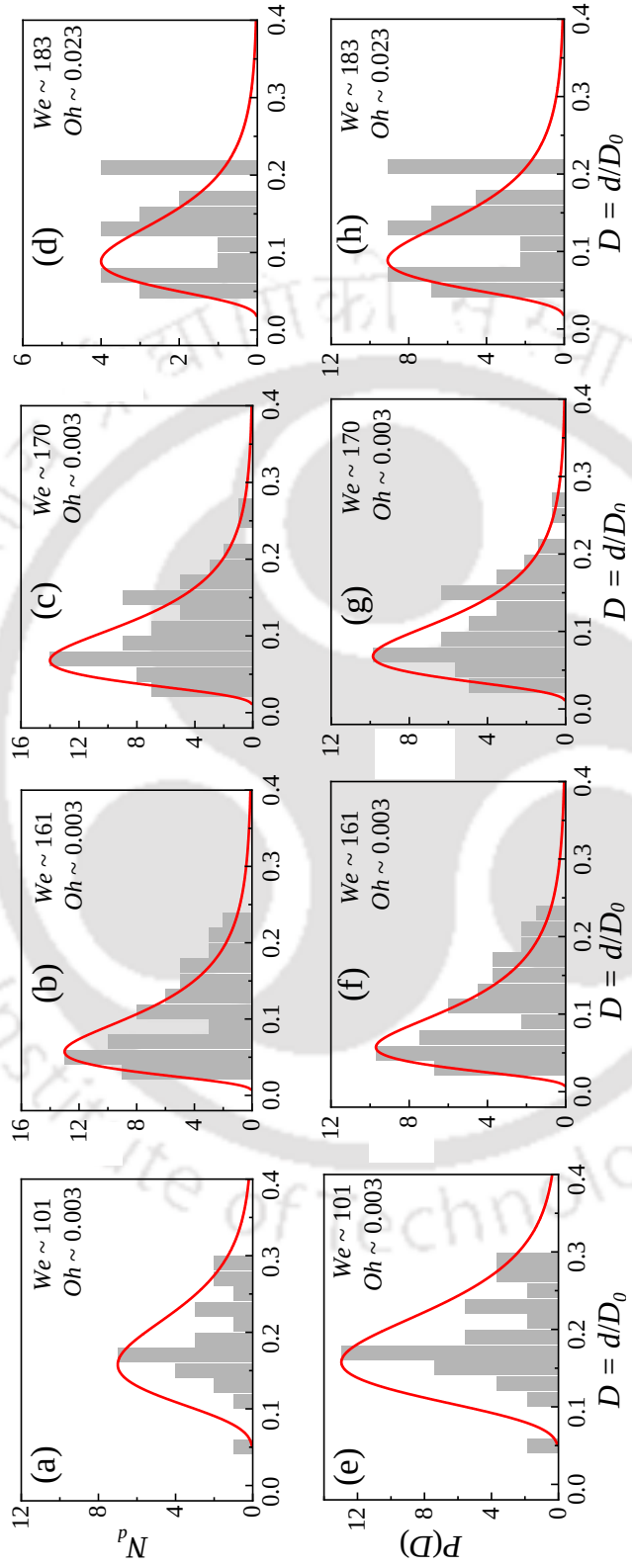


Figure 6.15: (a-d) Size distribution (d/D_0) of secondary droplets during splashing at different impact velocities and liquid viscosity. (e-f) Probability distribution functions, $P(D)$, corresponding to the size distribution in (a-d). The continuous red line indicates the fitting of the experimental data with a log-normal distribution.

TH-2590_156103041

$[P(D)]$ is defined as follows:

$$P(D) = \frac{1}{d\sigma_d\sqrt{2\pi}} exp\left(\frac{-(\ln d - \langle d\rangle)^2}{2\sigma_d^2}\right), \tag{6.8}$$

where, $\langle d\rangle$ and σ_d represent the mean and the standard deviation, respectively, defining the distribution characteristics. Notably, Shaikh *et al.* [417] has previously shown the relevance of this kind of log-normal distribution for secondary droplet size for immiscible impacts of droplets onto millimetric films. The similar distribution pattern of the secondary droplet sizes in both the present study and the previous study of droplet impact on a wet film can be attributed to the underlying mechanism of droplet generation by fluidic ligament fragmentation, which is, in general, a cascade-like event [417, 418]. Interestingly, for all the impact velocities and liquid viscosity exhibiting splashing, the resulting size distributions of d always conform to the log-normal distribution, as shown in Figures 6.15(a)-6.15(d). The corresponding normalized probability densities, $P(D)$, also apparently adhere to the log-normal distribution, as shown in Figures 6.15(e)-6.15(h). The distributions of d and $P(D)$ in Figure 6.15 further indicate that the mean shifts towards lower values as the impact We increases. Also, for a nearly equal impact velocity, a larger mean of the size distribution is obtained if the viscosity of the droplet is increased.

Furthermore, considering the disintegration of the ligaments originating from the liquid rim as the dominant mechanism of droplet generation during liquid splash, it can be intuitively argued that both the surface tension as well as viscous boundary layer within the liquid rim will affect the droplet size distribution [404, 417–419]. As such, it can be intuitively argued that both the We and Re should appear in the empirical correlation of time-averaged secondary droplet size, such that:

$$d_{32}/D_0 = f(We, Re) \sim C_2 We^d Re^e, \tag{6.9}$$

where, C_2, d, and e are the empirical constants. Notably, the Sauter mean diameter (d_{32}) is considered as the representative of the secondary droplet size, defined as follows:

$$d_{32} = \frac{\sum_{i=1}^{N_d} n_i d_i^3}{\sum_{i=1}^{N_d} n_i d_i^2} \quad , \tag{6.10}$$

where, d_i is the diameter of the i^{th} secondary droplet and N_d is the total number of

TH-2590_156103041

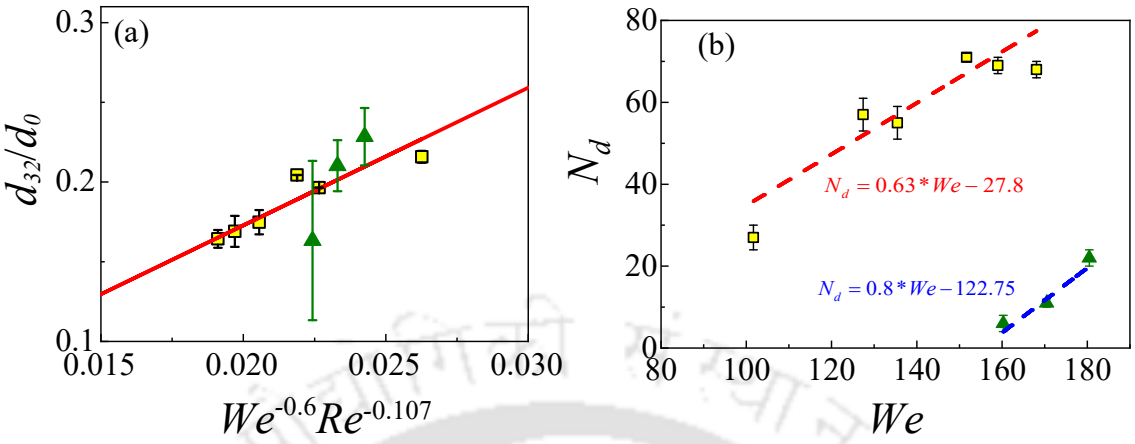


Figure 6.16: Variation of the (a) mean size [i.e., Sauter mean diameter, d_{32}] of the droplet, expressed in a non-dimensionalized form, i.e., d_{32}/D_0, as a function of the We and Re. The red dashed line is derived from Eq. 6.9. (b) No. of droplets, N_d as a function of the impact We.

secondary droplets. A thorough regression analysis results in the following empirical constants: $C_2 = 8.641 \pm 10.2$, $d = -0.6 \pm 0.198$, and $e = -0.107 \pm 0.039$. Interestingly, apart from the scaling law in Eq. 6.9, the empirical constants are also similar to that of the scalings proposed by Han *et al.* [419] during droplet impaction on a heated surface. The aforesaid observations infer that the ligament breakup is the dominant mechanism for secondary droplet production during splashing in both situations. Figure 6.16(a) shows that all the experimentally obtained droplet size during splashing, across viscosity and impact velocities, collapse to a single curve following the scaling in Eq. 6.9, thereby validating the current empirical correlation. The inverse dependency of the mean droplet size (d_{32}/D_0) on the We refers to the fact that, with an increase in the impact velocity, smaller secondary droplets are produced in the splashing regime. Again, the experiments show that the number of secondary droplets (N_d) increases monotonically with the increase in the impact velocity at a specific viscosity [see the note regarding no. of secondary droplets in Section E.2 of Appendix E]. Figure 6.16(b) strongly corroborates the aforementioned claim, wherein two different linear scaling laws are seen at two different viscosities. For the splashing of DIW droplets on the current CSNPs coated superhydrophobic surface, the suitable scaling is found as $N_d = 0.63\ We - 27.8$, whereas the scaling law regarding the number of secondary droplets produced after splashing of 50% glycerol-water droplets on the same surface is found as $N_d = 0.8\ We - 122.75$. Notably, the slopes of the two theoretical curves (dashed line) in Figure 6.16(b) have a meager

TH-2590_156103041

difference in their numerical values, thereby validating the dominance of ligament breakup mode during splashing of viscous droplets.

6.3.7 Partial rebound dynamics

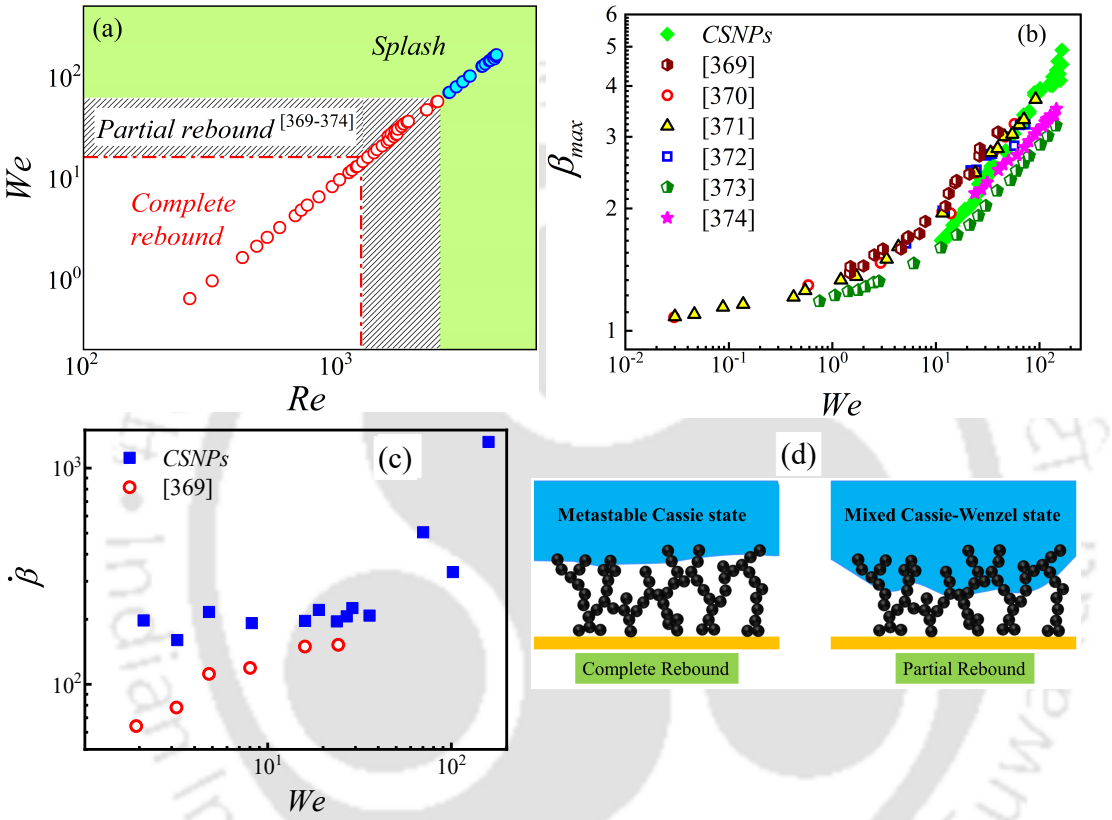


Figure 6.17: (a) We-Re regime map showing complete rebound, partial rebound, and splashing regimes during the impact of water droplets on various soot-coated superhydrophobic surfaces. Variation of (b) maximum spreading ratio and (c) retraction rate with the We for the impact of water droplets on different soot-coated superhydrophobic surfaces. (d) Schematic depicting the proposed mechanisms of the complete rebound and partial rebound regime.

The existence of the partial rebound phenomenon during droplet impact on a superhydrophobic surface is a critical factor affecting the design of the same. During the partial rebound regime, which succeeds the complete rebound regime, the elongated liquid droplet is disintegrated at the end of the retraction phase and subsequently bounces off the surface leaving behind a considerable liquid volume (see the experimental snapshots corresponding to $U_0 = 2.50$ m/s in Figure 6.4(b). Fun-

TH-2590_156103041

damentally, the partial rebound event indicates the (partial) Cassie to Wenzel transition, wherein the liquid-air interface of the droplet impales the superhydrophobic coating. Therefore, different methodologies have been adopted to inhibit the aforesaid impalement transition to increase the robustness of the concerned SHPs. In the case of silica-based SHPs used in previous studies[369–374], for the impact of water droplets on the same, partial rebound event is reported to occur in the range $\sim 15 \leq We <60$ [shown with the help of shaded area in Figure 6.17(a)]. Deng *et al.* [369] suggested that the local CWT is the driving mechanism for the occurrence of the partial rebound regime in their study. Remarkably, for the present CSNPs coated SHPs, no partial rebound (or partial pinning) is ever seen during the impact of water droplets up to $We \approx 125$. Instead, in this study, the dynamics of droplet impact directly enter from the complete rebound state to the splashing state as shown in Figures 6.6 and 6.17(a). This contrasting behavior is quite significant as both the present CSNPs coated SHPs and the referred silica-coated SHPs [369] have identical surface morphology [refer to Figure 6.3]. While the debate regarding the origin of this partial CWT in the case of superhydrophobic surfaces is still ongoing, generally, the aforesaid transition is elucidated in terms of the competing wetting and anti-wetting pressures during droplet impact. The relevant wetting pressures are the dynamic pressure, P_D ($= 0.5\rho U_0^2$) [420], originating from droplet inertia and the water hammer pressure, P_{EWH} ($= k\rho C U_0$) [420], emanating from the instantaneous compression of the liquid at the contact stage. The effective water-hammer pressure, P_{EWH} dominates the early stages of droplet impact, which subsequently releases its shock energy after overtaking the moving liquid-air interface of the droplet. Consequently, the dynamic pressure, P_D, dominates the dynamics of droplet spreading later. Notably, the prefactor k can assume a broad range of values, depending upon the complex interaction between the solid surface and liquid front, ranging from 0.2[420] to 0.002[421]. Also, both P_D and P_H increase monotonously with an increase in the impact velocity, U_0. Considering the velocity of sound in water, $C \approx$ 1497 m/s, for the complete range of impact velocity of water droplets (U_0 = 0.2-3.2 m/s, Table 6.2), P_D ranges from 0.02 kPa to 5 kPa and P_H ranges from 72 kPa to 1.1 MPa (considering $k = 0.2$). Again, the droplet can impale the coating only when the combination of these two wetting pressures exceeds the anti-wetting pressure or capillary pressure (P_C), i.e., $P_D + P_H > P_C$. Deng *et al.* [369] suggested that impalement of droplets on a fractal type rough SHPs predominantly occurs via the *depinning mode*, wherein the liquid interface constantly slides along the micro/nano-

TH-2590_156103041

structures beyond the material advancing contact angle (θ_{adv}). Considering a pore size of r_p in the superhydrophobic surface, the anti-wetting pressure is defined as, $P_C = -2\sqrt{2}\gamma \cos\theta_{adv}/r_p$ [369, 370, 420]. The anti-wetting pressure changes considerably with the change in pore spacing, r_p and intrinsic wettability of the material (θ_{adv}).

With the definitions of wetting and anti-wetting pressures put in place, the non-impaling phenomenon of the water droplet on the CSNPs coated SHPs is expected to be originated from the dense network of the soot nanoparticles as shown in Figure 6.3. In the velocity range (U_0 = 0.95-1.9 m/s, or We = 15-60) corresponding to the partial rebound regime shown by Deng *et al.* [369], P_D varies from 0.5 kPa to 1.76 kPa, and P_H varies from $\sim$ 340 kPa to $\sim$ 675 kPa. To avoid impalement, $P_C >$ 675 kPa on the proposed CSNPs coated surface. Considering, $\theta_{adv} \approx 161°$, the corresponding spacing between the protrusions is roughly calculated as $r_p \sim$ 0.2 μm, which matches approximately the surface topology shown in Figure 6.3. Deng *et al.* [369] argued that, the liquid-air interface partially impales the coating via depinning mode beyond a threshold impact velocity (U_{pin}^{cr} or We_{pin}^{cr}) and the corresponding penetration depth increases with an increase in the impact velocity [369, 422]. The liquid-air interface occupies the inner spaces of the overhangs after displacing the air [shown schematically in the right panel of Figure 6.17(d)] during the spreading stage, and as a result, the contact line experiences enormous resistance once it reaches the wetted area during the retraction, consequently leading to the bifurcation of the parent droplet [369]. This dynamic wetting state can be termed as the *mixed Cassie-Wenzel state* [422]. On the other hand, the absence of the partial rebound phenomena in this study is anticipated to have originated from a larger value of P_C restricting the liquid front from touching the inner overhangs of the fractal network as depicted schematically in the left panel of Figure 6.17(d). This state of the dynamic wetting behavior can be termed as the metastable Cassie state [369]. As a result, even though the droplet elongates to some extent at the end of the retraction stage, the contact line successfully pulls itself upwards, leading to a complete rebound situation. The impact dynamics in this concerned regime are analogous to the *partially penetrated bouncing* (PPB) regime indicated by Kwon and Lee [423]. However, the slightest penetration on the surface at hand has to be verified through control experiments.

The contrasting dynamic wetting behavior between the two nearly identical superhydrophobic surfaces can be convincingly argued to have emanated from the

TH-2590_156103041

additional silica layer on the surfaces engineered by Deng *et al.* [368, 369]. The difference in the top-coatings leads to the change in the overall fractal network, which may have affected the fractal dimensions of the surfaces [424, 425] and consequently altering the static and dynamic wetting behavior of the impacting droplets. In this regard, the comment of Malavasi *et al.* [426] regarding the role of surface chemistry in the dynamic wetting behavior can also be invoked. Interestingly, the absence of partial rebound behavior also results in a higher retraction rate ($\dot{\beta}$) of the TPCL in the bare CSNPs coated SHPs in comparison to the silica-coated SHPs [369], as shown in Figure 6.17(c). It is to note that, to avail a one-to-one comparison with Deng *et al.* [369], the definition proposed by the former is considered for calculating the retraction rate, i.e., $\dot{\beta} \equiv max(-dD/dt)/d_{max}$. The additional viscous dissipation within the porous structures during the retraction phase can be considered the primary reason behind the substantial difference in $\dot{\beta}$. Interestingly, the variation of the maximum spreading ratio, β_{max} along with the We, is nearly similar in all the different SHPs as shown in Figure 6.17(b). However, the partial rebound regime's aforementioned interesting behavior should be explored in the near future, considering all the possibilities with more sophisticated experimentation to further the knowledge of low-cost SHPs. The absence of impalement of the target superhydrophobic surface during the impact of low viscosity droplets is one of the significant contributions of this study.

6.4 Summary

This chapter shows that a simple fabrication method of flame deposition of carbon soot nanoparticles on a PDMS-derived surface can produce a superior quality superhydrophobic surface. Although the static wetting characterization has previously been carried out elsewhere [379, 427], it is essential to elucidate the dynamic wetting behaviour of the surface at hand to use it in different processes, specifically in outdoor applications. As such, a detailed appraisal of the impact dynamics of viscous droplets on the produced surfaces is carried out in this study. Here, the impact dynamics are characterized in the purview of the temporal evolution of several vital parameters, which include spreading ratio, contact time, coefficient of restitution, splashing parameter, and size of the secondary droplets engendered by splashing. The produced surface retains its superhydrophobicity even at higher viscosity (up

TH-2590_156103041

to 20 times the viscosity of DI-water) and high impact velocity (up to $V_0 = 2.4$ m/s at $Oh = 0.062$). Remarkably, for the impact of water droplets, the present surface does not exhibit *partial rebound* dynamics, unlike a host of existing SHPs of similar topology. However, beyond a threshold impact velocity ($V_0 \geq 3.0$ m/s) and viscosity ($Oh \geq 0.062$), a permanent Cassie-Baxter state to the Wenzel state transition is observed. The dynamics of contact time, rebound, and splashing are a function of the impact velocity and liquid viscosity. The number of secondary droplets increases monotonically during splashing, with an increase in the impact velocity, and is inversely proportional to the liquid viscosity. Again, the secondary droplets' mean size decreases with an increase in the impact velocity and increases with an increase in the liquid viscosity. Finally, the current CSNPs coated superhydrophobic surface is compared and contrasted against the existing superhydrophobic surface regarding the critical droplet impact parameters mentioned previously. Considering the experimental data of contact time, spreading ratio, and restitution coefficient associated with the impact of DI-water droplets on various superhydrophobic surfaces, the current CSNPs coated surface exhibits superior or comparable water-repelling behaviour. Such inspiring results are expected to establish the studied surface as a strong candidate for utilizing it as an affordable and easy to fabricate superhydrophobic coating in industrial applications, specifically in outdoor coatings.

TH-2590_156103041

Chapter 7

Conclusions and scope of future work

7.1 Conclusions

In the present thesis work, an experimental investigation and subsequent characterization of the different microfluidics systems involving droplets have been carried out. Specifically, the thesis work focuses on elucidating the dynamics of deformation and subsequent atomization of the liquid-vapour interface of a droplet in the presence of several different kinds of external stimulations. In this regard, four separate physical systems are explored, wherein the primary driving potentials acting on the liquid droplets are electric field potential, magnetic potential, gravitational potential, and imposed inertia. Apart from the magnitude of the external fields, the present work considers the effect of the substrates' wettability and elasticity and the thermophysical properties of the experimental fluid while elucidating the dynamics of the liquid droplets in different physical systems. Notably, the characterization of the droplet dynamics is carried out by considering the spatiotemporal evolution of different parameters associated with the three-phase contact line, (apparent) contact angle, and droplet geometry during the experiments. Additionally, the process of secondary droplet generation has also been characterized as per the requirement of the study. The experimental results from each chapter are also complemented by theoretical analysis based on non-dimensional numbers and also by numerical simulations if required. The excellent agreement between the experimental results

TH-2590_156103041

to the theoretical scaling laws elucidates the driving mechanisms of the concerned rich physical systems and also reflects the robustness of the experimental methods. In this chapter, the important findings of each chapter are summarized below.

All the experimental studies are conducted using a high-speed visualization system, as discussed in Chapter 2. A novel image processing technique has also been developed to extract desired quantitative information from high-speed experimental videos. The main conclusions from Chapter 2 are as follows:

- A high-speed videography system, comprised of a high-speed camera, zooming lens, and high-intensity backlighting, is chosen to carry out experimental investigations in this thesis. Additionally, a number of selection criteria associated with essential parameters of the high-speed imaging system are discussed and defined in the purview of the current thesis work. The concerned parameters are *frame rate, interframe time, exposure time, shutter speed, illuminance time, magnification, triggering mode*, among many others.

- A novel image processing method is developed by combining the image processing tools of ImageJ [164] and an in-house C++ code. The aforesaid method has been able to nullify the shortcomings of the high-speed videography method, precisely the issue of the central white regime in the acquired images. The code has been validated against several experimental images.

A yarn-based droplet generation system is discussed in Chapter 3. The spontaneous capillary flow of the liquids through the yarn's tortuous network facilitates the formation of a liquid droplet at the freely hanging end of the yarn, which has been explored in a simple, yet robust experimental setup. Various experimental fluids are chosen with a broad range of thermophysical properties to elucidate the universality of such a capillary flow-mediated yarn-based droplet generation system. A detailed appraisal of the droplet's contact line dynamics is presented, which further helped demarcate different growth regimes and compare the dynamics to existing drop-on-demand systems comprised of solid no-wettable capillary tubes. The salient conclusions from the chapter are as follows:

- Based on the spatiotemporal evolution of the three-phase contact line, the dynamics of the droplet growth can be divided into three distinct stages, namely *radial growth*, *axial growth*, and *motion*. During the radial growth stage, the radius of the drop expands rapidly with a relatively moderate rate of increase

TH-2590_156103041

in its length. The *tip* (or *TPCL*) of the drop moves upward in this stage, while the *bottom* remains fixed approximately at $z = 0$. A relatively high rate of increment of the droplet length and a relatively lower rate of radial expansion the characteristics of the second stage, i.e., axial growth stage. Here, the tip of the drop remains fixed to its position till the end of the stage, with the bottom point continuously moving away from the datum. The second stage comes to completion on the droplet reaching a critical volume, thereby enabling it to overcome the resisting forces preventing it from sliding downwards. The aforementioned three stages, seen during droplet growth in a yarn, are rarely observed in the conventional capillary tube-based drop generation systems.

- The contact line dynamics during the motion stage appear to be self-similar, irrespective of the initial experimental conditions. This universal behaviour of the TPCL can be described by a scaling law based on the driving and resisting forces. The scaling law suggests that the gravity force dominates the capillary forces during the motion stage.

- Furthermore, another self-similar behaviour is observed for the temporal evolution of the droplet radius in the radial growth and axial growth stage. The derived asymptomatic relation suggests that the surface tension force dominates the droplet's growth rate during the initial two stages, which, in turn, controls the final droplet volume. By using a number of different fluids spanning across a wide range of viscosity, it is found that for the macroscale contact line dynamics occurring over a physical timescale, viscosity plays the role of rate limiter.

- The critical volume required for the drop to initiate sliding is 65%-75% of the final drop volume after pinch-off, a value deduced from the quantitative analysis of the experimental images, as well as obtained theoretically. The contact line's movement is found to be similar to that of drop formation in a wettable nozzle [149].

- The low flow rates during the experiments direct the dynamics of drop formation in the *static-pinch-off* regime.

The findings of this study may stimulate further investigations on the dynamics of a droplet generating from a yarn with different chemical and physical textures. Also,

TH-2590_156103041

more experiments with liquids having wider ranges of the relevant properties, including nonwetting fluids, can be performed to extend the validity of the proposed asymptotic relations. Moreover, careful numerical simulations may shed light on understanding the dynamics of drop formation in many naturally observed and synthetic hierarchical porous structures.

In Chapter 4, a detailed appraisal of the magnetowetting dynamics of paramagnetic droplets resting atop a soft viscoelastic surface is discussed. While the magnetic field's effect on the wetting dynamics of the sessile magnetic droplets has been discussed exhaustively in the previous studies, this chapter unravels that the enhanced substrate elasticity further alters such wetting dynamics. In a non-uniform magnetic field, the droplet's morphological evolution may even lead to irreversible shape change and, subsequently, engender secondary droplets by splitting. By considering the temporal evolution of the contact angle and the TPCL during magnetowetting on soft-substrates different regimes have been explored. Some of the significant conclusions from the experiments in Chapter 4 are:

- The (apparent) contact angle decreases due to the continuous elongation of the sessile droplet in a direction parallel to the magnetic field. During magnetowetting on a rigid substrate, the contact angle decrease appears to be lesser than that of the soft substrate. On the other hand, the contact line motion is often restricted on the soft-substrate due to enhanced pinning aided by substrate compliance. Contrarily, on the rigid substrates, the contact line experiences less hindrance during the magnetowetting period.

- The contact line exhibits *stick-slip* motion on an apparently rigid surface, whereas, in the case of a soft surface *pinning* dynamics are observed. The pinning dynamics are controlled by the *stick-break* mechanism of the large wetting ridge formed on soft substrates during magnetowetting. An energy budget analysis of the Gibbs free energy for overcoming resistance offered by the wetting ridge on soft substrates agrees well with our experimental results.

- Due to the dominant pinning dynamics on soft surfaces, the *initial pinning* period increases considerably compared to rigid substrates. Also, the time period of magnetowetting increases significantly with an increase in the softness of the underlying substrate in the presence of a magnetic field of similar strength.

TH-2590_156103041

- The extreme elongation of the magnetic droplet in the non-uniform magnetic field eventually leads to the primary droplet's bifurcation, thereby resulting in secondary droplets. The secondary droplet size increases as the surface's softness increases, indicating a higher mass transfer rate at a similar magnetic environment.

The present study can be extended to see the effect of a higher magnetic field and explore the contact line motion in related cases. The study is highly relevant to the magnetic droplet printing applications or applications involving ferrofluid droplet generation.

Chapter 5 presents an experimental investigation of a system wherein intense electrical energy has been deposited inside a sessile droplet. The confinement of the shock waves inside the droplet resulted in some awe-striking hydrodynamics, namely the formation of *liquid crown*, *long slender jet*, and the *explosion* of the droplet. The results corroborate that a variation of the electric field can shift the dynamics from one regime to another. Again, the change in thermophysical properties of the droplet, namely viscosity, and conductivity, also lead to a change in hydrodynamics. The study reports a novel method for controlling such violent dynamics to make it worthwhile for many industrial processes. The primary conclusions obtained are as follows:

- Emulating an EWOD setup, the droplet sitting on a cathode-isolator pair is integrated with an anode from the top to confine the discharge in the liquid. Beyond a critical field intensity, the dielectric breakdown generates a discharge in the form of releasing localized light and/or thermal energies, which in turn causes actuation, expansion, and collapse of cavitation bubbles in the droplet. Subsequently, several discharge-mediated hydrodynamics, such as bursting, jetting, and crown formation, have been observed. The crowns are characterized by the formation of a metastable cylindrical liquid sheet topped by a developed rim decorated with periodic liquid spikes. On the other hand, the liquid jets show an upward movement before breaking into an array of secondary droplets. Further, in comparison to the previously reported laser-based setups [5], a simpler, as well as economic (in terms of the mechanical energy conversion efficiency) alternative of *bursting* of a droplet into an array of microdroplets in a few milliseconds, is proposed in this chapter [43]. Conditionally, a host of interesting flow morphologies are observed, which include

TH-2590_156103041

high-aspect-ratio microjets, end-pinching of a liquid jet, high-aspect-ratio liquid spikes riding on the rim of a crown, and the capillary breakup of a liquid jet, among others. The energy conversion efficiency of bursting is approximately 25%-30%, while the same has been less than 2% for the jetting or crown formation.

- The simulations uncover that the location of dielectric breakdown under the droplet can be one of the important factors for developing different flow morphologies. For example, a bursting phenomenon can be expected at high field intensity when the breakdown is immediately under the anode (i.e., at the center of the droplet-base). In contrast, jetting (crowning) can be observed at lower (intermediate) field intensities when the breakdown occurs near the droplet's three-phase contact line. The deviation of the discharge location from the center-of-gravity of the droplet is another factor found to decide the type of flow morphology observed after discharge. Interestingly, the transition of flow morphologies can be done by tuning the thermodynamic factors such as the applied electric field intensity and/or the droplet size and the kinetic parameters such as the electrical conductivity and/or viscosity of the droplet. While a higher electrical conductivity ($\geq$ 0.5 M) and field intensity ($>$ 15 kV/cm) facilitate bursting, a lower field intensity leads to the crown formation or jetting. Again, for a given field intensity and conductivity, different flow morphologies can be obtained by tuning the droplet's viscosity. The theoretical and experimental timescales for the discharge mediated formation and sealing of liquid-crown, formation, and the breakup of a jet, and bursting of the droplet are discussed based on the balances of the electric field, surface tension, and the viscous forces.

- During the jetting, in the front, the bulbous secondary droplet is formed following the well-known *end-pinching* mechanism [320] while the rest of the jet breaks following the *Plateau-Rayleigh instability* (primarily in case of viscous jets). About five-to-ten-fold miniaturization of the primary droplet is observed during such a process. In contrast, the bursting of the droplet leads to approximately thirty-to-forty-fold miniaturization, highlighting the potential of the proposed method in the development of liquid sprays or atomizers.

- The droplet atomization strategy proposed here is competitive, if not similar

TH-2590_156103041

or superior, to the processes available, in terms of energy efficiency. However, such comparative studies are to be explored considering the difference in underlying mechanisms involving light, sound, electric, or magnetic fields. Also, the overall efficiency of the current method is to be compared and contrasted against some of the commonly employed droplet atomization techniques [4, 12, 13, 334–337]. In the near future, alongside exploring the fundamental and applied aspects of the proposed phenomenon, the applications of the same for inkjet printing [19], electro-spraying [219], droplet miniaturization, tissue ablation [299], electroporation [300] or biomedical devices [132] can also be explored.

In chapter 6, a detailed experimental investigation of the dynamic wetting behaviour of candle soot coated superhydrophobic surface is presented. The flame deposition of carbon soot nanoparticles *(CSNPs)* on a thin PDMS film-coated hydrophobic surface ensures the formation of a fractal network of CSNPs and results in extreme water repellency. The static wetting characteristics of such types of surfaces have been studied beforehand [379]. The dynamic wetting behaviour of the target surface is ensured through the analysis of the impact dynamics of viscous droplets on the proposed surface. The significant outcomes of the study are listed below:

- During the impact of water droplets on silica-coated SHPs, Deng *et al.* [369] and subsequent studies [370–374] have observed the *partial rebound* behavior within the experimental range $15 \leq We \leq 60$, preceding the *splashing regime*. In this study, with bare soot-coated SHPs, no such pinning regime has been observed within the same experimental range. Instead, in the latter study, the droplet impact dynamics directly enter the splashing regime from the *complete rebound* regime. Notably, the partial pinning regime is the indicator of the *Cassie-to-Wenzel* transition in droplet impact and is considered undesirable for self-cleaning applications. This difference in the wetting behavior further affects the retraction dynamics of the droplet contact line on both bare and silica-coated, CSNPs based superhydrophobic surfaces, resulting in a slower retraction rate in the latter.

- With an increase in the liquid viscosity, the *complete rebound* events are suppressed, and *partial rebound* (or *partial pinning*) phenomenon is observed. For very high viscosity droplets, post-impact, the dynamics are shifted from

TH-2590_156103041

the *Cassie-Baxter* mode to the *Wenzel* mode, thereby resulting in enhanced pinning during droplet retraction.

- Both the spreading and retraction rate of the contact line decreases with an increase in the liquid viscosity. On the other hand, the maximum spreading ratio increases with an increase in the impact speed. Further, the droplet's retraction rate follows the *Taylor-Culick* prediction for all the impact velocities studies herein.

- The contact time, defined as the time from the instant of impact to the instant the droplet lifts itself, increases with an increase in the Weber number. Again, for similar experimental conditions, the contact time is substantially higher for viscous droplet impact than that of the less viscous droplet. Additionally, the contact time exhibits a strong dependency on the spreading parameter for all liquids with different viscosity, expressed through a scaling law based on non-dimensional parameters We and Re.

- When the liquid velocity is increased beyond a threshold limit, the prompt splashing of the impacting drop is observed in the case of less viscous solutions. In this regime, the mean size of the secondary droplets engendered reduces with an increase in the Weber number. In contrast, the splashing of viscous droplets produces secondary droplets of larger mean size than that of the less viscous droplets in similar experimental conditions. Besides, the number of secondary droplets increases with an increase in the We, whereas, tend to decrease with an increase in the liquid viscosity in similar impact conditions.

- The current CSNPs coated superhydrophobic surface shows similar or competitive, if not superior, water-repelling behaviour to the existing superhydrophobic surfaces. This is determined based on the comparison of restitution coefficient, contact time, spreading ratio, and retraction rate for different superhydrophobic surfaces during the impact of water droplets.

The studied CSNPs coated non-functionalized superhydrophobic surface shows extreme water-repelling behaviour. Surprisingly, the surface retained its superhydrophobicity even at very high velocity and viscosity (up to 20 times higher than that of DI-water), as shown by the dynamic wetting characteristics. As such, it can be a viable alternative to the family of outdoor superhydrophobic coatings.

TH-2590_156103041

Again, considering the comparatively easier one-step fabrication method as well as lower fabrication cost, the current CSNPs coated surface can be a great choice for applications aiming at low-cost superhydrophobic/superamphiphobic surfaces.

7.2 Scope of future work

The present dissertation work experimentally investigates a few interesting physical systems in the purview of digital microfluidics. The current work makes an honest attempt to provide a detailed appraisal of the physical systems under consideration by considering different parametric studies. However, many potential areas are yet to be explored in the physical systems considered in this thesis work. In this regard, a few possible extensions that may form the basis of future research are mentioned as future scope below:

- The yarn-based droplet generators are expected to behave differently for non-wetting fluids, thereby exhibiting additional dynamics of droplet growth. Also, the yarn can be functionalized with external coatings, and the dynamics of droplet growth can be studied in detail.

- The combined effect of substrate elasticity and nanoparticle concentration on the soft magnetowetting phenomenon can shed light on the transition of the contact line dynamics from *stick-slip* to *stick-break* mode. Besides, the strength, as well as the direction of the applied magnetic field, can introduce additional dynamics during magnetowetting.

- The dielectric-discharge-mediated droplet breakup dynamics can be explored further considering the effect of the substrate wettability. Moreover, the effect of the anode size and its orientation can be assessed to provide full control of the ensuing hydrodynamic features. Also, the effect of the droplet volume and the dynamic contact angle of the droplet on the observed hydrodynamics can be an interesting aspect to be explored in the near future.

- The experimental fluids employed in this thesis work are mostly Newtonian fluids. Again, a wide variety of non-Newtonian fluids are ubiquitously used in a plethora of applications. Generally, the viscosity of the non-Newtonian fluids depends on the applied shear rate or the shear rate history. Hence,

TH-2590_156103041

it can be envisaged that such a shear rate-dependent viscous behaviour of the experimental fluids may alter the ensuing flow morphologies in all the physical systems discussed in this thesis. Furthermore, the velocity of the ejected secondary droplets from the rim of the expanding droplet can also be explored in future works with the help of state-of-the-art instruments such as micro-PIV or 4D-confocal microscopy.

TH-2590_156103041

References

[1] Stone H.A., Stroock A.D., and Ajdari A. (2004) 'Engineering flows in small devices: microfluidics toward a lab-on-a-chip', *Annu. Rev. Fluid Mech.*, vol. 36, pp. 381–411.

[2] Low L.A., Mummery C., Berridge B.R., Austin C.P., and Tagle D.A. (2020) 'Organs-on-chips: Into the next decade', *Nat. Rev. Drug Discov.*, vol. 36, pp. 1–17.

[3] Choi K., Ng A.H., Fobel R., and Wheeler A.R. (2012) 'Digital microfluidics', *Annu. Rev. Anal. Chem.*, vol. 5, pp. 413–440.

[4] Taylor G.I. (1964) 'Disintegration of water drops in an electric field', *Proc. R. Soc. Lond. A*, vol. 280(1382), pp. 383–397.

[5] Klein A.L., Bouwhuis W., Visser C.W., Lhuissier H., Sun C., Snoeijer J.H., Villermaux E., Lohse D., and Gelderblom H. (2015) 'Drop shaping by laser-pulse impact', *Phys. Rev. Appl.*, vol. 3(4), p. 044018.

[6] Kumar S., Sarma B., Dasmahapatra A.K., Dalal A., Basu D.N., and Bandyopadhyay D. (2017) 'Field induced anomalous spreading, oscillation, ejection, spinning, and breaking of oil droplets on a strongly slipping water surface', *Faraday Discuss.*, vol. 199, pp. 115–128.

[7] Vadivukkarasan M., Dhivyaraja K., and Panchagnula M.V. (2020) 'Breakup morphology of expelled respiratory liquid: From the perspective of hydrodynamic instabilities', *Phys. Fluids*, vol. 32(9), p. 094101.

[8] Abkarian M., Mendez S., Xue N., Yang F., and Stone H.A. (2020) 'Speech can produce jet-like transport relevant to asymptomatic spreading of virus', *Proc. Natl. Acad. Sci. U.S.A.*, vol. 117(41), pp. 25237–25245.

TH-2590_156103041

[9] Marston J.O., Truscott T.T., Speirs N.B., Mansoor M.M., and Thoroddsen S.T. (2016) 'Crown sealing and buckling instability during water entry of spheres', *J. Fluid Mech.*, vol. 794, pp. 506–529.

[10] Janzen C., Fleige R., Noll R., Schwenke H., Lahmann W., Knoth J., Beaven P., Jantzen E., Oest A., and Koke P. (2005) 'Analysis of small droplets with a new detector for liquid chromatography based on laser-induced breakdown spectroscopy', *Spectrochim. Acta B*, vol. 60(7-8), pp. 993–1001.

[11] Ravi A.D., Sadhna D., Nagpaal D., and Chawla L. (2015) 'Needle free injection technology: a complete insight', *Int. J. Pharm. Invest.*, vol. 5(4), p. 192.

[12] Gañán-Calvo A.M. (1998) 'Generation of steady liquid microthreads and micron-sized monodisperse sprays in gas streams', *Phys. Rev. Lett.*, vol. 80(2), pp. 285–288.

[13] DePonte D., Weierstall U., Schmidt K., Warner J., Starodub D., Spence J., and Doak R. (2008) 'Gas dynamic virtual nozzle for generation of microscopic droplet streams', *J. Phys. D: Appl. Phys.*, vol. 41(19), p. 195505.

[14] Cassie A.B.D. and Baxter S. (1944) 'Wettability of porous surfaces', *Trans. Faraday Soc.*, vol. 40, pp. 546–551.

[15] Wenzel R.N. (1936) 'Resistance of solid surfaces to wetting by water', *Ind. Eng. Chem.*, vol. 28(8), pp. 988–994.

[16] Marmur A. (2006) 'Soft contact: measurement and interpretation of contact angles', *Soft Matter*, vol. 2(1), pp. 12–17.

[17] Bormashenko E., Pogreb R., Stein T., Whyman G., Erlich M., Musin A., Machavariani V., and Aurbach D. (2008) 'Characterization of rough surfaces with vibrated drops', *Phys. Chem. Chem. Phys.*, vol. 10(27), pp. 4056–4061.

[18] Whyman G., Bormashenko E., and Stein T. (2008) 'The rigorous derivation of young, cassie–baxter and wenzel equations and the analysis of the contact angle hysteresis phenomenon', *Chem. Phys. Lett.*, vol. 450(4-6), pp. 355–359.

[19] Hoath S.D., *Fundamentals of inkjet printing: the science of inkjet and droplets* (John Wiley & Sons, New York, 2016).

TH-2590_156103041

[20] Chen X., Wu J., Ma R., Hua M., Koratkar N., Yao S., and Wang Z. (2011) 'Nanograssed micropyramidal architectures for continuous dropwise condensation', *Adv. Funct. Mater.*, vol. 21(24), pp. 4617–4623.

[21] Shanahan M. (1988) 'The spreading dynamics of a liquid drop on a viscoelastic solid', *J. Phys. D: Appl. Phys.*, vol. 21(6), p. 981.

[22] Shield T., Bogy D., and Talke F. (1987) 'Drop formation by dod ink-jet nozzles: A comparison of experiment and numerical simulation', *IBM J. Res. Dev.*, vol. 31(1), pp. 96–110.

[23] Eggers J. and Villermaux E. (2008) 'Physics of liquid jets', *Rep. Prog. Phys.*, vol. 71(3), p. 036601.

[24] Subramani H.J., Yeoh H.K., Suryo R., Xu Q., Ambravaneswaran B., and Basaran O.A. (2006) 'Simplicity and complexity in a dripping faucet', *Phys. Fluids*, vol. 18(3), p. 032106.

[25] Wilson S. (1988) 'The slow dripping of a viscous fluid', *J. Fluid Mech.*, vol. 190, pp. 561–570.

[26] Omocea I.L., Patrascu C., Turcanu M., and Balan C. (2016) 'Breakup of liquid jets', *Energy Procedia*, vol. 85, pp. 383–389.

[27] Borthakur M.P., Biswas G., and Bandyopadhyay D. (2017) 'Formation of liquid drops at an orifice and dynamics of pinch-off in liquid jets', *Phys. Rev. E.*, vol. 96(1), p. 013115.

[28] Lamorgese A. and Mauri R. (2015) 'Buoyancy-driven detachment of a wall-bound pendant drop: Interface shape at pinchoff and nonequilibrium surface tension', *Phys. Rev. E*, vol. 92(3), p. 032401.

[29] Worthington A.M. (1876) 'On the forms assumed by drops of liquids falling vertically on a horizontal plate', *Proc. R. Soc. Lond.*, vol. 25, pp. 261–271.

[30] Worthington A.M. and Cole R.S. (1897) 'Impact with a liquid surface, studied by the aid of instantaneous photography', *Phil. Trans. R. Soc. Lond. A*, vol. 189, pp. 137–148.

TH-2590_156103041

[31] Worthington A.M. and Cole R.S. (1900) 'Impact with a liquid surface studied by the aid of instantaneous photography. paper II', *Phil. Trans. R. Soc. Lond. A*, vol. 194, pp. 175–199.

[32] Oguz H.N. and Prosperetti A. (1990) 'Bubble entrainment by the impact of drops on liquid surfaces', *J. Fluid Mech.*, vol. 219, pp. 143–179.

[33] Shin J. and McMahon T.A. (1990) 'The tuning of a splash', *Phys. Fluids A: Fluid Dynamics*, vol. 2(8), pp. 1312–1317.

[34] Rein M. (1993) 'Phenomena of liquid drop impact on solid and liquid surfaces', *Fluid Dyn. Res.*, vol. 12(2), pp. 61–93.

[35] Morton D., Rudman M., and Jong-Leng L. (2000) 'An investigation of the flow regimes resulting from splashing drops', *Phys. Fluids*, vol. 12(4), pp. 747–763.

[36] Howison S.D., Ockendon J.R., Oliver J.M., Purvis R., and Smith F.T. (2005) 'Droplet impact on a thin fluid layer', *J. Fluid Mech.*, vol. 542, pp. 1–23.

[37] Bartolo D., Josserand C., and Bonn D. (2006) 'Singular jets and bubbles in drop impact', *Phys. Rev. Lett.*, vol. 96(12), p. 124501.

[38] Yarin A.L. (2006) 'Drop impact dynamics: splashing, spreading, receding, bouncing', *Annu. Rev. Fluid Mech.*, vol. 38, pp. 159–192.

[39] Deng Q., Anilkumar A.V., and Wang T.G. (2007) 'The role of viscosity and surface tension in bubble entrapment during drop impact onto a deep liquid pool', *J. Fluid Mech.*, vol. 578, pp. 119–138.

[40] Boulton-Stone J.M. and Blake J.R. (1993) 'Gas bubbles bursting at a free surface', *J. Fluid Mech.*, vol. 254, pp. 437–466.

[41] Duchemin L., Popinet S., Josserand C., and Zaleski S. (2002) 'Jet formation in bubbles bursting at a free surface', *Phys. Fluids*, vol. 14(9), pp. 3000–3008.

[42] Liger-Belair G., Polidori G., and Jeandet P. (2008) 'Recent advances in the science of champagne bubbles', *Chem. Soc. Rev.*, vol. 37(11), pp. 2490–2511.

[43] Thoroddsen S.T., Takehara K., Etoh T.G., and Ohl C.D. (2009) 'Spray and microjets produced by focusing a laser pulse into a hemispherical drop', *Phys. Fluids*, vol. 21(11), p. 112101.

TH-2590_156103041

[44] MacIntyre F. (1968) 'Bubbles: a boundary-layer 'microtome' for micron-thick samples of a liquid surface', *J. Phys. Chem.*, vol. 72(2), pp. 589–592.

[45] Thoroddsen S.T., Etoh T.G., and Takehara K. (2007) 'Microjetting from wave focusing on oscillating drops', *Phys. Fluids*, vol. 19(5), p. 052101.

[46] Hogrefe J.E., Peffley N.L., Goodridge C.L., Shi W.T., Hentschel H.G.E., and Lathrop D.P. (1998) 'Power-law singularities in gravity-capillary waves', *Physica D*, vol. 123(1-4), pp. 183–205.

[47] Zeff B.W., Kleber B., Fineberg J., and Lathrop D.P. (2000) 'Singularity dynamics in curvature collapse and jet eruption on a fluid surface', *Nature*, vol. 403(6768), p. 401.

[48] James A.J., Vukasinovic B., Smith M.K., and Glezer A. (2003) 'Vibration-induced drop atomization and bursting', *J. Fluid Mech.*, vol. 476, pp. 1–28.

[49] Ohl C.D. and Ikink R. (2003) 'Shock-wave-induced jetting of micron-size bubbles', *Phys. Rev. Lett.*, vol. 90(21), p. 214502.

[50] Antkowiak A., Bremond N., Le Dizès S., and Villermaux E. (2007) 'Short-term dynamics of a density interface following an impact', *J. Fluid Mech.*, vol. 577, pp. 241–250.

[51] Tjan K.K. and Phillips W.R.C. (2007) 'On impulsively generated inviscid axisymmetric surface jets, waves and drops', *J. Fluid Mech.*, vol. 576, pp. 377–403.

[52] Borthakur M.P., Biswas G., Bandyopadhyay D., and Sahu K.C. (2019) 'Dynamics of an arched liquid jet under the influence of gravity', *Eur. J. Mech. B: Fluids*, vol. 74, pp. 1–9.

[53] Worthington A.M., *A Study of Splashes* (Longmans, Green, and Company, 1908).

[54] Versluis M. (2013) 'High-speed imaging in fluids', *Exp. Fluids*, vol. 54(2), p. 1458.

[55] Truscott T.T., Epps B.P., and Belden J. (2014) 'Water entry of projectiles', *Annu. Rev. Fluid Mech.*, vol. 46, pp. 355–378.

TH-2590_156103041

[56] Wagner H. (1932) 'Uber Stoss-und Gleitvorgänge an der Oberflache von Flussigkeiten', *Z. Angew. Math. Mech.*, vol. 12(4), pp. 193–215.

[57] Scolan Y.M. and Korobkin A.A. (2001) 'Three-dimensional theory of water impact. part 1. inverse wagner problem', *J. Fluid Mech.*, vol. 440, pp. 293–326.

[58] Krechetnikov R. (2010) 'Stability of liquid sheet edges', *Phys. Fluids*, vol. 22(9), p. 092101.

[59] Peters I.R., van der Meer D., and Gordillo J.M. (2013) 'Splash wave and crown breakup after disc impact on a liquid surface', *J. Fluid Mech.*, vol. 724, pp. 553–580.

[60] Marston J.O., Mansoor M.M., Thoroddsen S.T., and Truscott T.T. (2016) 'The effect of ambient pressure on ejecta sheets from free-surface ablation', *Exp. Fluids*, vol. 57(5), p. 61.

[61] May A. (1952) 'Vertical entry of missiles into water', *J. Appl. Phys.*, vol. 23(12), pp. 1362–1372.

[62] Rayleigh L. (1882) 'Xx. on the equilibrium of liquid conducting masses charged with electricity', *Philos. Mag.*, vol. 14(87), pp. 184–186.

[63] Macky W. (1931) 'Some investigations on the deformation and breaking of water drops in strong electric fields', *Proc. R. Soc. Lond. A*, vol. 133(822), pp. 565–587.

[64] Collins R.T., Jones J.J., Harris M.T., and Basaran O.A. (2008) 'Electrohydrodynamic tip streaming and emission of charged drops from liquid cones', *Nat. Phys.*, vol. 4(2), pp. 149–154.

[65] Achtzehn T., Müller R., Duft D., and Leisner T. (2005) 'The coulomb instability of charged microdroplets: dynamics and scaling', *Eur. Phys. J. D*, vol. 34(1-3), pp. 311–313.

[66] Fenn J.B., Mann M., Meng C.K., Wong S.F., and Whitehouse C.M. (1989) 'Electrospray ionization for mass spectrometry of large biomolecules', *Science*, vol. 246(4926), pp. 64–71.

TH-2590_156103041

[67] Collins R.T., Sambath K., Harris M.T., and Basaran O.A. (2013) 'Universal scaling laws for the disintegration of electrified drops', *Proc. Natl. Acad. Sci. U.S.A.*, vol. 110(13), pp. 4905–4910.

[68] Brosseau Q. and Vlahovska P.M. (2017) 'Streaming from the equator of a drop in an external electric field', *Phys. Rev. Lett.*, vol. 119(3), p. 034501.

[69] Lipmann G. (1875) 'On a property of an electrized water-surface', *Philos. Mag*, vol. 50(330), pp. 254–254.

[70] Lee J. and Kim C.J., 'Liquid micromotor driven by continuous electrowetting', in 'Proceedings MEMS 98. IEEE. Eleventh Annual International Workshop on Micro Electro Mechanical Systems. An Investigation of Micro Structures, Sensors, Actuators, Machines and Systems', (IEEE, 1998), pp. 538–543.

[71] Wang Y. and Zhao Y.P. (2012) 'Electrowetting on curved surfaces', *Soft Matter*, vol. 8(9), pp. 2599–2606.

[72] Lomax D.J., Kant P., Williams A.T., Patten H.V., Zou Y., Juel A., and Dryfe R.A. (2016) 'Ultra-low voltage electrowetting using graphite surfaces', *Soft Matter*, vol. 12(42), pp. 8798–8804.

[73] Taherian F., Leroy F., Heim L.O., Bonaccurso E., and van der Vegt N.F. (2016) 'Mechanism for asymmetric nanoscale electrowetting of an ionic liquid on graphene', *Langmuir*, vol. 32(1), pp. 140–150.

[74] Beni G. and Hackwood S. (1981) 'Electro-wetting displays', *Appl. Phys. Lett.*, vol. 38(4), pp. 207–209.

[75] Girault H.H. (2006) 'Shake, rattle and roll', *Nat. Mater.*, vol. 5(11), pp. 851–852.

[76] Dhindsa M., Heikenfeld J., Weekamp W., and Kuiper S. (2011) 'Electrowetting without electrolysis on self-healing dielectrics', *Langmuir*, vol. 27(9), pp. 5665–5670.

[77] Berge B. (1993) 'Electrocapillarity and wetting of insulator films by water', *C. R. Acad. Sci. II*, vol. 317(2), pp. 157–163.

TH-2590_156103041

[78] Lee S.J., Hong J., Kang K.H., Kang I.S., and Lee S.J. (2014) 'Electrowetting-induced droplet detachment from hydrophobic surfaces', *Langmuir*, vol. 30(7), pp. 1805–1811.

[79] Yang Q., Li B.Q., and Ding Y. (2013) 'A numerical study of nanoscale electrohydrodynamic patterning in a liquid film', *Soft Matter*, vol. 9(12), pp. 3412–3423.

[80] Sharma A., Tiwari V., Kumar V., Mandal T.K., and Bandyopadhyay D. (2014) 'Localized electric field induced transition and miniaturization of two-phase flow patterns inside microchannels', *Electrophoresis*, vol. 35(20), pp. 2930–2937.

[81] Mugele F., Staicu A., Bakker R., and van den Ende D. (2011) 'Capillary stokes drift: a new driving mechanism for mixing in ac-electrowetting', *Lab Chip*, vol. 11(12).

[82] Timung S., Chaudhuri J., Borthakur M.P., Mandal T.K., Biswas G., and Bandyopadhyay D. (2017) 'Electric field mediated spraying of miniaturized droplets inside microchannel', *Electrophoresis*, vol. 38(11), pp. 1450–1457.

[83] Dubois P., Marchand G., Fouillet Y., Berthier J., Douki T., Hassine F., Gmouh S., and Vaultier M. (2006) 'Ionic liquid droplet as e-microreactor', *Anal. Chem.*, vol. 78(14), pp. 4909–4917.

[84] Miljkovic N., Preston D.J., Enright R., and Wang E.N. (2014) 'Jumping-droplet electrostatic energy harvesting', *Appl. Phys. Lett.*, vol. 105(1), p. 013111.

[85] Bhattacharjee M., Pasumarthi V., Chaudhuri J., Singh A.K., Nemade H., and Bandyopadhyay D. (2016) 'Self-spinning nanoparticle laden microdroplets for sensing and energy harvesting', *Nanoscale*, vol. 8(11), pp. 6118–6128.

[86] Wang K.L. and Jones T. (2005) 'Electrowetting dynamics of microfluidic actuation', *Langmuir*, vol. 21(9), pp. 4211–4217.

[87] Quilliet C. and Berge B. (2001) 'Electrowetting: a recent outbreak', *Curr. Opin. Colloid Interface Sci.*, vol. 6(1), pp. 34–39.

TH-2590_156103041

[88] etulipa (2006), 'Electro wetting display technology offers many possibilities', `https://etulipa.com/grid-independent-no-light-pollution/`, accessed: 2020-12-03.

[89] Deladi S., Suijver J., Shi Y., Shahzad K., De Boer B., Rademakers A., Van Der Vleuten C., Jankovic L., Bongers E., Harks E., et al. (2010) 'Miniaturized ultrasound scanner by electrowetting', *Appl. Phys. Lett.*, vol. 97(6), p. 064102.

[90] Chen J., Kutana A., Collier C., and Giapis K. (2005) 'Electrowetting in carbon nanotubes', *Science*, vol. 310(5753), pp. 1480–1483.

[91] Verplanck N., Galopin E., Camart J.C., Thomy V., Coffinier Y., and Boukherroub R. (2007) 'Reversible electrowetting on superhydrophobic silicon nanowires', *Nano Lett.*, vol. 7(3), pp. 813–817.

[92] Manukyan G., Oh J., Van Den Ende D., Lammertink R.G., and Mugele F. (2011) 'Electrical switching of wetting states on superhydrophobic surfaces: a route towards reversible cassie-to-wenzel transitions', *Phys. Rev. Lett.*, vol. 106(1), p. 014501.

[93] Dhindsa M.S., Smith N.R., Heikenfeld J., Rack P.D., Fowlkes J.D., Doktycz M.J., Melechko A.V., and Simpson M.L. (2006) 'Reversible electrowetting of vertically aligned superhydrophobic carbon nanofibers', *Langmuir*, vol. 22(21), pp. 9030–9034.

[94] Wheeler A.R. (2008) 'Putting electrowetting to work', *Science*, vol. 322(5901), pp. 539–540.

[95] Krupenkin T. and Taylor J.A. (2011) 'Reverse electrowetting as a new approach to high-power energy harvesting', *Nat. Commun.*, vol. 2(1), pp. 1–8.

[96] Chandrasekhar S., *Hydrodynamic and Hydromagnetic Stability* (Courier Corporation, 1961).

[97] Davidson P.A., *An introduction to magnetohydrodynamics* (American Association of Physics Teachers, 2002).

[98] Rosensweig R.E., *Ferrohydrodynamics* (Cambridge University Press, Cambridge ; New York, 1985), 1st Ed.

TH-2590_156103041

[99] Rosensweig R.E. (1987) 'Magnetic fluids', *Annu. Rev. Fluid Mech.*, vol. 19(1), pp. 437–461.

[100] Egatz-Gómez A., Melle S., García A.A., Lindsay S., Márquez M., Domínguez-García P., Rubio M.A., Picraux S., Taraci J., Clement T., et al. (2006) 'Discrete magnetic microfluidics', *Appl. Phys. Lett.*, vol. 89(3), p. 034106.

[101] Beetz A., Gollwitzer C., Richter R., and Rehberg I. (2008) 'Response of a ferrofluid to traveling-stripe forcing', *J. Phys. Condens. Matter*, vol. 20(20), p. 204109.

[102] Rinaldi C. and Zahn M. (2004) 'Ferrohydrodynamic instabilities in dc magnetic fields', *J. Visualization*, vol. 7(1), pp. 8–8.

[103] Torres-Díaz I. and Rinaldi C. (2014) 'Recent progress in ferrofluids research: novel applications of magnetically controllable and tunable fluids', *Soft Matter*, vol. 10(43), pp. 8584–8602.

[104] Kumar D., Chandra P., and Sinha P. (1993) 'Ferrofluid lubrication of externally pressurized circular plates and conical bearings', *Int. J. Eng. Sci.*, vol. 31(4), pp. 593–604.

[105] Kong L. and Chen W. (2014) 'Carbon nanotube and graphene-based bioinspired electrochemical actuators', *Adv. Mater.*, vol. 26(7), pp. 1025–1043.

[106] Oh D.W., Jin J.S., Choi J.H., Kim H.Y., and Lee J.S. (2007) 'A microfluidic chaotic mixer using ferrofluid', *J. Micromech. Microeng.*, vol. 17(10), p. 2077.

[107] Engelmann S., Nethe A., Scholz T., and Stahlmann H.D. (2004) 'Force enhancement on a ferrofluid-driven linear stepping motor model', *J. Magn. Magn. Mater.*, vol. 272, pp. 2345–2347.

[108] Bellamkonda R., John T., Mathew B., DeCoster M., Hegab H., and Davis D. (2009) 'Fabrication and testing of a conicu/cu cpp-gmr nanowire-based microfluidic biosensor', *J. Micromech. Microeng.*, vol. 20(2), p. 025012.

[109] Murariu V. and Sergeant P. (2007) 'Modelling of the separation process in a ferrohydrostatic separator using discrete element method', *Phys. Sep. Sci. Eng.*, vol. 2007.

TH-2590_156103041

[110] Lai D.m., Deng L., Li J., Liao B., Guo Q.x., and Fu Y. (2011) 'Hydrolysis of cellulose into glucose by magnetic solid acid', *ChemSusChem*, vol. 4(1), pp. 55–58.

[111] Zhang Q., Su H., Luo J., and Wei Y. (2012) 'A magnetic nanoparticle supported dual acidic ionic liquid: a "quasi-homogeneous" catalyst for the one-pot synthesis of benzoxanthenes', *Green Chem.*, vol. 14(1), pp. 201–208.

[112] Raj K., Moskowitz B., and Casciari R. (1995) 'Advances in ferrofluid technology', *J. Magn. Magn. Mater.*, vol. 149(1-2), pp. 174–180.

[113] Shannon M.A., Bohn P.W., Elimelech M., Georgiadis J.G., Marinas B.J., and Mayes A.M., 'Science and technology for water purification in the coming decades', in 'Nanoscience and technology: a collection of reviews from nature Journals', (World Scientific, 2010), pp. 337–346.

[114] Nguyen N.T., Zhu G., Chua Y.C., Phan V.N., and Tan S.H. (2010) 'Magnetowetting and sliding motion of a sessile ferrofluid droplet in the presence of a permanent magnet', *Langmuir*, vol. 26(15), pp. 12553–12559.

[115] Nguyen N.T. (2012) 'Micro-magnetofluidics: interactions between magnetism and fluid flow on the microscale', *Microfluid. Nanofluid.*, vol. 12(1), pp. 1–16.

[116] Zhang Y. and Nguyen N.T. (2017) 'Magnetic digital microfluidics–a review', *Lab Chip*, vol. 17(6), pp. 994–1008.

[117] Zhang K., Liang Q., Ma S., Mu X., Hu P., Wang Y., and Luo G. (2009) 'On-chip manipulation of continuous picoliter-volume superparamagnetic droplets using a magnetic force', *Lab Chip*, vol. 9(20), pp. 2992–2999.

[118] Ody T., Panth M., Sommers A., and Eid K. (2016) 'Controlling the motion of ferrofluid droplets using surface tension gradients and magnetoviscous pinning', *Langmuir*, vol. 32(27), pp. 6967–6976.

[119] Huang G., Li M., Yang Q., Li Y., Liu H., Yang H., and Xu F. (2017) 'Magnetically actuated droplet manipulation and its potential biomedical applications', *ACS Appl. Mater. Interfaces*, vol. 9(2), pp. 1155–1166.

[120] Rigoni C., Ferraro D., Carlassara M., Filippi D., Varagnolo S., Pierno M., Talbot D., Abou-Hassan A., and Mistura G. (2018) 'Dynamics of ferrofluid

TH-2590_156103041

drops on magnetically patterned surfaces', *Langmuir*, vol. 34(30), pp. 8917–8922.

[121] Beyzavi A. and Nguyen N.T. (2009) 'Programmable two-dimensional actuation of ferrofluid droplet using planar microcoils', *J. Micromech. Microeng.*, vol. 20(1), p. 015018.

[122] Timonen J.V., Latikka M., Leibler L., Ras R.H., and Ikkala O. (2013) 'Switchable static and dynamic self-assembly of magnetic droplets on superhydrophobic surfaces', *Science*, vol. 341(6143), pp. 253–257.

[123] Kumar S., Faridi M.R.A., Dasmahapatra A.K., and Bandyopadhyay D. (2016) 'Magnetic field induced push–pull motility of liquibots', *RSC advances*, vol. 6(108), pp. 107049–107056.

[124] Jamin T., Py C., and Falcon E. (2011) 'Instability of the origami of a ferrofluid drop in a magnetic field', *Phys. Rev. Lett.*, vol. 107(20), p. 204503.

[125] Wu Y., Fu T., Ma Y., and Li H.Z. (2013) 'Ferrofluid droplet formation and breakup dynamics in a microfluidic flow-focusing device', *Soft Matter*, vol. 9(41), pp. 9792–9798.

[126] Kahkeshani S. and Di Carlo D. (2016) 'Drop formation using ferrofluids driven magnetically in a step emulsification device', *Lab Chip*, vol. 16(13), pp. 2474–2480.

[127] Hermans T.M., Frauenrath H., and Stellacci F. (2013) 'Droplets out of equilibrium', *Science*, vol. 341(6143), pp. 243–244.

[128] Py C., Reverdy P., Doppler L., Bico J., Roman B., and Baroud C.N. (2007) 'Capillary origami: spontaneous wrapping of a droplet with an elastic sheet', *Phys. Rev. Lett.*, vol. 98(15), p. 156103.

[129] Apitz I. and Vogel A. (2005) 'Material ejection in nanosecond er: Yag laser ablation of water, liver, and skin', *Appl. Phys. A*, vol. 81(2), pp. 329–338.

[130] Blake J.R. and Gibson D.C. (1981) 'Growth and collapse of a vapour cavity near a free surface', *J. Fluid Mech.*, vol. 111, pp. 123–140.

TH-2590_156103041

[131] Gibson D.C. (1968), 'The third australasian conference on hydraulic and fluid mechanics sydney', .

[132] Fletcher D.A. and Palanker D.V. (2001) 'Pulsed liquid microjet for microsurgery', *Appl. Phys. Lett.*, vol. 78(13), pp. 1933–1935.

[133] Palanker D.V., Fletcher D.A., Miller J., Huie P., Marmor M., and Blumenkranz M.S. (2002) 'Pulsed liquid microjet for intravascular injection', *Proc. SPIE Opt. Technol.*, vol. 4611, pp. 72–75.

[134] Fletcher D.A., Palanker D.V., Huie P., Miller J., Marmor M.F., and Blumenkranz M.S. (2002) 'Intravascular drug delivery with a pulsed liquid microjet', *Arch. Ophthalmol.*, vol. 120(9), pp. 1206–1208.

[135] Vankov A. and Palanker D. (2007) 'Nanosecond plasma-mediated electrosurgery with elongated electrodes', *J. Appl. Phys.*, vol. 101(12), p. 124701.

[136] Obreschkow D., Kobel P., Dorsaz N., de Bosset A., Nicollier C., and Farhat M. (2006) 'Cavitation bubble dynamics inside liquid drops in microgravity', *Phys. Rev. Lett.*, vol. 97(9), p. 094502.

[137] Robert E., Lettry J., Farhat M., Monkewitz P.A., and Avellan F. (2007) 'Cavitation bubble behavior inside a liquid jet', *Phys. Fluids*, vol. 19(6), p. 067106.

[138] Kodama T., Takayama K., and Nagayasu N. (1996) 'The dynamics of two air bubbles loaded by an underwater shock wave', *J. Appl. Phys.*, vol. 80(10), pp. 5587–5592.

[139] Kodama T. and Tomita Y. (2000) 'Cavitation bubble behavior and bubble–shock wave interaction near a gelatin surface as a study of in vivo bubble dynamics', *Appl. Phys. B*, vol. 70(1), pp. 139–149.

[140] Villermaux E. (2007) 'Fragmentation', *Annu. Rev. Fluid Mech.*, vol. 39, pp. 419–446.

[141] Villermaux E. and Bossa B. (2009) 'Single-drop fragmentation determines size distribution of raindrops', *Nat. Phys.*, vol. 5(9), p. 697.

[142] Singh P.I. and Knight C.J. (1980) 'Pulsed laser-induced shattering of water drops', *AIAA J.*, vol. 18(1), pp. 96–100.

TH-2590_156103041

[143] Zhang J.Z., Lam J.K., Wood C.F., Chu B.T., and Chang R. (1987) 'Explosive vaporization of a large transparent droplet irradiated by a high intensity laser', *Appl. Opt.*, vol. 26(22), pp. 4731–4737.

[144] Lindinger A., Hagen J., Socaciu L.D., Bernhardt T.M., Wöste L., Duft D., and Leisner T. (2004) 'Time-resolved explosion dynamics of H_2O droplets induced by femtosecond laser pulses', *Appl. Opt.*, vol. 43(27), pp. 5263–5269.

[145] Avila S.R.G. and Ohl C.D. (2016) 'Fragmentation of acoustically levitating droplets by laser-induced cavitation bubbles', *J. Fluid Mech.*, vol. 805, pp. 551–576.

[146] Stan C.A., Milathianaki D., Laksmono H., Sierra R.G., McQueen T.A., Messerschmidt M., Williams G.J., Koglin J.E., Lane T.J., Hayes M.J., and Guillet S.A. (2016) 'Liquid explosions induced by X-ray laser pulses', *Nat. Phys.*, vol. 12(10), pp. 966–971.

[147] Snyder H.E. and Reitz R.D. (1998) 'Direct droplet production from a liquid film: a new gas-assisted atomization mechanism', *J. Fluid Mech.*, vol. 375, pp. 363–381.

[148] Banine V.Y., Koshelev K.N., and Swinkels G.H.P.M. (2011) 'Physical processes in euv sources for microlithography', *J. Phys. D*, vol. 44(25), p. 253001.

[149] Chang B., Nave G., and Jung S. (2012) 'Drop formation from a wettable nozzle', *Commun. Nonlinear Sci. Numer. Simul.*, vol. 17(5), pp. 2045–2051.

[150] Gerber J., Lendenmann T., Eghlidi H., Schutzius T.M., and Poulikakos D. (2019) 'Wetting transitions in droplet drying on soft materials', *Nat. Commun.*, vol. 10(1), pp. 1–10.

[151] Edgerton H.E. and Killian J.R., *Flash!: Seeing the unseen by ultra high-speed photography* (CT Branford Company, 1954).

[152] Hutchings I., Martin G., and Hoath S. (2007) 'High speed imaging and analysis of jet and drop formation', *J. Imaging Sci. Technol.*, vol. 51(5), pp. 438–444.

[153] Döring M. (1982) 'Ink-jet printing', *Philips tech. Rev.*, vol. 40, pp. 192–198.

TH-2590_156103041

[154] Chen A.U. and Basaran O.A. (2002) 'A new method for significantly reducing drop radius without reducing nozzle radius in drop-on-demand drop production', *Phys. Fluids*, vol. 14(1), pp. L1–L4.

[155] Song Q., Zhang G., and Qiu Z. (2003) 'Drop growth monitoring and drop volume measurement based on image drop analysis with ccd', *Instrum. Sci. Technol.*, vol. 31(1), pp. 1–13.

[156] Dong H., Carr W.W., and Morris J.F. (2006) 'An experimental study of drop-on-demand drop formation', *Phys. Fluids*, vol. 18(7), p. 072102.

[157] Photron (2015), 'Fastcam mini ux 100', `https://photron.com/mini-ux/`, accessed: 2020-10-13.

[158] Ohl C.D., Arora M., Ikink R., De Jong N., Versluis M., Delius M., and Lohse D. (2006) 'Sonoporation from jetting cavitation bubbles', *Biophys. J.*, vol. 91(11), pp. 4285–4295.

[159] Rossner M. and Yamada K.M. (2004) 'What's in a picture? the temptation of image manipulation', *J. Cell Biol.*, vol. 166(1), pp. 11–15.

[160] Nature (2006) 'Not picture-perfect.', *Nature*, vol. 439, pp. 891–892.

[161] Burger W. and Burge M., *Principles of Digital Image Processing: Core Algorithms*, Undergraduate Topics in Computer Science (Springer London, 2010).

[162] Burger W. and Burge M., *Principles of Digital Image Processing: Fundamental Techniques*, Undergraduate Topics in Computer Science (Springer London, 2010).

[163] Burger W. and Burge M., *Principles of Digital Image Processing: Advanced Methods*, Undergraduate Topics in Computer Science (Springer London, 2013).

[164] Schneider C.A., Rasband W.S., and Eliceiri K.W. (2012) 'Nih image to imagej: 25 years of image analysis', *Nature methods*, vol. 9(7), p. 671.

[165] MATLAB, *version 7.10.0 (R2010a)* (The MathWorks Inc., Natick, Massachusetts, 2010).

[166] The ImageMagick Development Team, 'Imagemagick', `https://imagemagick.org`, accessed: 2020-10-13.

TH-2590_156103041

[167] Bezanson J., Edelman A., Karpinski S., and Shah V.B. (2017) 'Julia: A fresh approach to numerical computing', *SIAM Rev.*, vol. 59(1), pp. 65–98.

[168] Lage-Freitas A., Frery A.C., Oliveira N.D., Ribeiro R.P., and Sarmento R., 'Cloudarray: Easing huge image processing', in '2016 IEEE International Geoscience and Remote Sensing Symposium (IGARSS)', (IEEE, 2016), pp. 631–634.

[169] Van der Walt S., Schönberger J.L., Nunez-Iglesias J., Boulogne F., Warner J.D., Yager N., Gouillart E., and Yu T. (2014) 'scikit-image: image processing in python', *Peer J.*, vol. 2, p. e453.

[170] Yoo T.S., Ackerman M.J., Lorensen W.E., Schroeder W., Chalana V., Aylward S., Metaxas D., and Whitaker R. (2002) 'Engineering and algorithm design for an image processing api: a technical report on itk-the insight toolkit', *Stud. Health. Technol. Inform.*, pp. 586–592.

[171] Bradski G. (2000) 'The OpenCV Library', *Dr. Dobb's Journal of Software Tools*.

[172] Russ J.C., *The image processing handbook* (CRC press, 2016).

[173] Washburn E.W. (1921) 'The dynamics of capillary flow', *Phys. Rev.*, vol. 17(3), p. 273.

[174] Richards L.A. (1931) 'Capillary conduction of liquids through porous mediums', *J. Appl. Phys.*, vol. 1(5), pp. 318–333.

[175] Hollies N.R., Kaessinger M.M., and Bogaty H. (1956) 'Water transport mechanisms in textile materials1 part i: the role of yarn roughness in capillary-type penetration', *Text. Res. J.*, vol. 26(11), pp. 829–835.

[176] Brown S.R. (1987) 'Fluid flow through rock joints: The effect of surface roughness', *J. Geophys. Res.*, vol. 92(B2), pp. 1337–1347.

[177] Danino D. and Marmur A. (1994) 'Radial capillary penetration into paper: limited and unlimited liquid reservoirs', *J. Colloid Interface Sci.*, vol. 166(1), pp. 245–250.

TH-2590_156103041

[178] Conrath M., Canfield P., Bronowicki P., Dreyer M.E., Weislogel M.M., and Grah A. (2013) 'Capillary channel flow experiments aboard the international space station', *Phys. Rev. E.*, vol. 88(6), p. 063009.

[179] Tsai C.C., Gu Y., and Kornev K.G. (2014) 'Wetting of nanofiber yarns', *Colloids Surf. A Physicochem Eng. Asp.*, vol. 459, pp. 22 – 30.

[180] Hsieh Y.L. (1995) 'Liquid transport in fabric structures', *Text. Res. J.*, vol. 65(5), pp. 299–307.

[181] Tang K.P.M., Chau K.H., Kan C.W., and Fan J.T. (2015) 'Characterizing the transplanar and in-plane water transport properties of fabrics under different sweat rate: Forced flow water transport tester', *Sci. Rep.*, vol. 5, p. 17012.

[182] Benjamin W. and Beckwith S. (1999) 'Resin transfer moulding–sampe monograph no. 3', *Covina, CA: Sampe International Business Office*.

[183] Reches M., Mirica K.A., Dasgupta R., Dickey M.D., Butte M.J., and Whitesides G.M. (2010) 'Thread as a matrix for biomedical assays', *ACS Appl. Mater. Interfaces*, vol. 2(6), pp. 1722–1728.

[184] Safavieh R., Zhou G.Z., and Juncker D. (2011) 'Microfluidics made of yarns and knots: from fundamental properties to simple networks and operations', *Lab Chip*, vol. 11, pp. 2618–2624.

[185] Cherenack K. and van Pieterson L. (2012) 'Smart textiles: challenges and opportunities', *J. Appl. Phys.*, vol. 112(9), p. 091301.

[186] White B. (1986) 'Bloodstain patterns on fabrics: the effect of drop volume, dropping height and impact angle', *Can. Soc. Forensic Sci. J.*, vol. 19(1), pp. 3–36.

[187] Li Q., Wang J., and Hurren C. (2017) 'A study on wicking in natural staple yarns', *J. Nat. Fibers*, vol. 14(3), pp. 400–409.

[188] Fourt L., Sookne A.M., Frishman D., and Harris M. (1951) 'The rate of drying of fabrics', *Text. Res. J.*, vol. 21(1), pp. 26–33.

[189] Pan N. and Gibson P., *Thermal and moisture transport in fibrous materials* (Woodhead Publishing, 2006).

TH-2590_156103041

[190] Hollies N.R.S., Kaessinger M.M., and Bogaty H. (1956) 'Water transport mechanisms in textile materials1 part i: the role of yarn roughness in capillary-type penetration', *Text. Res. J.*, vol. 26(11), pp. 829–835.

[191] Hollies N.R.S., Kaessinger M.M., Watson B.S., and Bogaty H. (1957) 'Water transport mechanisms in textile materials: Part ii: Capillary-type penetration in yarns and fabrics', *Text. Res. J.*, vol. 27(1), pp. 8–13.

[192] Kissa E. (1996) 'Wetting and wicking', *Text. Res. J.*, vol. 66(10), pp. 660–668.

[193] Perwuelz A., Mondon P., and Caze C. (2000) 'Experimental study of capillary flow in yarns', *Text. Res. J.*, vol. 70(4), pp. 333–339.

[194] Liu T., Choi K.f., and Li Y. (2008) 'Wicking in twisted yarns', *J. Colloid Interface Sci.*, vol. 318(1), pp. 134–139.

[195] Beyhaghi S., Geoffroy S., Prat M., and Pillai K.M. (2014) 'Wicking and evaporation of liquids in porous wicks: A simple analytical approach to optimization of wick design', *AIChE J.*, vol. 60(5), pp. 1930–1940.

[196] Shield T., Bogy D., and Talke F. (1987) 'Drop formation by dod ink-jet nozzles: A comparison of experiment and numerical simulation', *IBM J. Res. Dev.*, vol. 31(1), pp. 96–110.

[197] Basaran O.A., Gao H., and Bhat P.P. (2013) 'Nonstandard inkjets', *Annu. Rev. Fluid Mech.*, vol. 45, pp. 85–113.

[198] Sirignano W.A., *Fluid dynamics and transport of droplets and sprays* (Cambridge university press, 2010), 2nd Ed.

[199] Ashgriz N., *Handbook of atomization and sprays: theory and applications* (Springer, 2011).

[200] Service R.F. (1998) 'Microchip arrays put dna on the spot', *Science*, vol. 282(5388), p. 396.

[201] Umbanhowar P., Prasad V., and Weitz D.A. (2000) 'Monodisperse emulsion generation via drop break off in a coflowing stream', *Langmuir*, vol. 16(2), pp. 347–351.

TH-2590_156103041

[202] Thorsen T., Roberts R.W., Arnold F.H., and Quake S.R. (2001) 'Dynamic pattern formation in a vesicle-generating microfluidic device', *Phys. Rev. Lett.*, vol. 86(18), p. 4163.

[203] Zhang X. and Basaran O.A. (1995) 'An experimental study of dynamics of drop formation', *Phys. Fluids*, vol. 7(6), pp. 1184–1203.

[204] Clanet C. and Lasheras J.C. (1999) 'Transition from dripping to jetting', *J. Fluid Mech.*, vol. 383, pp. 307–326.

[205] D'Innocenzo A., Paladini F., and Renna L. (2002) 'Experimental study of dripping dynamics', *Phys. Rev. E*, vol. 65, p. 056208.

[206] Ambravaneswaran B., Subramani H.J., Phillips S.D., and Basaran O.A. (2004) 'Dripping-jetting transitions in a dripping faucet', *Phys. Rev. Lett.*, vol. 93(3), p. 034501.

[207] Schulkes R. (1994) 'The evolution and bifurcation of a pendant drop', *J. Fluid Mech.*, vol. 278, pp. 83–100.

[208] Zhang D. and Stone H. (1997) 'Drop formation in viscous flows at a vertical capillary tube', *Phys. Fluids*, vol. 9(8), pp. 2234–2242.

[209] Chen A.U., Notz P.K., and Basaran O.A. (2002) 'Computational and experimental analysis of pinch-off and scaling', *Phys. Rev. Lett.*, vol. 88(17), p. 174501.

[210] Castrejón-Pita J.R., Castrejón-Pita A.A., Thete S.S., Sambath K., Hutchings I.M., Hinch J., Lister J.R., and Basaran O.A. (2015) 'Plethora of transitions during breakup of liquid filaments', *Proc. Natl. Acad. Sci. U.S.A.*, p. 201418541.

[211] Rubio-Rubio M., Taconet P., and Sevilla A. (2018) 'Dripping dynamics and transitions at high bond numbers', *Int. J. Multiph. Flow*, vol. 104, pp. 206–213.

[212] Dong H., Carr W.W., and Morris J.F. (2006) 'Visualization of drop-on-demand inkjet: Drop formation and deposition', *Rev. Sci. Instrum.*, vol. 77(8), p. 085101.

TH-2590_156103041

[213] Hauser E., Edgerton H., Holt B., and Cox Jr J. (1936) 'The application of the high-speed motion picture camera to research on the surface tension of liquids.', *J. Phys. Chem. A*, vol. 40(8), pp. 973–988.

[214] Peregrine D.H., Shoker G., and Symon A. (1990) 'The bifurcation of liquid bridges', *J. Fluid Mech.*, vol. 212, pp. 25–39.

[215] Notz P.K., Chen A.U., and Basaran O.A. (2001) 'Satellite drops: Unexpected dynamics and change of scaling during pinch-off', *Phys. Fluids*, vol. 13(3), pp. 549–552.

[216] Taur A., Doshi P., and Yeoh H.K. (2015) 'Dripping dynamics of newtonian liquids from a tilted nozzle', *Eur. J. Mech. B Fluids*, vol. 51, pp. 8–15.

[217] Miskin M.Z. and Jaeger H.M. (2012) 'Droplet formation and scaling in dense suspensions', *Proc. Natl. Acad. Sci. U.S.A.*

[218] Zhmud B., Tiberg F., and Hallstensson K. (2000) 'Dynamics of capillary rise', *J. Colloid Interface Sci.*, vol. 228(2), pp. 263–269.

[219] Li H., Gan Y., Chen X., Tong Y., and Hu M., 'Experimental study on electrospraying of ethanol based on PDA measurement', in 'Energy Technol. 2017', (Springer International Publishing, 2017), pp. 87–92.

[220] Randive P., Dalal A., Sahu K.C., Biswas G., and Mukherjee P.P. (2015) 'Wettability effects on contact line dynamics of droplet motion in an inclined channel', *Phys. Rev. E.*, vol. 91(5), p. 053006.

[221] Wu Y. and Gao S., 'Development of free adjustable function generator for drop-on-demand droplets generation', in 'Advances in Future Computer and Control Systems', (Springer, 2012), pp. 477–481.

[222] Castrejón-Pita J., Willis S., and Castrejón-Pita A. (2015) 'Dynamic nozzles for drop generators', *Rev. Sci. Instrum.*, vol. 86(11), p. 115101.

[223] Patnaik A., Rengasamy R.S., Kothari V.K., and Ghosh A. (2006) 'Wetting and wicking in fibrous materials', *Textile Progress*, vol. 38(1), pp. 1–105.

[224] Lorenceau É., Clanet C., and Quéré D. (2004) 'Capturing drops with a thin fiber', *J. Colloid Interface Sci.*, vol. 279(1), pp. 192–197.

TH-2590_156103041

[225] Yarin A.L., Liu W., and Reneker D.H. (2002) 'Motion of droplets along thin fibers with temperature gradient', *J. Appl. Phys.*, vol. 91(7), pp. 4751–4760.

[226] Weyer F., Duchesne A., and Vandewalle N. (2017) 'Switching behavior of droplets crossing nodes on a fiber network', *Sci. Rep.*, vol. 7(1), p. 13309.

[227] Harkins W.D. and Brown F. (1919) 'The determination of surface tension (free surface energy), and the weight of falling drops: The surface tension of water and benzene by the capillary height method.', *J. Am. Chem. Soc.*, vol. 41(4), pp. 499–524.

[228] Tate T. (1864) 'Xxx. on the magnitude of a drop of liquid formed under different circumstances', *Philos. Mag.*, vol. 27(181), pp. 176–180.

[229] Whitesides G.M. (2006) 'The origins and the future of microfluidics', *Nature*, vol. 442(7101), p. 368.

[230] i Solvas X.C. and DeMello A. (2011) 'Droplet microfluidics: recent developments and future applications', *Chem. Commun.*, vol. 47(7), pp. 1936–1942.

[231] Odenbach S. (2003) 'Ferrofluids—magnetically controlled suspensions', *Colloids Surf. A*, vol. 217(1-3), pp. 171–178.

[232] Bormashenko E., Pogreb R., Bormashenko Y., Musin A., and Stein T. (2008) 'New investigations on ferrofluidics: ferrofluidic marbles and magnetic-field-driven drops on superhydrophobic surfaces', *Langmuir*, vol. 24(21), pp. 12119–12122.

[233] Latikka M., Backholm M., Timonen J.V., and Ras R.H. (2018) 'Wetting of ferrofluids: Phenomena and control', *Curr. Opin. Colloid Interface Sci.*, vol. 36, pp. 118–129.

[234] Katsikis G., Breant A., Rinberg A., and Prakash M. (2018) 'Synchronous magnetic control of water droplets in bulk ferrofluid', *Soft matter*, vol. 14(5), pp. 681–692.

[235] Sero-Guillaume O., Zouaoui D., Bernardin D., and Brancher J. (1992) 'The shape of a magnetic liquid drop', *J. Fluid Mech.*, vol. 241, pp. 215–232.

TH-2590_156103041

[236] Chen C.Y. and Cheng Z.Y. (2008) 'An experimental study on rosensweig instability of a ferrofluid droplet', *Phys. Fluids*, vol. 20(5), p. 054105.

[237] Zhu G.P., Nguyen N.T., Ramanujan R.V., and Huang X.Y. (2011) 'Nonlinear deformation of a ferrofluid droplet in a uniform magnetic field', *Langmuir*, vol. 27(24), pp. 14834–14841.

[238] Lee C.P., Yang S.T., and Wei Z.H. (2012) 'Field dependent shape variation of magnetic fluid droplets on magnetic dots', *J. Magn. Magn. Mater.*, vol. 324(24), pp. 4133–4135.

[239] Vieu T. and Walter C. (2018) 'Shape and fission instabilities of ferrofluids in non-uniform magnetic fields', *J. Fluid Mech.*, vol. 840, pp. 455–497.

[240] Cowley M. and Rosensweig R.E. (1967) 'The interfacial stability of a ferromagnetic fluid', *J. Fluid Mech.*, vol. 30(4), pp. 671–688.

[241] Manukyan S. and Schneider M. (2016) 'Experimental investigation of wetting with magnetic fluids', *Langmuir*, vol. 32(20), pp. 5135–5140.

[242] Rigoni C., Pierno M., Mistura G., Talbot D., Massart R., Bacri J.C., and Abou-Hassan A. (2016) 'Static magnetowetting of ferrofluid drops', *Langmuir*, vol. 32(30), pp. 7639–7646.

[243] Banerjee U. and Sen A. (2018) 'Shape evolution and splitting of ferrofluid droplets on a hydrophobic surface in the presence of a magnetic field', *Soft matter*, vol. 14(15), pp. 2915–2922.

[244] Extrand C. and Kumagai Y. (1996) 'Contact angles and hysteresis on soft surfaces', *J. Colloid Interface Sci.*, vol. 184(1), pp. 191–200.

[245] Pericet-Camara R., Auernhammer G.K., Koynov K., Lorenzoni S., Raiteri R., and Bonaccurso E. (2009) 'Solid-supported thin elastomer films deformed by microdrops', *Soft Matter*, vol. 5(19), pp. 3611–3617.

[246] Style R.W. and Dufresne E.R. (2012) 'Static wetting on deformable substrates, from liquids to soft solids', *Soft Matter*, vol. 8(27), pp. 7177–7184.

[247] Style R.W., Boltyanskiy R., Che Y., Wettlaufer J., Wilen L.A., and Dufresne E.R. (2013) 'Universal deformation of soft substrates near a contact line and

TH-2590_156103041

the direct measurement of solid surface stresses', *Phys. Rev. Lett.*, vol. 110(6), p. 066103.

[248] Squires T.M. (2013) 'Drops on soft surfaces learn the hard way', *Proc. Natl. Acad. Sci. U.S.A.*, vol. 110(31), pp. 12505–12506.

[249] Bico J., Reyssat É., and Roman B. (2018) 'Elastocapillarity: When surface tension deforms elastic solids', *Annu. Rev. Fluid Mech.*, vol. 50, pp. 629–659.

[250] Pu G., Ai J., and Severtson S.J. (2010) 'Drop behavior on a thermally-stripped acrylic polymer: influence of surface tension induced wetting ridge formation on retention and running', *Langmuir*, vol. 26(15), pp. 12696–12702.

[251] Park S.J., Weon B.M., San Lee J., Lee J., Kim J., and Je J.H. (2014) 'Visualization of asymmetric wetting ridges on soft solids with x-ray microscopy', *Nat. Commun.*, vol. 5, p. 4369.

[252] Park S., Bostwick J., De Andrade V., and Je J. (2017) 'Self-spreading of the wetting ridge during stick-slip on a viscoelastic surface', *Soft matter*, vol. 13(44), pp. 8331–8336.

[253] Lopes M.C. and Bonaccurso E. (2012) 'Evaporation control of sessile water drops by soft viscoelastic surfaces', *Soft Matter*, vol. 8(30), pp. 7875–7881.

[254] Lopes M.C. and Bonaccurso E. (2013) 'Influence of substrate elasticity on particle deposition patterns from evaporating water–silica suspension droplets', *Soft Matter*, vol. 9(33), pp. 7942–7950.

[255] Howland C.J., Antkowiak A., Castrejón-Pita J.R., Howison S.D., Oliver J.M., Style R.W., and Castrejón-Pita A.A. (2016) 'It's harder to splash on soft solids', *Phys. Rev. Lett.*, vol. 117(18), p. 184502.

[256] Dey R., Daga A., DasGupta S., and Chakraborty S. (2015) 'Electrically modulated dynamic spreading of drops on soft surfaces', *Appl. Phys. Lett.*, vol. 107(3), p. 034101.

[257] Biswas S., Pomeau Y., and Chaudhury M.K. (2016) 'New drop fluidics enabled by magnetic-field-mediated elastocapillary transduction', *Langmuir*, vol. 32(27), pp. 6860–6870.

TH-2590_156103041

[258] Style R.W., Che Y., Park S.J., Weon B.M., Je J.H., Hyland C., German G.K., Power M.P., Wilen L.A., Wettlaufer J.S., et al. (2013) 'Patterning droplets with durotaxis', *Proc. Natl. Acad. Sci. U.S.A.*, vol. 110(31), pp. 12541–12544.

[259] Autumn K., Liang Y.A., Hsieh S.T., Zesch W., Chan W.P., Kenny T.W., Fearing R., and Full R.J. (2000) 'Adhesive force of a single gecko foot-hair', *Nature*, vol. 405(6787), p. 681.

[260] Grandgeorge P., Krins N., Hourlier-Fargette A., Laberty-Robert C., Neukirch S., and Antkowiak A. (2018) 'Capillarity-induced folds fuel extreme shape changes in thin wicked membranes', *Science*, vol. 360(6386), pp. 296–299.

[261] Marchand A., Das S., Snoeijer J.H., and Andreotti B. (2012) 'Contact angles on a soft solid: From young's law to neumann's law', *Phys. Rev. Lett.*, vol. 109(23), p. 236101.

[262] Lubbers L.A., Weijs J.H., Botto L., Das S., Andreotti B., and Snoeijer J.H. (2014) 'Drops on soft solids: free energy and double transition of contact angles', *J. Fluid Mech.*, vol. 747.

[263] Jedynak R. (2017) 'New facts concerning the approximation of the inverse langevin function', *J. Non-Newtonian Fluid Mech.*, vol. 249, pp. 8 – 25.

[264] Tokarev A., Lee W.K., Sevonkaev I., Goia D., and Kornev K.G. (2014) 'Sharpening the surface of magnetic paranematic droplets', *Soft Matter*, vol. 10(12), pp. 1917–1923.

[265] Zuo B., Zheng F.F., Zhao Y.R., Chen T., Yan Z.H., Ni H., and Wang X. (2012) 'Stick–slip phenomenon in measurements of dynamic contact angles and surface viscoelasticity of poly (styrene-b-isoprene-b-styrene) triblock copolymers', *Langmuir*, vol. 28(9), pp. 4283–4292.

[266] Gutowski W.V. and Dodiuk H., *Recent advances in adhesion science and technology in honor of Dr. Kash Mittal* (CRC Press, 2013).

[267] Varagnolo S., Ferraro D., Fantinel P., Pierno M., Mistura G., Amati G., Biferale L., and Sbragaglia M. (2013) 'Stick-slip sliding of water drops on chemically heterogeneous surfaces', *Phys. Rev. Lett.*, vol. 111(6), p. 066101.

TH-2590_156103041

[268] Karpitschka S., Das S., van Gorcum M., Perrin H., Andreotti B., and Snoeijer J.H. (2015) 'Droplets move over viscoelastic substrates by surfing a ridge', *Nat. Commun.*, vol. 6, p. 7891.

[269] Kajiya T., Daerr A., Narita T., Royon L., Lequeux F., and Limat L. (2013) 'Advancing liquid contact line on visco-elastic gel substrates: stick-slip vs. continuous motions', *Soft Matter*, vol. 9(2), pp. 454–461.

[270] Shanahan M.E. (1995) 'Simple theory of" stick-slip" wetting hysteresis', *Langmuir*, vol. 11(3), pp. 1041–1043.

[271] Moffat J.R., Sefiane K., and Shanahan M.E. (2009) 'Effect of tio2 nanoparticles on contact line stick- slip behavior of volatile drops', *J. Phys. Chem. B*, vol. 113(26), pp. 8860–8866.

[272] Bormashenko E., Musin A., and Zinigrad M. (2011) 'Evaporation of droplets on strongly and weakly pinning surfaces and dynamics of the triple line', *Colloids Surf. A*, vol. 385(1-3), pp. 235–240.

[273] Oksuz M. and Erbil H.Y. (2014) 'Comments on the energy barrier calculations during "stick–slip" behavior of evaporating droplets containing nanoparticles', *J. Phys. Chem. C*, vol. 118(17), pp. 9228–9238.

[274] Uman M.A., *The Lightning Discharge* (Courier Corporation, 2001).

[275] Meek J.M. (1940) 'A theory of spark discharge', *Phys. Rev.*, vol. 57(8), p. 722.

[276] Mahmoudi S.R., Adamiak K., and Castle G.S.P. (2011) 'Spreading of a dielectric droplet through an interfacial electric pressure', *Proc. R. Soc. A*, vol. 467, pp. 3257–3271.

[277] Xie G., He F., Liu X., Si L., and Guo D. (2016) 'Sessile multidroplets and salt droplets under high tangential electric fields', *Sci. Rep.*, vol. 6, p. 25002.

[278] Dubinov A.E., Kozhayeva J.P., Golovanov V.V., and Selemir V.D. (2018) 'Coalescence of liquid droplets under effect of pulsed-periodic spark discharges', *IEEE Trans. Plasma Sci.*, vol. 47(1), pp. 76–80.

[279] Waymouth J.F., *Electrical Discharge Lamps* (Cambridge, MA: MIT Press, 1971).

TH-2590_156103041

[280] Grace J.M. and Marijnissen J.C.M. (1994) 'A review of liquid atomization by electrical means', *J. Aerosol Sci.*, vol. 25(6), pp. 1005–1019.

[281] Sarma B., Shahapure V., Dalal A., and Basu D.N. (2020) 'Magnetowetting dynamics of sessile ferrofluid drops on soft surfaces', *Soft Matter*, vol. 16, pp. 970–982.

[282] Adebayo I.T. and Matar O.K. (2017) 'Droplet impact on flowing liquid films with inlet forcing: the splashing regime', *Soft Matter*, vol. 13(41), pp. 7473–7485.

[283] Che Z. and Matar O.K. (2017) 'Impact of droplets on liquid films in the presence of surfactant', *Langmuir*, vol. 33(43), pp. 12140–12148.

[284] Scharfman B.E., Techet A.H., Bush J.W.M., and Bourouiba L. (2016) 'Visualization of sneeze ejecta: steps of fluid fragmentation leading to respiratory droplets', *Exp. Fluids*, vol. 57(2), p. 24.

[285] Tomotika S. (1935) 'On the instability of a cylindrical thread of a viscous liquid surrounded by another viscous fluid', *Proc. R. Soc. Lond. A*, vol. 150(870), pp. 322–337.

[286] Roach P., Shirtcliffe N.J., and Newton M.I. (2008) 'Progess in superhydrophobic surface development', *Soft Matter*, vol. 4(2), pp. 224–240.

[287] Yang V. and Anderson W., *Liquid Rocket Engine Combustion Instability* (Washington, DC: AIAA, 1995).

[288] Lad N., Aroussi A., and Muhamad Said M.F. (2011) 'Droplet size measurement for liquid spray using digital image analysis technique', *J. Appl. Sci*, vol. 11(11), pp. 1966–1972.

[289] Priest C., Quinn A., Postma A., Zelikin A.N., Ralston J., and Caruso F. (2008) 'Microfluidic polymer multilayer adsorption on liquid crystal droplets for microcapsule synthesis', *Lab. Chip*, vol. 8(12), pp. 2182–2187.

[290] Cossali G.E., Marengo M., and Santini M. (2008) 'Thermally induced secondary drop atomisation by single drop impact onto heated surfaces', *Int. J. Heat Fluid Flow*, vol. 29(1), pp. 167–177.

TH-2590_156103041

[291] Karri B., Ohl S.W., Klaseboer E., Ohl C.D., and Khoo B.C. (2012) 'Jets and sprays arising from a spark-induced oscillating bubble near a plate with a hole', *Phys. Rev. E*, vol. 86, p. 036309.

[292] de Goede T.C., Laan N., de Bruin K.G., and Bonn D. (2017) 'Effect of wetting on drop splashing of newtonian fluids and blood', *Langmuir*, vol. 34(18), pp. 5163–5168.

[293] Ray B., Biswas G., and Sharma A. (2012) 'Oblique drop impact on deep and shallow liquid', *Commun. Comput. Phys.*, vol. 11(4), pp. 1386–1396.

[294] Kolinski J.M., Mahadevan L., and Rubinstein S.M. (2014) 'Drops can bounce from perfectly hydrophilic surfaces', *Europhys. Lett.*, vol. 108(2), p. 24001.

[295] Zhang L.V., Brunet P., Eggers J., and Deegan R.D. (2010) 'Wavelength selection in the crown splash', *Phys. Fluids*, vol. 22(12), p. 122105.

[296] Lhuissier H. and Villermaux E. (2012) 'Bursting bubble aerosols', *J. Fluid Mech.*, vol. 696, pp. 5–44.

[297] Fuster D., Agbaglah G., Josserand C., Popinet S., and Zaleski S. (2009) 'Numerical simulation of droplets, bubbles and waves: state of the art', *Fluid Dyn. Res.*, vol. 41(6), p. 065001.

[298] Mugele F. and Baret J.C. (2005) 'Electrowetting: from basics to applications', *J. Phys. Condens. Matter*, vol. 17(28), p. R705.

[299] Lee B.I., Rodriguez E.R., Notargiocomo A., Ferrans V.J., Chen Y., and Fletcher R.D. (1986) 'Thermal effects of laser and electrical discharge on cardiovascular tissue: Implications for coronary artery recanalization and endocardial ablation', *J. Am. Coll. Cardiol.*, vol. 8(1), pp. 193–200.

[300] Potter H. and Heller R. (2018) 'Transfection by electroporation', *Curr. Protoc. Mol. Biol.*, vol. 121(1), pp. 9–3.

[301] Tan L.S. and Mark J.E. (1999) 'Polymer data handbook', *NY, Oxford*.

[302] Krishnan S. (2007) *On the manufacture of very thin elastomeric films by spin-coating*, Ph.D. thesis, Massachusetts Institute of Technology.

TH-2590_156103041

[303] Goldsack D.E. and Franchetto R. (1977) 'The viscosity of concentrated electrolyte solutions. i. concentration dependence at fixed temperature', *Can. J. Chem*, vol. 55(6), pp. 1062–1072.

[304] Leroy P., Lassin A., Azaroual M., and André L. (2010) 'Predicting the surface tension of aqueous 1: 1 electrolyte solutions at high salinity', *Geochim. Cosmochim. Acta*, vol. 74(19), pp. 5427–5442.

[305] Sarathi R. and Nagesh G. (2008) 'UHF technique for identification of discharges initiated by liquid droplet in epoxy nanocomposite insulation material under ac voltages', *J. Phys. D: Appl. Phys.*, vol. 41(15), p. 155407.

[306] Schultz T., Pfeiffer M., and Franck C.M. (2015) 'Optical investigation methods for determining the impact of rain drops on HVDC corona', *J. Electrostat.*, vol. 77, pp. 13–20.

[307] Kogelschatz U. (2003) 'Dielectric-barrier discharges: their history, discharge physics, and industrial applications', *Plasma Chem. Plasma Process.*, vol. 23(1), pp. 1–46.

[308] Corke T.C., Enloe C.L., and Wilkinson S.P. (2010) 'Dielectric barrier discharge plasma actuators for flow control', *Annu. Rev. Fluid Mech.*, vol. 42, pp. 505–529.

[309] Shapiro B., Moon H., Garrell R.L., and Kim C.J. (2003) 'Equilibrium behavior of sessile drops under surface tension, applied external fields, and material variations', *J. Appl. Phys.*, vol. 93(9), pp. 5794–5811.

[310] Karri B., Pillai K.S., Klaseboer E., Ohl S.W., and Khoo B.C. (2011) 'Collapsing bubble induced pumping in a viscous fluid', *Sens. Actuators A Phys.*, vol. 169(1), pp. 151 – 163.

[311] Jones H.M. and Kunhardt E.E. (1995) 'Pulsed dielectric breakdown of pressurized water and salt solutions', *J. Appl. Phys.*, vol. 77(2), pp. 795–805.

[312] Watson P.K. (1985) 'Electrostatic and hydrodynamic effects in the electrical breakdown of liquid dielectrics', *IEEE Trans. Electr. Insul.*, vol. 2, pp. 395–399.

TH-2590_156103041

[313] Padilla-Martinez J.P., Ramirez-San-Juan J.C., Korneev N., Banks D., Aguilar G., and Ramos-Garcia R. (2013) 'Breaking the rayleigh-plateau instability limit using thermocavitation within a droplet', *At. Sprays*, vol. 23(6).

[314] Lauterborn W., Kurz T., Mettin R., and Ohl C.D., 'Experimental and theoretical bubble dynamics', in I. Prigogine and S.A. Rice, (Editors) 'Advances in Chemical Physics', vol. 110 (John Wiley & Sons, New York, 1999), pp. 295–380.

[315] Shima A. (1997) 'Studies on bubble dynamics', *Shock Waves*, vol. 7(1), pp. 33–42.

[316] Rayleigh L. (1917) 'On the pressure developed in a liquid during the collapse of a spherical cavity', *Phil. Mag.*, vol. 34(200), pp. 94–98.

[317] Bruning M.A., Costalonga M., Snoeijer J.H., and Marin A. (2019) 'Turning drops into bubbles: Cavitation by vapor diffusion through elastic networks', *Phys. Rev. Lett.*, vol. 123, p. 214501.

[318] Han B., Köhler K., Jungnickel K., Mettin R., Lauterborn W., and Vogel A. (2015) 'Dynamics of laser-induced bubble pairs', *J. Fluid Mech.*, vol. 771, pp. 706–742.

[319] Vukasinovic B., Smith M.K., and Glezer A. (2007) 'Mechanisms of free-surface breakup in vibration-induced liquid atomization', *Phys. Fluids*, vol. 19(1), p. 012104.

[320] Stone H.A., Bentley B.J., and Leal L.G. (1986) 'An experimental study of transient effects in the breakup of viscous drops', *J. Fluid Mech.*, vol. 173, pp. 131–158.

[321] Rayleigh L. (1879) 'On the capillary phenomena of jets', *Proc. R. Soc. London*, vol. 29, pp. 71–97.

[322] Rumscheidt F.D. and Mason S.G. (1962) 'Break-up of stationary liquid threads', *J. Colloid Sci.*, vol. 17(3), pp. 260–269.

[323] Lee W.K. and Flumerfelt R.W. (1981) 'Instability of stationary and uniformly moving cylindrical fluid bodies—i. newtonian systems', *Int. J. Multiph. Flow*, vol. 7(4), pp. 363–383.

TH-2590_156103041

[324] McKinley G.H. (2005) 'Dimensionless groups for understanding free surface flows of complex fluids', *Soc. Rheol. Bull.*, vol. 74, pp. 6 – 9.

[325] Bush J.W.M., *Interfacial Phenomena* (Massachusetts Institute of Technology: MIT OpenCourseWare, 2010).

[326] Rao D.C.K. and Karmakar S. (2018) 'Crown formation and atomization in burning multi-component fuel droplets', *Exp. Therm. Fluid Sci.*, vol. 98, pp. 303 – 308.

[327] Taylor G. (1950) 'The instability of liquid surfaces when accelerated in a direction perpendicular to their planes. i', *Proc. R. Soc. Lond. A*, vol. 201(1065), pp. 192–196.

[328] Krechetnikov R. and Homsy G.M. (2009) 'Crown-forming instability phenomena in the drop splash problem', *J. Colloid Interface Sci.*, vol. 331(2), pp. 555–559.

[329] Schneider C.A., Rasband W.S., and Eliceiri K.W. (2012) 'NIH Image to ImageJ: 25 years of image analysis', *Nat. Methods*, vol. 9(7), p. 671.

[330] Avila S.R.G., Song C., and Ohl C.D. (2015) 'Fast transient microjets induced by hemispherical cavitation bubbles', *J. Fluid Mech.*, vol. 767, p. 31.

[331] Tan M.K., Friend J.R., and Yeo L.Y. (2009) 'Interfacial jetting phenomena induced by focused surface vibrations', *Phys. Rev. Lett.*, vol. 103(2), p. 024501.

[332] Tomita Y. (2014) 'Jet atomization and cavitation induced by interactions between focused ultrasound and a water surface', *Phys. Fluids*, vol. 26(9), p. 097105.

[333] Jagadeesh G., Prakash G.D., Rakesh S., Allam U.S., Krishna M.G., Eswarappa S.M., and Chakravortty D. (2011) 'Needleless vaccine delivery using microshock waves', *Clin. Vaccine Immunol.*, vol. 18(4), pp. 539–545.

[334] De La Mora J.F. and Loscertales I.G. (1994) 'The current emitted by highly conducting taylor cones', *J. Fluid Mech.*, vol. 260, pp. 155–184.

[335] Rosell-Llompart J. and Gañán-Calvo A.M. (2008) 'Turbulence in pneumatic flow focusing and flow blurring regimes', *Phys. Rev. E*, vol. 77(3), p. 036321.

TH-2590_156103041

[336] Cruz-Mazo F., Wiedorn M.O., Herrada M., Bajt S., Chapman H., and Gañán-Calvo A.M. (2019) 'Aerodynamically stabilized taylor cone jets', *Phys. Rev. E*, vol. 100(3), p. 031101.

[337] Gamero-Castaño M. (2019) 'Dissipation in cone-jet electrosprays and departure from isothermal operation', *Phys. Rev. E*, vol. 99(6), p. 061101.

[338] Delrot P., Modestino M.A., Gallaire F., Psaltis D., and Moser C. (2016) 'Inkjet printing of viscous monodisperse microdroplets by laser-induced flow focusing', *Phys. Rev. Appl.*, vol. 6(2), p. 024003.

[339] Onuki H., Oi Y., and Tagawa Y. (2018) 'Microjet generator for highly viscous fluids', *Phys. Rev. Appl.*, vol. 9(1), p. 014035.

[340] Vogel A., Noack J., Nahen K., Theisen D., Busch S., Parlitz U., Hammer D., Noojin G., Rockwell B., and Birngruber R. (1999) 'Energy balance of optical breakdown in water at nanosecond to femtosecond time scales.', *Appl. Phys. B*, vol. 68(2), p. 271–280.

[341] Klein A.L., Kurilovich D., Lhuissier H., Versolato O.O., Lohse D., Villermaux E., and Gelderblom H. (2020) 'Drop fragmentation by laser-pulse impact', *J. Fluid Mech.*, vol. 893, p. A7.

[342] Barthlott W. and Neinhuis C. (1997) 'Purity of the sacred lotus, or escape from contamination in biological surfaces', *Planta*, vol. 202(1), pp. 1–8.

[343] Koch K. and Barthlott W. (2009) 'Superhydrophobic and superhydrophilic plant surfaces: an inspiration for biomimetic materials', *Philos. Mag.*, vol. 367(1893), pp. 1487–1509.

[344] Wisdom K.M., Watson J.A., Qu X., Liu F., Watson G.S., and Chen C.H. (2013) 'Self-cleaning of superhydrophobic surfaces by self-propelled jumping condensate', *Proc. Natl. Acad. Sci. U.S.A.*, vol. 110(20), pp. 7992–7997.

[345] Oh J., Dana C.E., Hong S., Román J.K., Jo K.D., Hong J.W., Nguyen J., Cropek D.M., Alleyne M., and Miljkovic N. (2017) 'Exploring the role of habitat on the wettability of cicada wings', *ACS Appl. Mater. Interfaces*, vol. 9(32), pp. 27173–27184.

TH-2590_156103041

[346] Blossey R. (2003) 'Self-cleaning surfaces—virtual realities', *Nat. Mater.*, vol. 2(5), pp. 301–306.

[347] Mouterde T., Lehoucq G., Xavier S., Checco A., Black C.T., Rahman A., Midavaine T., Clanet C., and Quéré D. (2017) 'Antifogging abilities of model nanotextures', *Nat. Mater.*, vol. 16(6), pp. 658–663.

[348] Pogodin S., Hasan J., Baulin V.A., Webb H.K., Truong V.K., Nguyen T.H.P., Boshkovikj V., Fluke C.J., Watson G.S., Watson J.A., et al. (2013) 'Biophysical model of bacterial cell interactions with nanopatterned cicada wing surfaces', *Biophys. J.*, vol. 104(4), pp. 835–840.

[349] Ivanova E.P., Hasan J., Webb H.K., Truong V.K., Watson G.S., Watson J.A., Baulin V.A., Pogodin S., Wang J.Y., Tobin M.J., et al. (2012) 'Natural bactericidal surfaces: mechanical rupture of pseudomonas aeruginosa cells by cicada wings', *Small*, vol. 8(16), pp. 2489–2494.

[350] Han Z., Mu Z., Li B., Niu S., Zhang J., and Ren L. (2016) 'A high-transmission, multiple antireflective surface inspired from bilayer 3d ultrafine hierarchical structures in butterfly wing scales', *Small*, vol. 12(6), pp. 713–720.

[351] Lafuma A. and Quéré D. (2003) 'Superhydrophobic states', *Nat. Mater.*, vol. 2(7), pp. 457–460.

[352] Papadopoulos P., Mammen L., Deng X., Vollmer D., and Butt H.J. (2013) 'How superhydrophobicity breaks down', *Proc. Natl. Acad. Sci. U.S.A.*, vol. 110(9), pp. 3254–3258.

[353] Mishchenko L., Hatton B., Bahadur V., Taylor J.A., Krupenkin T., and Aizenberg J. (2010) 'Design of ice-free nanostructured surfaces based on repulsion of impacting water droplets', *ACS nano*, vol. 4(12), pp. 7699–7707.

[354] Zhang Q., He M., Chen J., Wang J., Song Y., and Jiang L. (2013) 'Anticing surfaces based on enhanced self-propelled jumping of condensed water microdroplets', *Chem. Commun.*, vol. 49(40), pp. 4516–4518.

[355] Kreder M.J., Alvarenga J., Kim P., and Aizenberg J. (2016) 'Design of anticing surfaces: smooth, textured or slippery?', *Nat. Rev. Mater.*, vol. 1(1), pp. 1–15.

TH-2590_156103041

[356] Quéré D. (2005) 'Non-sticking drops', *Rep. Prog. Phys.*, vol. 68(11), p. 2495.

[357] Genzer J. and Efimenko K. (2006) 'Recent developments in superhydrophobic surfaces and their relevance to marine fouling: a review', *Biofouling*, vol. 22(5), pp. 339–360.

[358] Rothstein J.P. (2010) 'Slip on superhydrophobic surfaces', *Annu. Rev. Fluid Mech.*, vol. 42, pp. 89–109.

[359] Zhou X., Zhang Z., Xu X., Guo F., Zhu X., Men X., and Ge B. (2013) 'Robust and durable superhydrophobic cotton fabrics for oil/water separation', *ACS Appl. Mater. Interfaces*, vol. 5(15), pp. 7208–7214.

[360] Ju J., Bai H., Zheng Y., Zhao T., Fang R., and Jiang L. (2012) 'A multi-structural and multi-functional integrated fog collection system in cactus', *Nat. Commun.*, vol. 3(1), pp. 1–6.

[361] Roach P., McHale G., Evans C., Shirtcliffe N., and Newton M. (2007) 'De-coupling of the liquid response of a superhydrophobic quartz crystal microbalance', *Langmuir*, vol. 23(19), pp. 9823–9830.

[362] Nosonovsky M. and Bhushan B. (2009) 'Superhydrophobic surfaces and emerging applications: non-adhesion, energy, green engineering', *Curr. Opin. Colloid Interface Sci.*, vol. 14(4), pp. 270–280.

[363] Erbil H.Y. (2020) 'Practical applications of superhydrophobic materials and coatings: Problems and perspectives', *Langmuir*, vol. 36(10), pp. 2493–2509.

[364] Zhang X., Shi F., Niu J., Jiang Y., and Wang Z. (2008) 'Superhydrophobic surfaces: from structural control to functional application', *J. Mater. Chem.*, vol. 18(6), pp. 621–633.

[365] Levkin P.A., Svec F., and Fréchet J.M. (2009) 'Porous polymer coatings: a versatile approach to superhydrophobic surfaces', *Adv. Funct. Mater.*, vol. 19(12), pp. 1993–1998.

[366] Khan F., Rabnawaz M., Li Z., Khan A., Naveed M., Tuhin M.O., and Rahimb F. (2019) 'Simple design for durable and clear self-cleaning coatings', *ACS Appl. Polym. Mater.*, vol. 1(10), pp. 2659–2667.

TH-2590_156103041

[367] Mordor Intelligence (2018), 'Superhydrophobic coatings market - growth, trends, and forecast (2020 - 2025)', `https://www.mordorintelligence.com/industry-reports/`, accessed: 2020-10-06.

[368] Deng X., Mammen L., Butt H.J., and Vollmer D. (2012) 'Candle soot as a template for a transparent robust superamphiphobic coating', *Science*, vol. 335(6064), pp. 67–70.

[369] Deng X., Schellenberger F., Papadopoulos P., Vollmer D., and Butt H.J. (2013) 'Liquid drops impacting superamphiphobic coatings', *Langmuir*, vol. 29(25), pp. 7847–7856.

[370] Zhao B., Wang X., Zhang K., Chen L., and Deng X. (2017) 'Impact of viscous droplets on superamphiphobic surfaces', *Langmuir*, vol. 33(1), pp. 144–151.

[371] Guo J., Lin S., Zhao B., Deng X., and Chen L. (2018) 'Spreading of impinging droplets on nanostructured superhydrophobic surfaces', *Appl. Phys. Lett.*, vol. 113(7), p. 071602.

[372] Lin S., Zhao B., Zou S., Guo J., Wei Z., and Chen L. (2018) 'Impact of viscous droplets on different wettable surfaces: Impact phenomena, the maximum spreading factor, spreading time and post-impact oscillation', *J. Colloid Interface Sci.*, vol. 516, pp. 86–97.

[373] de Goede T.C., de Bruin K.G., Shahidzadeh N., and Bonn D. (2019) 'Predicting the maximum spreading of a liquid drop impacting on a solid surface: Effect of surface tension and entrapped air layer', *Phys. Rev. Fluids*, vol. 4(5), p. 053602.

[374] Yu F., Lin S., Yang J., Fan Y., Wang D., Chen L., and Deng X. (2020) 'Prompting splash impact on superamphiphobic surfaces by imposing a viscous part', *Adv. Sci.*, vol. 7(4), p. 1902687.

[375] Qu M., He J., and Cao B. (2010) 'Facile fabrication of large-scale stable superhydrophobic surfaces with carbon sphere films by burning rapeseed oil', *Appl. Surf. Sci.*, vol. 257(1), pp. 6–9.

[376] Liu S., Sakai M., Liu B., Terashima C., Nakata K., and Fujishima A. (2013) 'Facile synthesis of transparent superhydrophobic titania coating by using soot as a nanoimprint template', *RSC Adv.*, vol. 3(45), pp. 22825–22829.

TH-2590_156103041

[377] Seo K., Kim M., et al. (2014) 'Candle-based process for creating a stable superhydrophobic surface', *Carbon*, vol. 68, pp. 583–596.

[378] Yuan Z., Huang J., Peng C., Wang M., Wang X., Bin J., Xing S., Xiao J., Zeng J., Xiao X., et al. (2016) 'Facile preparation of superhydrophobic candle soot coating and its wettability under condensation', *Appl. Phys. A*, vol. 122(2), p. 125.

[379] Iqbal R., Majhy B., and Sen A. (2017) 'Facile fabrication and characterization of a pdms-derived candle soot coated stable biocompatible superhydrophobic and superhemophobic surface', *ACS Appl. Mater. Interfaces*, vol. 9(36), pp. 31170–31180.

[380] Qahtan T.F., Gondal M.A., Alade I.O., and Dastageer M.A. (2017) 'Fabrication of water jet resistant and thermally stable superhydrophobic surfaces by spray coating of candle soot dispersion', *Sci. Rep.*, vol. 7(1), pp. 1–7.

[381] Butt H.J., Roisman I.V., Brinkmann M., Papadopoulos P., Vollmer D., and Semprebon C. (2014) 'Characterization of super liquid-repellent surfaces', *Curr. Opin. Colloid Interfaces Sci.*, vol. 19(4), pp. 343–354.

[382] Shen Y., Tao J., Wang G., Zhu C., Chen H., Jin M., and Xie Y. (2018) 'Bioinspired fabrication of hierarchical-structured superhydrophobic surfaces to understand droplet bouncing dynamics for enhancing water repellency', *J. Phys. Chem. C*, vol. 122(13), pp. 7312–7320.

[383] Chen L., Xiao Z., Chan P.C., Lee Y.K., and Li Z. (2011) 'A comparative study of droplet impact dynamics on a dual-scaled superhydrophobic surface and lotus leaf', *Appl. Surf. Sci.*, vol. 257(21), pp. 8857–8863.

[384] Sbragaglia M., Peters A.M., Pirat C., Borkent B.M., Lammertink R.G., Wessling M., and Lohse D. (2007) 'Spontaneous breakdown of superhydrophobicity', *Phys. Rev. Lett.*, vol. 99(15), p. 156001.

[385] Martouzet G., Lee C., Pirat C., Ybert C., and Biance A.L. (2020) 'Drag reduction on drop during impact on multiscale superhydrophobic surfaces', *J. Fluid Mech.*, vol. 892.

TH-2590_156103041

[386] Zhang L., Wu J., Hedhili M.N., Yang X., and Wang P. (2015) 'Inkjet printing for direct micropatterning of a superhydrophobic surface: toward biomimetic fog harvesting surfaces', *J. Mater. Chem. A*, vol. 3(6), pp. 2844–2852.

[387] Rioboo R., Tropea C., and Marengo M. (2001) 'Outcomes from a drop impact on solid surfaces', *Atomization Sprays*, vol. 11(2).

[388] Park J. and Moon J. (2006) 'Control of colloidal particle deposit patterns within picoliter droplets ejected by ink-jet printing', *Langmuir*, vol. 22(8), pp. 3506–3513.

[389] Zhang Z., Zhang X., Xin Z., Deng M., Wen Y., and Song Y. (2013) 'Controlled inkjetting of a conductive pattern of silver nanoparticles based on the coffee-ring effect', *Adv. Mater.*, vol. 25(46), pp. 6714–6718.

[390] Xu L., Zhang W.W., and Nagel S.R. (2005) 'Drop splashing on a dry smooth surface', *Phys. Rev. Lett.*, vol. 94(18), p. 184505.

[391] Massinon M. and Lebeau F. (2012) 'Experimental method for the assessment of agricultural spray retention based on high-speed imaging of drop impact on a synthetic superhydrophobic surface', *Biosyst. Eng.*, vol. 112(1), pp. 56–64.

[392] Laan N., de Bruin K.G., Bartolo D., Josserand C., and Bonn D. (2014) 'Maximum diameter of impacting liquid droplets', *Phys. Rev. Appl.*, vol. 2(4), p. 044018.

[393] Laan N., De Bruin K.G., Slenter D., Wilhelm J., Jermy M., and Bonn D. (2015) 'Bloodstain pattern analysis: implementation of a fluid dynamic model for position determination of victims', *Sci. Rep.*, vol. 5(1), pp. 1–8.

[394] Li H., Cai Z., and Wang Y. (2020) 'Impact behaviors on superhydrophobic surfaces for water droplets of asymmetric double-chain quaternary ammonium surfactants', *Langmuir*, vol. 36(46), pp. 14113–14122.

[395] Biance A.L., Chevy F., Clanet C., Lagubeau G., and Quéré D. (2006) 'On the elasticity of an inertial liquid shock', *J. Fluid Mech.*, vol. 554, p. 47.

[396] Clanet C., Béguin C., Richard D., and Quéré D. (2004) 'Maximal deformation of an impacting drop', *J. Fluid Mech.*, vol. 517, p. 199.

TH-2590_156103041

[397] Barberoglou M., Zorba V., Stratakis E., Spanakis E., Tzanetakis P., Anastasiadis S., and Fotakis C. (2009) 'Bio-inspired water repellent surfaces produced by ultrafast laser structuring of silicon', *Appl. Surf. Sci.*, vol. 255(10), pp. 5425–5429.

[398] Bertola V. (2009) 'An experimental study of bouncing leidenfrost drops: comparison between newtonian and viscoelastic liquids', *Int. J. Heat Mass Transf.*, vol. 52(7-8), pp. 1786–1793.

[399] Stratakis E., Mateescu A., Barberoglou M., Vamvakaki M., Fotakis C., and Anastasiadis S.H. (2010) 'From superhydrophobicity and water repellency to superhydrophilicity: smart polymer-functionalized surfaces', *Chem. Commun.*, vol. 46(23), pp. 4136–4138.

[400] Antonini C., Amirfazli A., and Marengo M. (2012) 'Drop impact and wettability: From hydrophilic to superhydrophobic surfaces', *Phys. Fluids*, vol. 24(10), p. 102104.

[401] Pearson J.T., Maynes D., and Webb B.W. (2012) 'Droplet impact dynamics for two liquids impinging on anisotropic superhydrophobic surfaces', *Exp. Fluids*, vol. 53(3), pp. 603–618.

[402] Aria A.I. and Gharib M. (2014) 'Physicochemical characteristics and droplet impact dynamics of superhydrophobic carbon nanotube arrays', *Langmuir*, vol. 30(23), pp. 6780–6790.

[403] Riboux G. and Gordillo J.M. (2014) 'Experiments of drops impacting a smooth solid surface: A model of the critical impact speed for drop splashing', *Phys. Rev. Lett.*, vol. 113(2), p. 024507.

[404] Wang Y. and Bourouiba L. (2018) 'Unsteady sheet fragmentation: droplet sizes and speeds', *J. Fluid Mech.*, vol. 848, pp. 946–967.

[405] Gordillo J.M., Riboux G., and Quintero E.S. (2019) 'A theory on the spreading of impacting droplets', *J. Fluid Mech.*, vol. 866, pp. 298–315.

[406] Roy D., Pandey K., Banik M., Mukherjee R., and Basu S. (2019) 'Dynamics of droplet impingement on bioinspired surface: insights into spreading, anomalous stickiness and break-up', *Proc. R. Soc. A*, vol. 475(2229), p. 20190260.

TH-2590_156103041

[407] Wang F. and Fang T. (2020) 'Retraction dynamics of water droplets after impacting upon solid surfaces from hydrophilic to superhydrophobic', *Phys. Rev. Fluids*, vol. 5(3), p. 033604.

[408] Lee J.B., Derome D., Dolatabadi A., and Carmeliet J. (2016) 'Energy budget of liquid drop impact at maximum spreading: Numerical simulations and experiments', *Langmuir*, vol. 32(5), pp. 1279–1288.

[409] Patil N.D., Gada V.H., Sharma A., and Bhardwaj R. (2016) 'On dual-grid level-set method for contact line modeling during impact of a droplet on hydrophobic and superhydrophobic surfaces', *Int. J. Multiph. Flow*, vol. 81, pp. 54–66.

[410] Khojasteh D., Kazerooni M., Salarian S., and Kamali R. (2016) 'Droplet impact on superhydrophobic surfaces: A review of recent developments', *Ind. Eng. Chem. Res.*, vol. 42, pp. 1–14.

[411] Bartolo D., Josserand C., and Bonn D. (2005) 'Retraction dynamics of aquous drops upon impact on nonwetting surfaces', *J. Fluid Mech.*, vol. 545, pp. 329–338.

[412] Taylor G.I. (1959) 'The dynamics of thin sheets of fluid. iii. disintegration of fluid sheets', *Proc. R. Soc. Lond*, vol. 253(1274), pp. 313–321.

[413] Culick F. (1960) 'Comments on a ruptured soap film', *J. Appl. Phys.*, vol. 31(6), pp. 1128–1129.

[414] Bird J.C., Dhiman R., Kwon H.M., and Varanasi K.K. (2013) 'Reducing the contact time of a bouncing drop', *Nature*, vol. 503(7476), pp. 385–388.

[415] Xie F.F., Lv S.H., Yang Y.R., and Wang X.D. (2020) 'Contact time of a bouncing nanodroplet', *J. Phys. Chem. Lett.*, vol. 11(8), pp. 2818–2823.

[416] Quintero E.S., Riboux G., and Gordillo J.M. (2019) 'Splashing of droplets impacting superhydrophobic substrates', *J. Fluid Mech.*, vol. 870, pp. 175–188.

[417] Shaikh S., Toyofuku G., Hoang R., and Marston J. (2018) 'Immiscible impact dynamics of droplets onto millimetric films', *Exp. Fluids*, vol. 59(1), p. 7.

TH-2590_156103041

[418] Marmottant P. and Villermaux E. (2004) 'Fragmentation of stretched liquid ligaments', *Phys. Fluids*, vol. 16(8), pp. 2732–2741.

[419] Han Z., Xu Z., and Trigui N. (2000) 'Spray/wall interaction models for multidimensional engine simulation', *Int. J. Engine Res.*, vol. 1(1), pp. 127–146.

[420] Deng T., Varanasi K.K., Hsu M., Bhate N., Keimel C., Stein J., and Blohm M. (2009) 'Nonwetting of impinging droplets on textured surfaces', *Appl. Phys. Lett.*, vol. 94(13), p. 133109.

[421] Maitra T., Tiwari M.K., Antonini C., Schoch P., Jung S., Eberle P., and Poulikakos D. (2014) 'On the nanoengineering of superhydrophobic and impalement resistant surface textures below the freezing temperature', *Nano Lett.*, vol. 14(1), pp. 172–182.

[422] Papadopoulos P., Vollmer D., and Butt H.J. (2016) 'Long-term repellency of liquids by superoleophobic surfaces', *Phys. Rev. Lett.*, vol. 117(4), p. 046102.

[423] Kwon D.H. and Lee S.J. (2012) 'Impact and wetting behaviors of impinging microdroplets on superhydrophobic textured surfaces', *Appl. Phys. Lett.*, vol. 100(17), p. 171601.

[424] Onda T., Shibuichi S., Satoh N., and Tsujii K. (1996) 'Super-water-repellent fractal surfaces', *Langmuir*, vol. 12(9), pp. 2125–2127.

[425] Jiang G., Hu J., and Chen L. (2020) 'Preparation of a flexible superhydrophobic surface and its wetting mechanism based on fractal theory', *Langmuir*, vol. 36(29), pp. 8435–8443.

[426] Malavasi I., Veronesi F., Caldarelli A., Zani M., Raimondo M., and Marengo M. (2016) 'Is a knowledge of surface topology and contact angles enough to define the drop impact outcome?', *Langmuir*, vol. 32(25), pp. 6255–6262.

[427] Majhy B., Iqbal R., and Sen A. (2018) 'Facile fabrication and mechanistic understanding of a transparent reversible superhydrophobic–superhydrophilic surface', *Sci. Rep.*, vol. 8(1), pp. 1–11.

[428] Del Rıo O. and Neumann A.W. (1997) 'Axisymmetric drop shape analysis: computational methods for the measurement of interfacial properties from the

TH-2590_156103041

shape and dimensions of pendant and sessile drops', *J. Colloid Interface Sci.*, vol. 196(2), pp. 136–147.

[429] Levenberg K. (1944) 'A method for the solution of certain non-linear problems in least squares', *Q. Appl. Math.*, vol. 2(2), pp. 164–168.

[430] Marquardt D.W. (1963) 'An algorithm for least-squares estimation of nonlinear parameters', *SIAM J. Appl. Math.*, vol. 11(2), pp. 431–441.

[431] Rudawska A. and Jacniacka E. (2009) 'Analysis for determining surface free energy uncertainty by the owen–wendt method', *Int. J. Adhes. Adhes.*, vol. 29(4), pp. 451–457.

TH-2590_156103041

LIST OF PUBLICATIONS

International Journal

1. **Sarma, B.**, Dalal, A., Basu, D. N., Interfacial dynamics of viscous droplets impacting a Superhydrophobic candle soot surface: Overview and comparison. (*Under review in Langmuir*).

2. **Sarma, B.**, Kumar, S., Dalal, A., Basu, D. N., Bandyopadhyay, D., Electric discharge mediated jetting, crowning, bursting, and atomization of a droplet. (2021) *Physical Review Applied*, vol. **15**, pp. 014005.

3. **Sarma, B.**, Shahapure, V., Dalal, A., Basu, D. N., Magnetowetting dynamics of sessile ferrofluid drops on soft surface. (2020) *Soft Matter*, vol. **16**, pp. 970-982.

4. **Sarma, B.**, Shahapure, V., Dalal, A., Basu, D. N., Experimental characterization of the growth dynamics during capillarity-driven droplet generation, 2019, *Physical Review E*, vol. **100**, pp. 013106.

5. Kumar, S., **Sarma, B.**, Dasmahapatra, A. K., Dalal, A., Basu, D. N., Bandyopadhyay, D. (2017), Field-induced anomalous spreading, oscillation, ejection, spinning, and breaking of oil droplets on a strongly slipping water surface, *Faraday Discussions*, vol. **199**, pp. 115-128.

International Conference

1. **Sarma, B.**, Dalal, A., and Basu, D. N., Capillary flow mediated dynamics of liquid droplet generation from a yarn. *APS March Meeting 2021*, 15 – 19 March, 2021, Virtual, CDT (USA).

2. **Sarma, B.**, Dalal, A., and Basu, D. N., Universal scaling laws in drop-on-demand generation from a yarn. *8^{th} International and 47^{th} National Conference on Fluid Mechanics & Fluid Power* **(FMFP2020)**, 9 - 11 December, 2020, IIT Guwahati, India.

3. **Sarma, B.**, Dalal, A., and Basu, D. N., "Stick-slip" or "Stick-break?": Stiffness Mediated Magnetowetting Dynamics of Sessile Droplets. *73^{rd} Annual Meeting of the APS Division of Fluid Dynamics* **(APSDFD)**, 22 – 24 November, 2020, Virtual, CT (Chicago time).

TH-2590_156103041

4. **Sarma, B.**, Capillary Flow Mediated Drop Formation in a Yarn-based Microfluidic System. *InterPore 2020*, 31 August - 3 September, 2020 (Virtual).

5. **Sarma, B.**, Soft Magnetowetting. *UK Colloids 2020*, 21 July, 2020 (Virtual).

6. **Sarma, B.**, S. Kumar, A. Dalal, D. N. Basu, and D. Bandyopadhyay, Electric Discharge Mediated Transient Interfacial Dynamics of a Sessile Liquid Droplet: Plethora of Hydrodynamic Features. *APS March Meeting 2020*, 2 - 6 March, 2020, Denver, Colorado.

7. **Sarma, B.**, Dalal, A., and Basu, D. N., Altered Energy Landscape of Hydrophobic Surfaces: Role of Soot Nanoparticles, 6^{th} *International Conference on Advanced Nanomaterial and Nanotechnology* **(ICANN2019)**, 18 - 21 December, 2019, IIT Guwahati, India.

8. **Sarma, B.**, Dalal, A., and Basu, D. N., Transient Interfacial Dynamics of Viscous Droplets Impacting on Superhydrophobic Surfaces, 25^{th} *National and* 3^{rd} *International ISHMT-ASTFE Heat and Mass Transfer Conference* **(IHMTC-2019)**, 28 - 31 December, 2019, IIT Roorkee, India.

9. **Sarma, B.**, Dalal, A., and Basu, D. N., Impact Dynamics of Viscous Droplets on Superhydrophobic Surface, *Fluids and Health 2019: Fluid Dynamics of Disease Transmission*, 23 July- 3 August, 2019, The Cargese Institute of Scientific Studies, France.

10. **Sarma, B.**, Basu, D. N., and Dalal, A., Dynamics of Droplet Generation in a Critically Low Weber Number Flow, 4^{th} *Indian Conference on Applied Mechanics* **(INCAM 2019)**, 3 - 5 July, 2019, IISc Bangalore, India.

11. **Sarma, B.**, Shahapure, V., Dalal, A., and Basu, D. N., Self-similar Temporal Dynamics of Liquid Droplets Evolving from a Yarn, *Research Conclave*, 14 - 17 March, 2019, IIT Guwahati.

12. Shahapure, V., **Sarma, B.**, Dalal, A., and Basu, D. N., Role of High-Speed Imaging and Image Analysis in Droplet Dynamics, *Research Conclave*, 14 - 17 March, 2019, IIT Guwahati.

13. **Sarma, B.**, Dalal, A., and Basu, D. N., Universal Scaling Laws in Drop-on-Demand Generation from a Yarn, 7^{th} *International and* 45^{th} *National Confer-*

TH-2590_156103041

ence on Fluid Mechanics and Fluid Power **(FMFP 2018)**, 10 - 12 December, 2018, IIT Bombay, India.

14. Shahapure, V., **Sarma, B.**, Dalal, A., and Basu, D. N., High-Speed Imaging And Analysis of Drop Formation, *7th International and 45th National Conference on Fluid Mechanics and Fluid Power* **(FMFP 2018)**, 10 - 12 December, 2018, IIT Bombay, India.

15. **Sarma, B.**, Pokhrel, S., Kumar, S., Dalal, A., Bandyopadhyay, D., and Basu, D. N., Prediction of Sauter Mean Diameter of Spray During Electric Discharge Mediated Bursting of a Droplet, *International Conference on Recent Innovations and Developments in Mechanical Engineering*, 8 - 10 November, 2018, NIT Meghalaya, India.

16. **Sarma, B.**, Kumar, S., Bandyopadhyay, D., Dalal, A., Basu, D. N., and Dasmahapatra, A. K., Electrowetting-on-Liquid (EWOL): A Novel Technique for Microfluidics Based Applications, *Research Conclave*, 8 - 10 March, 2018, IIT Guwahati.

17. Kumar, S., **Sarma, B.**, Dasmahapatra, A. K., Dalal, A., Basu, D. N., and Bandyopadhyay, D., Field Induced Anomalous Spreading, Oscillation, Ejection, Spinning, and Breaking of Oil Droplets on a Strongly Slipping Water Surface, Chemical Physics of Electroactive Materials Faraday Discussion, 10-12 April, 2017, Cambridge, United Kingdom.

18. **Sarma, B.**, Kumar, S., Dalal, A., Basu, D. N., Dasmahapatra, A. K., and Bandyopadhyay, D., On Demand Magnetic Manipulation of Nanoparticle Laden Droplets on Micro-Fiber Highway, *REFLUX 2017*, 14 - 16 March, 2017, IIT Guwahati.

19. **Sarma, B.**, Kumar, S., Dalal, A., Basu, D. N., Dasmahapatra, A. K., and Bandyopadhyay, D., Dynamics of Electrolyte Droplet in Presence of Electric Field, *Research Conclave 2017*, 8 - 10 March, 2017, IIT Guwahati.

20. **Sarma, B.**, Kumar, S., Dalal, A., Basu, D. N., and Bandyopadhyay, D., Dasmahapatra, A. K., and Bandyopadhyay, D., Directional motion of Nanoparticle Laden Droplets on Micro-Fiber Highway, NANO INDIA 2017, IIT Delhi (supported by Department of Science & Technology (DST)).

TH-2590_156103041

21. **Sarma, B.**, Kumar, S., Dalal, A., Basu, D. N., Dasmahapatra, A. K., and Bandyopadhyay, D., Instability and Breaking of Aqueous Droplet on a Dielectric Coated Electrode, *COMPFLU 2016*, IIIT Hyderabad.

TH-2590_156103041

TH-2590_156103041

TH-2590_156103041

Appendix A

Cleaning methodology of glass substrates

A.1 Cleaning process of ITO-coated glass

ITO-coated glasses are initially sonicated with a soap solution for 30 min and afterward rinsed with DI-water for 4-5 min. The substrates are then sonicated with acetone and isopropyl alcohol consecutively each for 15 min. The ITO-coated glasses are then dried with nitrogen before placing it in an oxygen plasma chamber for 20 min (power: $\sim$ 1 W, $\sim$ 350 V, and 3 mA). The freshly cleaned ITO substrates are then spin-coated with the PDMS solution.

A.2 Cleaning process of glass micro-slides

Glass micro-slides are usually cut in the desired size (usually in 15 mm $\times$ 15 mm) before soaking them in detergent solutions for 30 min. After that, hard brushing is done on pre-soaked glass slides (usually 200 strokes/2 min of brushing) and subsequently sonicated in the same detergent solution for 15 min. Next, the sonicated slides are boiled in in a bath of acetone (60 ml) at 100°C for 10 min and subsequently, in a bath of ethanol (60 ml) for boiling again at 100°C. Later on, the glass slides are subjected to sonication on the same ethanol for 15 min. Afterward, they are rinsed in DI-water for 1-2 min and subsequently boiled in 5:1:1 ($H_2O : NH_3 : H_2O_2$)

TH-2590_156103041

solution for 15 mins. The glass slides are again rinsed with DI-water for 4-5 min in the last step. These cleaned glass micro-slides are then dried with N_2 and put to use before contamination occurs.

TH-2590_156103041

Appendix B

Droplet on a yarn

B.1 Estimation of the drop shape

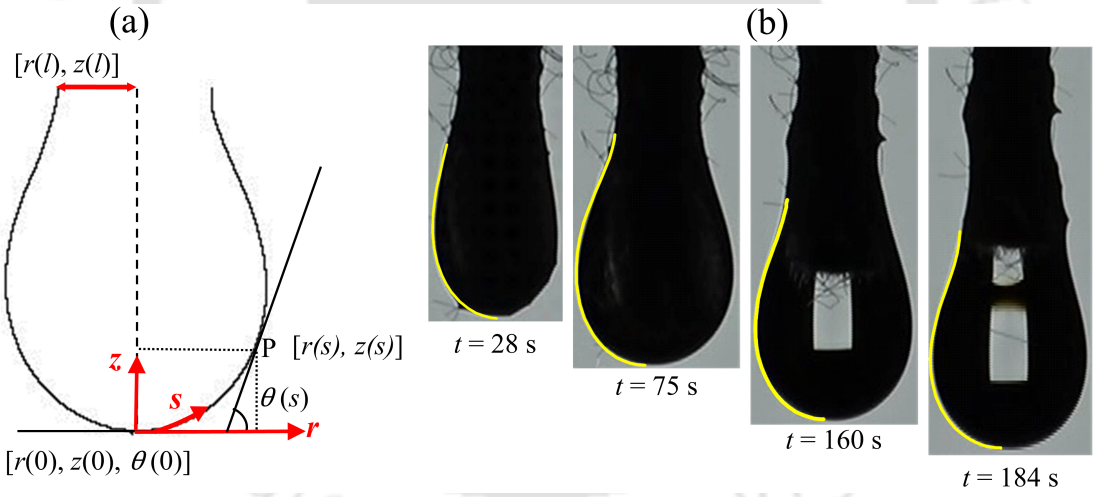


Figure B.1: (a) Schematic of an axisymmetric drop attached to a capillary with all the spatial and angular variables defining the shape at each instant. (b) Comparison between the numerically obtained droplet shape (yellow curve) with the droplet shape obtained experimentally by fitting the former upon the latter. The axisymmetric equations can describe the shape well, as the yellow curve fits the experimental shapes completely. The experimental conditions encountered are, Q^{Twn20} = 8.68 $\times 10^{-11}$ m^3/s, We = 5.03 $\times 10^{-8}$, Oh = 0.0063, and Fr = 5.73 $\times 10^{-4}$.

In Chapter 3, although drop formation has been engendered by a flow field with a low flow rate, the well-established Young-Laplace equation could predict the shape of

TH-2590_156103041

the drop at all three stages of droplet growth mentioned previously. The differential equations that define the axisymmetric shape of a growing drop attached to the yarn are as follows [149];

$$\frac{dr}{ds} = \cos(\theta), \tag{B.1}$$

$$\frac{dz}{ds} = \sin(\theta), \tag{B.2}$$

$$\frac{d\theta}{ds} = 2\kappa_0 - (\frac{1}{L_{cap}^2})z - \frac{\sin(\theta)}{r}, \tag{B.3}$$

with the initial conditions prescribed as;

$$r(0) = 0;\ z(0) = z_{min} \text{ and } \theta(0) = 0 \quad .$$

As shown in Figure B.1(a), s represents the arc length, κ_0 is the curvature at the apex, z_{min} is the position of the apex, and L_{cap} is the capillary length as defined previously. The droplet shapes obtained after solving Eqs. (B.1)-(B.3) numerically when fitted over the experimentally generated droplet shapes, shows good match as shown in Figure B.1(b), wherein the yellow curve is the shape of the interface obtained numerically. Figure B.1(b) corresponds to the different stages of growth of a drop of tween 20 solution from a yarn with experimental conditions, $Q^{Twn20} = 8.68 \times 10^{-11}$ m^3/s, $We = 5.03 \times 10^{-8}$, $Oh = 0.0063$, and $Fr = 5.73 \times 10^{-4}$. Also, as ascribed in Chang *et al.*, [149] the contact angle has not been considered as boundary conditions due to the prevalence of contact angle hysteresis between the advancing and receding contact angle while moving along the yarn. Further, the good agreement between the experimental data and theoretical prediction also confirms the universality of the *Young-Laplace axisymmetric equations* describing the interfacial shape change of a drop growing in a yarn.

B.2 Details of regression analysis

By having a closer look in the Figure 3.8(a), the relationship between z_{tp}^* and t^* in the *motion* stage can be defined as below:

$$z_{tp}^* = 1 - [We^a Oh^b Fr^c exp(dt^*)], \tag{B.4}$$

TH-2590_156103041

where, a, b, c, and d are experimentally fitted constants. The regression analysis is carried out using the *Levenberg-Marquardt algorithm*, which is being popularly used in many industrial optimization processes, including the pendant drop shape optimization routines [428]. This nonlinear least-square optimization algorithm combines the speed and the accuracy of both *Gauss-Newton optimization* and the *Steepest Descent Method* and optimizes the iterations by considering the minimization of the sum of the squared residuals between each experimental data point and corresponding theoretical data point [429, 430]. The parametric convergence criteria have been set as $1E^{-8}$ for the present regression analysis, which resulted in 38 iterations for evaluation of the constants of Eq. B.4. The regression analysis of the experimental data resulted in the following equation,

$$z^*_{tp} = 1 - \left(\frac{We^{0.633} Oh^{0.407}}{Fr^{1.116}} exp(4.232t^*) \right). \tag{B.5}$$

The standard values of the fitted coefficients in Eq. B.5 are, $a = 0.633 \pm .031$, $b = 0.407 \pm .015$, $c = -1.116 \pm .064$, and $d = 4.323 \pm 0.109$. The corresponding values of the regression coefficient, R^2, and the *mean squared error (MSE)* are found out to be 0.930, and 0.009, respectively.

A similar type of regression analysis has been carried out for obtaining the scaling relation, Eq. 3.6, between r^*_d and t^*. The values and range of the fitted coefficients a, b, c, and d, in case of Eq. 3.6 are found out to be, $0.281 \pm .022$, $0.122 \pm .008$, $0.670 \pm .048$, and -3.410 ± 0.045, respectively. The value of the regression coefficient, R^2, is 0.963, whereas, the MSE is found out as 0.0001.

TH-2590_156103041

TH-2590_156103041

Appendix C

Soft magnetowetting

C.1 Magnetic Bernoulli equation

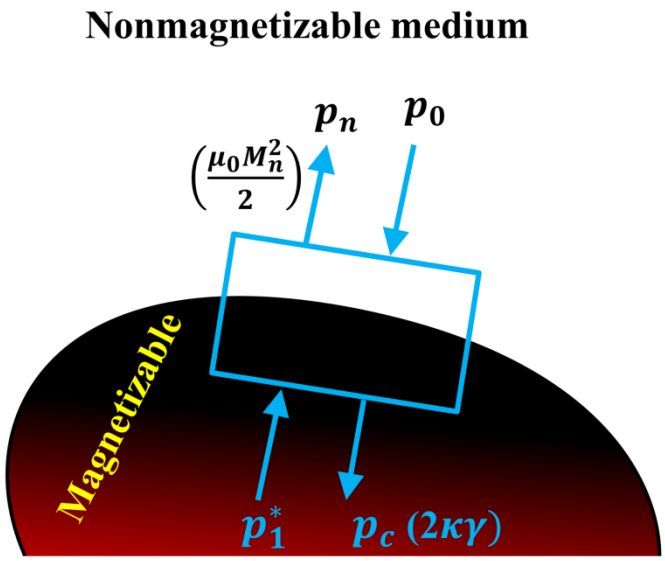


Figure C.1: Schematic representation of the force balance at the interface between the magnetizable liquid medium (1) and non-magnetizable surrounding (2). The same has been written as FHD boundary condition in Eq. C.2.

The process of continuous elongation by elevating the apex for water-based FF

TH-2590_156103041

droplets, surrounded by a non-magnetizable medium, in a non-uniform magnetic field can be explained with the help of augmented *magnetic Bernoulli equation* [98, 240, 241] as written below:

$$p^* + \rho g h_{intf} + \frac{\rho v_{intf}^2}{2} - p_m = const, \tag{C.1}$$

subjected to the boundary condition,

$$p^* + p_n = p_0 + p_c, \tag{C.2}$$

where, ρ is the density of the ferrofluid, v_{intf} is the velocity, and h_{intf} is the height of the interface and n is unit vector normal to the interface.

Equations C.1 and C.2 have been derived considering a sessile FF droplet continuously evolving in a magnetic field of strength, H and following the basic assumptions of incompressible, inviscid, and isothermal flow. Here, $p_m = \mu_0 \int_0^H M dH$, is the fluid magnetic pressure, with M being the magnetization corresponding to and parallel to the field H, $p_n = \mu_0 M_n^2/2$ is the magnetic normal pressure with M_n representing the normal component of magnetization, $p_c = 2\kappa\gamma$ is the capillary pressure acting at an interface of curvature κ, p_0 is the pressure of the surrounding nonmagnetic fluid and $p^* = p(\rho, T) + p_m + p_s$ is the modified pressure combining the effect of thermodynamic pressure, $p\ (\rho, T)$, magnetorestrictive pressure, p_s, and the fluid magnetic pressure, p_m. The permeability of vacuum has the value of, $\mu_0 = 4\ \pi \times\ 10^{-7}$ N/A^2. The direction of all the pressure components is shown schematically in Figure C.1.

In the present study, substituting $v_{intf} = v_{intf}^1 = v_{intf}^2 = 0$ and $p_1 = p_2$, considering a stationary droplet, into the magnetic Bernoulli equation, Eq. C.1, Eq. C.3 is obtained as below,

$$h_{intf}^2 - h_{intf}^1 = \frac{\mu_0 H M}{\rho g}, \tag{C.3}$$

where,

$$\overline{M} = \frac{1}{H} \int_0^H M dH = \frac{1}{H} \int_0^H \chi H dH. \tag{C.4}$$

Here, $\overline{M}$ represents average magnetization in the direction of the non-uniform field, and χ is equal to the initial magnetic susceptibility. Equation C.3, with a positive

TH-2590_156103041

right-hand side for water-based FF droplets, clearly explains the continuous elongation and ascent in the sessile condition, which finally triggers splitting of the droplet.

To add further, the magnetic surface force density at the interface can be calculated by introducing a surface stress tensor, T_m, as below,

$$t_{nn} = nT_m n = p_m + p_n = \mu_0 \int_0^H MdH + \mu_0 M_n^2/2. \tag{C.5}$$

The surface stress tensor is useful for obtaining the elongation of the FF droplet, where the former is a function of both the magnetic field strength and magnetization of the FF as shown in Eq. C.5. Notably, the stress tensor is primarily directed away from the magnetizable medium towards the non-magnetizable medium in the case of water-based FF's.

C.2 Evaporation of ferrofluid droplets

The temporal variations in dynamic contact angle, θ_d and contact radius, r_c is shown in Figures C.2(a) and C.2(b) for evaporation of a 3 μL FF droplet on substrates with different elasticity (E = 1.5, 0.06, and 0.02 MPa) in the absence of magnetic field. The temporal scale has been non-dimensionalized with the evaporation time scale, (t_{evap} = 35 min). Further, to aid the reader, the variations of θ_d and r_c during magnetowetting on same substrate [corresponds to Figure 4.3 in the main manuscript, i.e., B = 450 mT and Bo_m = 131] is plotted in the inset of Figures C.2(a) and C.2(b). It can be discerned that the variations in the concerned quantities are quite sharp during magnetowetting, whereas the contact line dynamics during evaporation has comparatively slower dynamics. The change in the mass of the droplet is also negligible within the time scale of deformation and splitting, as shown in Figure C.2(c). This further strengthens the previous claim regarding the negligible effect of droplet evaporation on the dynamics of magnetowetting observed for the present set of experimental data.

TH-2590_156103041

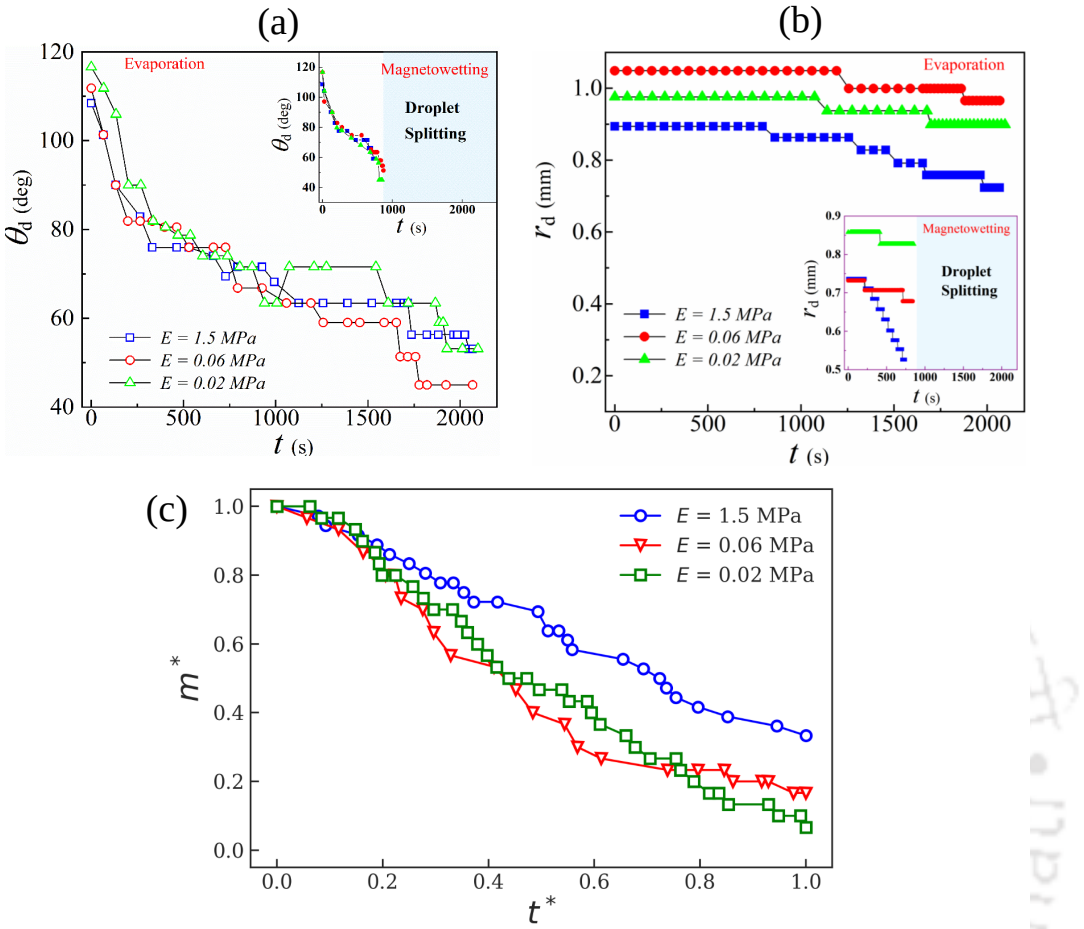


Figure C.2: Temporal variation of the (a) dynamic contact angle, θ_d, and (b) contact radius, r_c during the evaporation of FF droplets ($\phi_0 = 3$ μL) in absence of magnetic field dispensed atop three substrates with different elastic moduli, $E = 1.5$, 0.06, and 0.02 MPa. The time scale has been non-dimensionalized with the evaporation time scale, (t_e). The magnetowetting behavior of the same FF droplets is shown in the inset for $B = 450$ mT ($Bo_m = 131$). (c) Shows the variation of mass of FF droplets during evaporation on substrates of different stiffness.

C.3 Comparison of surface energy

The magnitudes of the surface energy for all the three surfaces (10:1, 30:1, and 50:1 PDMS film), considered in Chapter 4, are listed in Table C.1. The table highlights a meager difference in the surface energies (γ_{sv}) between the surfaces with different stiffness. The previous observation implies that changing the PDMS base to cross-linker ratio does not significantly alter the surface energy. In contrast, the stiffness decreases nearly by three orders. Therefore, it can be concluded that the differences

TH-2590_156103041

in the contact line and contact angle dynamics between the soft and apparently rigid substrates originate from the changing stiffness of the underlying substrate. Notably, a rigid glass surface has a substantially higher surface energy value than the PDMS film-coated substrates, as shown in Table C.1.

Here, the surface energy is measured using the most popular *Owens-Wendt method* [431]. In this method, an unknown surface's surface energy is measured by using a few referencing liquids with known liquid-vapour surface tension components (dispersive and polar parts). The probing liquids for surface energy measurements of this study are water, glycerol, and ethylene glycol with surface tension values (γ_{sv}) as listed in Table C.2.

Table C.1: Surface energy of different substrates measured by Owens-Wendt method.

Substrate	γ_{sv} (mN/m)
Glass	63.9 ± 2.25
10:1 PDMS surface (E =1.5 MPa)	10.71 ± 1.27
30:1 PDMS surface (E =0.06 MPa)	9.47 ± 0.65
50:1 PDMS surface (E =0.02 MPa)	7.02 ± 1.45

Table C.2: Surface tension of probing liquids with respective polar and dispersive components.

Liquid	γ_{lv} (mN/m)	γ_{lv}^{D} (dispersive)	γ_{lv}^{P} (polar)
Water	72.8	21.8	51.0
Ethylene glycol	47.7	30.9	16.8
Glycerol	63.4	37.0	26.4

TH-2590_156103041

TH-2590_156103041

Appendix D

Discharge-driven droplet atomization

D.1 Effect of contact angle

The equilibrium contact angle (θ_{eq}) of the experimental fluids on the prepared PDMS film-coated ITO-glass substrates are shown in Table D.1. It can be inferred that θ_{eq} does not vary substantially for different compositions of the salt concentration and viscosity. The maximum value of the θ_{eq} ($= 110.7 \pm 6$) is seen in case of 1.0 M aqueous solution (solution 5). Further, the values of the θ_{eq} in Table D.1, clearly supports the aforementioned claim [in Section 5.3 of Chapter 5] that the dynamics of jetting, crowning, and bursting are not much influenced by the equilibrium contact angle (or *initial contact angle*). On the other hand, we believe that the observed hydrodynamics are greatly influenced by the advancing contact angle [θ_{a0}, refer to Figure D.1(b) for definition] prior to discharge. This can be attributed to the discharge-assisted spreading of the droplet [276], leading to a change in the contact angle in most cases. The spreading of the droplet is prominent in the case of viscous glycerol-water droplets. However, a detailed appraisal of the effect of the θ_{a0} on the observed discharge-assisted hydrodynamics is beyond the scope of this study.

TH-2590_156103041

Table D.1: Equilibrium contact angle, θ_{eq} (in degrees), of the experimental solutions.

Solution	θ_{eq}
Solution 3	108.6 ± 3.5
Solution 4	107.9 ± 5
Solution 5	110.7 ± 6
Solution 6	107.4 ± 7
Solution 7	105.2 ± 5
Solution 8	108.9 ± 3
Solution 9	106 ± 6

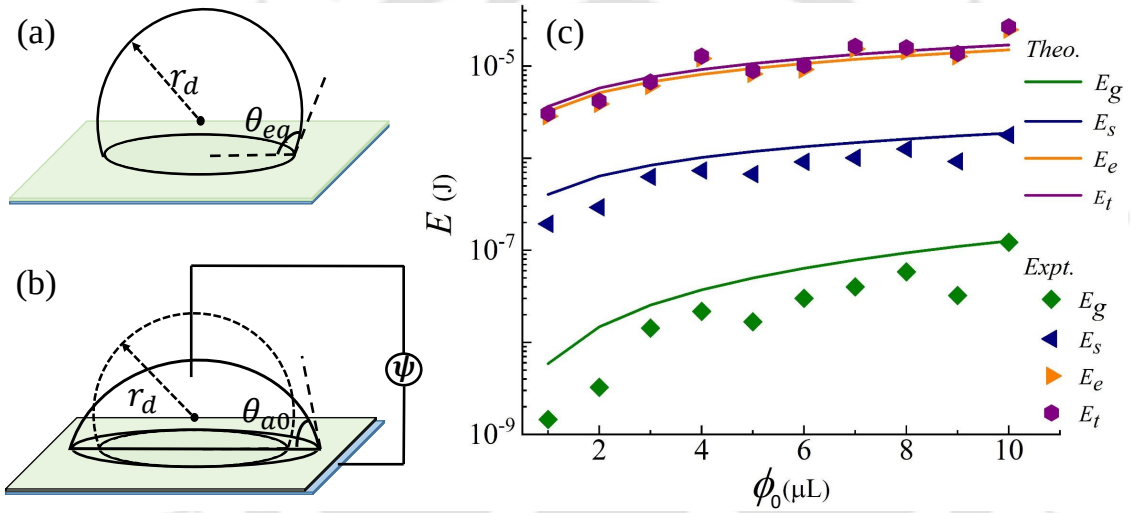


Figure D.1: Image (a) shows the equilibrium configuration of a conducting sessile droplet resting on an isolator-substrate pair. The notations r_d and θ_{eq} denote the radius of the droplet and equilibrium contact angle, respectively. Image (b) shows the droplet in equilibrium when a potential difference (ψ) is applied between the flat bottom (blue colour) and pointed top electrodes. The notation θ_{a0} corresponds to the advancing contact angle of the drop due to electric stress accumulated at the contact line. The plot (c) shows the variations in interfacial potential energy (E_s), gravitational potential energy (E_g), the potential energy of the dielectric layer under electric field (E_e), and the total energy (E_t) with the variation in the droplet volume (ϕ_0), obtained from both experimental as well as theoretical analysis, for a droplet configuration as shown in the image (b).

D.2 Comparison of different potential energy

Figure D.1(a) shows the equilibrium state of sessile drop resting on an isolator-substrate pair in the absence of electric field. The shape of the drop is assumed to

TH-2590_156103041

be a sphere cut by a solid plane at the bottom, as previously discussed by Shapiro *et al.* [309]. With the help of geometrical analogy the different interfacial areas have been evaluated as, $A_{ls} = \pi r_d^2 \sin^2\theta_{eq}$ and $A_{lg} = 2\pi r_d^2(1 - \cos\theta_{eq})$, where the subscripts l, s, and g denote liquid, solid, and gas phases, respectively and A_{ij} represents the interfacial area. Here, the notations r_d and θ_{eq} indicate the radius of the sessile droplet (spherical shape approximation) and its equilibrium contact angle, respectively.

Assuming the interfacial/surface tension values to be constant, the potential energy, (E_s) can be calculated as [309],

$$E_s = (\gamma_{ls} - \gamma_{sg})A_{ls} + \gamma_{lg}A_{lg} = \pi r_d^2 \gamma_{lg}(2 - 3\cos\theta_{eq} + cos^3\theta_{eq}), \tag{D.1}$$

where, γ_{ij} refers to the surface tension coefficients with units of energy per unit area. Further, the gravitational potential energy, E_g for the sessile drop shown in Figure D.1(a) is given by,

$$E_g = \frac{2\pi}{3}\rho g r_d^4 \sin^6\theta_{eq}(3 + \cos\theta_{eq}), \tag{D.2}$$

where g is the acceleration due to gravity. Again, the application of the electric field to a droplet resting on a solid dielectric layer generates Maxwell's stress at the TPCL because the dielectric layer acts as a charging capacitor, as shown in Figure D.1(b). The corresponding electrical energy (E_e) stored in the solid dielectric layer is calculated as,

$$E_e = \frac{\epsilon_0 \epsilon_p \psi^2 A_{ls}}{2h}, \tag{D.3}$$

where the notations, ϵ_0, ϵ_p, ψ, A_{ls} and h denote the permittivity of the free space, the dielectric constant of the solid, applied electric potential, solid-liquid interfacial area, and thickness of the dielectric layer, respectively. Therefore, the total energy E_t of the system shown in Figure D.1(b) is,

$$E_t = E_s + E_g + E_e. \tag{D.4}$$

Equations D.1 - D.4 are solved for different volumes of the droplet (ϕ_0) ranging from 1 μL to 10 μL considering $\theta_{eq} = 100°$, $\psi = 300$ V. The theoretical values obtained for E_s, E_g, E_e, and E_t have been shown as the solid lines in Figure D.1(c). The E_s, E_g, E_e, and E_t are also evaluated experimentally by noting down the

TH-2590_156103041

change in the θ_{eq}, and r_d for the droplets having, ϕ_0, in the range of 1 µL - 10 µL. The symbols in Figure D.1(c) depict the experimental results, which are in close agreement with the corresponding theoretical values. The figure suggests that the contribution from the gravitational force is significantly less while the electric field force dominates over the other forces especially when, $\phi_0 < 5$ µL. Thus, the droplet volume used in the reported experiments is 5 µL, unless stated otherwise, and in the subsequent analysis the effect of gravity has not been considered.

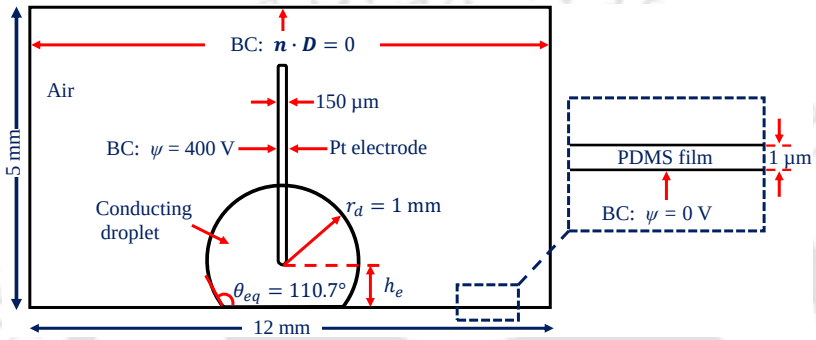


Figure D.2: The computational domain for the numerical simulations.

D.3 Numerical simulation of electric field

Considering the irrotational electric field, $\boldsymbol{\Psi}$, to follow the field, $\boldsymbol{\Psi} = -\boldsymbol{\nabla}\psi$, the Gauss's law can be written in the following form, in which ψ is the electric potential applied,

$$\boldsymbol{\nabla} \cdot \boldsymbol{D} = q_v, \tag{D.5}$$

where, $\boldsymbol{D}$ represents the electric displacement field, defined as, $\boldsymbol{D} = \epsilon_0 \boldsymbol{\Psi} + \boldsymbol{P}$ ($\boldsymbol{P}$ is polarization vector field), for a dielectric medium and q_v is the charge density.

Equation D.5 is solved by using the finite element method (FEM) in a commercial software COMSOL Multiphysics^{TM} 5.0 (Electrostatic Module) for a 2-D geometry shown in Figure D.2. The governing equation [Eq. D.5] is solved using the boundary conditions discussed next. The *electric potential* boundary conditions, $\psi = 400$ and $\psi = 0$, are used at the Pt electrode (anode) and the cathode, respectively. The *zero charge* [i.e., $\boldsymbol{n} \cdot \boldsymbol{D} = 0$] boundary condition is used at the rest of the boundaries. The domain is discretized with nearly 70000 triangular elements, which is obtained through the grid independence test. Second-order elements are used

TH-2590_156103041

for the discretization of the electric potential. The *Multifrontal Massively Parallel Sparse direct solver (MUMPS)* has been used for solving the governing equation. The corresponding results are discussed in the context of Figures 5.4 and 5.5 in Chapter 5.

D.4 Instability of viscous jets

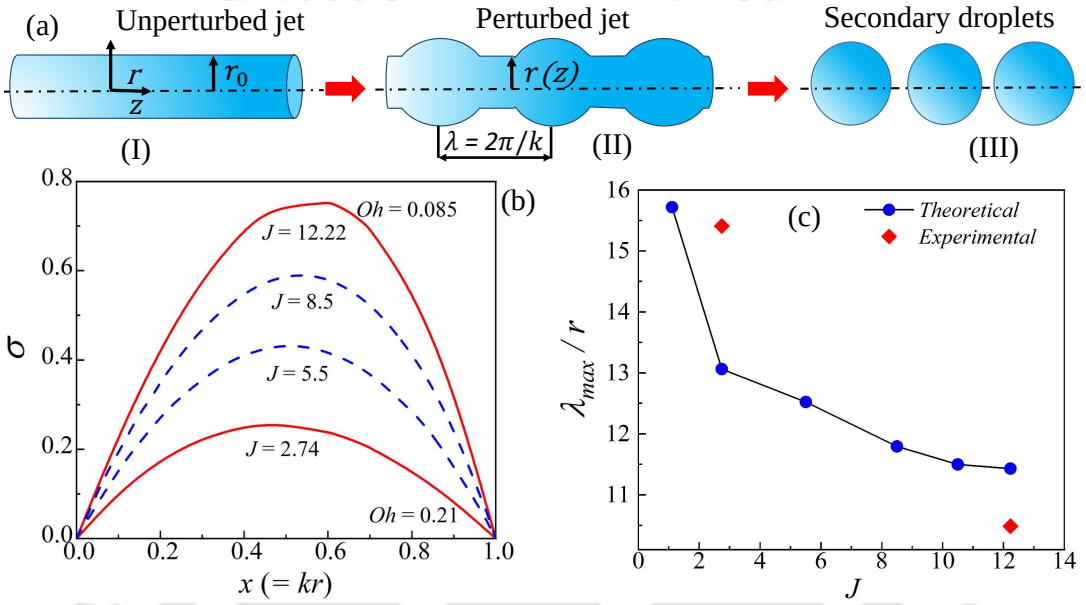


Figure D.3: Image (a) schematically shows the different stages of the instability of an infinite cylindrical jet leading to the generation of secondary droplets. The plot (b) shows the dispersion curves (σ vs. x) in which the effect of viscosity on the capillary instability of an infinite cylinder has been shown. The red coloured solid lines for, $J = 2.74$ and $J = 12.22$, are associated with solutions 8 and 9 in Table 5.2. The broken lines show the variation of σ for a range of viscosity values. Plot (c) shows the variation of λ_{max}/r with J derived from Eqs. D.6 and D.7, as shown by the continuous lines. The red symbols correspond to solutions 8 and 9 in Table 5.2.

The instabilities of the viscous jets have been shown previously by Chandrasekhar [96] with the help of theoretical analyses in his monograph. The same theoretical framework is employed to explain the experimental observations of viscous jet bifurcation in Chapter 5. For this purpose, the equation for a continuously deforming perturbed surface is considered [shown in Figure D.3(a)] as, $\varpi = r_0 + \varepsilon e^{i(kz+m\phi)}$, to

TH-2590_156103041

obtain the following dispersion relations [Eqs. D.6 and D.7], formulated by Chandrasekhar [96], and subsequently, identify the dominant wavelength (λ_{max}) of the instability of cylindrical jets,

$$\frac{\sigma r^2}{\nu} = x^2 - y^2, \tag{D.6}$$

$$2x^2(x^2+y^2)\frac{I_1'(x)}{I_0(x)}\left[1 - \frac{2xy}{x^2+y^2}\frac{I_1(x)}{I_1(y)}\frac{I_1'(y)}{I_1'(x)}\right] - (x^4 - y^4) = J\frac{xI_1(x)}{I_0(x)}(1-x^2). \tag{D.7}$$

Here, ϖ being the horizontal distance from the jet axis, z is the direction of the axis of the jet, ε is a function of time defined as $\varepsilon = \varepsilon_0 e^{\sigma t}$, r_0 is the radius of the unperturbed cylinder, k is the wavenumber of the perturbation in z-direction, and m is an integer having any real value. Further, σ is the growth rate, $x = kr$, is the wave number, $J = \frac{\gamma}{\rho r^3}(\frac{r^2}{\nu})^2 = \frac{\gamma r}{\rho \nu^2}$, is the additional parameter arise out of the effect of viscosity, and I_n are the modified Bessel functions of first kind. The dispersion curves (σ vs. x) in Figure D.3(b) suggest that as the viscosity values are increased (decreasing J) the magnitude of the maximum growth rate (σ_{max}) is reduced and shifted towards smaller values of x. Figure D.3(c) shows the variation in the λ_{max}/r with J obtained from the dispersion Eqs. D.6 and D.7 [325]. The theoretical values of λ_{max}/r are in close agreement with the experimental values of λ/r as shown in Figure 5.9 in Chapter 5.

TH-2590_156103041

Appendix E

Droplet impaction on a superhydrophobic surface

E.1 Comparison of the spreading parameter

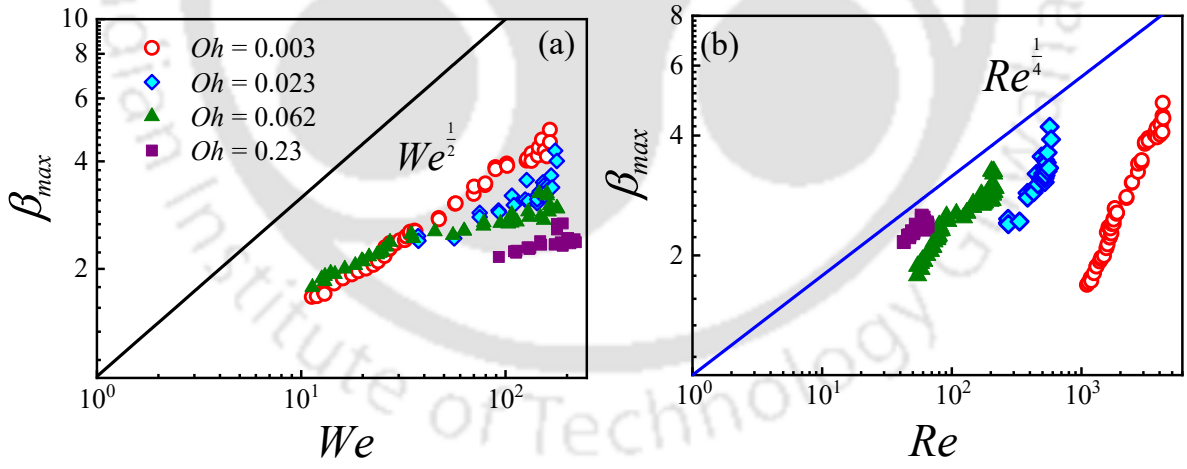


Figure E.1: Maximum spreading ratio, β_{max}, variation with the impact (a) We, when the theoretical scaling law, $\beta_{max} = We^{\frac{1}{2}}$ is applied and (b) Re, when the theoretical scaling law, $\beta_{max} = Re^{\frac{1}{4}}$ is applied.

The maximum spreading diameter, r_{max} of liquid droplets impacting wetting/non-wetting surfaces, is crucial for many practical applications. Many theoretical laws are available for defining the maximum spreading parameter, such as, $\beta_{max} = We^{\frac{1}{2}}$

TH-2590_156103041

and $\beta_{max} = Re^{\frac{1}{4}}$ for the impact of droplets. However, these independent laws are found insufficient in explaining the concerned experimental observations [refer to Figure 6.8] of Chapter 6 convincingly. This can be attributed to the fact that the dynamics of the spreading (and retraction) regime is primarily dependent on the three competing forces: inertial, capillary, and viscous force. As such, a crossover regime is expected between the limits of the capillary regime and viscous regime [392]. In this similar note, Laan *et al.* [392] have proposed a theoretical model for predicting the maximum extent of spreading after considering the spreading parameter P ($\equiv f(We\ Re^{-\frac{2}{5}})$) as, $\left(\frac{D_{max}}{D_0}\right)\ Re^{-\frac{1}{5}} = \frac{P^{\frac{1}{2}}}{A+P^{\frac{1}{2}}}$. The above model approaches the limit of viscous regime asymptotically when $P >> 1$. A similar result is also shown by Zhao *et al.* [370], where the scaling law, $\beta_{max} = Re^{\frac{1}{4}}$ is shown to follow the experimental results in the limit of very high viscosity ($\eta > 82$ mPa s). Hence, it has been previously claimed that these independent laws do not agree well with the concerned experimental results [Figure 6.8] within the limit of viscosity values considered in Chapter 6. Interestingly, the scaling law of Gordillo *et al.* [405], based on the conservation of mass and momentum fluxes of a spreading rim, agrees strongly with the experimental data as shown in Figure 6.9 of Chapter 6.

$$2\ We^{-1}\ r_{max}^2 + 0.45\ \lambda\ Re^{-\frac{1}{2}}\ r_{max}^{\frac{5}{2}} - 0.45 = 0, \tag{E.1}$$

where λ ($= 0.4$) is a free constant signifying the friction factor between the droplet and the superhydrophobic surface and accounts for slip length in the case of SHPs. The value of λ has been adjusted experimentally to absorb all the assumptions in deriving the Eq. E.1 [405]. Another noteworthy point regarding Eq. E.1 is that herein the continuously developing viscous boundary layer has been considered to analyze the dynamics of the liquid sheet bounded by a rim, whereas the existing studies considered a fixed height of the boundary layer, thereby imparting error to the viscous dissipation term [370]. Hence, the theoretical values obtained from Eq E.1 are compared with the experimental data of Figure 6.8 in Chapter 6. Interestingly, Gordillo *et al.* [405] have shown that Eq. E.1 can be made equivalent to the spreading parameter based expression of Laan *et al.* [392], considering $r_{max} = Re^{\frac{1}{5}} f$. The aforementioned discussions further highlight the universality of Eq. E.1.

TH-2590_156103041

E.2 Total number of secondary droplets from splashing

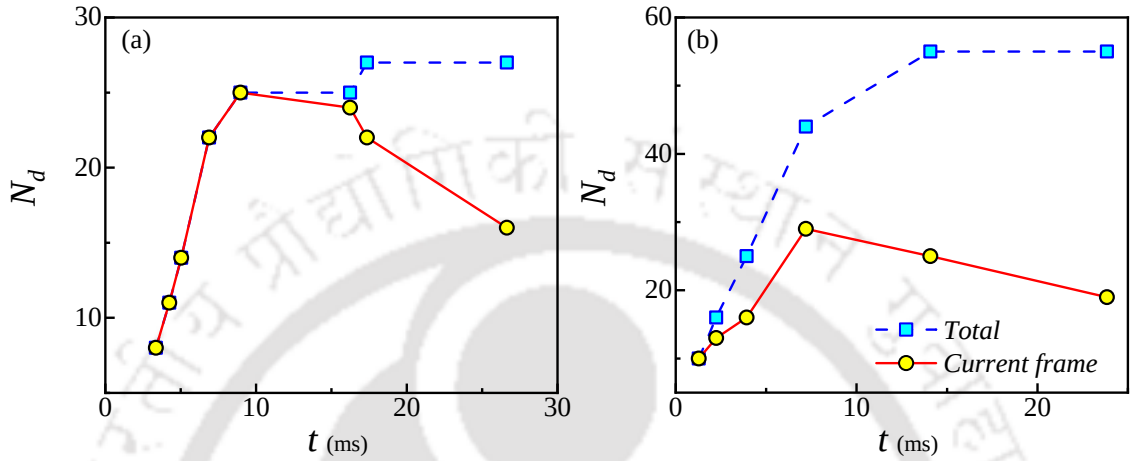


Figure E.2: (a),(b) Comparison between the two representative methods of secondary droplet counting, namely: number of droplets in the current frame and total number of droplets.

This section discusses an essential concept regarding the counting of secondary droplets engendered by liquid droplet splashing, which positively refers to the total number of secondary droplets generated from the beginning of impact (t =0) to the end of the droplet retraction process ($t = t_c$). Generally, there are two different secondary droplet counting approaches: the number of droplets in the current frame and the total number of droplets. In the first method, the total number of droplets is added from each frame (even if they are out of frame) to give a cumulative overview. In the latter concept, one considers the secondary droplets detected within the frame at a specific time instant. As shown in Figure E.2, both these concepts offer different perspectives in elucidating splashing scenarios. In the concerning figure, the data of secondary droplets engendered from splashing are shown from two different incidents (two different impact velocities) to elucidate the differences in the aforementioned two approaches. In Figure E.2(a), it is seen that at $t \approx 9$ ms, both the total number and the number of secondary droplets in the current frame matches exactly, highlighting the fact that all the secondary droplets generated at this moment are within the recording area. However, at the instant $t = 16.24$ ms, the number of secondary droplets at the relevant frame is slightly lower than the total number of secondary droplets. This is because a few of these secondary droplets have moved out of the

TH-2590_156103041

recording area, whereas the total number of droplets is still the same as that of the previous frame. The difference between the total number and no. of secondary droplets in the current frame increases as the time increases, as secondary droplets are newly generated in these instants. However, more number of secondary droplets move out of the recording area owing to their high ejection velocity.

Figure E.2(b) sheds more light on the aforementioned concept. Here, the recording is performed at a higher magnification, which simultaneously reduces the field of view. As such, the secondary droplets move out of the recording frame faster. Consequently, the difference between the total number and number of secondary droplets in the current frame becomes more prominent. In that scenario, both these definitions are bound to offer different perspectives regarding the mean size of the spray of secondary droplets. The situation becomes more critical as the impact velocity increases in the splashing regime. The secondary droplets ejected from the rim acquire high velocity and rapidly move out of the recording frame. In Chapter 6, the concept of the total number of droplets [i.e., the number of droplets are added from each frame, even if they move out of frame in the next instant] to describe the size distribution of the secondary droplets, which eventually gives more flexibility in the high-speed recording process and offers a wholesome perspective of splashing dynamics [see the corresponding discussion in Section 6.3.6 of Chapter 6].

TH-2590_156103041